MBE-growth and characterization of Zn3N2 and Mg3N2 : from epitaxy to materials science

Philipp Maximilian John

To cite this version:

Philipp Maximilian John. MBE-growth and characterization of Zn3N2 and Mg3N2 : from epitaxy to materials science. Other [cond-mat.other]. Université Côte d'Azur, 2021. English. NNT : 2021COAZ4045 . tel-03507255

HAL Id: tel-03507255

https://theses.hal.science/tel-03507255

Submitted on 3 Jan 2022

THÈSE DE DOCTORAT

Croissance EJM et caractérisation de Zn_3N_2 et Mg_3N_2

De l'épitaxie à la science des matériaux

Philipp Maximilian JOHN
Centre de Recherche sur l'Hétéroépitaxie et ses Applications, CNRS

Présentée en vue de l'obtention
du grade de docteur en Physique
d'Université Côte d'Azur

Dirigée par :
Jesús Zúñiga-Pérez, DR, CNRS-CRHEA

Soutenue le : 29/06/2021

Devant le jury, composé de :
Amparo Fuertes, Prof., ICMAB-CSIC
Marius Grundmann, Prof., Universität Leipzig
Eva Monroy, DR, CEA-IRIG
Guillaume Saint-Girons, DR, INL
Tim Veal, Prof., University of Liverpool
Philippe Vennéguès, HdR, CNRS-CRHEA

Croissance EJM et caractérisation de Zn_3N_2 et Mg_3N_2

De l'épitaxie à la science des matériaux

Jury:

Président

Guillaume Saint-Girons, Directeur de Recherche, INL (CNRS-Ecole Centrale de Lyon), France

Rapporteurs

Eva Monroy, Directrice de Recherche, IRIG (CEA-CNRS), Grenoble, France

Guillaume Saint-Girons, Directeur de Recherche, INL (CNRS-Ecole Centrale de Lyon), France

Examinateurs

Amparo Fuertes, Professeure, ICMAB (CSIC), Barcelona, Espagne

Tim Veal, Professeur, University of Liverpool, Royaume-Uni

Marius Grundmann, Professeur, Universität Leipzig, Allemagne

Philippe Vennéguès, Ingénieur de Recherche, HdR, CRHEA (CNRS), Valbonne, France

Croissance EJM et caractérisation de Zn_3N_2 et Mg_3N_2 : de l'épitaxie à la science des matériaux

Résumé :

Les semi-conducteurs cubiques à base de nitrures du groupe II sont presque inconnus dans la communauté scientifique, même si beaucoup d'entre eux sont constitués d'éléments présents en abondance sur terre. Le Zn_3N_2 et le Mg_3N_2, par exemple, ne sont pas toxiques et ont des bandes interdites d'environ 1 eV et 3 eV, respectivement, ce qui en fait des candidats intéressants pour des applications dans des dispositifs optoélectroniques. Cependant, afin d'évaluer la potentialité de ces matériaux pour des applications, il est nécessaire de les synthétiser avec une qualité cristalline suffisamment élevée et de caractériser leurs propriétés physiques fondamentales.

Dans le cadre de cette thèse, nous développons la croissance épitaxiale de couches minces de Zn_3N_2 et de Mg_3N_2 par EJM. Afin d'éviter la décomposition des films minces de Mg_3N_2 à l'air, des couches de protection de MgO polycrystallin ont été déposées *in-situ* dans la chambre d'EJM. Cette couche augmente la durée de vie du Mg_3N_2 passant de quelques minutes à plusieurs semaines à l'air, permettant ainsi une caractérisation approfondie. L'orientation des couches minces, à la fois de Zn_3N_2 et de Mg_3N_2, sur des substrats de MgO (100) peut être contrôlée à façon, passant de (100) à (111) suite à une variation des conditions de croissance. Par ailleurs, le Zn_3N_2 (100) est épitaxié sur YSZ (100) et le Mg_3N_2 (111) est epitaxié sur des substrats YSZ (100) et MgO (111). Les relations épitaxiales et la qualité structurale de chaque combinaisons couche mince-substrat ont été déterminées en utilisant la diffraction d'électrons à haute énergie en incidence rasante, la diffraction de rayons X et / ou la microscopie électronique en transmission. Grâce à cela nous pouvons proposer une image précise de l'épitaxie de nitrures du groupe II et de leur microstructure, jamais rapportée précédemment dans la littérature.

En plus de leurs propriétés structurales, nous avons exploré certaines des propriétés physiques fondamentales du Zn_3N_2 et du Mg_3N_2. En raison de la sensibilité des nitrures du groupe II à l'humidité, une détermination fiable de la bande interdite optique du Zn_3N_2 et du Mg_3N_2 est difficile. En utilisant des mesures de photoluminescence, de réflectance diffuse et de transmittance, nous avons mesuré la bande interdite de Mg_3N_2, sur nos couches minces, et dont la valeur est 2.9 eV à température ambiante. Nous avons mesuré aussi celle du Zn_3N_2 qui vaut 1.0 eV à température ambiante (et se décale vers le bleu en fonction de la concentration de porteurs en raison de l'effet Moss-Burstein). Alors que les couches minces de Zn_3N_2 sont de type n et dégénérées, avec des concentrations de porteurs entre 10^{19} cm^{-3} et 10^{21} cm^{-3}, les couches minces de Mg_3N_2 se révèlent être électriquement isolantes. Enfin, la dilatation du réseau cristallin hors plan était surveillée en fonction de la température pour les couches minces de Zn_3N_2 et Mg_3N_2, permettant l'extraction de leurs coefficients de dilatation thermiques, des paramètres importants pour la conception d'hétérostructures épitaxiales. Nous avons établi des valeurs moyennes de 1.5×10^{-5} K^{-1} et 1.1×10^{-5} K^{-1} dans une gamme de température de 300 K à 700 K-800 K pour Zn_3N_2 et Mg_3N_2, respectivement, trois à quatre fois plus élevées que celles des nitrures du groupe III.

Mots clés : Epitaxie sous jets moléculaires, Nitrures du groupe II, Diffraction, Caractérisation optique et électriques des couches minces, Microscopie électronique en transmission

MBE-growth and characterization of Zn_3N_2 and Mg_3N_2: From epitaxy to materials science

Abstract:

Cubic group II-nitride materials are almost unknown in the scientific community, even though many of them consists of earth-abundant elements. Zn_3N_2 and Mg_3N_2, for instance, are non-toxic and have band gaps of around 1 eV and 3 eV, respectively, making them attractive candidates for the application in optoelectronic devices. However, in order to evaluate these materials for device applications it is necessary to grow them in a sufficiently high quality, and characterize their fundamental physical properties.

In this work we develop the epitaxial growth of Zn_3N_2 and Mg_3N_2 thin films by MBE. To prevent the decomposition of Mg_3N_2 thin films in air, we employed polycrystalline MgO capping layers grown *in-situ* in the MBE chamber, thereby increasing the Mg_3N_2 lifetime from a few minutes to several weeks in air and enabling further characterization. The film orientation of both Zn_3N_2 and Mg_3N_2 on MgO (100) substrates can be tuned from epitaxial (100) to (111) by varying the growth conditions. Apart from that, epitaxial Zn_3N_2 (100) is obtained on YSZ (100), whereas epitaxial Mg_3N_2 (111) is obtained on YSZ (100) and MgO (111) substrates. The epitaxial relationships and structural qualities are analyzed for all thin film-substrate combinations using reflection high-energy electron diffraction, x-ray diffraction and/or transmission electron microscopy, giving thereby a detailed insight into group-II nitride epitaxy and their film microstructure, as never reported before in the literature.

Besides their structural properties, we explored some of the fundamental physical properties of Zn_3N_2 and Mg_3N_2. Due to the sensitivity of II-nitrides towards humidity, a reliable determination of the optical band gap of Zn_3N_2 and Mg_3N_2 is challenging. By employing photoluminescence, diffuse reflectance and transmittance measurements we measure the band gap of our MBE-grown Mg_3N_2 thin films to be 2.9 eV at room temperature, as well as the band gap of MBE-grown Zn_3N_2 as a function of carrier concentration (1.0 eV at room temperature, blue-shifted due to the Moss-Burstein effect). While Zn_3N_2 thin films were found to be n-type and degenerate, with carrier concentrations between 10^{19} cm^{-3} and 10^{21} cm^{-3}, consistent with previous literature work, Mg_3N_2 thin films turn out to be electrically insulating. Finally, we monitored the out-of-plane lattice dilatation as a function of temperature for Zn_3N_2 and Mg_3N_2 thin films, enabling the extraction of their linear thermal expansion coefficients therefrom, an important parameter for the design of epitaxial heterostructures. We established average values of 1.5×10^{-5} K^{-1} and 1.1×10^{-5} K^{-1} in a temperature range from 300 K to 700 K-800 K for Zn_3N_2 and Mg_3N_2, respectively, three to four times higher than III-nitrides.

Keywords: Molecular beam epitaxy, Group II-nitrides, X-ray diffraction, Optical and electrical characterization of thin films, Transmission electron microscopy

Acknowledgments

This thesis is obviously not based on my work alone, but many collaborators, colleagues, friends and of course my family contributed to enable this journey. Besides the scientific problems that we addressed during these three years of research, there were several non-scientific ones that needed to be faced, from which some of them were simply linked to the fact that: "C'est la France".

When I decided to go to the Côte d'Azur for my PhD, I had to find an apartment to live. Although this task seems generally quite straightforward, it was accompanied by several problems. In order to move into an apartment in France, it is necessary to possess a French bank account, which is, in turn, only possible if you have a permanent residence address in France. After some communication in "Franglais" (a mixture of French and English) with my future landlord, it was somehow possible to circumvent this issue. Suddenly, however, he also wanted a warrant resident in France, who guarantees the rent by providing his/her salary papers of the last three months. Since I did not know any person to fulfill these conditions, I was a bit desperate and decided therefore to contact my PhD advisor in order to ask him what to do. Surprisingly, he sent me his salary papers right away and I was very happy, though a bit frustrated at the same time. Frustrated, because I saw the salary of a CNRS researcher, which is, in my opinion, not really appropriate for the degree of education and work that is needed in order to get this position. But still very happy, because I was touched that a person who I saw only once before in my life trusts me enough to be my warrant and thereby enabled that I could move into my future apartment at the Côte d'Azur. The fact that my warrant was my PhD advisor had another advantage: I could just stop paying my rent anytime whenever I was treated badly on work. As you may already imagine, this never happened during my stay in CRHEA, since it turned out that we had a very nice relationship.

Actually, while writing this paragraph, I was sending a fun e-mail to my advisor saying that I want register for a conference in Corsica that had absolutely nothing to do with my research. My main motivation was my office mate and very good friend Renato who was going there and we could have spent some time at the beach, drinking some beers and having fun after a long writing period and the even longer lasting COVID-19 pandemic. A few hours later he came to my office and told me that I could go, even though I would have to work a bit on my PhD defense presentation there. So before finishing this acknowledgments section, I already registered to go to Corsica. The first real travel after more than one year... nice!

Coming to the acknowledgments

If you asked me how were my three years of PhD, I would answer: very, very quick! This was mainly due to the "CRHEA family". I am very grateful that I could get to know all of you. For someone who moves to a new place it may be a bit difficult at the beginning to get in contact with new people, especially when you don't speak their language. Literally **everyone in CRHEA** was very friendly and very welcoming with me since the beginning. That's why I consider you all my second family. Also work-wise you all made an effort helping to start my PhD. It helps a lot to feel welcomed and accepted and it is very motivating to see that you try your best to make things working. Thanks to you all I got to know all the machines necessary to do measurements and growth, increased my theoretical knowledge in this area and, besides, learned a new language: French. I am very grateful to everyone of you for making my stay really enjoyable! In the following I want to give my special thanks to some members of the CRHEA family:

My biggest thanks goes to my PhD advisor **Jesús Zúñiga Pérez**, who enabled me my best professional experience of my life. Jesús, I find it very admirable how you are. I was coming as a student with Chemistry background to a Physics laboratory, having basically not really a clue of semiconductors. Nevertheless, you gave me a chance to start my PhD in CRHEA, you always treated me equally and during my stay here I did not only learn everything worth knowing on semiconductors, but especially how to make science. For every question, whether scientifically or not, you took your time to give advice and helped me to grow as a scientist as well as an individual. Besides our professional relationship, I really appreciated our personal one that we built in these three years. We had many funny discussions during coffee breaks. Sometimes you would pretend that you were angry with me although it wasn't actually the case. Sometimes you would join me and some friends to go to a bar in Antibes just because I randomly met you in the street. I hope we will stay in touch and have the possibility to meet and to work together in the future again.

Next, I would like to express my thanks to **Philippe Vennéguès** who taught me a lot about TEM and even had the "courage" to read my PhD manuscript. I remember one time that we were going to Marseille for TEM measurements with your private car. After two days of work, where it turned out that no measurement was working, we were coming back to CRHEA. On the highway a little stone was hitting the front window of your car and made a small crack there, which did not help to increase our mood. Arriving back in CRHEA, Jesús asked us, full of expectations, how it was and what were the results. We just answered him: "Nothing worked, the car is broken, but we were eating in a good restaurant at the Port of Marseille, so finally it was quite nice." It was always cool to work with you and I still hope that we have this chance in the future again. I would be really happy to learn how to do TEM from you.

Thank you also **Mathieu Leroux** for your help in optical experiments, as well as for correcting my articles and my PhD manuscript. The other PhD students were telling me that you can be quite strict and I remember that I had a lot of questions on photoluminescence at the beginning. However, besides teasing me a bit because I am Chemist, you did not seem strict at all. I thought first you gave up with me from the very beginning, but I continued with the experiments, learning little by little. I think you made an effort too for explaining me stuff in an easy way and, finally, we could work together and I can say now that I learned a lot from you (even though I am a Chemist). Thank you for your patience, for staying available any time and helping me in several kind of issues.

There are more members in the CRHEA family who contributed that my stay he became very unique and enjoyable. Among them are **Christiane Deparis**, **Hélène Rotella**, **Sébastian Chenot**, **Blandine Alloing**, **Patrice Genevet**, **Jean-Yves Duboz**, **Mohamed Al Khalfioui**, **Fabrice Semond**, **Virginie Brändli** and **Stéphane Vézian**. Christiane, I remember the first weeks where you showed me the MBE machine and explained me everything in "Franglais", it was really fun. Séb, we did unfortunately not work so much together, because "mes échantillons font trop chier", but discussing with you about politics was very nice, although you destroyed all my hopes for a better world. Patrice, although I am not a member of your team, you invited me often to Flatlight dinners. It was always funny to pass evenings with you and your group. Thank you all for the nice experiences that I had in CRHEA.

A professional experience in a new environment is closely linked to the personal impressions that one has from this place. Therefore I want to specially thank the members of the Open Space in CRHEA, who included my directly in their group and became very good friends of mine. We did not only share our office, but we spend evenings, parties, weekends and entire holidays together, making my stay in CRHEA an unforgettable one. **Victor Fan-Arcara**, we got along well from the very beginning of my arrival. I am impressed how easily you get in contact with new people and I will never forget our travel in Brasil and your wedding there. **Renato Juliano-Martins**, thank you for teaching me how make good caipirinhas! This is maybe the most practical skill for daily life that I learned during my PhD. **Max Meunier**, you are the best baby-foot player of CRHEA and I had the pleasure to learn some of your skills and to regularly got kicked my ass. Furthermore I want to thank **Valeria Bonito-Oliva** for all the nice parties, **Mario Ferraro** to be the CRHEA grandmother and **Rajath Sawanth** and **Sandeep Yadav Golla** for indian dinners.

I acknowledge also the support that I got from collaborators outside CRHEA. Thank you **Antonia Welk** and **Marius Grundmann** from Universität Leipzig to welcome me for two weeks, show me your laboratories and enable optical and electrical measurements. Furthermore I would like to thank **Gabriel Monge** from CEMEF MINES ParisTech, **Guillaume Saint-Girons** and **Romain Bachelet** from INL Lyon for high-temperature XRD measurements. A great thank also to **Frédéric Georgy** from CEMEF MINES ParisTech to measure XPS for us. Besides I acknowledge the financial support from the ANR project ZONE, making this work possible.

I end up thanking my family, who, from near or far, have given me support, help, an open ear and also a good mood during this thesis. Without my parents **Ute** and **Gerald**, my entire studies would not have been possible. They are always supporting me and giving me advice no matter what I did and decide I want to do. Also my sister **Nina** and my brother in law **Mario** with my little niece **Mia** are supporting me from far and help me to go through all kind of ups and downs that arrive in life. I am so happy that we have each other and that I can always count on you, no matter what comes. Thank you all for your love!

DANKESCHÖN!

Contents

Introduction

THE *digital revolution*, also referred to as third industrial revolution, started in the 20th century with the development of the first computers in the 1940s [1] and led to radical changes of everyone's daily life. Although initially with poor calculation power, computers gained in performance, were already indispensable for the moon landing in 1969 [2] and became finally connected by the world wide web in 1989 [3]. Nowadays, the world is digitalized and nearly everyone uses personal computers, as well as optoelectronic devices addressing an increasing number of applications, for example in data storage (CDs, DVDs, USB flash drives), communications (mobile phones) and projection (flat panel displays, video projectors).

Many of the above-mentioned products are not manufacturable without the use of *semiconductors*. Integrated circuits, for instance, the base of microchips and hence, computers, are composed of numerous transistors, a semiconductor device that allows the switching and amplification of electric current. The first transistor made of germanium (Ge) was already demonstrated by Bell Labs in 1947 [4]. However, early transistors suffered from high leakage currents and low operation temperatures of 70 °C due to the small Ge band gap of 0.67 eV [5]. They were therefore replaced by silicon (Si) transistors in 1954 [6], which became the dominating semiconductor material up to now. While semiconductors were initially used in their bulk form, nowadays' electronic devices consist of semiconducting *thin films*, which are commonly grown on Si substrates. On the one hand, the use of thin films reduces the amount of utilized material, allowing the production of cheaper and smaller devices, such as microchips. On the other hand, the confinement in one dimension down to nanometric scales leads to the occurrence of quantum effects, which enabled the improvement of optoelectronic devices, such as light-emitting diodes (LEDs) and semiconductor lasers.

A breakthrough for solid state lightening was certainly the development of efficient white-light LEDs based on group III-nitrides, which was awarded with the Nobel Prize for Physics in 2014 [7]. III-nitride materials are nowadays well-established in the commercial market of opto- and microelectronic devices, as in lasers [8], LEDs [9] and transistors [10]. These versatile applications are, after all, feasible due to the physical properties of III-nitrides, i.e. a direct, widely tunable band gap from the near infrared (IR) to the deep ultraviolet (UV) spectral range, as well as the possibility to fabricate n- and p-type doped III-nitride materials. The final application of GaN and related III-nitrides in devices was accomplished thanks to the development of high-quality epitaxial thin films coupled with efficient device designs.

In the last years, the advent of a new industrial revolution can be foreseen: in 2010, the number of devices connected through internet was for the first time larger than the number of human beings on this planet [2]. These devices will be soon connected with the 5G technology, whose development was initiated in 2016 [11], enabling data-communication of machines with each other. The so-called "Internet of things", requiring new concepts of smart devices that perceive their environment, is predicted to eventually lead to large energy savings [12] (although one might express some skepticism about this argument suggested so many times). To realize this goal, research in semiconductor sensing technology (e.g. development of electronic noses or electronic tongues), in communication between the devices (e.g. by new platforms), as well as in the application side (e.g. new devices for smart lighting) is necessary.

The III-nitride system will be surely contributing to the development of these applications. Nevertheless, there are some limitations associated with this material system: when it comes to optoelectronic applications, it suffers from low efficiencies in the wavelength range above 550 nm (i.e. in the red visible spectrum). Quantum wells of gallium nitride (GaN) and indium gallium nitride (InGaN) with large indium (In) concentrations are required to cover this spectral range. However, these layers are challenging to grow with sufficiently high quality, leading to a drop of external quantum efficiency (EQE) to lower than 20 % in the red spectral range, as shown in Figure 1(a) [13], although more recent advances enable III-nitrides to eventually cover the full visible spectrum with large efficiencies [14]. The reason for the low EQE lies, on the one hand, in an increased quantum confined Stark effect (QCSE) for InGaN with larger In concentration, reducing thereby the overlap between electron and hole wave-functions [15, 16]. On the other hand, the InGaN material quality decreases, probably due to the differences in optimum growth temperature and lattice parameters of the binary GaN and indium nitride (InN) compounds, as indicated in Figure 1(b), leading to larger non-radiative recombination rates [13]. Another factor may be increased random fluctuations of the In content in InGaN, naturally occurring in such ternary alloys and leading to statistical spreads of the electronic states, thereby reducing the LED efficiency too [13, 17, 18].

Besides the physical limitations of III-nitride materials, there is another limitation that will probably become more critical in the future: In and Ga are "critical elements", i.e. they are rare, present in very low concentrations or unevenly distributed, leading to a critical availability and high prices [19, 20].

Thus, to realize the above-mentioned applications, more research in semiconductor materials, especially on earth abundant ones, is necessary. Besides new device designs, it is important to seek for novel semiconductors that can eventually complement or substitute the existing ones. The development of well-controlled, high-quality epitaxial thin films plays a key role in this research, allowing to reliably explore the fundamental physical properties of these unknown materials and, eventually, exploit them in devices.

In contrast to III-nitrides, the research on II-nitride materials is almost in-existent and

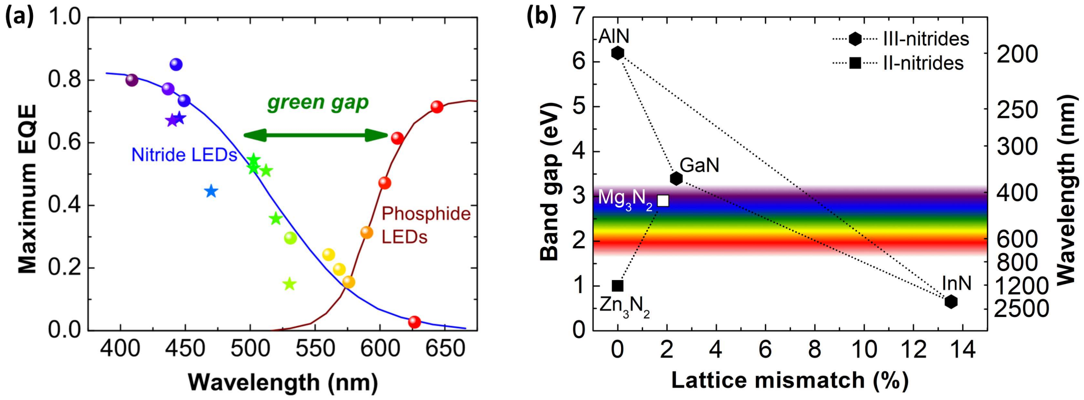

Figure 1: (a) Maximum External Quantum Efficiency of III-nitride LEDs as a function of their emission wavelength, reprinted from [13]. Note that reference [13] dates back to 2016 and the efficiencies of nitride LEDs in the green and red spectral range are continuously improved. (b) Comparison of III- and II-nitride band gaps as a function of their lattice mismatch. Note that the III-nitride lattice mismatches are calculated with respect to AlN and the II-nitride lattice mismatches with respect to Zn_3N_2. The dotted lines indicate the corresponding ternary compounds (bowing parameters are neglected).

some of their basic physical properties are still unknown. Magnesium nitride (Mg_3N_2), for instance, was first observed as early as 1857 [21]. Nevertheless, its epitaxial growth was in-existent at the beginning of this PhD and many of its properties, such as band gap, electrical characteristics or linear thermal expansion coefficient were still under controversial discussion or, in most cases, unknown. This is quite surprising, given that magnesium (Mg) metal and nitrogen (N) are earth abundant elements. Furthermore, Mg_3N_2 was detected as a parasitic phase in highly Mg-doped GaN, where it decreases its doping efficiency [22], which demonstrates also the technological relevance of this material and which might have pushed the community to address its fundamental properties.

Another, and probably the most studied, II-nitride material is zinc nitride (Zn_3N_2), attracting attention due to the strong interest to fabricate p-type doped zinc oxide (ZnO) in the 2000s. In this context, several attempts were made to achieve p-type ZnO, e.g. by (partial) oxidation of Zn_3N_2 [23–31] or by fabricating nitrogen-doped ZnO from Zn_3N_2 targets, as demonstrated by pulsed laser ablation [32]. This led also to increased research activity on Zn_3N_2 itself, including first demonstrations of Zn_3N_2-based devices, such as thin film transistors (TFTs) [33–41].

A material that emerged from these approaches is zinc oxynitride (ZnON), proposed by Samsung Electronics as an alternative in flat panel displays to replace hydrogenated amorphous silicon (a-Si:H) TFTs, having a limited electron mobility of $\sim 1\,\mathrm{cm^2V^{-1}s^{-1}}$ [42–45]. This ternary ZnON alloy was designed to deactivate oxygen vacancies naturally occurring in ZnO, and to enable electron mobilities as large as $100\,\mathrm{cm^2V^{-1}s^{-1}}$, even in an amorphous matrix, making it highly promising for the next generation of displays.

Although alloying of two (or more) materials is known to allow the manipulation of material properties according to the requirements necessary for device production (as also demonstrated for many III-V semiconductors), nobody tried to apply this approach on II-nitride materials at the beginning of this project. In particular, the Zn_3N_2/Mg_3N_2 system offers several possible advantages in the context of material engineering. Due to the very similar ionic radii of the Zn^{2+} and Mg^{2+} cations [46], being both hosted in the cubic anti-bixbyite structure, the two materials have a relatively low lattice mismatch, as indicated in Figure 1(b). Hence, once these materials can be epitaxially grown in sufficiently high quality, it should be relatively straightforward to grow also its ternary $(Zn_{1-x}Mg_x)_3N_2$ compound in a large compositional range, thereby covering almost the whole visible spectral range and enabling to address a wide range of applications. Finally, the compounds Zn_3N_2 and Mg_3N_2 consist of earth abundant elements, enabling in principle the possibility of cheap and large scale production.

In this work, we develop the epitaxial growth of Zn_3N_2 and Mg_3N_2 using plasma assisted molecular beam epitaxy (MBE) with crystalline qualities never reported before in literature. We explored some of their basic physical properties, such as band gaps, linear thermal expansion coefficients and electrical characteristics and proposed strategies to improve their quality further. These developments are the base for addressing the growth of ternary II-nitride compounds, such as $(Zn_{1-x}Mg_x)_3N_2$, where we obtained first epitaxial thin films by the end of this PhD.

In the **first chapter**, we introduce the II-nitride system, being the materials of interest in the context of this thesis. Epitaxy and the associated occurrence of strain and defects, as well as the choice of adequate substrates for II-nitride heteroepitaxy are discussed. Subsequently, we address the anti-bixbyite crystal structure, the reactivity of II-nitrides and the fundamental physical properties of Mg_3N_2 and Zn_3N_2, as established before the beginning of this PhD. Finally, the state of development and applications up to date, as well as the motivation for this thesis, are discussed.

The **second chapter** covers the principles of MBE as a technique for epitaxial thin film growth. Moreover, the techniques employed during this thesis for structural, optical and electrical characterization of the grown thin films are briefly introduced. We discuss in more detail techniques using diffraction as a means of characterization, since they allow the evaluation of the film microstructure and crystalline quality, which are the key figures of merit for the development of epitaxial growth and have been systematically employed during this PhD.

The epitaxial growth of Zn_3N_2 is discussed in the **third chapter**. We report epitaxy for two Zn_3N_2 orientations on two different substrates, investigate the epitaxial relationships and the crystalline quality of the thin films. Furthermore, we investigated the thermal expansion coefficient of Zn_3N_2, an important parameter for growth optimization, and discuss strategies to improve the crystalline quality in epitaxial Zn_3N_2. To evaluate its applicability in devices, we measured the electrical and optical properties of Zn_3N_2, paying special attention to their correlation with crystallinity and carrier concentrations, respectively.

The **fourth chapter** deals with Mg_3N_2 epitaxy. A growth process for a protective MgO capping layer was developed in order to prevent the otherwise irreversible decomposition of Mg_3N_2 in air. Epitaxial Mg_3N_2 was obtained in two film orientations and on three different substrates. The epitaxial relationships and the structural quality for each film-substrate combination is addressed. Furthermore, we performed in-depth structural analysis on Mg_3N_2 (111) grown on MgO (100) using advanced diffraction techniques, allowing us to develop a growth model and to discuss strategies for further growth optimization, also thanks to the investigation of its thermal expansion coefficient. At last, we investigated the optical properties of our Mg_3N_2 thin films and compared them to commercially available Mg_3N_2 micro-particles.

Finally, the **last chapter** summarizes this thesis and discusses perspectives for future work in this direction.

Chapter 1

Epitaxy and II-nitride thin films

In this Chapter, epitaxial growth in general, its application to the II-nitride material system, as well as the fundamental physical properties of Zn_3N_2 and Mg_3N_2 are addressed (as established in 2018, i.e. at the beginning of this PhD). This chapter covers:

- Epitaxy, choice of the substrate and defects in thin films
- II-nitride materials, their crystal structure and reactivity in air, with a particular focus on Zn_3N_2 and Mg_3N_2
- Band structure and electronic properties of Zn_3N_2 and Mg_3N_2
- State of the art and applications of Zn_3N_2, Mg_3N_2 and their alloys
- Motivation for the PhD work

1.1 Epitaxial thin film growth

A thin film is a condensed layer of solid matter deposited on a bulk material, referred to as substrate. Among various classifications that can be made to differentiate thin films (as for example by their composition or material properties), they can be classified according to their microstructure, being commonly assigned to three main groups: Amorphous, polycrystalline and single crystalline (epitaxial) thin films, as shown in Figure 1.1. While amorphous thin films show an unorganized atomic arrangement, without any long-range order, epitaxial thin films are fully crystalline and exhibit one definite orientation with respect to their crystalline substrate. Polycrystalline thin films are an intermediate case, as they consist of crystallites (grains), which are randomly oriented on the substrate and separated by grain boundaries. The synthesis of crystalline thin films is commonly referred to as *growth*.

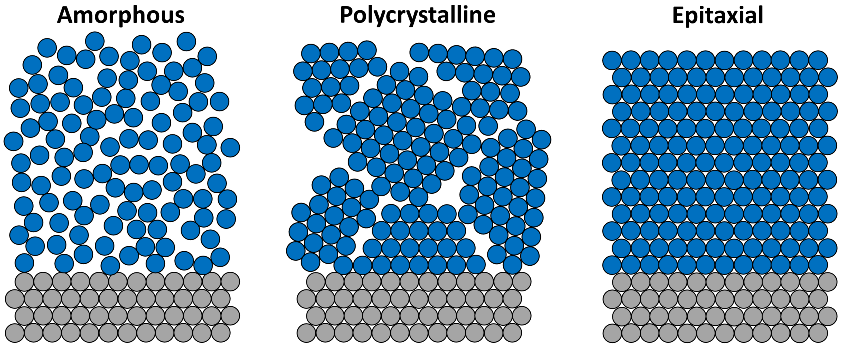

Figure 1.1: Different thin film microstructures.

In the frame of this project we develop the epitaxial growth of II-nitride thin films by MBE with the aim of obtaining high quality films, as achieved by this technique on many other material systems (for MBE see Section 2.1). Besides the strict qualitative requirements that thin films have to fulfill for the application in opto- and microelectronic devices, the growth of epitaxial, high quality II-nitride thin films has the advantage that basic physical properties, such as band gap, thermal expansion coefficient, etc., being partially unknown up to now, are less influenced by the presence of defects, as will be discussed in the following, and should be measured more reliably.

1.1.1 The choice of the substrate

There are several factors that influence the quality of epitaxial thin films. The choice of the substrate plays probably the most crucial role, which can either consist of the same material (homoepitaxy) or, more commonly, of a different material than the growing film (heteroepitaxy). The application of homoepitaxy is rather limited, because the desired single crystalline substrates are often expensive, if even commercially available. On the other hand, due to the

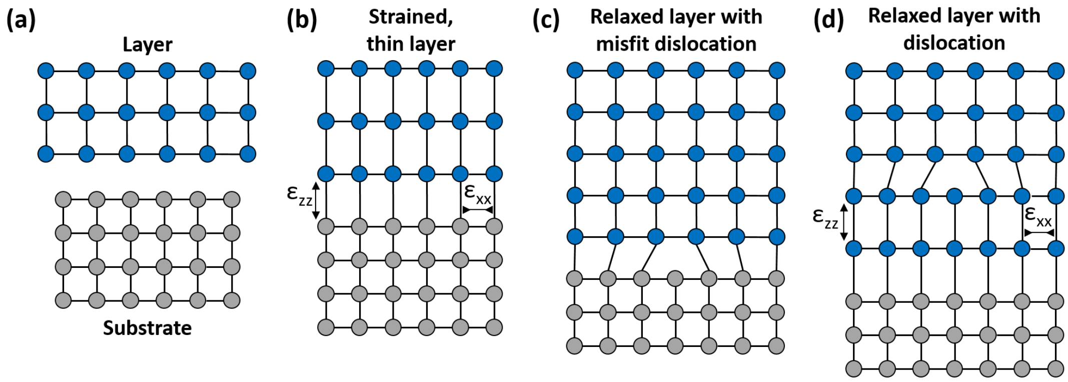

Figure 1.2: (a) Lattices of the substrate and a free-standing layer. (b) Pseudomorphic, defect-free layer. (c) Relaxed layer with misfit dislocation at the film-substrate interface. (d) Relaxed layer with dislocation within the thin film volume.

differences of thin film and substrate in chemical composition, crystal structure, orientation and/or lattice parameter, heteroepitaxial thin films often exhibit comparatively high defect concentrations. In the context of II-nitrides, the issue of lattice mismatch between film and substrate is particularly challenging due to the large lattice parameters of anti-bixbyite materials (for the cubic anti-bixbyite crystal structure, see Figure 1.7 in Section 1.2.1). Lattice mismatches, as shown in Figure 1.2(a), induce strain in the growing crystal. In the case of very thin films, the layer can stay pseudomorphic, i.e. it adopts the lattice parameter of the substrate while undergoing an elastic deformation, as shown in Figure 1.2(b). However, in case of thicker layers relaxation takes place and the strain is released by the formation of defects such as misfit dislocations at the film-substrate interface [see Figure 1.2(c)], or dislocations within the thin film volume [see Figure 1.2(d)]. In this case the layer undergoes an irreversible, plastic deformation.

Therefore, for the selection of an appropriate substrate the lattice mismatch between the respective M_3N_2 layer to be grown (where M denotes the corresponding metal cation) and the possible substrate material has to be considered. We therefore calculated the mismatch between Mg_3N_2 and Zn_3N_2 with selected substrate materials according to

$$M = \frac{a_L - a_S}{a_S}, \tag{1.1}$$

where a_L and a_S are the in-plane lattice parameters of the layer and the substrate, respectively. Hence, a positive M indicates compressive strain with $a_L > a_S$ (see Figure 1.2), whereas a negative M indicates tensile strain, where $a_L < a_S$. However, epitaxial growth is commonly done at temperatures higher than room temperature. Due to the differences in linear thermal expansion coefficient of thin film and substrate, the lattice mismatch varies as a function of temperature. For mature semiconductors (such as GaAs or GaN), this phenomenon is known and taken into account when considering the film-substrate configuration. For II-nitrides, such as Zn_3N_2

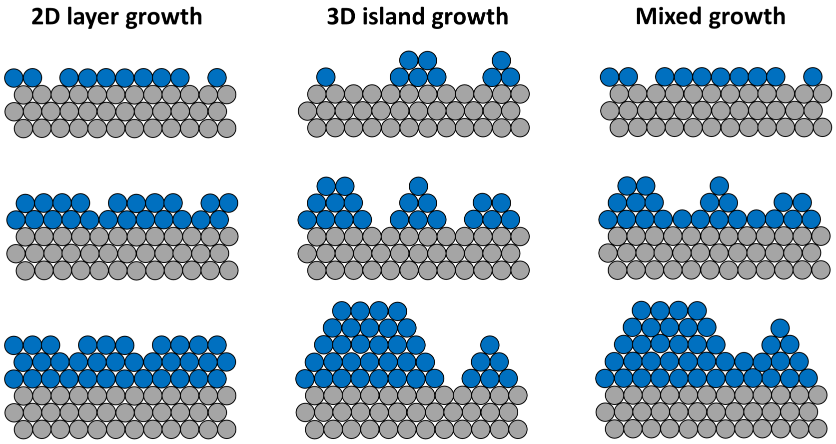

Figure 1.3: Different growth modes of a thin film.

and Mg_3N_2, however, neither the exact growth temperatures for epitaxy, nor the linear thermal expansion coefficients were known at the beginning of this project.

Another factor influencing the growth process is the chemical composition of layer and substrate, determining the interaction strengths between the arriving adatoms and the surface (see Figure 1.3). If the chemical interaction strength between the adatoms themselves is stronger than between the adatoms and the surface, the nucleating atoms tend to conglomerate and form three-dimensional (3D) islands, and the growth mode is referred to as 3D island growth (or Volmer-Weber growth). On the opposite, if the interaction strength is stronger between the adatoms and the surface than between the adatoms themselves, the nucleating atoms form a two-dimensional (2D) layer, and the growth mode is referred to as 2D layer growth (also Franck-van der Merwe growth). An intermediate case is the so-called mixed (or Stranski–Krastanov) , consisting in an initial 2D layer growth that turns into 3D island growth subsequently, due to a competition between the energies associated to the adatoms/surface system and the adatoms system alone. Once the thickness is sufficiently large, the interaction between adatoms overcomes the adatoms/surface interaction.

Besides the lattice parameter and composition, determining the rotational symmetry of a substrate around its out-of-plane axis (being perpendicular to the sample surface), determined by its crystal structure and orientation, is crucial. A symmetry mismatch between the substrate and the growing epilayer can lead to the formation of rotational epitaxial domains, i.e. energetically equivalent crystallites that exhibit different in-plane rotation angle with respect to the substrate. In general, crystal twinning needs to be avoided, since it leads to boundaries between the twins themselves, which may deteriorate the optical and electrical properties of the thin film. The minimum number of energetically equivalent epitaxial domains is entirely dependent on the symmetry relation between the substrate and the epilayer, with their C_n and C_m rotational axes around the surface normal having n and m-fold symmetries, respectively [47].

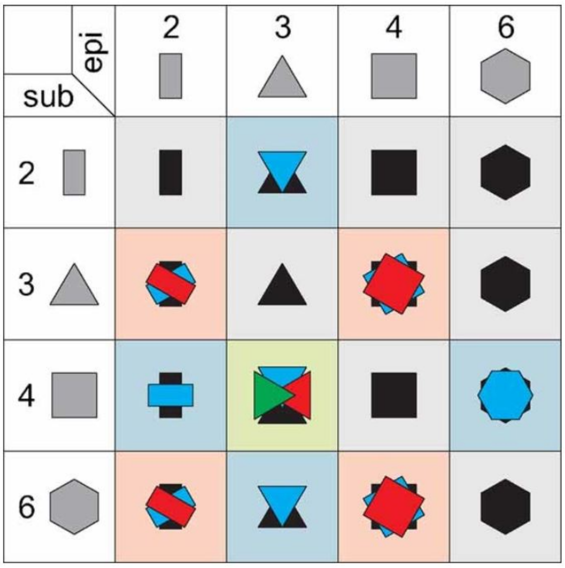

Figure 1.4: Schematic representation of the number of epitaxial domains, depending on the substrate (sub) and epilayer (epi) symmetries, reprinted from [47].

The number of rotational domains is given by

$$N_{domains} = \frac{\mathrm{lcm}(n,m)}{m}, \tag{1.2}$$

where $n, m \in \{1,2,3,4,6\}$ and lcm denotes their least common multiple. Figure 1.4 shows the numbers and arrangements of the energetically equivalent rotational domains originating from different substrate-epilayer symmetries. Note that the actual number of domains occurring in epitaxy may be higher than calculated in Equation 1.2, which provides the minimum number one should obtain based on symmetry considerations alone.

The crystallographic parameters of Zn_3N_2 and Mg_3N_2 and those of selected substrate materials, namely magnesium oxide (MgO), yttria stabilized zirconia (YSZ) and a-plane sapphire, are summarized in Table 1.1. MgO and YSZ have a cubic structure and exhibit thus the same symmetry as the M_3N_2 layers, being therefore both in principle suitable substrate materials. However, the unit cells of Zn_3N_2 and Mg_3N_2 are approximately two times larger than the ones of MgO and YSZ. Therefore, considering a domain matching epitaxy [48], we multiplied the substrate lattice parameter by two when using Equation 1.1 to calculate the lattice mismatch to the respective M_3N_2 material.

The large lattice mismatch to MgO (100) will impose a high compressive strain to the growing M_3N_2 (100) crystal (if epitaxy is even possible in this configuration), leading probably to high defect densities. The lattice mismatch between YSZ (100) and M_3N_2 (100) is smaller, hence, the defect densities occurring in this configuration might be lower than on MgO. Note again that, in these cases, the lattice mismatches are calculated using two substrate unit cells with one M_3N_2 unit cell.

Table 1.1: Crystallographic parameters of selected substrates and their lattice mismatch to Zn_3N_2 and Mg_3N_2. Note that the lattice mismatches of the respective M_3N_2 crystal to MgO, YSZ and *a*-plane sapphire were calculated using two substrate unit cells with one M_3N_2 unit cell. The literature lattice parameters were obtained from [49–52].

	Mg_3N_2	**Zn_3N_2**	**MgO**	**YSZ**	**Sapphire**
Crystal structure	anti-bixbyite	anti-bixbyite	rocksalt	fluorite	corundum
Orientation	(100)	(100)	(100)	(100)	$(11\bar{2}0)$
Symmetry	4-fold	4-fold	4-fold	4-fold	2-fold
Lattice parameter a (Å)	9.953	9.769	4.211	5.145	4.758
Lattice parameter c (Å)	—	—	—	—	12.983
Lattice mismatch Mg_3N_2	—	1.9 %	18.2 %	−3.3 %	4.6 %/−23.3 %
Lattice mismatch Zn_3N_2	−1.8 %	—	16.0 %	−5.1 %	2.7 %/−24.8 %

Interestingly, epitaxial Zn_3N_2 was reported on *a*-plane sapphire [53], although the lattice mismatch along the in-plane *c*-direction is very high and symmetry mismatch between sapphire and Zn_3N_2 leads necessarily to two epitaxial twins. However, instead of growing along the [100] direction, the Zn_3N_2 layer was found to be oriented along [111], thereby reducing the lattice mismatch with the substrate to 6.5 %, which did however not prevent the occurrence of two twin domains (see Figure 1.4). This example demonstrates that epitaxy can still occur on materials that may be at first appearance not suitable as substrate material. The final orientations of the growing crystal with respect to its substrate, also referred to as *epitaxial relationships*, are difficult to predict and may change as a function of growth parameters. Therefore, it is indispensable to perform growth on several different substrates in order to find out the most suitable configuration.

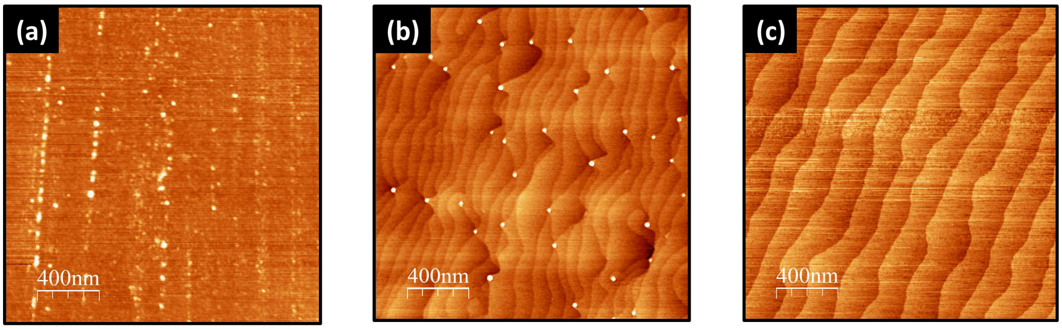

Figure 1.5: 2×2 μm^2 AFM micrographs of different single-crystalline substrate surfaces. (a) MgO (100) without any surface treatment. (b) MgO (100) and (c) YSZ (100), both annealed for 2 min under O_2 atmosphere at 1150 °C.

Besides the lattice parameter and symmetry of the substrate, its surface quality is crucial for epitaxial growth. While sapphire and Si substrates are commercially available as "epi-ready" (i.e. with a high surface quality, hence, ready for epitaxy right after delivery) in numerous orientations and sizes, MgO and YSZ, for instance, are available only in selected orientations and sizes, and with limited surface quality. Figure 1.5(a) shows an AFM image of an as-delivered $10\times20\,\mathrm{cm}^2$ MgO (100) substrate (for more details about AFM, see Section 2.3.1). The surface is dominated by agglomerates that are oriented along more or less parallel lines. These agglomerates are probably residues of the chemical-mechanical polishing process that is used for surface smoothening of the substrate and may lead to perturbations during the nucleation process. Interestingly, by applying a rapid thermal annealing (RTA) procedure under oxygen atmosphere in CRHEA's clean-room, one can achieve high surface qualities, as shown in Figure 1.5(b). The step-and-terrace morphology is due to a voluntary introduced miscut, which usually promotes the nucleation process, where the measured step height corresponds to one MgO unit cell. Note that the annealing process did not eliminate all the agglomerates from the surface, which either diffuse to the rinks of the atomic steps, or, on the contrary, prevent the diffusion of the atoms surrounding them, leading to the same result. On the other hand, Figure 1.5(c) shows an AFM micrograph of a $10\times20\,\mathrm{cm}^2$ YSZ (100) substrate, annealed under the same conditions as the MgO substrate. While also in this case a step-and-terrace morphology is present after annealing, where the step height corresponds also in this case to one YSZ unit cell, the residues of the chemical-mechanical polishing procedure could be successfully removed, leading to a higher surface quality.

1.1.2 Defects in crystals

All crystals, even bulk ones, exhibit imperfections. These defects can be classified according to their dimensionality into point defects, line defects (e.g. dislocations), surface defects (e.g. stacking faults, grain boundaries) and volume defects (e.g. misorientations, precipitates, bubbles) [54]. All of these defects lead to deviations of the atoms from their ideal crystallographic positions and influence hence the mechanical, electrical and optical properties of the crystal [54–58]. The defect concentrations of a crystal depend, among others, on its synthesis conditions. Hence, in the context of epitaxy they are determined by the film-substrate configuration, as mentioned in Section 1.1.1, as well as the growth method and growth conditions. In the following we restrict ourselves to point defects, grain boundaries and misorientations, being the most important defect classes found in the context of this project.

Intrinsic point defects are either missing atoms (vacancies) from a lattice site, additional (interstitial) atoms into a non-lattice site or anti-sites (i.e. exchanged anion and cation positions), causing very local distortions of the crystalline lattice. The equilibrium concentration of these defects depends, among others, on the growth temperature, since their formation energy is positive. However, thin film growth is a non-equilibrium process and, therefore, the defect concentration may be controlled, to some extent, by adapting the growth conditions.

This becomes particularly important in the case of extrinsic defects, i.e. impurities. Impurity atoms, which can either substitute atoms located on lattice sites or occupy interstitial sites, may be intentionally introduced and enable to control some of the crystal's properties. In semiconductors, for instance, the substitution of lattice atoms with impurities having ox-

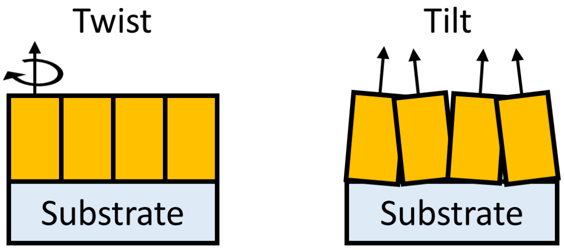

Figure 1.6: Schematic representation of misorientations (twist and tilt) that can occur in epitaxial thin films.

idation states different than the host atoms (doping), enables to introduce additional charge carriers and to control thereby the crystal's electrical properties.

Grain boundaries occur particularly in polycrystalline thin films, where they separate the crystallites the layer consists of. While the grains themselves are single-crystalline and exhibit the above-mentioned defects, the grain boundaries are two-dimensional interface defects, initiating a directional change of the crystalline lattice when passing from one grain to another. The nature of the grain boundaries is hence highly dependent on the rotational angle between two grains. Polycrystalline films exhibit mainly *high-angle* grain boundaries, since the rotational angle between the grains is large. The atomic structure of high-angle grain boundaries is usually rather complex, although periodic, and is described in more detail in reference [59].

A special case of high-angle grain boundaries is found between epitaxial twin domains. As discussed in Section 1.1.1, epitaxial twins are the consequence of a symmetry mismatch between the film and the substrate and are obtained by rotating one twin by usually 60°, 90° or 180° around the out-of-plane axis (see Figure 1.4). Due to this rotational symmetry of the twins with respect to each other, their boundary can, in the simplest case, consist of a shared atomic plane between both twin lattices, the so called twin plane [54]. Due to their well-defined geometrical relation, this same twin plane may be identical between all the present twins.

However, grain boundaries can also occur more generally in epitaxial thin films, as these films may consist of mosaic crystallites that are only slightly misoriented with respect to each other [60, 61]. As mentioned earlier, epitaxial thin films exhibit a certain crystallographic relationship to the substrate on which they are grown. Misorientations are rotational deviations of the crystallite's lattice with respect to this ideal epitaxial relationship. They are described by a rotational angle around the out-of-plane axis of the film (also referred to as *twist*) and a rotational angle around an in-plane axis (referred to as *tilt*). Figure 1.6 shows a schematic representation of twist and tilt that can occur in epitaxial mosaic crystals. The necessary consequence of these slight misorientations are grain boundaries. These so-called *low-angle* grain boundaries consist commonly of arrays of threading dislocations [54] that compensate the angular mismatch between the grains (similarly to misfit dislocations that compensate the lattice mismatch between film and substrate, see Figure 1.2). The larger the misorientation angles, the higher the threading dislocation density in the boundary that is needed for orientation compensation. More information about defects and, especially, dislocations can be found in reference [54].

1.2 II-nitride materials

To construct an imaginary crystalline II-nitride material one needs to combine an element in the +II oxidation state with the element nitrogen, exhibiting the -III oxidation state. The resulting chemical formula is then M_3N_2, where M denotes the corresponding metal cation. M_3N_2 compounds are known for alkaline earth metals in group 2 of the periodic table, such as Be_3N_2, Mg_3N_2, Ca_3N_2, which crystallize in the cubic anti-bixbyite structure [50, 62]. The crystal structures of Sr_3N_2 and Ba_3N_2 are not yet experimentally confirmed, but density functional theory (DFT) calculations propose the anti-bixbyite structure as the most stable polymorph for Sr_3N_2 and as one possible polymorph for Ba_3N_2 [63]. This structure is deduced from the crystal structure of the bixbyite mineral $(Mn, Fe)_2O_3$, but with inversed cation and anion positions.

Besides alkaline earth metals, many transition metals show +II oxidation states and can therefore possibly serve as cations for a II-nitride material, as it is for example the case for Zn_3N_2. Like the alkaline earth nitrides, Zn_3N_2 crystallizes in the cubic anti-bixbyite structure [50]. Due to the very similar ionic radii of Zn^{2+} and Mg^{2+} of 88 pm and 86 pm, respectively [46], Zn_3N_2 and Mg_3N_2 exhibit almost the same lattice parameters (see Table 1.1) making the growth of their ternary alloys or heterostructures particularly attractive. In the following we introduce the structural and physical properties of II-nitrides, with a focus on Zn_3N_2 and Mg_3N_2, being grown and investigated within this project.

1.2.1 Crystal structure of II-nitrides

Figure 1.7(a) shows an anti-bixbyite M_3N_2 unit cell (space group $Ia\bar{3}$, No. 206, for Wyckoff positions and symmetry operations see Figure A.1 of the Appendix), containing 80 atoms. The 48 M^{2+} cations, which are situated on crystallographically equivalent lattice sites, are tetrahedrally coordinated and occupy the 48e Wyckoff positions. On the other hand, the 32 N^{3-} anions are surrounded by M^{2+} in a distorted octahedral geometry and occupy two crystallographically non-equivalent lattice sites, Wyckoff 8b and 24d. The sixfold coordination of the N^{3-} anions can be considered as a deficient cubic one, as schematically shown in Figure 1.7(b).

The N^{3-} anions occupying the Wyckoff 8b sites exhibit two M-vacancies along the cube diagonal, leading to an equal bond length to all neighboring M^{2+} cations in the relaxed structure. On the contrary, the N^{3-} anions on the 24d sites exhibit two M-vacancies along the face diagonal of the cube, leading to an unequal relaxation and hence, the occurrence of three different bond lengths to the surrounding M^{2+} [64]. In this system, the M-vacancies form a specific network, situated on the 16c Wyckoff positions of the structure.

In the case of Mg_3N_2, these vacancies may play in important role when the material is ex-

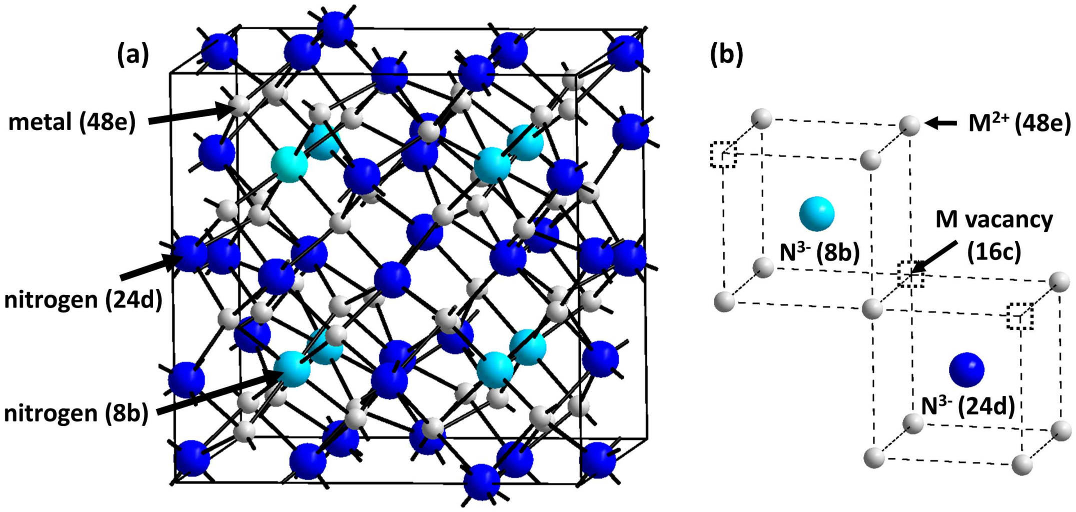

Figure 1.7: Crystal structure of a cubic anti-bixbyite material with the formula M_3N_2. (a) Representation of one unit cell. (b) Cooordination sphere of the two non-equivalent N sites (small dotted squares represent M vacancies).

posed to hydrogen. Theoretical calculations predict that the Mg-vacancy sites can be filled by hydrogen ions (resulting, formally, in the cubic CaF_2 fluorite crystal structure), making Mg_3N_2 an interesting candidate as a hydrogen storage material [64].

1.2.2 Reactivity towards humidity

Interestingly, most of the II-nitrides discussed above are sensitive to humidity and decompose to their corresponding oxides or hydroxides and ammonia, according to one of the following reactions [65–67]:

$$\mathrm{M_3N_2 + 6\,H_2O \longrightarrow 3\,M(OH)_2 + 2\,NH_3} \tag{1.3a}$$

$$\mathrm{M_3N_2 + 3\,H_2O \longrightarrow 3\,MO + 2\,NH_3}. \tag{1.3b}$$

The reason for this reactivity lies most probably in the low ionization energies of group II elements [68], leading also to a strong oxidation tendency of the alkaline earth metals themselves. Furthermore, the formation energies of M_3N_2 compounds in case of $M = Mg, Zn$ with respect to the elemental metal and molecular nitrogen are much smaller compared to their corresponding metal oxides ($\Delta H_f^0(Zn_3N_2) = -22.6$ kJ mol^{-1} vs. $\Delta H_f^0(ZnO) = -348.3$ kJ mol^{-1}, $\Delta H_f^0(Mg_3N_2) = -460.7$ kJ mol^{-1} vs. $\Delta H_f^0(MgO) = -601.7$ kJ mol^{-1}) [69]. This is mainly due to the high stability of the nitrogen bonds of the N_2 molecule, being a general problem when dealing with growth of metal nitrides [70].

To illustrate this reactivity, we monitored the decomposition of commercial Mg_3N_2 microparticles (Alfa Aesar, nominal particle size: 44 µm, purity 99.5 %). The initially yellowish powder becomes completely white and undergoes a drastic volume increase within 24 h upon air exposure, as shown in the inset of Figure 1.8(a). In order to better quantify the decomposition kinet-

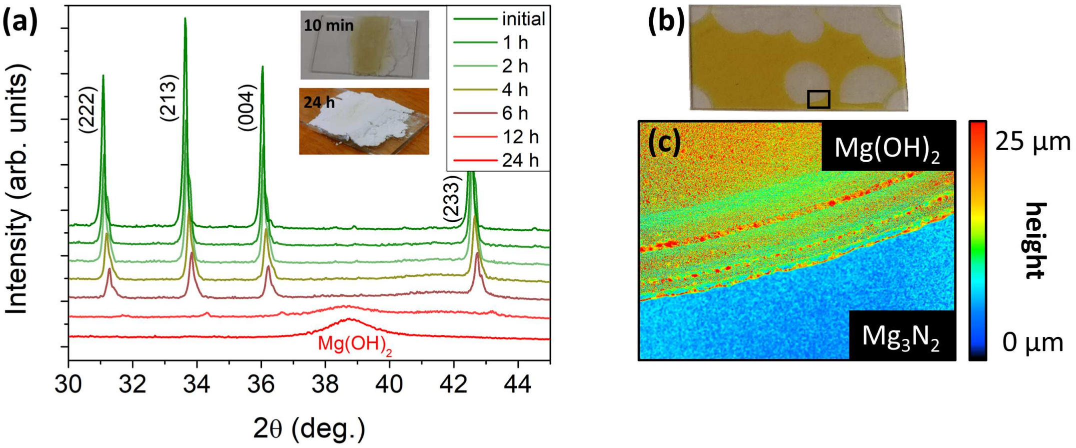

Figure 1.8: (a) Series of $2\theta/\omega$ scans on commercial Mg_3N_2 micro-particles in ambient conditions. The diffraction peaks for exposures shorter than 12 h correspond to Mg_3N_2. The insets show photographs of the initial and the decomposed powder. (b) Photograph of an Mg_3N_2 thin film capped with ~50 nm MgO after one week of air exposure. (c) Laser microscopy image of (b) in the area indicated by the black rectangle (measurements done in the Semiconductor Physics Group of the Leipzig University, Germany).

ics of the Mg_3N_2 micro-particles, we performed a series of XRD measurements as a function of time (for the theory of XRD see Section 2.2.1). As shown in Figure 1.8(a), the powder starts to decompose after only 1 h, indicated by a decrease in diffracted intensity, although no $Mg(OH)_2$ signal is yet detected. Indeed, the decomposition starts only on the surface of the micro-metric particles. Once the reaction spreads into the volume $Mg(OH)_2$ is detected, dominating the pattern after 24 h. Nevertheless, the final diffracted intensity from $Mg(OH)_2$ stays rather low, indicating that the product of the decomposition reaction exhibits a poor crystallinity. By evaluating the peak areas of the Mg_3N_2 reflections as a function of time, the decomposition kinetics can be quantified with an exponential fit using

$$A(t) = A_0 e^{-\frac{t}{\tau}}, \tag{1.4}$$

where A_0 is the initial peak area, $A(t)$ the peak area at the time t, and τ the decomposition time constant, indicating the moment where $\frac{A(t)}{A_0} = \frac{1}{e}$. Averaging the four reflections leads to a mean decomposition time constant of $\tau = (5.5 \pm 0.2)$ h for the Mg_3N_2 powder in ambient conditions. This fast reaction needs to be taken into account when dealing with II-nitride thin films, whose surface-to-volume ratio is considerably larger than the one of the micro-particles, leading to even faster reaction rates. Indeed, an investigation on the decomposition of 500 nm-thick Mg_3N_2 thin films finds a decomposition time constant of $\tau < 1$ min [71].

The high reactivity of II-nitride thin films towards humidity is probably the main reason limiting the research activity on these materials. Furthermore, it may account for the inaccuracy when determining the physical properties of II-nitrides, as will be discussed in the following sections. Therefore, the development of appropriate capping layers is indispensable when dealing with II-nitride film growth and, especially, their application in devices.

We investigated the decomposition of Mg_3N_2 thin films capped by a ~50 nm-thick polycrystalline MgO protection layer (grown *in-situ* in the MBE chamber). After one week of air exposure, the thin film starts to degrade in certain areas. Humidity enters probably around defects that are present in the MgO capping layer, as shown in Figure 1.8(b). Interestingly, once this process is initiated, the decomposed areas expand laterally and degrade thereby the whole Mg_3N_2 thin film within a few days. This process is accompanied by a volume increase, similarly to the decomposition of the Mg_3N_2 micro-particles, as measured by Laser-microscopy investigations shown in Figure 1.8(c). The development of an appropriate protecting MgO capping layer is discussed in detail in Section 4.2.2.

While Mg_3N_2 decomposes immediately in contact with air, Zn_3N_2 shows larger decomposition time constants, in the order of several days [66]. The uncapped Zn_3N_2 thin films grown within this project commonly decompose within 1 to 2 weeks, enabling still thorough thin film characterization. Therefore, we did in most cases not deposit capping layers on Zn_3N_2. Nevertheless, all grown samples were kept in a vacuum desiccator, ensuring the thin films to stay intact even for several years.

1.2.3 Band structure of Zn_3N_2 and Mg_3N_2

The calculated band structures of Zn_3N_2 and Mg_3N_2 are shown in Figure 1.9. For both materials, the valence band maximum (VBM) as well as the conduction band minimum (CBM) are located at the Γ-point of the Brillouin zone [see Figure 1.9(c)], indicating direct band gap semiconductors. Indeed, all theoretical calculations for Zn_3N_2 published so far find direct band gap behavior, although relatively large discrepancies are reported for the actual band gap energy (from completely metallic to 1.48 eV, depending on the calculation method) [72–77]. For Mg_3N_2, five of the theoretical studies find direct band gap transitions (ranging from 1.1 eV to 2.85 eV [64, 73, 78–80]), while one study suggests a 10 meV difference between a direct and an indirect transition around 2.25 eV, resulting in practice in a direct band gap character too [81].

DFT calculations find commonly largely scattered band gap energies, but their accuracy can be usually improved by taking into account experimentally measured values. However, it turns out that the determination of the band gap energies of Zn_3N_2 and Mg_3N_2 is not straightforward. The few experimental measurements for Mg_3N_2 suggest values ranging from 2.5 eV to 2.62 eV determined by UV-vis spectroscopy [82, 83], via 2.8 eV to 2.9 eV obtained by UV-vis spectroscopy and photoluminescence measurements [84–86], to a maximum value of 3.15 eV at room temperature obtained by UV-vis spectroscopy, too [84]. The discrepancy for Zn_3N_2 is even larger: Experimental values between 0.9 eV to 3.4 eV have been determined by various methods [23, 33, 35, 66, 87–101]. However, most of the recent reports, including photoluminescence measurements, find values in the range of 0.9 eV to 1.5 eV [23, 90–101]. Large discrepancies in band gap values are commonly observed as the band gap can be perturbed by

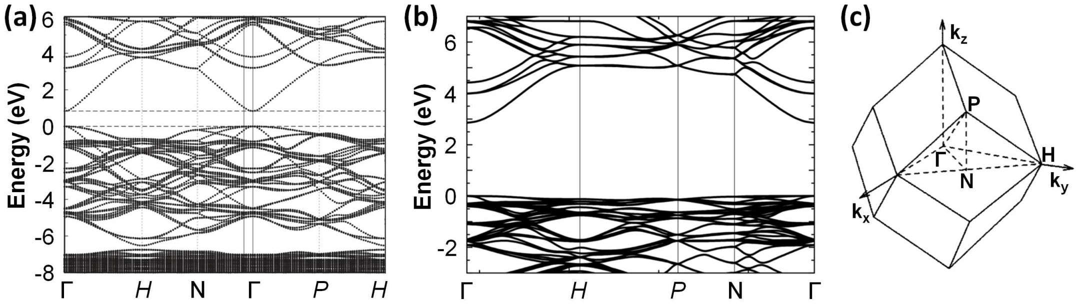

Figure 1.9: Calculated band structures of (a) Zn_3N_2 and (b) Mg_3N_2, reprinted from [72] and [78], respectively. The VBM and CBM of both materials are located at the Γ-point of the Brillouin zone, indicating direct band gaps. (c) First Brillouin zone of an anti-bixbyite material, reprinted from [79].

many factors, such as carrier concentration, crystalline quality and impurity atoms. An example is InN, whose band gap was thought for many years to be around 1.9 eV. With increased material quality, however, it was found to lay around 0.7 eV [102]. Indeed, due to the lack of single-crystalline II-nitrides, most of the experimental studies mentioned above are performed on polycrystalline materials, leading to large defect concentrations. This points out the need of fundamental research on II-nitrides, being necessary to increase their material quality and reliably measure their physical properties. Furthermore, it seems to be difficult to deposit non-degenerate II-nitrides. Most of the reports on Zn_3N_2, for instance, find high electron concentrations, larger than $10^{18}\,\mathrm{cm}^{-3}$ [71, 92, 96, 98, 99, 101, 103], which can shift the Fermi-level into the conduction band, leading to a larger apparent optical band gap due to the Moss-Burstein effect.

Nevertheless, the discrepancy in the reported band gap values, especially for Zn_3N_2, is too high to be explained by these effects. Hence, a different origin has to be considered, which is probably the strong tendency of the M_3N_2 compounds to oxidize in ambient conditions, as discussed in Section 1.2.2. Indeed, a change in chemical composition of a material leads necessarily to a change of its band gap energy. In case of a replacement of nitrogen atoms by oxygen ones, the band gap commonly increases due to the higher electro-negativity of oxygen [70]. This is probably the reason for the large reported band gap energies, of up to 3.4 eV for Zn_3N_2, which is close to the band gaps of ZnO and $Zn(OH)_2$, as also investigated by studies on intentionally oxidized Zn_3N_2 [66, 87, 91, 98, 104]. The tendency of oxidation explains, furthermore, the enormous number of reports dealing with transparent Zn_3N_2 thin films [33, 35, 89, 105], although commercial available Zn_3N_2 powder is black in color, indicating clearly a band gap in the infrared (IR) region.

Besides the actual band gap energies, the dispersion behavior of the bands is crucial for the evaluation whether or not a material is appropriate to be applied in devices, and which device is the most suitable one. A comparison of the electronic structure of Zn_3N_2 and Mg_3N_2 with InN and GaN, being widely applied in commercial devices, is given in Table 1.2. For both

Table 1.2: Summary of the electronic structure of Mg_3N_2 and Zn_3N_2, compared to GaN and InN.

	Type	E_g (eV)		$m_e(m_0)$		$m_h(m_0)$	
		calc.	exper.	calc.	exper.	calc.	exper.
Mg_3N_2 [a]	direct (Γ)	1.1 – 2.85	2.5 – 3.15	0.20	—	9.65 – 29.43	—
Zn_3N_2 [b]	direct (Γ)	0 – 1.48	0.9 – 1.5	0.08	0.08 – 0.37	0.99 – 1.20	—
GaN [c]	direct (Γ)	3.5	3.4	0.15 – 0.22	0.20	0.81 – 2.11	0.3 – 2.2
InN [d]	direct (Γ)	0.8	0.7	0.06 – 0.13	0.06	0.84 – 2.97	2.30 – 2.80

[a] References [64, 73, 78–86]
[b] References [23, 72–77, 90–101]
[c] References [106–112]
[d] References [102, 106–109, 109, 113–116]

Zn_3N_2 and Mg_3N_2 the valence bands, being mainly composed of N $2p$ orbitals (especially close to the VBM), are degenerate, in contrast to for example wurtzite materials like GaN. Mg_3N_2 exhibits a very flat valence band dispersion, leading to heavy calculated effective hole masses of $m_h = 9.647$ to $29.428\ m_0$, where m_0 denotes the free electron mass. The valence band of Zn_3N_2, on the other hand, shows a high dispersion with calculated hole masses of $m_h = 0.99$ to $1.20\ m_0$, approximately half of that of GaN. Due to the lack of reports on p-type Zn_3N_2 or Mg_3N_2, an experimental confirmation of these values for Zn_3N_2 or Mg_3N_2 is still missing.

The conduction bands of Zn_3N_2 and Mg_3N_2 are mainly composed of the s states of the respective cations (Zn $4s$ and Mg $3s$ for Zn_3N_2 and Mg_3N_2, respectively) with small contributions of N s states. Due to the high dispersion, both materials show quite low effective electron masses. Calculations suggest a low value for Zn_3N_2 down to around $m_e = 0.08\ m_0$, being close to experimentally reported ones of $m_e = 0.16$ to $0.37\ m_0$, depending on the carrier concentration, while a theoretical minimum was extrapolated from these experiments to be around $m_e = 0.08\ m_0$, close to the value of InN. This low electron effective mass leads to quite high electron mobilities in Zn_3N_2 layers, in the order of $100\ \mathrm{cm^2V^{-1}s^{-1}}$ [71, 92, 96, 98, 99, 101, 103], even though most of the studies are on polycrystalline or amorphous material with high electron concentrations. Due to their improved structural quality, one may expect even higher mobilities in case of epitaxial thin films, making Zn_3N_2 an attractive candidate as active layer for TFTs.

On the other hand, the electron effective mass of Mg_3N_2 has been calculated to lay around $m_e = 0.20\ m_0$, which is close to the value of GaN. Also here, experimental evidence is still missing, probably due to the extremely rapid decomposition of Mg_3N_2 in air, as discussed in Section 1.2.2, pointing out the necessity of fundamental research on this material.

1.2.4 State of the art: Applications and epitaxial growth

1.2.4.1 Applications of Zn_3N_2 and Mg_3N_2 binaries

Although some of their basic physical properties are still unknown, Zn_3N_2 and Mg_3N_2 have several applications. As discussed in Section 1.2.2, II-nitride materials are chemically quite

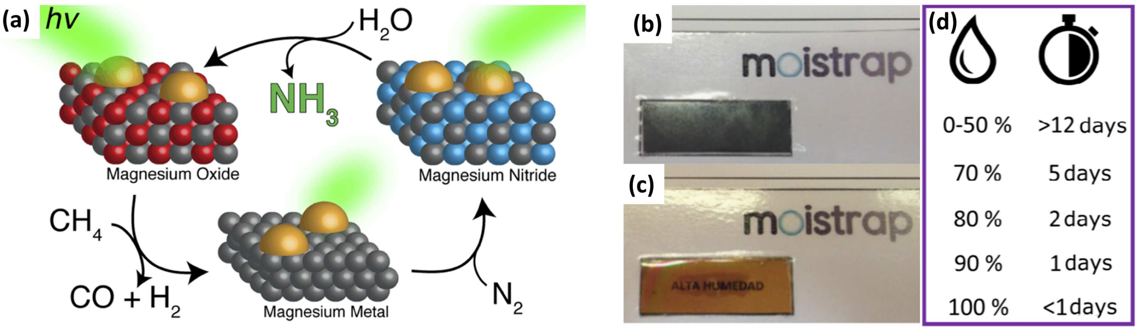

Figure 1.10: (a) NH_3 photo-synthesis using Mg_3N_2, reprinted from [117]. (b) Intact and (c) decomposed Zn_3N_2 humidity indicator on a flexible substrate with (d) its lifetime as a function of relative humidity, reprinted from [66].

reactive. In the case of bulk Mg_3N_2 this reactivity is utilized in chemical synthesis, e.g. as nitriding agent. The rapid hydrolysis of Mg_3N_2 with water according to Equation 1.3a, for instance, enables the synthesis of ammonia (NH_3), being the basic source of agricultural fertilizers [117]. The yearly industrial NH_3 production of 235 million tonnes (as in 2019 [118]) is done at high temperatures and pressures of around 500 °C and 200 bar, respectively [119]. Hence, a photo-synthesis process, as proposed with Mg_3N_2 [see Figure 1.10(a)], could possibly reduce the tremendous energy consumption needed for this so-called Haber-Bosch process [117]. Similarly, Mg_3N_2 allows the synthesis of IIIa-nitrides from their corresponding chlorides by metathesis exchange reactions, as demonstrated for scandium nitride and yttrium nitride [120], and has been used as a nitriding agent for the synthesis of AlN particles [121]. Furthermore, Mg_3N_2 is used in catalytic applications. It turned out that it was one of the first effective catalysts for the synthesis of cubic boron nitride (BN) [122], a material that is as hard as diamond. More recently, mixtures of Mg_3N_2 and Li_3N were evaluated for applications as hydrogen storage materials, due to the reversible formation of magnesium hydrides, amides or imides [123–126]. Interestingly, while the physico-chemical properties of Mg_3N_2 are largely utilized in these applications, its opto-electronic ones are not exploited in devices.

The chemical reactivity of II-nitride materials is also utilized in the case of Zn_3N_2. Although less reactive than Mg_3N_2, Zn_3N_2 decomposes slowly within several days in ambient conditions, while undergoing a drastic color change from black to completely transparent [66]. This slow, irreversible process together with the color change can be e.g. used for applications as humidity indicator during the transportation of goods [66]. Once the indicator is in contact with humidity, the Zn_3N_2 layer starts to decompose, which is visible by eye or can be e.g. electrically detected. By changing the layer thickness, one can adapt the decomposition time to the sensitivity of the product towards humid conditions [see Figure 1.10(b)-(d)].

Moreover, Zn_3N_2 got in the focus of research as material for thin film electronics. Originally evaluated as a precursor for the deposition of p-type ZnO [23–32], Zn_3N_2 is now itself applied as active channel layer in TFTs in several configurations [33–41, 127]. One of the advantages of Zn_3N_2 is its low growth temperature, enabling the deposition on flexible polymer substrates. Due to its low electron effective mass and its conduction band being mainly composed of spherical *s* states (see Section 1.2.3), high electron mobilities are achieved, even for polycrystalline and amorphous Zn_3N_2.

Despite the relatively wide range of applications of Mg_3N_2 and Zn_3N_2, their fundamental physical properties are still not yet completely unraveled. Their band gap energies and band offsets are under controversial discussion (see Section 1.2.3) and their linear thermal expansion coefficients above room temperature, being of large interest in the context of epitaxy, were completely unknown at the beginning of this project. Additionally, there is no report on the electrical properties of Mg_3N_2, being one of the sources for the ternary $(Zn_{1-x}Mg_x)_3N_2$ compound.

1.2.4.2 Epitaxial growth of Zn_3N_2 and Mg_3N_2 binaries

The epitaxial growth of both Zn_3N_2 and Mg_3N_2 is barely studied. Zn_3N_2 epitaxy has been achieved in [100] direction on MgO (100) and a-plane sapphire by MBE, as well as on YSZ (100) by sputtering (see Figure 1.11(a) and (b), respectively) [99, 103]. Furthermore, there is one study on Zn_3N_2 (111) on a-plane sapphire grown by MBE, as shown in Figure 1.11(c) [53]. Note that there is no data on the structural quality of these thin films and only two studies report the epitaxial relationships between film and substrate [53, 103]. Besides epitaxy, there is research activity on polycrystalline and amorphous Zn_3N_2 thin films due to its application as TFT channel material, for instance by sputtering (see e.g. [33, 34, 36–41, 92, 98, 101]) and metal-organic chemical vapor deposition (MOCVD) [100, 128], being important techniques for industrial applications.

Even more scare are the reports on Mg_3N_2 growth. Mg_3N_2 had not been grown at all epitaxially at the beginning of this project, the only report on Mg_3N_2 thin films being published in 2005 on polycrystalline material deposited by an electrochemical process [84], which has been recently supplemented by another study on polycrystalline Mg_3N_2 by sputtering (in 2020) [83]. One attempt to grow epitaxial Mg_3N_2 (100) on MgO (100) by MBE has then been made in 2018 (i.e. during the first year of this PhD) [82]. Nevertheless, the structural quality found in these layers is very low, the XRD intensity being "barely detectable" for films thinner than 800 nm according to the authors of this study, as shown in in Figure 1.11(b). The low diffraction intensity (much lower than in the case of polycrystalline Mg_3N_2 [83, 84]) was explained by the presence of the light elements Mg and N, leading to a low associated structure factor and hence, weak x-ray scattering strength, approximately five orders of magnitude smaller than the MgO substrate, which incidentally consists of light elements, too.

Despite their various applications, the few reports that exist on Zn_3N_2 and Mg_3N_2 thin film deposition, especially on their epitaxy, underline the need of fundamental research in this field. In order to improve the structural quality of new materials such as Zn_3N_2 and Mg_3N_2 and to implement them into opto-electronic devices, one has to understand their microstructure, which in turn influences their physical properties. The extracted structural information can be then utilized to optimize the growth conditions (e.g. by using buffer layers, post-growth annealings or different substrates) and to, eventually, achieve device quality.

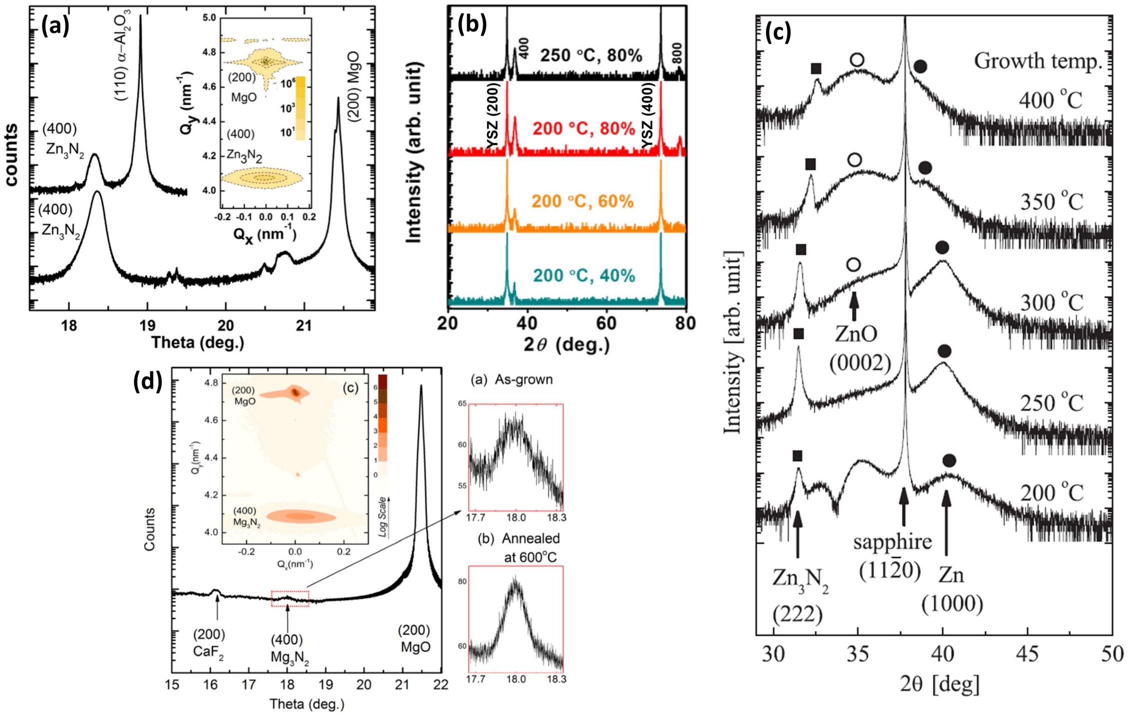

Figure 1.11: XRD of epitaxial Zn_3N_2 and Mg_3N_2 thin films. (a) MBE-grown Zn_3N_2 (100) on a-plane sapphire and MgO (100), reprinted from [99]. (b) Zn_3N_2 (100) on YSZ (100) grown by sputtering, reprinted from [103]. (c) MBE-grown Zn_3N_2 (111) on a-plane sapphire, reprinted from [53]. (d) MBE-grown Mg_3N_2 (100) on MgO (100), reprinted from [82].

1.2.4.3 Ternary and quaternary compounds containing Zn_3N_2 and Mg_3N_2

Besides the fundamental research on the II-nitride binary compounds, it is particularly interesting to study their alloy, $(Zn_{1-x}Mg_x)_3N_2$, since it allows to combine the advantages of both binaries Zn_3N_2 and Mg_3N_2. Similarly to $Zn_{1-x}Mg_xO$ or $In_xGa_{1-x}N$, a large range of band gap energies should be accessible in almost the entire visible spectral range. However, $Zn_{1-x}Mg_xO$ and $In_xGa_{1-x}N$ have the disadvantages that a variation of their stoichiometry involves either a change of crystal structure and lattice parameter, or solely of the lattice parameter (9 % difference between InN and GaN), respectively [13, 129], rendering the growth of high quality ternary crystals in the entire compositional range and their combination in heterostructures extremely difficult. Since Zn_3N_2 and Mg_3N_2 crystallize both in the anti-bixbyite structure with very similar lattice parameters (1.8 % mismatch), all compositions should be in principle accessible for $(Zn_{1-x}Mg_x)_3N_2$ with a rather constant crystalline quality, and their combination in heterostructures should be eased. Indeed, the only report on $(Zn_{1-x}Mg_x)_3N_2$, sputtered on YSZ (100) by Wu *et al.* in 2019 (i.e. in the second year of this PhD), confirms some of these

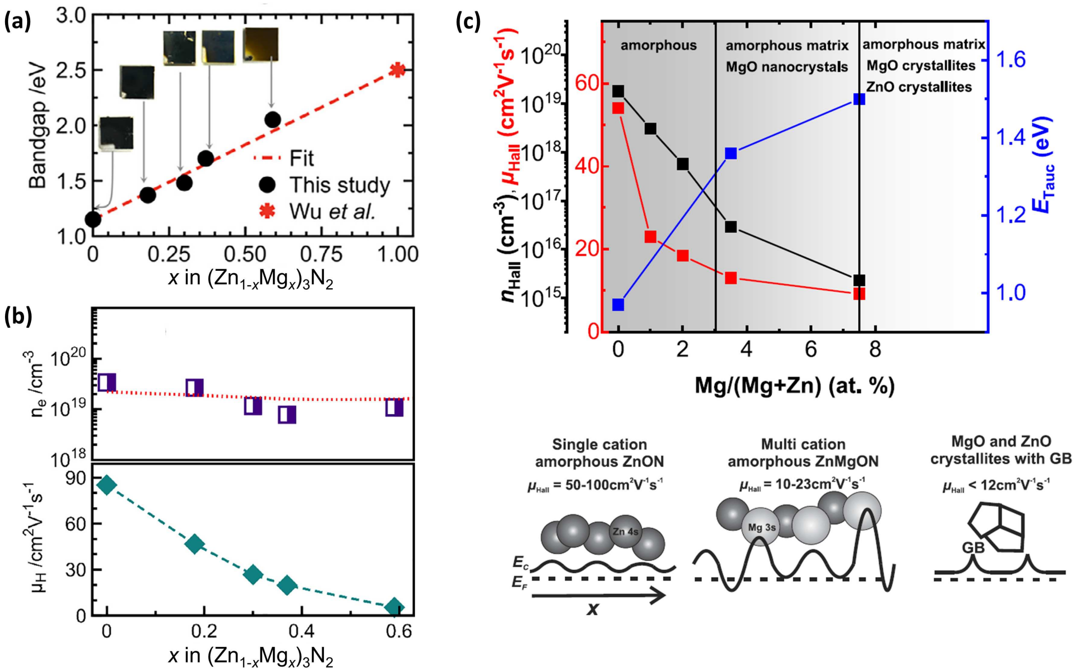

Figure 1.12: (a) Band gap energy as a function of Mg concentration in $(Zn_{1-x}Mg_x)_3N_2$ thin films, reprinted from [130]. (b) Carrier concentration and mobility as a function of Mg concentration in $(Zn_{1-x}Mg_x)_3N_2$ thin films, reprinted from [130]. (c) Carrier concentration, mobility and band gap energy as a function of Mg concentration in amorphous zinc magnesium oxynitride thin films, reprinted from [131]

.

considerations: A compositional range of $0.0 \leq x \leq 0.59$ was achieved, where epitaxial (100) growth was observed between $0.0 \leq x \leq 0.30$ that turned into amorphous thin films for compositions of $x > 0.30$ [130]. The authors were thereby able to control the band gap energy of the new ternary alloy between 1.2 eV to 2.5 eV, as shown in Figure 1.12(a). This result is particularly interesting in the context of photovoltaic absorbing layers, requiring a material with a direct, 1.4 eV-wide band gap for optimum absorption, which was obtained at an Mg concentration of $x = 0.18$ with an electron mobility of 47 $cm^2V^{-1}s^{-1}$. The epitaxial growth of this earth abundant $(Zn_{1-x}Mg_x)_3N_2$ semiconductor, achieved at a temperature as low as 140 °C, makes it a promising candidate for cheap thin film photovoltaics on large scale substrates.

While the electron mobility in $(Zn_{1-x}Mg_x)_3N_2$ decreases as a function of Mg content (from 87 to 5 $cm^2V^{-1}s^{-1}$), their concentration is found to stay at a high level, around 10^{19} cm^{-3} in the entire range, as shown in Figure 1.12(b). This large residual concentration is, however, detrimental for the application in many devices, such as LEDs or transistors. An interesting strategy to control the electron concentration in $(Zn_{1-x}Mg_x)_3N_2$ with low x was proposed very recently, and consisted in alloying this material with oxygen [131]. The new reported quarternary amorphous zinc magnesium oxynitride compound with Mg cation compositions between 1 at.% and 7.5 at.% and O anion compositions between 35 at.% and 70 at.% shows extremely tunable electron concentrations in the range of 10^{15} cm^{-3} to 10^{19} cm^{-3}, mobilities of 10 to 23 $cm^2V^{-1}s^{-1}$

and an absorption edge in the range of 1.3 eV to 1.7 eV, by combining a multi-anion with a multi-cation approach [see Figure 1.12(c)]. This result demonstrates the opportunities in exploring new, earth abundant semiconductors, enabling possibly cheap production methods and a potential application in numerous devices, such as TFTs and photovoltaics, among others. To achieve this goal, fundamental material research, i.e. the growth and thorough characterization of new semiconductors is absolutely indispensable.

1.2.5 Motivation

The motivation of this thesis is the development of epitaxial growth processes for Zn_3N_2 and Mg_3N_2 thin films by MBE and their potential use in TFTs and, eventually, solar cells. These binary compounds consist of earth abundant elements and can be, therefore, potentially produced at low cost and in large quantities, being an essential necessity in a more and more technologized world. Most of the reports up to date deal with amorphous or polycrystalline II-nitrides, preventing therefore the accurate determination of their fundamental physical properties, as well as the exploration of their full potential in terms of device application. Hence, growing crystalline, high-quality Zn_3N_2 and Mg_3N_2 thin films is indispensable in both fundamental and applied research. Although the range of potential applications of Zn_3N_2 and Mg_3N_2 is quite wide, as discussed earlier, most applications rely on the chemical reactivity of these II-nitride compounds, enabling mainly passive applications, e.g. as catalysts or synthetic reagents. For the possible application in (opto-)electronic devices, however, the problem of reactivity in ambient air has to be solved by developing proper methods of encapsulation, being a key step for a simple handling of these materials.

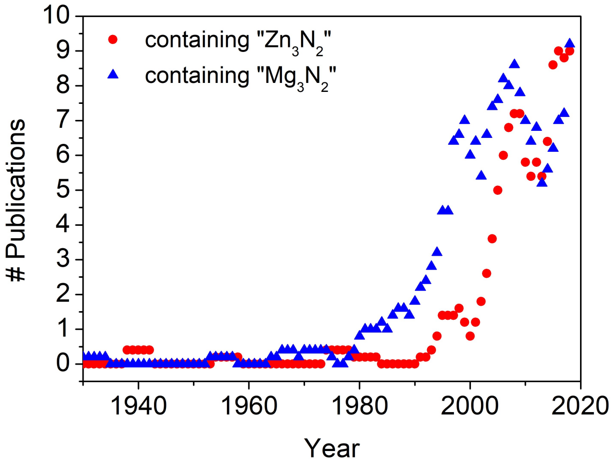

Figure 1.13: Number of articles per year containing "Zn_3N_2" and "Mg_3N_2", found on the Scopus webpage. Note that every point represents an average over 5 years in order to reduce the noise coming from the low number of publications

.

The difficulties that have to be faced when doing research on such compounds manifest also in the number of publications per year containing the keywords "Zn_3N_2" and "Mg_3N_2", found on the Scopus website, as graphically shown in Figure 1.13. Although a rapid growth of research activity is observed (starting in the 1980s for Mg_3N_2 and the 1990s for Zn_3N_2), the total number of articles is still very low.

Nevertheless, once these compounds can be successfully grown and stabilized, a playground of completely new materials may open by combining Zn_3N_2 and Mg_3N_2 to their ternary $(Zn_{1-x}Mg_x)_3N_2$ compound. Due to the identical crystal structure and very similar lattice parameters of Zn_3N_2 and Mg_3N_2, the whole compositional range of $(Zn_{1-x}Mg_x)_3N_2$ is in principle accessible without the creation of large defect densities, enabling thereby to cover a large band gap range of almost the entire visible spectral range from ca. 1 eV to 3 eV, which can be eventually enlarged by alloying this compound with oxygen, leading to the quarternary zinc magnesium oxynitride compound. Therefore, we intend to develop likewise the epitaxy of $(Zn_{1-x}Mg_x)_3N_2$ in a large compositional range in order to characterize and evaluate this new material in the context of possible device fabrication, as well as testing the introduction of oxygen into this material.

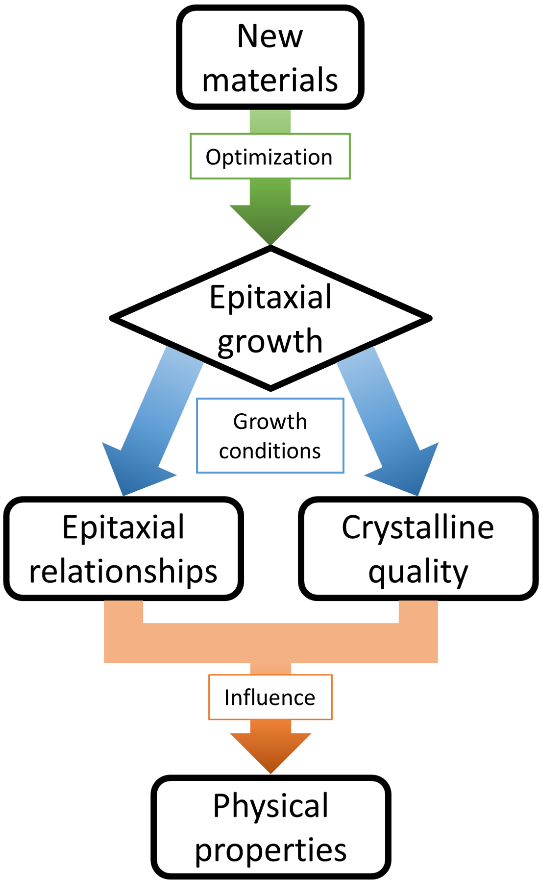

Figure 1.14: Schematic strategy for the epitaxial growth and characterization of new II-nitride materials.

The strategy employed in this PhD for the development of II-nitride epitaxy and their characterization, schematically shown in Figure 1.14, is as follows: the process conditions of the material to be grown are explored and optimized until epitaxy is achieved. Subsequently, the epitaxial relationships and the crystalline quality, which depend mainly on the underlying substrate as well as the growth conditions, are determined. Finally, the physical properties of the thin films are investigated in the context of their structural ones, in order to evaluate the influence of crystalline quality.

Chapter 2

Epitaxial growth by MBE and thin film characterization

THIS CHAPTER presents the principles of MBE as a technique for epitaxial film growth, including its advantages and disadvantages. Further, the theory and technical implementation of the characterization techniques most commonly employed in this PhD are briefly discussed. Note that this chapter intends to give a brief overview of the techniques used in this thesis. Deeper information can be found in the references given herein. This chapter covers:

- Epitaxial thin film growth using MBE
- Structural characterization using diffraction techniques, from XRD via RHEED to TEM
- Surface characterization by AFM and XRR
- Optical characterization, including transmittance and photoluminescence spectroscopy
- Electrical characterization using Hall effect

2.1 Molecular beam epitaxy

There are several techniques for epitaxial film growth available, such as vapor phase epitaxy, liquid phase epitaxy, pulsed laser deposition, etc. However, due to the ultra-high vacuum (UHV) conditions, MBE offers the advantage that the atoms/molecules are sent to the substrate as a molecular beam, i.e. their mean free path is larger than the source-substrate distance. Consequently, the atoms/molecules do not experience any collisions before reaching the substrate, leading to adsorbed species with a large kinetic energy, which may be further increased by substrate heating. Ideally, this allows the adsorbed species to find their perfect positions in the growing crystal.

MBE is a relatively young technique for film growth, the first conceptions being realized in the 1960s [132–134], with the aim to fabricate ultra pure materials and new heterostructures. Since then, large progress has been made in terms of UHV equipment, source materials and *in-situ* characterization. This allowed the development of growth processes for a variety of materials, such as group IV, III-V and II-VI semiconductors [135], oxides [136, 137], new nitrides [138], metals [137] and 2D materials [139]. More about the history of the MBE development can be found in reference [140].

A schematic representation of the MBE growth reactor used to grow thin films within this project is depicted in Figure 2.1. Knudsen effusion cells are used to evaporate elemental metals. Shutters in front of the cells enable the metal fluxes to be switched on and off. Oxygen and nitrogen gases are ionized using RF plasma cells in order to grow the compounds. The substrate rotation ensures conformal growth over the sample area.

Besides the molecular beams characteristics, MBE offers some additional advantages that makes it particularly interesting for research on new materials. Due to its simplicity, the chemical reactions for compound formation are straightforward and do not imply side reactions as the case for MOCVD, making it easier to identify growth mechanisms. MBE enables further very accurate thickness control down to mono-layer precision, as well as precise control of dopant concentrations. Furthermore, several *in-situ* characterization techniques can be used thanks to the UHV conditions. Among them, reflection high-energy electron diffraction (RHEED) is probably the most applied one, enabling the characterization of surface morphology, crystallinity and (in some cases) thickness during film growth, and making it a powerful tool in growth monitoring (for a more detailed explanation, see Section 2.2.2). Therefore, MBE is an adapted technique to grow high quality epitaxial films, in particular new materials.

However, the strong points making it an efficient tool in research are at the same time weak points when considering industrial applications. UHV conditions require expensive equipment, long pumping times and cooling of the reactor walls (mostly by liquid nitrogen), leading to limited throughputs and high maintenance costs. Moreover, the accurate thickness control being possible due to relatively low growth rates, increases time and cost even further, especially when growing thick layers. Therefore, MBE is industrially probably one of the least used

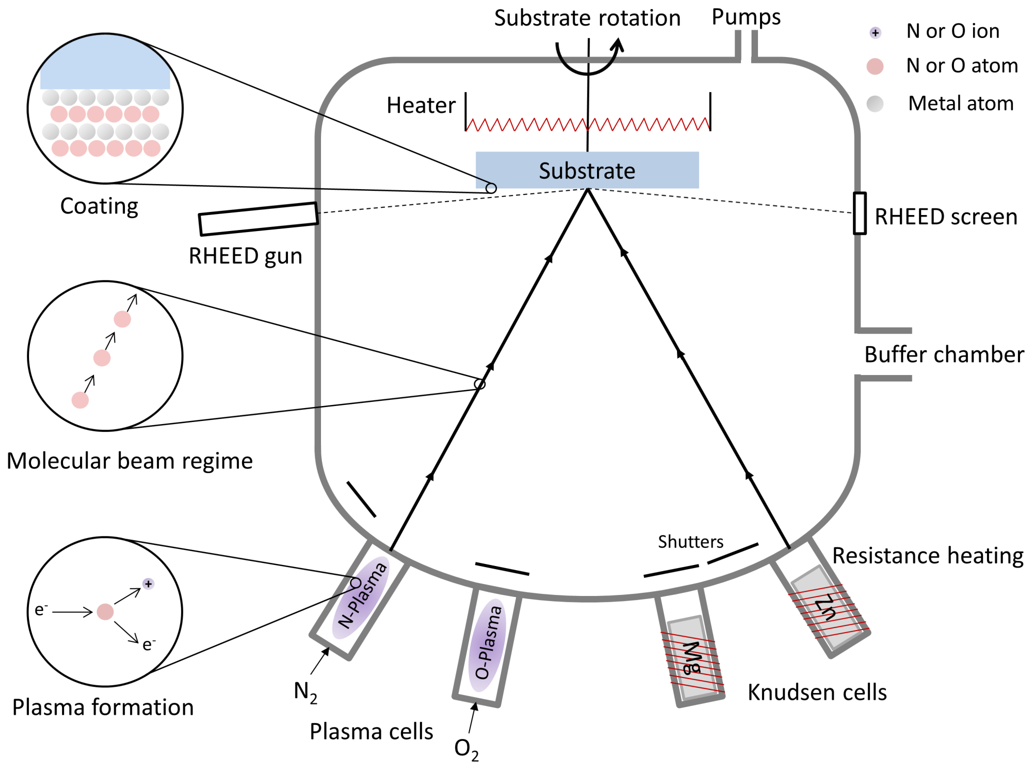

Figure 2.1: Schematic representation of an MBE growth reactor.

techniques for epitaxy among the ones listed above. Nevertheless the interest in industrial MBE techniques increases and this technique is applied in more and more niche applications, as for example for the production of high-quality RF transistors [141].

All thin films presented in this thesis were grown by plasma-assisted MBE in a Riber EPINEAT system. The substrates are loaded in an introduction chamber that is pumped to $\sim 10^{-8}$ Torr. A buffer chamber prior to the actual growth chamber allows the storage of several substrates and is kept at 10^{-9} Torr. Cooling of the reactor walls with liquid nitrogen allows to decrease the residual background pressure in the growth chamber below 10^{-9} Torr, in order to decrease the amount of possible impurities. Growth was performed on $10 \times 20\,\mathrm{mm}^2$ YSZ (100), MgO (100) and MgO (111) substrates, purchased from CrysTec GmbH and CRYSTAL GmbH. The substrates were prepared in CRHEA's cleanroom by rapid thermal annealing for 2 min at 1150 °C under 2000 sccm oxygen (JIPelec JetFirst 100 system) flow to obtain atomically flat surfaces. The MBE chamber is equipped with two Knudsen effusion cells for elemental Zn and one for elemental Mg (both with purities of 99.9999 %), serving as cation sources. Oxygen and nitrogen gases (both 99.9999 %, ionized using an RF plasma with powers between 360 W to 400 W) were used as anion sources. The pressure during growth was in the order of 10^{-5} Torr, depending on the gas flows. A pyrometer and two thermocouples were used to evaluate the growth temperature. *In-situ* optical reflectivity with a 650 nm laser and RHEED were applied to monitor the growth rate and surface crystallinity, respectively.

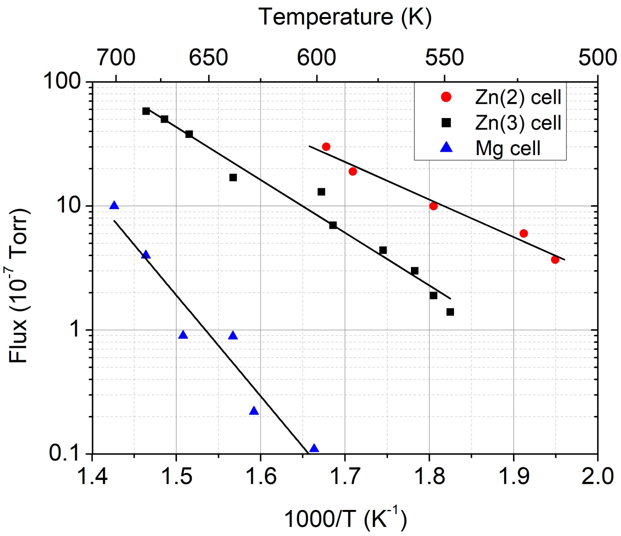

Figure 2.2: Metal flux as a function of cell temperature for the two Zn as well as the Mg effusion cell.

The two Zn effusion cells are redundant to allow long growth series even if one cell becomes empty. By measuring the metal flux as a function of cell temperature using a pressure gauge, one can assure the same Zn flux of both cells, even with different cell geometries. The Zn flux measured as a function of temperature for both cells is shown in Figure 2.2. The fluxes follow the Clausius-Clapeyron equation [142, 143], where

$$ln\left(\frac{p_1}{p_2}\right) = -\frac{\Delta H_{vap}}{R}\left(\frac{1}{T_1} - \frac{1}{T_2}\right). \tag{2.1}$$

Here p_1 and p_2 are the vapor pressures at the temperatures T_1 and T_2, respectively, ΔH_{vap} the enthalpy of vaporization and R the gas constant. Taking all the measured fluxes, average values of ΔH_{vap}(Zn(2)) = 85.3 kJ mol^{-1} and ΔH_{vap}(Zn(3)) = 123 kJ mol^{-1} are found for the Zn(2) and Zn(3) cells, respectively, which are close to the reported literature value of $\Delta H_{vap}(\mathrm{Zn_{lit}})$ = 115 kJ mol^{-1} [144]. The cell geometry, however, seems to slightly influence the evaporation characteristics, leading to a different slope for the two cells.

We performed the same analysis on the Mg effusion cell, where a much steeper slope is observed (see blue triangles in Figure 2.2). Fitting the fluxes using Equation 2.1 gives an average value of ΔH_{vap}(Mg) = 156 kJ mol^{-1}, indicating a lower vapor pressure of Mg when compared to Zn (literature value for Mg: $\Delta H_{vap}(\mathrm{Mg_{lit}})$ = 132 kJ mol^{-1} [144].)

2.2 Diffraction by a crystal

The structure of crystalline materials is commonly analyzed using diffraction techniques. In the following we restrict ourselves to x-ray and electron diffraction since these techniques were applied in the frame of this work. However, all diffraction techniques have in common that they rely on the scattering of the incident radiation with the material to be analyzed, and subsequent interference between the scattered beams. In case of constructive interference, an intensity maximum is observed and the process is called diffraction. In this thesis, three different diffraction techniques are used to analyze the structural properties of the grown films: XRD, RHEED and transmission electron microscopy (TEM). While XRD and RHEED rely on diffraction of reflected radiation (x-rays and electrons, respectively), TEM diffraction is the result of the interaction of a transmitted electron beam with the crystalline lattice. In the following, the kinematical scattering theory (assuming no re-diffraction of the scattered beam), which is applicable for diffraction of thin layers, is discussed in the context of x-ray and electron diffraction and can be e.g. found in references [145] and [146].

In a diffraction experiment, the incident beam is scattered by the atomic planes of a crystal, as shown in Figure 2.3(a). Constructive interference and, hence, diffraction occurs if the path difference of the interfering waves (indicated in green) is a multiple of the radiation wavelength. Using simple geometrical considerations, we can deduce Bragg's formulation of x-ray diffraction (also describing electron diffraction) [147] found in 1913

$$2d_{hkl}\sin(\theta) = n\lambda, \tag{2.2}$$

where d_{hkl} is the inter-planar distance of the (hkl) reflection, θ the diffraction angle, λ the wavelength and n the diffraction order. From Equation 2.2, the inter-planar distance can be determined experimentally just by measuring the diffraction angle. On the other hand, the scattering amplitude of a given reflection depends on the atomic scattering factors of the elements the diffracting planes consist of. The scattering factor of an element j is the Fourier transform of its electron probability density $\rho(r)$

$$f_j = \int_{space} e^{i\boldsymbol{Q_{hkl}}\boldsymbol{r}}\rho(r)\,dV, \tag{2.3}$$

where $\boldsymbol{Q_{hkl}}$ is the scattering vector of the (hkl) reflection and $\boldsymbol{r}$ a spatial vector in real space, running from the origin of the unit cell to the position of the atom j. From Equation 2.3, $\rho(r)dV$ (being the probability of an electron being in the volume dV) depends mainly on the atomic number Z. Therefore, f_j is sensitive to the kind of element causing the diffraction. For a given element, f_j depends then only on $\boldsymbol{Q_{hkl}}$, i.e. which (hkl) reflection is measured. The scattering amplitude of a whole unit cell is given by the structure factor

$$F_{hkl} = \sum_{j=1}^{N} f_j e^{-2\pi i(hx_j+ky_j+lz_j)}, \tag{2.4}$$

which is the summation over all atoms N of the unit cell, where x_j, y_j, and z_j are the fractional coordinates of $\boldsymbol{r}$. As indicated in the Equations 2.2 to 2.4, each (hkl) reflection of a crystal has a certain scattering amplitude and diffracts at a certain angle θ, depending on the inter-planar distance d_{hkl}. Consequently, one can construct an imaginary lattice containing all possible

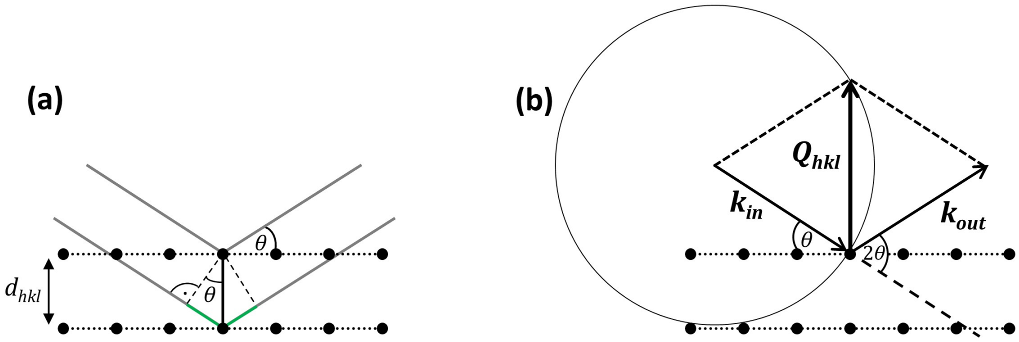

Figure 2.3: (a) Bragg conditions for diffraction. (b) Laue conditions for diffraction including the Ewald sphere.

(hkl) reflections associated to the crystal lattice. This is the important concept of *reciprocal space*, where the reciprocal lattice represents the Fourier transform of the direct, real space lattice. For a cubic crystal, the primitive vectors of the reciprocal lattice

$$\boldsymbol{b_1} = 2\pi \frac{\boldsymbol{a_2} \times \boldsymbol{a_3}}{\boldsymbol{a_1} \cdot (\boldsymbol{a_2} \times \boldsymbol{a_3})}, \quad \boldsymbol{b_2} = 2\pi \frac{\boldsymbol{a_3} \times \boldsymbol{a_1}}{\boldsymbol{a_1} \cdot (\boldsymbol{a_2} \times \boldsymbol{a_3})}, \quad \boldsymbol{b_3} = 2\pi \frac{\boldsymbol{a_1} \times \boldsymbol{a_2}}{\boldsymbol{a_1} \cdot (\boldsymbol{a_2} \times \boldsymbol{a_3})} \tag{2.5}$$

have the same direction, but the inverse length of primitive vectors $\boldsymbol{a_1}$, $\boldsymbol{a_2}$ and $\boldsymbol{a_3}$ of the direct lattice, where $\boldsymbol{a_1} \cdot (\boldsymbol{a_2} \times \boldsymbol{a_3})$ is the direct unit cell volume. Using the concept of reciprocal space together with the so-called Ewald sphere construction, one can derive which planes diffract for any given λ and diffraction geometry. Figure 2.3(b) shows an Ewald sphere construction that is equivalent to the Bragg condition discussed earlier. The radius of the Ewald sphere is the magnitude of the wave vectors $\boldsymbol{k_{in}}$ and $\boldsymbol{k_{out}}$

$$k_{in} = k_{out} = \frac{2\pi}{\lambda}. \tag{2.6}$$

Diffraction occurs when the reciprocal space vector $\boldsymbol{Q} = \boldsymbol{k_{out}} - \boldsymbol{k_{in}}$ ends in a reciprocal lattice point (hkl) and the Ewald sphere intersects this point (Laue-conditions of diffraction). With the geometry given in Figure 2.3(b), the magnitude of the reciprocal lattice vector $\boldsymbol{Q_{hkl}}$ is given by

$$Q_{hkl} = \frac{4\pi \sin(\theta)}{\lambda}. \tag{2.7}$$

To obtain the final intensity diffracted by a crystal, one has to take into account its thickness. The presence of a finite crystal thickness has two important consequences. First, the diffracted intensity is a function of the thickness; this is because the x-ray absorption length of the material is commonly large with respect to the film thickness, i.e. the more material diffracts, the larger the diffraction intensity. Second, the scattered beam interferes with the atomic planes of different unit cells due to the phase difference $\boldsymbol{r_j} \cdot \boldsymbol{Q_{hkl}}$ of the unit cells located at different $\boldsymbol{r_j}$.

This interference can be described by the interference function

$$J = \sum_{i} e^{2\pi i \boldsymbol{r}_j \cdot \boldsymbol{Q}_{hkl}}, \tag{2.8}$$

summing up the phase difference of all unit cells. The final intensity of a thin layer containing the interference term is then given by

$$I = F_{hkl}^2 J^2 = F_{hkl}^2 \frac{\sin^2(\pi n_{uc} \boldsymbol{q})}{\sin^2(\pi \boldsymbol{q})}. \tag{2.9}$$

where $\boldsymbol{q}$ is a small deviation of the diffraction vector $\boldsymbol{Q}_{hkl}$ and n_{uc} is the thickness in unit cells. For $\boldsymbol{q} = 0$ strong diffraction occurs as the Bragg condition is fulfilled. The first minimum in the interference term occurs at $n_{uc}\boldsymbol{q} = 1$, hence, the width of the diffraction peak is inversely dependent on the film thickness. We will make use of this equation for our thin film analyses discussed in the following chapters in order to extract the out-of-plane lattice parameter and thickness of the crystalline thin films. Interference of the diffracted beam can be, however, only observed in case of a high out-of-plane crystalline scattering coherence. Note that interference fringes are not visible in case of electron diffraction due to the high electron energies (short wavelengths) used in these techniques (see Section 2.2.2).

Using the relatively simple concept of reciprocal space, one can draw many characteristics from diffraction patterns of a given sample, such as:

- Crystallinity (is the sample crystalline or amorphous?)
- Crystal structure (which crystal structure(s) is/are present?)
- Orientation (how many and which orientation(s) is/are present?)
- Lattice parameter (is the sample relaxed, strained, etc.?)
- Thickness (in principle with mono-layer precision)

2.2.1 X-ray diffraction

Since the first XRD experiments on rock salt by Friedrich, Knipping and von Laue in 1912 [148] and the subsequent theoretical description by Bragg [147], Darwin [60], Ewald [149] and von Laue [150], XRD became an important technique to analyze crystalline materials in both basic research and device characterization. While crystal structures of new materials are mainly identified using single crystal XRD coupled with theoretical calculations, the structural properties of epitaxially grown materials are analyzed using thin film XRD. The theory explained here can be found with more details in references [145] and [146].

In a thin film XRD setup (Bragg-Brentano geometry), diffraction occurs from atomic planes parallel to the crystal surface (also referred to as symmetric planes), as indicated by dotted lines in Figure 2.3(a). From Equation 2.2, the inter-planar distance can be determined with XRD by measuring the diffraction angle with so-called $2\theta/\omega$ scans, which are scans along the Q_z component of $\boldsymbol{Q_{hkl}}$ in reciprocal space (also referred to as longitudinal scans), where the Q_x and Q_z components of $\boldsymbol{Q_{hkl}}$ are given by

$$Q_x = \frac{2\pi}{\lambda}(\cos(\omega) - \cos(2\theta - \omega)), \tag{2.10a}$$

$$Q_z = \frac{2\pi}{\lambda}(\sin(\omega) + \sin(2\theta - \omega)). \tag{2.10b}$$

To asses diffraction spots coming from planes non-parallel to the sample surface (asymmetric planes), one can apply an inclination angle χ according to the inter-planar angle between the surface and the plane to be measured (skew-geometry), thereby fulfilling the diffraction conditions. The measurement of the asymmetric plane is done by performing a $2\theta/\omega$ scan under these conditions, allowing the extraction of more detailed crystallographic information, such as in-plane orientation or in-plane lattice parameter of the grown crystal.

Once the basic crystallographic parameters of a sample are known, it may be interesting to extract further information about the crystalline quality of a sample, which is commonly done by measuring of rocking curves (ω scans) as shown in Figure 2.4, where ω is the rotational angle around an in-plane axis. In order to measure rocking curves, the source-detector geometry is stationary, aligned on the maximum of the diffraction spot to be observed in Q_z direction. The sample is then rotated around its ω axis, perpendicular to the paper plane in Figure 2.4, leading to a scan perpendicular to $\boldsymbol{Q_{hkl}}$ (i.e. along Q_x) in reciprocal space, also referred to as transverse scan.

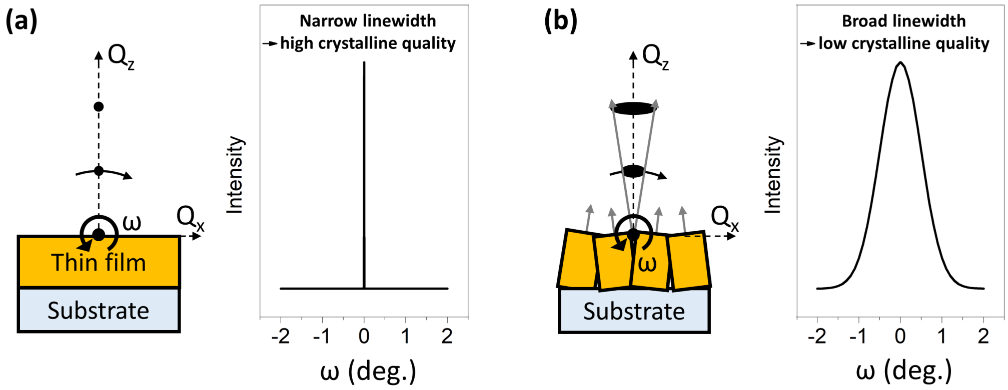

Figure 2.4: (a) Schematic rocking curve measurement on a perfect thin film, leading to a narrow line width. (b) Schematic rocking curve measurement on a thin film exhibiting tilt, leading to broad line widths.

The broadening of the diffraction spot in Q_x direction contains information about the crystalline quality of the sample and the in-plane size of the crystalline grains. In case of a perfect crystalline quality [see Figure 2.4(a)], the x-rays are scattered coherently from large sample ar-

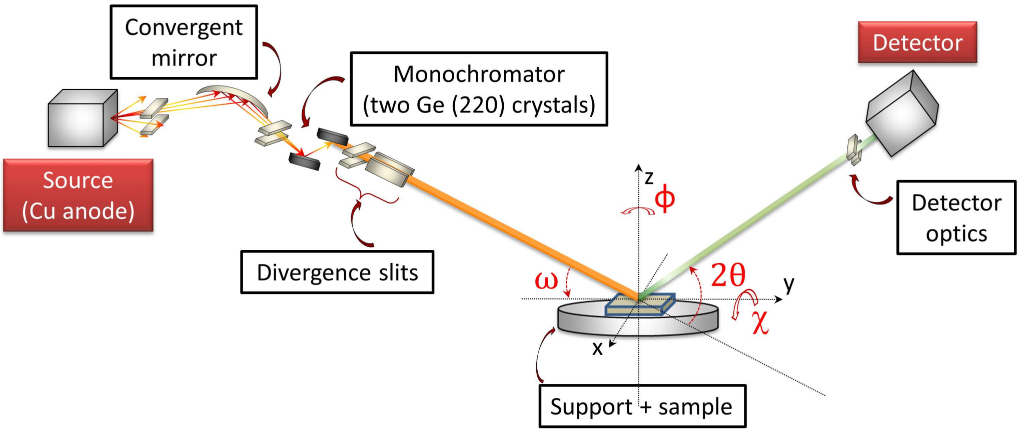

Figure 2.5: Schematic setup of the diffractometer used in this project.

eas and a narrow line width is predicted by kinematical scattering theory. On the other hand, defects such as finite crystallite sizes or lattice rotations (the latter occur due to the presence of dislocations, grain boundaries or misorientations) induce broadening of the reciprocal lattice spot in the Q_x direction, because coherent scattering is disturbed by their presence, as schematically shown in Figure 2.4(b). Symmetric reflections are broadened by tilt (and the vertical size of the grains), whereas asymmetric reflections are broadened by tilt and twist (plus vertical and in-plane size effects).

There are several instrumental setups enabling to perform XRD measurements. An important choice to make is the detector configuration. In many cases, a rough knowledge about presence and positions of the diffraction peaks is usually sufficient to determine the crystallinity, crystal structure and orientation of a sample. For this purpose, conventional fully-open detectors that offer high intensities, but relatively low angular precision are desired in order to detect even small amounts of crystalline material. For the precise determination of lattice parameters, the resolution of interference fringes and the evaluation of crystalline quality, a high-resolution optics is introduced in front of the detector, leading to a triple axis configuration. In this case the diffracted beam undergoes several reflections in an analyzer crystal before entering the detector, leading to a high precision in reciprocal space.

The measurements shown in this thesis were performed on a Panalytical X'Pert PRO MRD diffractometer, as shown in Figure 2.5, equipped with two detector optics: One leading to a conventional fully-open detector configuration and one equipped with a Ge crystal analyzer in triple axis configuration, in which the diffracted beam undergoes three (220) reflections before entering the detector. A Cu anode and a Ge (220) asymmetrical four-crystal monochromator provide incident Cu $K\alpha_1$ radiation (1.54056 Å). An x-ray mirror leads to a parallel beam with a divergence of less than 0.05°. High resolution rocking curves (transverse ω scans) and longitudinal $2\theta/\omega$ scans were measured using the detector in the triple axis configuration. Standard measurements were done using the conventional detector configuration, either fully-open or with a 1/4° slit in the diffraction path. We performed high-temperature XRD measurements on selected samples to evaluate their lattice parameter as a function of temperature. These measurements were performed either by G. Monge (CEMEF-MINES ParisTech, Valbonne, France), using a Empyrean Panalytical, or by R. Bachelet and G. Saint-Girons (INL, Lyon, France), using a Rigaku Smartlab diffractometer. In both cases Cu $K\alpha$ radiation was used and the sample was kept in a closed Anton Paar chamber.

2.2.2 Reflection high-energy electron diffraction

RHEED is a diffraction technique invented in 1928 by Nishikawa and Kikuchi [151]. Nowadays, it is widely used in MBE to analyze the surface crystallinity and morphology of the growing crystal *in-situ*. Since its first application in MBE in 1969 by Arthur and Lepore [152], it led to several breakthroughs in MBE growth, which in turn drove the development of better RHEED systems, becoming finally a standard measurement tool of growth monitoring in MBE.

In RHEED, a high-energy electron beam is sent to the sample surface at a very low incident angle, leading to diffraction from a few mono-layers below the sample surface, as seen in Figure 2.6. Due to the quasi 2D diffraction geometry, the reciprocal lattice consists of diffraction rods instead of points, as it is the case in XRD (see Section 2.2.1). These rods are consequently named by only two indices (hl) due to the lack of the third diffraction condition. Diffraction occurs at the intersection of the Ewald sphere with the diffraction rods and is detected by a luminescent screen. The radius of the Ewald sphere is again given by the magnitude of the wave vector $\boldsymbol{k_{in}}$, which can be calculated by inserting the De Broglie wavelength of the electrons

$$\lambda = \frac{h}{\sqrt{2m_0E + E^2c^2}} \tag{2.11}$$

in Equation 2.6, where E is the kinetic energy of the electrons (in our case 30 keV), m_0 the electron mass, h the Planck constant and c the speed of light in vacuum.

By simulating the collected diffraction patterns (usually recorded in several azimuthal angles), one can easily determine the orientation and crystallinity of the sample during growth. Furthermore, the distances between spots in the reciprocal lattice can be reproduced by taking into account the electron energy and chamber geometry, giving an idea of the lattice parameters of the structure. In practice, the lattice parameter of the growing thin film is obtained by comparing the observed distances in its RHEED pattern with the ones coming from reference samples with a known lattice parameter (e.g. the substrate prior to growth).

Due to the high energy of the electrons (of several keV) the Ewald shere in RHEED is quite large compared to XRD. Imperfections in the sample and beam divergence lead to broadening of the diffraction rods and the Ewald sphere, respectively, and can hence lead to the occurrence of elongated spots or streaks in the pattern, because sphere and rods intersect along large distances fulfilling the diffraction conditions. Nevertheless, in an optimized case, streaky RHEED patterns are commonly associated with a flat sample surface, whereas spotty patterns are associated with rougher surfaces (see Figure 1.3).

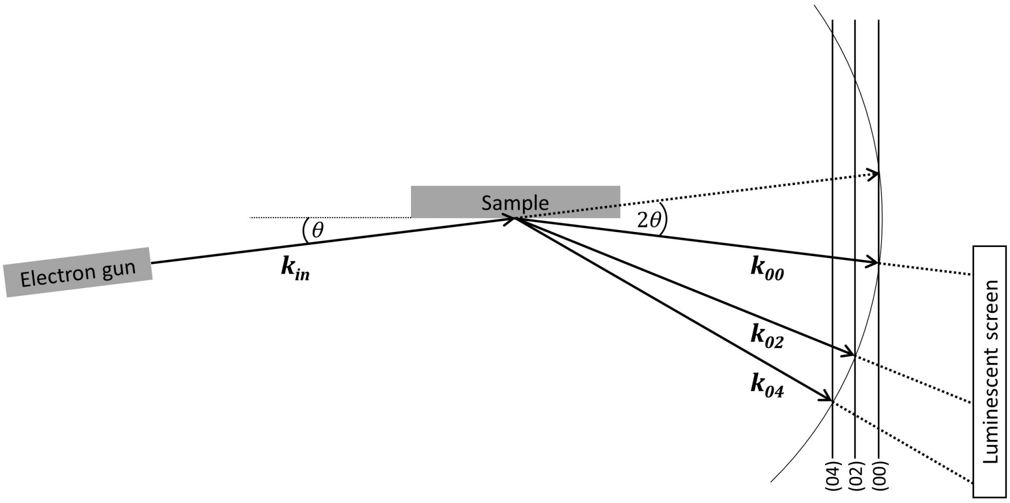

Figure 2.6: Diffraction conditions for a RHEED measurement.

For the extraction of qualitative information of RHEED patterns it is sufficient to apply the simple kinematic approach, assuming one single, elastic scattering process of the electrons with the sample surface. However, due to the low incident angle (leading to a large interaction surface) and the high scattering strength of electrons with matter, the beam can undergo multiple diffractions. This so-called dynamic scattering is the reason for the occurrence of e.g. Kikuchi-lines, connecting in some cases the diffraction spots in RHEED patterns, as e.g. seen in Figure 3.1 of Section 3.2.1, showing the RHEED pattern of an MgO substrate. Dynamic scattering also needs to be taken into account when analyzing the relative intensity of diffraction spots. The theory of RHEED and more information on the interpretation of RHEED patterns can be found in reference [153].

2.2.3 Transmission electron microscopy

The first electron microscope was built by Knoll and Ruska in 1931 [154], who worked on focusing electron beams with magnetic lenses, initially to optimize cathode-ray oscilloscopes. Although the achieved magnification was not better than in conventional light microscopes, Ruska continued the development of magnetic lenses further. He was able to achieve magnifications of more than 12,000 in 1934 [155], roughly 10 times better than light microscopes and received the Nobel Prize in physics in 1986 [156] for the development of transmission electron microscopy. A more detailed insight into the history of TEM development is found in reference [157].

The theoretical resolution limit M in any microscopy technique is given by the wavelength λ of the used radiation and the numerical aperture NA of the system.

$$M = \frac{\lambda}{2\mathrm{NA}}. \tag{2.12}$$

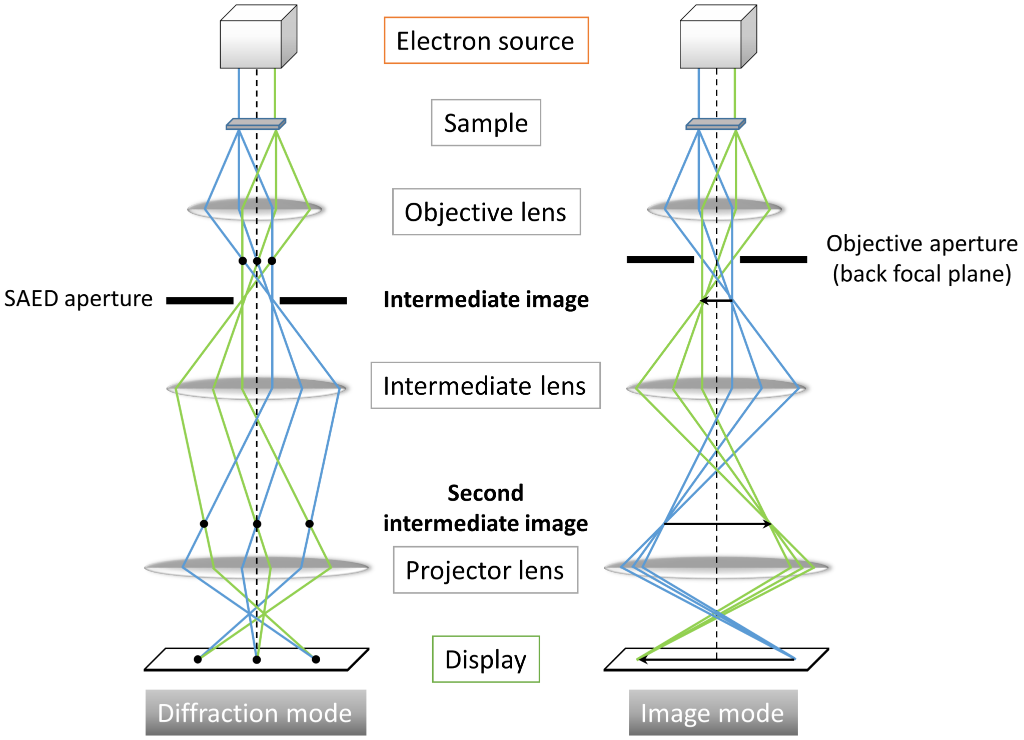

Figure 2.7: Schematic operation of a TEM.

Therefore, the resolution limit in optical microscopes is around 0.2 µm, approximately half of the wavelength of visible light. In electron microscopy, the wavelength of the used radiation is the De Broglie wavelength of the electrons as given in Equation 2.11. At typical TEM operation voltages (100 keV to 300 keV), the De Broglie wavelength is around 0.025 Å. However, in practice resolutions of approximately 0.5 Å are achieved nowadays, because a compromise has to be made between relatively large spherical aberrations and the diffraction limit [158]. Since interatomic distances are larger than this value, this resolution is still sufficient to achieve atomic resolution in crystalline materials.

In TEM, an electron beam is transmitted through a thin specimen sample, as schematically shown in Figure 2.7, with a thickness from a few nm to several tens of nm depending on the material to be analyzed. When an electron beam passes through a crystal, the main portion of electrons is either transmitted or elastically scattered (i.e. diffracted).

In order to see the diffraction pattern of the crystal, which can be used to determine its structure and orientation, one has select the back focal plane of the objective lens as an object for the intermediate lens. This operation mode, referred to as *Diffraction* mode, is possible by an adjustment of intermediate lens strength, leading to the projection of the diffraction pattern on the observation screen. In practice, a selected area electron diffraction (SAED) aperture is inserted in the image plane, which enables to select a certain sample area for the collection of the diffraction pattern.

The obtained SAED pattern consists of a bright central spot (containing directly transmit-

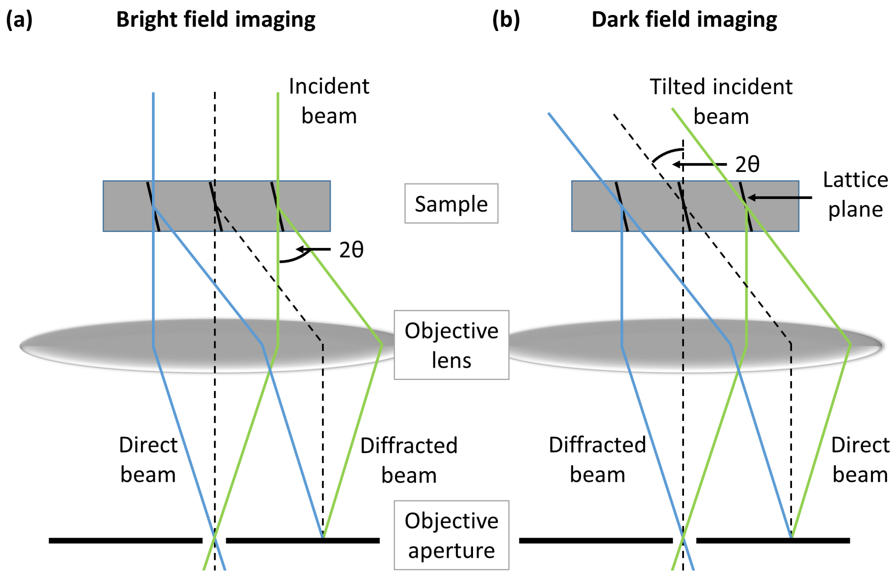

Figure 2.8: Schematic operation of (a) bright field and (b) dark field imaging.

ted electrons) and, in case of a crystalline sample, of diffraction spots surrounding the central one. If one wants to obtain an image of the sample, the strength of the intermediate lens is re-adjusted such that the image plane of the objective lens becomes the object of the intermediate lens, referred to as *Image* mode. The image is formed on the screen by either selecting the direct beam or by selecting one (or several) diffracted beams, realized due to the insertion of objective apertures.

The first case is referred to as *bright field* mode, where the objective aperture blocks the diffracted beams, as shown in Figure 2.8(a). The intensity contrast of the direct beam depends on the crystallinity, thickness and atomic mass of the specimen.

In the latter case, referred to as *dark field* mode [see Figure 2.8(b)], the direct beam is blocked by the objective aperture, leading to an image consisting of diffracted electrons, particularly sensitive to structural information of the sample, because sample areas that fulfill the selected diffraction conditions appear bright in the obtained image. This is realized by tilting the incident electron beam, so that it arrives at the specimen with an angle opposite to the diffraction angle, bringing the diffracted beam on axis.

For very thin specimens, the transmitted beams undergo mainly phase changes (since absorption becomes weak) leading to a phase contrast in the image. High-resolution transmission electron microscopy (HRTEM) uses this property to image the crystalline arrangement with atomic resolution. In practice, the phase difference in the transmitted beams is not measurable, but can be imaged by interfering the different electron beams (transmitted and diffracted). This leads, in turn, to an intensity contrast in the image plane that can be measured. Although this intensity contrast is highly sensitive to the sample thickness, the focus and aberrations of the microscope, the geometry of the crystalline lattice, the containing defects and the positions of the atoms are reproduced in the image. Furthermore, simulations based on atomic models enable to reproduce high-resolution images, enabling the full determination of the atomic arrangement.

Since the thin films presented in this thesis are sensitive to air, classical specimen preparation including a chemical-mechanical polishing approach is not possible since it would lead to sample degradation. Therefore, the preparation was performed under vacuum in a scanning electron microscope using focus ion beam sectioning with a FEI Helios 600 NanoLab dual beam instrument (CP2M, Marseille, France) by M. Cabie. Ions from a liquid Ga source were accelerated with 30 kV in order to obtain a thin specimen by ion beam milling. For final thinning, the specimen was exposed to Ga ions at 1 kV, minimizing sample damage by the ion beam. The transfer to the TEM was done in a vacuum desiccator to minimize the reaction with ambient air. The samples were investigated using a FEI Titan 80-300 objective-corrected microscope (CP2M, Marseille, France) at 200 keV by P. Vennéguès.

2.3 Surface and interface characterization

The surface of materials can be characterized using AFM, allowing to extract images of the surface morphology in nanometric scale and thereby to asses the surface roughness. While AFM provides information on short spatial scales, XRR can be used to obtain the average interface roughnesses on larger spacial scales, but also allows the measurement of the film thickness and density of the grown material, independent of its crystalline quality.

2.3.1 Atomic force microscopy

Among the characterization techniques discussed so far, AFM is the youngest technique, as it was developed by Binnig et al. in 1985 [159]. AFM combines the properties of a scanning tunneling microscope, i.e. surfaces can be laterally resolved in nanometric and vertically even in subnanometric scales, with those of a stylus profilometer, i.e. measurements are quick and can be performed in ambient air. During the measurement, a tip being attached to a cantilever scans the sample surface line by line, moving it with piezoelectric elements. Due to the interaction with the surface atoms, the cantilever bends differently as a function of tip position. This bending is assessed by a laser that is reflected from the back side of the cantilever and measured at a detector, consisting of several photodiodes, as seen in Figure 2.9. Changes in height and bending of the cantilever lead to intensity fluctuations in the photodiodes, enabling the extraction of morphological images of the sample surface.

From these images, the root mean square (RMS) roughness R_q can be extracted using

$$R_q = \sqrt{\frac{1}{L}\int_0^L (y(x))^2\, dx}, \tag{2.13}$$

where L is the length of one line profile and $y(x)$ is the height variation for each data point with

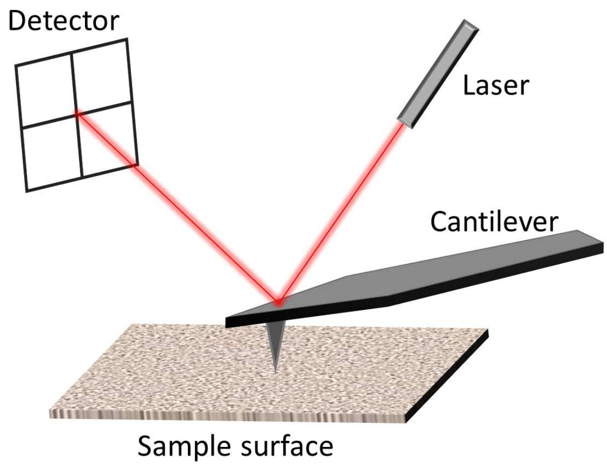

Figure 2.9: Schematic representation of an AFM measurement.

respect to their average height.

AFM images of 2×2 or 5×5 µm^2 were recorded using a Bruker Edge system equipped with a Si tip at a scanning frequency of 1 Hz in tapping mode.

2.3.2 X-ray reflectivity

If thin films exhibit a low crystalline quality and a lack of vertical x-ray coherence, it may be difficult or even impossible to extract their thickness using Equation 2.9. Another way to assess the thickness of thin films, including poorly crystalline and amorphous ones, is XRR, as explained in [146, 160, 161]. In an XRR experiment the incident x-rays impinge the sample at very low angles (around 0.2° to 5°) and their reflection is measured using $2\theta/\omega$ scans. Total reflection takes place due to the refractive index of the material being generally smaller than unity for x-rays, until a critical angle θ_c is reached. At angles above θ_c, the incident beam penetrates into the film and interference between x-rays reflected from the sample surface and from the film-substrate interface takes place. This leads to a drop of reflected intensity and the occurrence of interference fringes as a function of angle, as shown in Figure 3.2 of Section 3.2.1. The thickness d is linked with the angular positions θ_n of the maxima (or minima) having the order n with Snell's and Fresnel's laws as follows

$$\theta_n^2 = \left(\frac{\lambda}{2d}\right)^2 n^2 + \theta_c. \tag{2.14}$$

In case of several maxima (or minima) being present, a linear plot of θ_n^2 against n^2 exhibits the slope of $(\lambda/2d)^2$ and enables hence the determination of the film thickness. However, XRR curves contain additional information about the material being analyzed. The position of the critical angle θ_c depends on its refractive index and, hence, electron density ρ_e as follows

$$\theta_c = \sqrt{\frac{\lambda^2 r_e}{\pi}\rho_e}, \tag{2.15}$$

where r_e is the classical electron radius, giving the possibility to extract information about the materials' mass density. Furthermore, the damping of the interference fringes depends on the interface qualities, especially their roughness. The rougher the interfaces, the stronger the damping, because the x-rays are randomly scattered and are therefore not allowed to interfere. The exact dependence of the reflectivity curve on the interface roughnesses is rather complex and is given in the references cited above.

A fit of the XRR curves using appropriate simulation softwares allows the extraction of these additional information and further enables the analysis of multiple layer systems, as will be seen in the following chapters.

XRR experiments were performed in the same diffractometer as used for XRD (see Section 2.2.1), using the crystal analyzer detector in triple axis configuration in order to enable the resolution of interference fringes. Fitting of the curves was performed using the GenX [162] software.

2.4 Optical characterization

When electromagnetic radiation arrives from the vacuum to a material, the photons interact with the particles this material consists of. In general, light can be reflected, transmitted or absorbed.

In case of absorption, the energy of the incident radiation is transferred to the material leading to excitations. The nature of the excitations is mainly dependent on the incident light energy. Microwaves usually lead to rotational, IR radiation to vibrational and visible and UV radiation to electronic excitations. The latter process is particularly interesting for semiconductors, since the energy of band-to-band transitions can be assessed. Furthermore x-rays can excite core electrons and lead to ionization. In this section, optical characterization using photoluminescence (PL) and transmittance spectroscopy (light intensity that is neither absorbed, nor reflected) in the UV-vis-near infrared (NIR) region are briefly explained in order to evaluate the band gap energy of the materials studied in this thesis. Detailed information about the theory of light-matter interactions can be found e.g. in reference [163].

2.4.1 Photoluminescence

In PL, a UV-laser is used to excite electrons from the valence band to the conduction band, creating an electron-hole pair. Due to the excess of laser excitation energy with respect to the band gap, the electrons are excited to high energetic conduction band states. Non-radiative

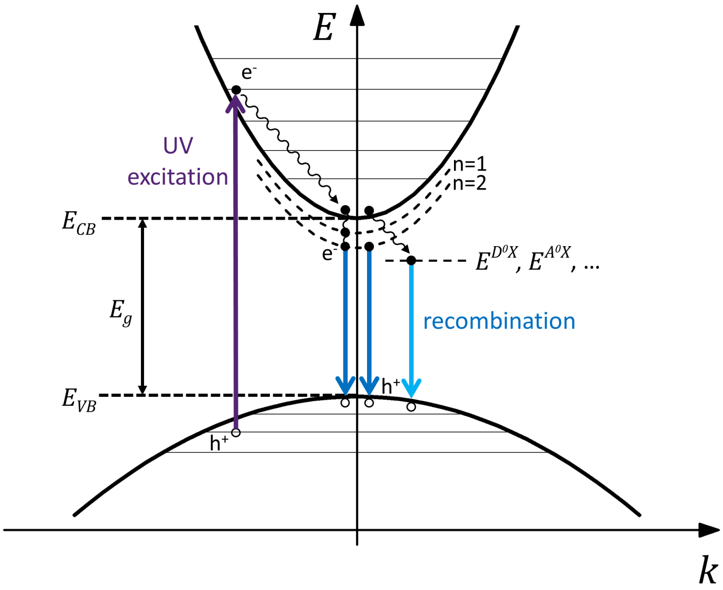

Figure 2.10: Schematic band gap diagram for radiative transitions.

relaxation of the electrons to the conduction band minimum, with the energy E_{CB}, takes place by exciting lattice phonons and changing their momentum k, as shown in Figure 2.10. On the other hand, the created holes in the valence band relax to its maximum, with the energy E_{VB}.

Direct recombination of electrons and holes between the conduction band minimum and valence band maximum create photons with the energy of the band gap E_g. However, electrons and holes can attract each other due to Coulomb interactions forming so-called excitons, whose energy levels lie within the band gap. These free excitons can, furthermore, bind to lattice defects or impurities, thereby reducing their energy further. The observed energy $h\nu$ of emission coming from bound exciton transitions is given by

$$h\nu = E_g - E^{Y^zX} - \frac{e^2}{4\pi\epsilon R_B}, \tag{2.16}$$

where E^{Y^zX} is the binding energy to the impurity state (being zero for free excitons), Y denotes the nature of impurity species and z the charge of the impurity (e.g. E^{D^0X} indicates binding to a neutral donor, E^{A^0X} to a neutral acceptor, etc.). The last term denotes the coulomb energy as discussed above, with the electron charge e, the absolute permittivity ϵ and the exciton Bohr radius R_B. By measuring the energy of the emitted photons, one can therefore infer information about the band gap energy and eventually the type and density of impurities.

In practice, lowest energy transitions are most commonly observed, because the probability of a certain energy level being occupied follows Boltzmann statistics

$$\frac{N_i}{N_{tot}} = e^{-\frac{E_i}{k_B T}}, \tag{2.17}$$

where N_{tot} denotes the total number of states of the system and N_i the number of possibly occupied states of a level i with an energy E_i, k_B is the Boltzmann constant and T the temperature. Equation 2.17 indicates that PL measurements are strongly dependent on temperature. Higher temperatures generally allow the occupation of higher energy levels, but broaden the peaks and lower the emission efficiency. Nevertheless, higher energy levels can also be assessed by increasing the laser intensity and thereby completely filling the lowest energy states. More detailed information about the theory of PL can be found in the references [164] and [165].

PL measurements were done using a frequency doubled Ar laser, leading to an excitation wavelength of 244 nm, or a HeCd laser with an excitation wavelength of 325 nm. For the Ar laser, a Si CCD camera was used as a detector, whereas for the HeCd laser the emitted light was detected by a photomultiplier after passing through a monochromator. The samples were kept under vacuum in a liquid helium cryostat, allowing a minimum measurement temperature of around 10 K.

2.4.2 Transmittance

By analyzing the properties of light that is transmitted through a sample, one can also deduce some of its basic optical properties. It enables for instance the evaluation of the absorption coefficient $\alpha(\lambda)$ of semiconductors, which can be used to deduce the band gap energy E_g. The advantage of this technique is that the sample does not have to be crystalline and exhibit a low density of defects, as it does not need to exhibit radiative emission. As mentioned above, light can be principally reflected, absorbed or transmitted from the sample. The transmitted portion $T(\lambda)$ can be calculated after the Lambert-Beer's law [166–168]

$$\frac{I}{I_0} = T(\lambda) = e^{-\alpha(\lambda)d}, \tag{2.18}$$

where I is the measured intensity and I_0 the incident light intensity. The measurement of $T(\lambda)$ allows therefore the determination of $\alpha(\lambda)$, which, in turn, can be used to determine the optical band gap energy of the sample. J. Tauc et al. [169] showed in 1966 that a representation of the absorption coefficient as a function of photon energy $h\nu$ can be used for the determination of the optical band gap. Close to the band edge, the absorption coefficient depends on the photon energy as follows

$$(\alpha(\lambda)h\nu)^{1/r} \propto (h\nu - E_g), \tag{2.19}$$

where $r = 1/2$ for direct and $r = 2$ for indirect transitions. The band gap is hence given by extrapolating the linear regime of this so-called Tauc plot and determining its intersection with the x-axis.

White light transmission measurements were performed at CRHEA using a home-built system, where the transmitted light passes via a monochromator to a photomultiplier that serves as the detector. Measurements including the NIR range were done by U. Teschner in the Felix-

Bloch-Institut für Festkörperphysik, Leipzig, Germany, using a PerkinElmer Lambda 19 spectrometer, equipped with a photomultiplier tube for the UV-vis range and a PbS detector for the NIR range.

2.5 Electrical characterization

In the context of device fabrication, it is extremely important to know the electrical properties of a sample, especially the type, concentration as well as mobility of the carriers present in the thin film. One possibility to determine these parameters is to perform Hall effect measurements using the van der Pauw method, developed in 1958 [170]. Using four ohmic contacts placed on the boundary of a sample, as shown in Figure 2.11(a), one can determine a resistance $R_{AB,CD}$ by applying a current to two of the contacts (here A and B) and measuring the voltage drop across the other ones (here C and D). After Ohm's law

$$R_{AB,CD} = \frac{V_{CD}}{I_{AB}}, \tag{2.20}$$

where I_{AB} is the applied current between A and B, and V_{CD} the measured voltage between C and D. Another resistance, $R_{CD,AB}$, can be similarly measured by simply applying the current between C and D and measuring the voltage drop across A and B. Van der Pauw showed that these two resistances are linked to the resistivity ρ by

$$e^{-\pi d \frac{R_{AB,CD}}{\rho}} + e^{-\pi d \frac{R_{CD,AB}}{\rho}} = 1, \tag{2.21}$$

where ρ/d is the sheet resistance and d the film thickness. If $R_{AB,CD} = R_{CD,AB} = R$ (being the case for geometrically perfect symmetric samples), Equation 2.21 simplifies to

$$\rho = \frac{\pi d R}{ln(2)}. \tag{2.22}$$

In the case of asymmetric samples, a geometrical correction factor, depending on the ratio of $R_{AB,CD}$ and $R_{CD,AB}$, can be introduced to Equation 2.22. The expression for this factor is given in reference [170].

Once the resistivity is known, one can do the actual Hall effect measurement (already discovered in 1879 by E. Hall [171]), as shown in Figure 2.11(b). A magnetic field is applied perpendicularly to the sample. When a current is flowing between two diagonal contacts, the charge carriers are deviated according to the Lorentz force

$$F_L = evB, \tag{2.23}$$

where e is the elemental charge, B the magnetic field strength and v the the average drift ve-

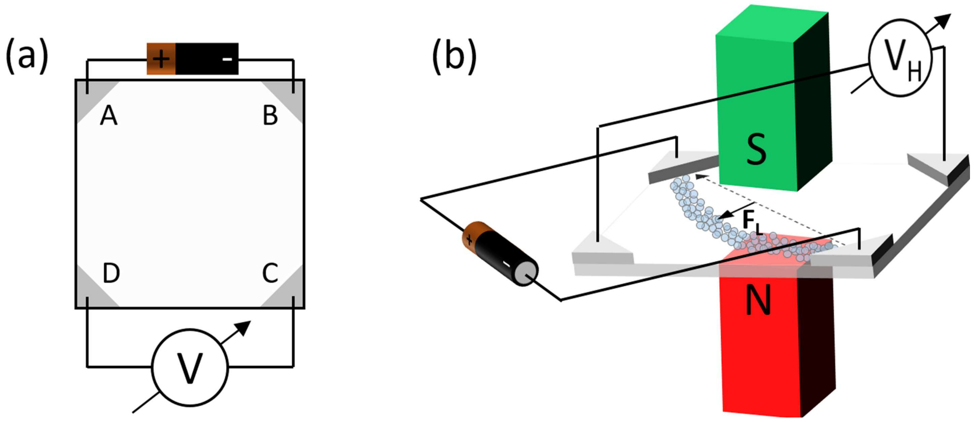

Figure 2.11: (a) Schematic resistivity measurement using the van der Pauw method. (b) Schematic Hall effect measurement. The magnetic field lines were omitted for clarity, but they originate in the north pole and point towards the south pole of the magnets.

locity of the carriers, which can be calculated by

$$v = \frac{I_{el}}{n_H A e}. \tag{2.24}$$

Here, I_{el} is the electric current, n_H the carrier concentration and A the cross sectional area of the (semi-)conductor. The electric field created by the deviation of the carriers is obtained by combining Equation 2.23 and 2.24, leading to

$$E = \frac{I_{el} B}{n_H A e}. \tag{2.25}$$

This electric field can be measured as a Hall voltage (taking into account the width of the sample)

$$V_H = \frac{I_{el} B}{n_H d e}, \tag{2.26}$$

which can be used to calculate n_H. The direction of the deviation determines the sign of V_H, containing therefore information about the type of the majority carriers (electrons or holes). The carrier mobility μ_H can then be calculated using the resistivity and the carrier concentration obtained from the measurements

$$\mu_H = \frac{1}{n_H \rho e}. \tag{2.27}$$

The mobility of the carriers is influenced by the number of scattering processes they experience when propagating through the material. This property is, in turn, determined by the materials crystallinity (number and type of defects, disorder, grain boundaries, etc.), the impurity concentration (intentional dopants or unintentional impurities), the carrier concentration itself (leading to scattering between the carriers) and scattering with lattice phonons. The sum of these effects determines the overall transport characteristics of a material. More details to electrical transport, e.g. about the temperature dependence of the mobility, can be found in reference [165].

The Hall effect measurements in the frame of this thesis were performed using a self built system, equipped with an electromagnet at a magnetic flux density of 0.8 T. Temperature dependent Hall effect measurements of selected samples were done by A. Welk with a Physical Property Measurement System (PPMS) from Quantum Design Europe in a range of 30 K to 300 K and a magnetic flux density up to 9 T (Felix-Bloch-Institut für Festkörperphysik, Leipzig, Germany).

Chapter 3

MBE growth and characterization of Zn_3N_2 thin films

In this Chapter, the development of epitaxial Zn_3N_2 thin film growth is discussed. We present the effect of the substrate material and the growth conditions on the film orientation and quality, and identify the epitaxial relationships of the grown thin films to their substrates [MgO (100) and YSZ (100)]. Subsequently, the fundamental physical properties, such as linear thermal expansion coefficient, electrical transport characteristics and band gap of Zn_3N_2 thin films are addressed. This chapter covers:

- Epitaxy of Zn_3N_2: Growth orientation tuning
- Structural characterization by XRD and RHEED: From epitaxial relations to crystalline quality
- Linear thermal expansion coefficients of Zn_3N_2
- Electrical transport in Zn_3N_2
- Band gap as a function of electron concentration

3.1 State of the art: Reminder

Although Zn_3N_2 epitaxy has been studied previously by MBE and sputtering on MgO (100), YSZ (100) and a-plane sapphire (see Section 1.2.4), a detailed description of the effect of substrate and growth conditions on the structural film properties, such as crystallinity, orientation and morphology, is still missing. Similarly, there is no report on the evaluation of the structural quality in epitaxial Zn_3N_2 up to now, although such investigations are necessary to develop strategies for the improvement of film qualities, and their use in devices. Furthermore, the linear thermal expansion coefficient of Zn_3N_2, a crucial parameter for the design of heterostructures, was not reported before this PhD.

Besides, the band gap of Zn_3N_2 is still under controversial discussion, experimental values ranging from 0.9 eV to 3.4 eV, as discussed in Section 1.2.3. This may be, on the one hand, connected to the immaturity of Zn_3N_2 growth, leading to low structural qualities that perturb the determination of the band gap. On the other hand, it seems clear that this large range or band gap energies is (at least partially) linked to the oxidation of Zn_3N_2 in air to ZnO and/or $Zn(OH)_2$, leading to an overestimation of the band gap energy [66, 87, 91, 98, 104]. Taking this effect into account, the Zn_3N_2 band energy is nowadays estimated to lay in a range of 0.9 eV to 1.5 eV.

On the contrary, the electrical properties of Zn_3N_2 are quite well established, probably due to its application as channel layer in TFTs. A low electron effective mass of 0.08 m_0 is accepted, leading to a high electron mobility of 395 $cm^2V^{-1}s^{-1}$ [99], which seems to be relatively independent of the crystalline quality of Zn_3N_2. Nevertheless, the growth of non-degenerate Zn_3N_2 is still challenging, with only one study displaying electron concentrations below 10^{18} cm^{-3} [92]. This is probably due to N-vacancies, Zn interstitials and/or oxygen contamination [72, 74, 75, 103].

3.2 Epitaxial growth of Zn_3N_2 by MBE

In the following, the development of Zn_3N_2 epitaxy, starting from the first attempts until the achievement of epitaxial thin films, is discussed. Since Zn_3N_2 epitaxy has not been established in CRHEA before the beginning of this project, the entire growth process needed to be explored and optimized. We point out the optimization necessary to achieve epitaxial Zn_3N_2 and demonstrate the possibility to control the film orientation by changing the growth conditions. Finally, the epitaxial relationships of the thin films to their crystalline substrates [MgO (100) and YSZ (100)] using XRD and RHEED are addressed, and their structural quality is evaluated as a function of the substrate and film orientation.

3.2.1 First attempts towards Zn_3N_2

In the literature, Zn_3N_2 epitaxy has been carried out in a quite large temperature range from 140 °C to 400 °C [53, 99, 103], which was used as a starting point for the substrate temperatures used in the first attempts to develop a Zn_3N_2 growth process by MBE in CRHEA. The XRD patterns of three early grown Zn_3N_2 thin films on MgO (100) are shown in Figure 3.1(a), grown at the conditions given in Table 3.1.

Sample I is grown at a relatively high substrate temperature of 400 °C, as well as a high Zn/N ratio. Although the peak at ~31.5° originates from (111)-oriented Zn_3N_2, there is a broad contribution close to the MgO (200) substrate reflection which is assigned to metallic Zn, indicating a too large Zn/N ratio during growth. Reducing the substrate temperature to 275 °C (sample II) leads to an increased intensity of the Zn_3N_2 (222) signal and a concomitant decrease of Zn (010). However, a third signal occurs, which can be assigned to ZnO (002). Similar results were obtained by Oshima *et al.* [see Figure 1.11(c)], who attributed the occurrence of ZnO to an increased activation of residual oxygen in the MBE chamber at high temperatures, since they were able to decrease the ZnO contamination by reducing the substrate temperature [53]. An alternative explanation for the occurrence of the ZnO peak could be a partial oxidation of Zn_3N_2 in air after the growth or the diffusion of oxygen from the substrate.

Table 3.1: Growth conditions of some of the first Zn_3N_2 thin films on MgO (100) grown at CRHEA.

Sample	Growth temp. (°C)	Zn flux (10^{-7} Torr)	Nitrogen flow (sccm)	Thickness (nm)	Growth rate (nm min^{-1})
I	400	30	0.35	45	0.33
II	275	30	0.35	~55	~0.36
III	200	2.7	1.0	42	0.8

Therefore, we reduced the growth temperature further and changed the Zn/N ratio towards more N-rich conditions, in order to avoid ZnO contamination, as well as the occurrence of metallic Zn. In sample III two signals, both originating from diffraction of Zn_3N_2 planes [(222) and (400)], are observed, giving rise to a polycrystalline thin film, but without any additional parasitic phase. This sample was used as a starting point for further optimization towards epitaxial Zn_3N_2. The associated RHEED pattern taken along the MgO [011] axis is a superposition of two diffraction patterns [see Figure 3.1(c)], where the streaky pattern corresponds to diffraction of Zn_3N_2 (222) and the spotty one to diffraction of Zn_3N_2 (400) planes, as will be demonstrated in the following section.

Interestingly, the growth is initiated by Zn_3N_2 (111), as no spots are observed in the RHEED pattern at an early stage. As the growth proceeds, the spotty pattern occurs and becomes more intense, until it finally dominates the RHEED. This phenomenon is discussed in more detail in the following sections, too.

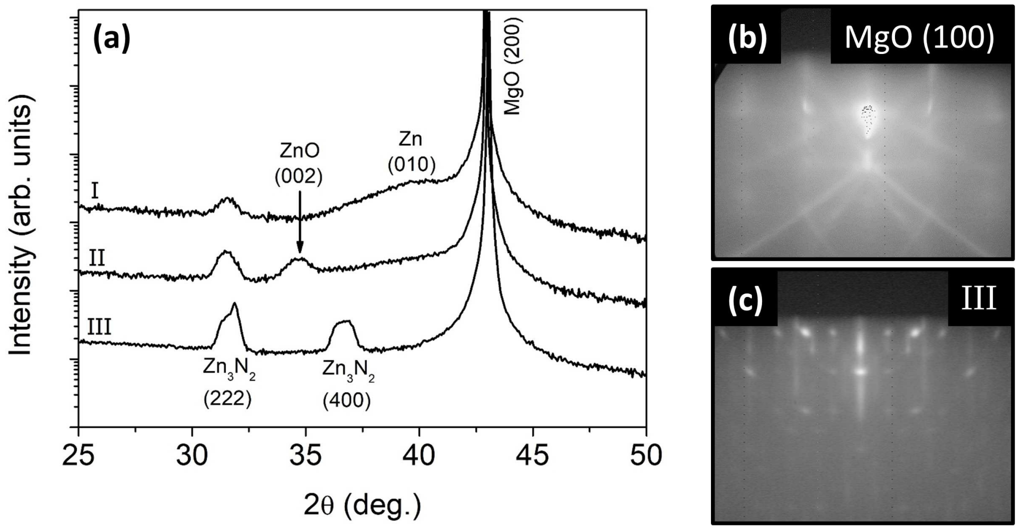

Figure 3.1: (a) $2\theta/\omega$ scans of the first samples aiming to grow Zn_3N_2, measured with a fully open detector in order to detect all contributions from parasitic phases. The numbers I to III refer to the growth conditions reported in Table 3.1, the curves are vertically shifted for clarity. The RHEED patterns of the MgO substrate and of sample III, both taken along the MgO [011] axis, are shown in (b) and (c), respectively.

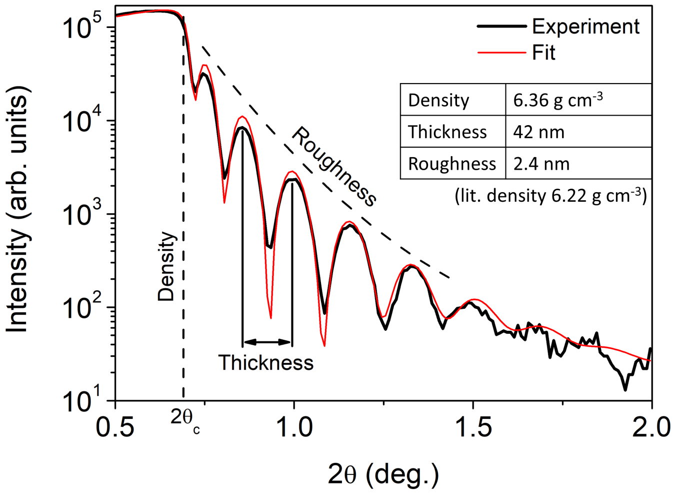

Figure 3.2: XRR curve of sample III. The density, thickness and roughness given in the inset are extracted using a fit based on the characteristics indicated in the curve and explained in Section 2.3.2.

The thicknesses of the samples I and III were obtained by XRR measurements, as shown for sample III in Figure 3.2. Besides the extraction of thickness, it is worth mentioning that for this sample the obtained density from the fit is close to the established Zn_3N_2 value of 6.22 g cm^{-3}, indicating a compact thin film with a stoichiometry close to ideal Zn_3N_2.

We employed systematically XRR for all grown Zn_3N_2 to extract their thicknesses. Note that in some cases (as e.g. for sample II), interference fringes are not visible in XRR due to high surface roughness and/or large thicknesses. In these cases, we estimated the thickness using *in-situ* reflectivity and/or extrapolation of the growth rate from similar samples and indicate this by the insertion of a "~" symbol wherever the thickness value is given.

3.2.2 From polycrystalline to epitaxial Zn_3N_2: Tuning of film orientation

After some optimization starting from sample III of the previous section, we investigated systematically the effect of the Zn/N ratio and the growth temperature on the film microstructure on two grown Zn_3N_2 series. Note that prior to growth the substrates were exposed for 10 min to N-plasma as well as Zn flux at a temperature of 300 °C. Although no growth takes place under these conditions, an improvement of the RHEED pattern is observed, indicating an improved surface crystallinity.

Effect of Zn/N ratio:
In order to change the Zn/N ratio, a Zn_3N_2 series with varying Zn flux is grown on MgO (100), at a substrate temperature of 100 °C. The growth conditions are given in Table 3.2.

Figure 3.3(a) shows the effect of Zn/N ratio on the growth orientation of the Zn_3N_2 thin films. At the highest Zn fluxes (samples i and ii), the thin films do not show any diffraction intensity besides the MgO (200) substrate reflection, indicating an amorphous film microstructure. Decreasing the Zn/N ratio leads to crystallization of the thin films along the [100]-direction, as observed in sample iii. While one may already announce the achievement of epitaxial Zn_3N_2 due to the unique presence of Zn_3N_2 (400) planes, the crystallinity of this thin film is still rather poor, indicated by a low diffraction intensity as well as spots elongated along circular arcs in the RHEED pattern (see Figure A.2 of the Appendix). Both features indicate a poor in-plane orientation.

A further decrease of the Zn/N ratio leads to the occurrence of a second peak, as observed for the samples iv to vi, which is assigned to the crystallization of (111)-oriented grains, concomitantly present with the Zn_3N_2 (100) grains that still dominate the diffraction pattern. Interestingly, the growth along the [111]-direction becomes dominant as the Zn/N ratio is further decreased (see sample vii), which may be used as a first step towards a tuning of Zn_3N_2 film orientation by adjusting the growth conditions.

The growth rate of this Zn_3N_2 series increases linearly as a function of Zn flux, as shown in Figure 3.3(b). At high growth temperatures, the growth rate usually increases initially as

Table 3.2: Growth conditions of Zn_3N_2 thin films on MgO (100) with varying Zn flux.

Sample	Growth temp. (°C)	Zn flux (10^{-7} Torr)	Nitrogen flow (sccm)	Thickness (nm)	Growth rate (nm min^{-1})
i	100	4.0	0.85	31	1.29
ii	100	3.1	0.85	31	1.0
iii	100	2.4	0.85	44	0.72
iv	100	2.0	0.85	35	0.56
v	100	1.6	0.85	42	0.42
vi	100	1.3	0.85	36	0.26
vii	100	1.1	0.85	30	0.24

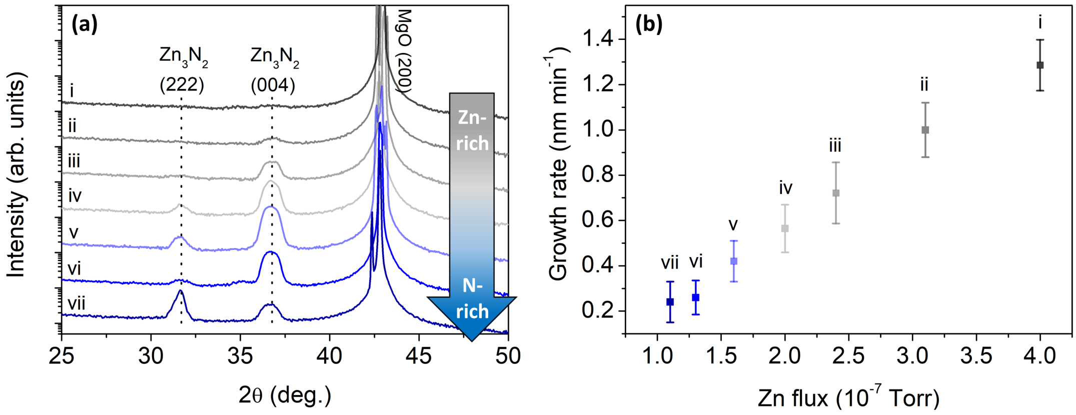

Figure 3.3: (a) $2\theta/\omega$ scans of Zn_3N_2 thin films as a function of Zn flux, measured with a fully open detector. The numbers i to vii refer to the growth conditions given in Table 3.2 and the curves are vertically shifted for clarity. (b) Growth rates of the samples in (a).

a function of metal flux until it reaches a saturation limit, indicating an increased metal re-evaporation rate when passing from the anion-rich to the metal-rich growth regime (see e.g. [172]). However, the low growth temperature of 100 °C chosen here prevents significant Zn re-evaporation. Hence, no saturation is observed and all Zn atoms arriving at the substrate are incorporated to the growing layer, leading to metal-rich stoichiometries when grown at high Zn fluxes, as discussed later.

Unfortunately, the determination of Zn-rich and N-rich growth regimes from this data is not straightforward and can be only estimated, given that no plateau is observed. We assumed Zn-rich conditions for the samples i to iii, where comparatively high growth rates and the transition from amorphous to crystalline Zn_3N_2 are found. On the other hand, the low growth rates of samples vi and vii indicate a lack of Zn, indicating N-rich conditions.

Effect of growth temperature:

In order to grow epitaxial Zn_3N_2, we also investigated the effect of substrate temperature on the film orientation, grown at an intermediate Zn/N ratio, as illustrated in Figure 3.4. The growth temperature was varied between 50 °C to 250 °C, with the conditions reported in detail in Ta-

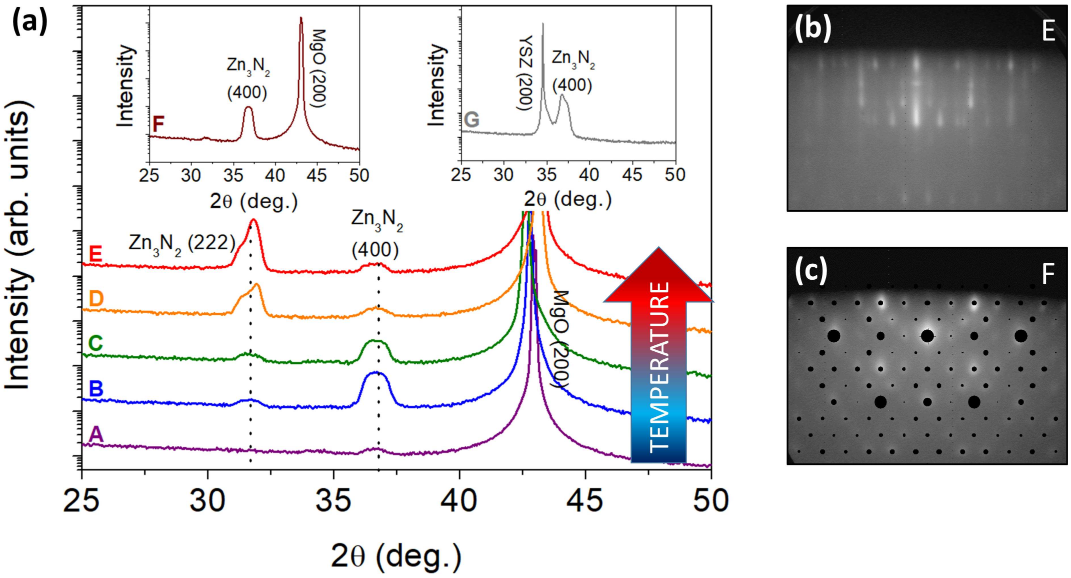

Figure 3.4: (a) $2\theta/\omega$ scans of Zn_3N_2 thin films as a function of growth temperature, measured with a fully open detector. The letters A to G refer to the growth conditions given in Table 3.3, the curves are vertically shifted for clarity. The RHEED patterns of the samples E and F, taken along the MgO [011] axis, are shown in (b) and (c), respectively. A simulated diffraction pattern corresponding to the Zn_3N_2 (011) plane of the reciprocal lattice is superimposed the RHEED of sample F, indicated by black dots.

ble 3.3.

At the lowest temperature of 50 °C (sample A), the thin film is nanocrystalline/amorphous, as no significant signals besides the MgO (200) substrate peak are detected. An increase of growth temperature leads to crystallization of the Zn_3N_2 thin films. In the samples B and C, grown at 100 °C and 150 °C, respectively, the Zn_3N_2 (400) reflection dominates the diffraction pattern. Hence, the majority of the grains are oriented along the [100]-direction, although a low-intensity contribution coming from Zn_3N_2 (222) planes is present. A further increase of substrate temperature leads to a stabilization of Zn_3N_2 (111), as found for the samples D and E (grown at 200 °C and 250 °C, respectively), since the (222) reflection is this time dominating the XRD pattern. Nevertheless, a parasitic contribution coming from Zn_3N_2 (100) grains is still present.

Interestingly, the growth of the samples B to E starts always with Zn_3N_2 (111) as discussed before, since no traces of (100)-oriented Zn_3N_2 could be detected by RHEED in the initial growth stage, as shown in Figure 3.4(b). The associated RHEED pattern of sample E is streaky, indicating a low surface roughness (XRR roughness was found to be 2.3 nm), and consists of numerous diffraction rods. The epitaxial relationships generating such a RHEED pattern are discussed in Section 3.2.3. Let us now focus on the fact that, as the growth proceeds, the Zn_3N_2 (111) layer is overgrown by (100)-oriented Zn_3N_2, as indicated by the parasitic Zn_3N_2 (400) reflection in XRD and the occurrence of additional spots in the RHEED pattern (inset III of Fig-

Table 3.3: Growth conditions of Zn_3N_2 thin films with varied substrate temperature.

Sample	Substrate	Growth temp. (°C)	Zn flux (10^{-7} Torr)	Nitrogen flow (sccm)	Thickness (nm)	Growth rate (nm min^{-1})
A	MgO (100)	50	2.2	1.0	48	0.69
B	MgO (100)	100	2.2	1.0	44	0.69
C	MgO (100)	150	2.2	1.0	38	0.60
D	MgO (100)	200	2.2	1.0	37	0.59
E	MgO (100)	250	2.2	1.0	41	0.54
F	MgO (100)	100	2.8	0.85	65	1.08
G	YSZ (100)	200	2.0	0.85	25	0.72

ure 3.1). Indeed, in cubic materials, (100) surfaces are commonly the most stable ones due to a low dangling bond density compared to other orientations, as for example reported for rocksalt and perovskite structures [173].

The initial (111)-oriented growth could be explained by the lattice parameter mismatch of Zn_3N_2 to MgO. In a $[100]_{Zn_3N_2} \parallel [100]_{MgO}$ configuration, the lattice mismatch is +16.0 %, as reported in Table 1.1. However, in the configuration found here the average lattice mismatch is reduced to around +8 % (see Section 3.2.3). From this point of view, one could argue that at initial growth stages the substrate-film interaction dominates, while for larger thicknesses thermodynamics takes over. Although a lattice mismatch of +8 % is still large, the substrate imposes a (111) orientation to the nucleating Zn_3N_2, which reorients along the thermodynamically more stable [100] direction subsequently.

By slightly adjusting the Zn/N ratio we were able to grow epitaxial Zn_3N_2 (100) at 100 °C (see sample F in the left inset of Figure 3.4). The RHEED pattern associated to this sample and taken along the MgO [011] axis is spotty (XRR roughness 2.7 nm), but can be perfectly reproduced using a single theoretical diffraction pattern corresponding to the Zn_3N_2 (011) plane of the reciprocal lattice, as shown by the black dots superimposed to the RHEED in Figure 3.4(c). However, small traces of Zn_3N_2 (111) are still present at 31.7°, in agreement with our statement of a (111) oriented inter-layer at the nucleation stage.

In order to avoid the parasitic Zn_3N_2 (111) phase being present at the film-substrate interface, we performed growth on YSZ (100) substrates, having a lower lattice parameter mismatch to Zn_3N_2 (−5.1 % in a $[100]_{Zn_3N_2} \parallel [100]_{YSZ}$ configuration, as reported in Table 1.1). Indeed, no parasitic Zn_3N_2 (111) phase is observed in the XRD pattern of sample G, grown at 200 °C and shown in the right inset of Figure 3.4, giving rise to epitaxial Zn_3N_2 (100). The RHEED pattern of this thin film is very similar to that of Zn_3N_2 (100) on MgO (100), as shown in Figure 3.9(c) of Section 3.2.3.

In this series, there was no (or very slow) growth observed above a substrate temperature of 250 °C, indicating the onset of Zn re-evaporation, consistent with some of the previous studies on epitaxial Zn_3N_2 [99, 103]. Note that we grew samples at 400 °C, as discussed in the context of Figure 3.1, but with a low growth rate of 0.33 nm min^{-1}, although a Zn flux one order of magnitude higher than in this series was used (see Table 3.1).

To conclude this section, we successfully established Zn_3N_2 growth in CRHEA and are able to grow amorphous, polycrystalline and epitaxial Zn_3N_2 by MBE. Furthermore, the film orientation can be controlled by varying the growth conditions, Zn_3N_2 (111) is stable on MgO (100) in the first ~40 nm at a substrate temperature of 250 °C and occurs generally as inter-layer on MgO (100). On the other hand Zn_3N_2 (100) is the thermodynamically more stable orientation, and is achieved at 100 °C on MgO (100), as well as at 200 °C on YSZ (100).

3.2.3 Epitaxial relationships of Zn_3N_2 on different substrates

In order to identify the epitaxial relationships of the grown Zn_3N_2 (100) and (111) thin films (i.e. their in-plane orientation with respect to their substrate) and assess their epitaxial character, we measured XRD Φ scans on asymmetric Zn_3N_2 planes, where Φ denotes the azimuthal angle around the growth direction. The Φ scan on Zn_3N_2 (440) planes of sample E [Zn_3N_2 (111) on MgO (100)] is shown in Figure 3.5(a). Given that the film orientation is (111), three peaks are in principle expected for a rotation of $\Phi = 360°$. However, 12 peaks are experimentally observed.

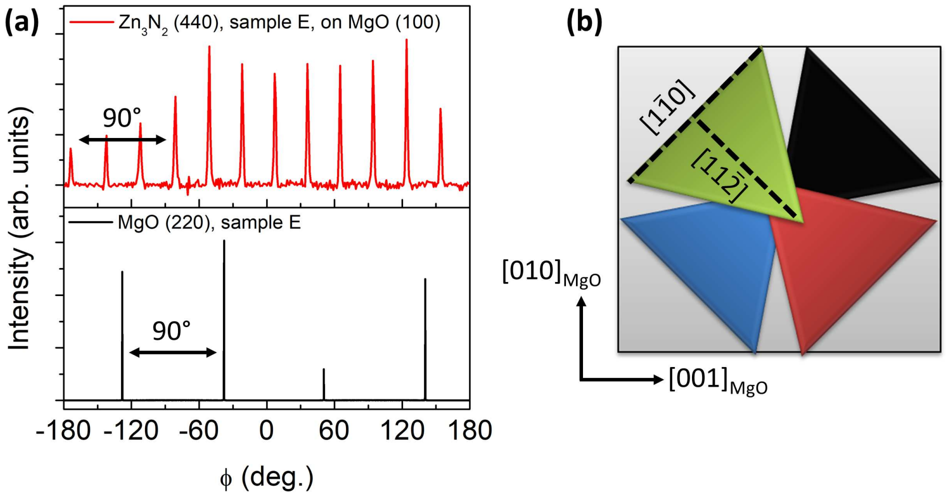

Figure 3.5: (a) Φ scan on asymmetric Zn_3N_2 (440) planes of sample E [Zn_3N_2 (111) on MgO (100)] compared to the Φ scan on the MgO (220) substrate planes. (b) Schematic epitaxial relationships resulting from (a).

In order to explain this discrepancy one has to reconsider the theory of epitaxial rotational domains as explained in Section 1.1.1: For a cubic [111]-oriented thin film (having 3-fold rotational symmetry) grown on a cubic [100]-oriented substrate (with 4-fold rotational symmetry), there are four energetically equivalent in-plane arrangements. Therefore, four epitaxial domains are expected, as schematically illustrated in Figure 3.5(b), leading, in turn, to the observation of 12 peaks in the Φ scan. Note that the Zn_3N_2 (440) peaks occur at a different azimuthal angle than the MgO (220) substrate peaks, indicating a 45° in-plane rotation of the four epitaxial domains with respect to the substrate. The in-plane epitaxial relationships for Zn_3N_2 (111)

on MgO (100) are hence given by

$$[1\bar{1}0]\ Zn_3N_2 \parallel [011]\ MgO \tag{3.1a}$$

$$[11\bar{2}]\ Zn_3N_2 \parallel [01\bar{1}]\ MgO \tag{3.1b}$$

plus the three additional epitaxial domains obtained by 90°, 180°, and 270° rotations of one triangular Zn_3N_2 domain around the [111] growth axis. For clarity, the projections of the Zn_3N_2 $[1\bar{1}0]$ and $[11\bar{2}]$ directions are indicated in one epitaxial domain in the schematic structure of Figure 3.5(b).

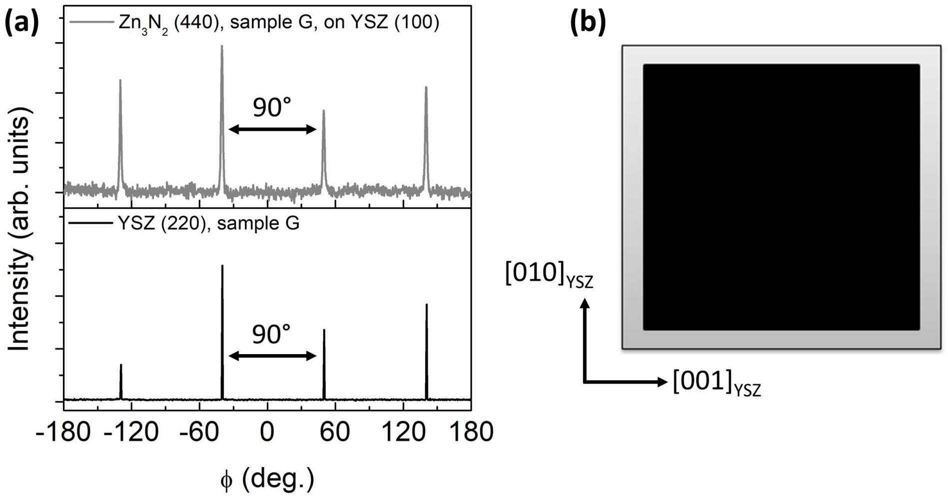

Figure 3.6: (a) Φ scan on asymmetric Zn_3N_2 (440) planes of sample G [Zn_3N_2 (100) on YSZ (100)] compared to the Φ scan on the YSZ (220) substrate planes. (b) Schematic epitaxial relationships resulting from (a).

The presence of four epitaxial domains leads also to the presence of the numerous diffraction rods observed in the RHEED pattern of this sample (see Figure 3.4), due to a superposition of the diffraction pattern belonging to each individual domain family. The diffraction patterns of such thin films is discussed in more detail in Section 4.3.2 and 4.3.3, where we show simulations to reproduce a similar RHEED obtained for the growth of iso-structural Mg_3N_2 thin films, also along the [111] direction on MgO (100).

Figure 3.6(a) shows the Φ scan on Zn_3N_2 (440) planes of sample G [Zn_3N_2 (100) on YSZ (100)]. As expected for a (100)-oriented 4-fold symmetric thin film, four peaks are found experimentally, which occur at the same azimuthal angles as the YSZ (220) peaks. Consequently, the epitaxial relationships [shown schematically in Figure 3.6(b)] are

$$[100]\ Zn_3N_2 \parallel [100]\ YSZ \tag{3.2a}$$

$$[011]\ Zn_3N_2 \parallel [011]\ YSZ. \tag{3.2b}$$

The same epitaxial relationships were found for Zn_3N_2 (100) on MgO (100) (sample F, Φ scan shown in Figure A.3 of the Appendix), as confirmed by the RHEED pattern observed for this sample [see Figure 3.4(c)], where diffraction of Zn_3N_2 (011) planes was observed along the MgO [011] direction. Hence, Zn_3N_2 (100) shows the same epitaxial relationships on both MgO (100) and YSZ (100), without additional rotational domains.

3.2.4 Out-of plane lattice parameter

In order to assess the out-of-plane lattice parameter of the grown Zn_3N_2 thin films, being a measure of their strain state, we measured high-resolution XRD on the symmetric Zn_3N_2 reflections of the different thin film-substrate configurations discussed above. Figure 3.7(a) shows the high-resolution $2\theta/\omega$ scan of sample E [Zn_3N_2 (111) on MgO (100)]. Finite thickness interference fringes surrounding the (222) main reflection are clearly observed, indicating a high out-of-plane x-ray scattering coherence, as explained in Section 2.2. Representing Equation 2.9 in angular coordinates allows us to simulate the theoretical diffraction pattern (considering a perfect crystal without interface roughness) using

$$I \propto \frac{\sin^2(2\pi n_{uc} d_{hkl} \sin\theta/\lambda)}{\sin^2(2\pi d_{hkl} \sin\theta/\lambda)}. \tag{3.3}$$

Note that the experimental thickness fringes surrounding the (222) main peak exhibit an asymmetry between the higher/lower 2θ angles, with higher intensity on the smaller 2θ-side. This indicates a change of the out-of-plane lattice parameter as a function of thickness, which can be interpreted as a strain/compositional gradient. Inserting a d_{hkl} that can vary as a function of thickness into Equation 3.3 allows to reproduce this asymmetry. Lichtensteiger [174] developed a software based on a d_{hkl} that changes gradually as a function of thickness according to

$$d_{hkl} = Ae^{N_{uc}/B} + C, \tag{3.4}$$

where N_{uc} is the running unit cell number and A, B and C are fitting parameters.

Using her simulation software, a good agreement is achieved for Sample E, where an average d_{222} of 2.826 ± 0.001 Å is obtained, as well as a thickness of 40.1 ± 0.3 nm, in agreement with the value of 41 nm obtained from XRR (see Table 3.3). The out-of-plane inter-planar distance is somewhat larger than the literature value of 2.820 Å for fully relaxed Zn_3N_2, indicating a global in-plane compressive strain state of the layer. Plotting the inter-planar d_{222} distance obtained from the simulation as a function of thickness [Figure 3.7(b)], reveals a d_{222} that is largest at the film-substrate interface, and relaxes to the literature value of unstrained Zn_3N_2 (222) as the growth proceeds.

To account for this behavior, the determination of the lattice mismatch in this configuration, according to the epitaxial relationships determined in the previous section, is necessary. Along the Zn_3N_2 $[11\bar{2}]$ direction, a small lattice mismatch of +0.54 % is obtained using Equa-

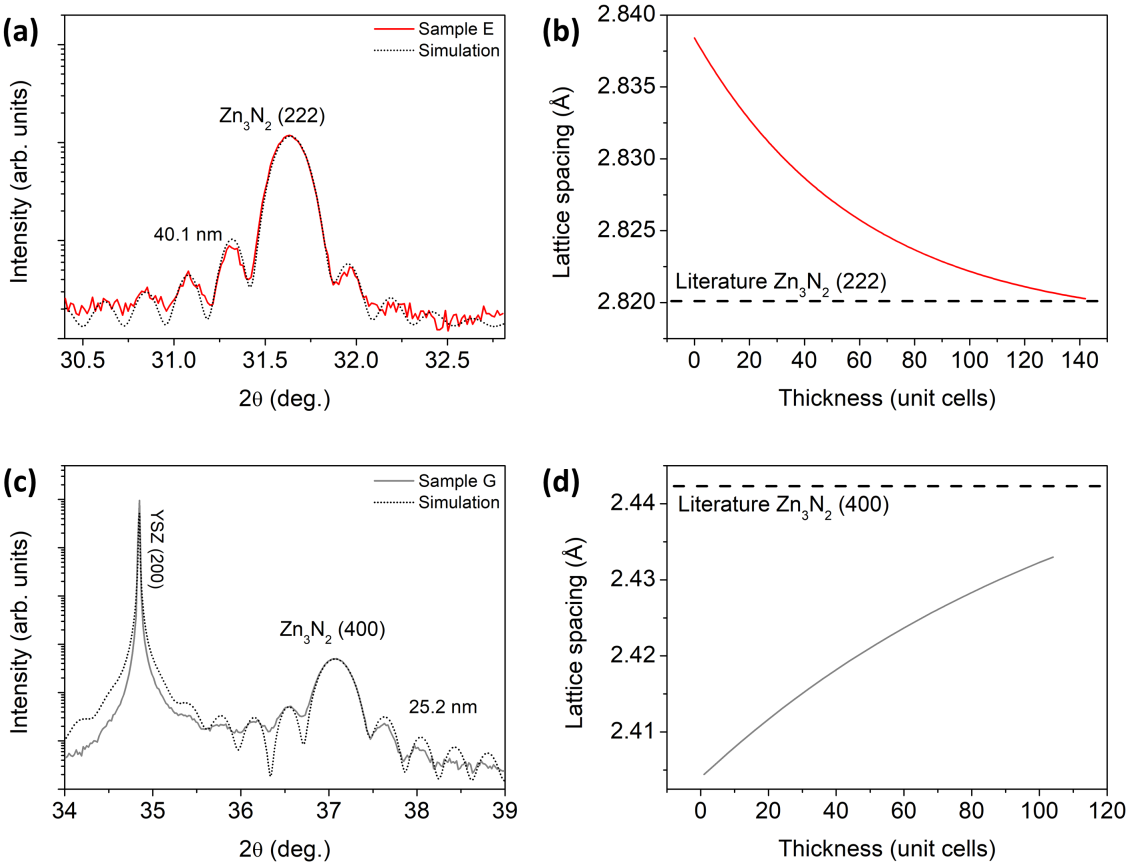

Figure 3.7: HRXRD on symmetric Zn_3N_2 reflections around (a) Zn_3N_2 (222) [sample E, Zn_3N_2 (111) on MgO (100)], with the extracted depth-dependent lattice parameter indicated in (b), and (c) Zn_3N_2 (400) [sample G, Zn_3N_2 (100) on YSZ (100)], with the extracted depth-dependent lattice parameter indicated in (d). The curves were recorded with the crystal analyzer detector.

tion 1.1. On the other hand, along Zn_3N_2 $[1\bar{1}0]$, a mismatch of +16.0 % is present. Hence, the substrate imposes its smaller lattice parameter to the nucleating Zn_3N_2 layer, leading to an in-plane compressive strain at the film-substrate interface and, therefore, to an expansion of the out-of-plane lattice spacing. As the thickness is increased, the strain is released by the introduction of defects, such as dislocations (see Figure 1.2). Note that the lattice mismatch is calculated using two MgO unit cells with one Zn_3N_2 unit cell, due to the large lattice parameters present in the anti-bixbyite crystal structure.

Similarly, the high-resolution $2\theta/\omega$ scan of sample G [Zn_3N_2 (100) on YSZ (100)] is presented in Figure 3.7(c). Also the symmetric (400) reflection of this sample is surrounded by finite thickness interference fringes, indicating coherent x-ray scattering from large areas. The average d_{400} was found to be 2.420 ± 0.001 Å and the thickness extracted from the simulation was 25.2 ± 0.3 nm, consistent with the XRR thickness of 25 nm. This time, the d_{400} lattice spacing is smaller than the literature value of fully relaxed Zn_3N_2 (2.442 Å), indicating a global tensile strain due to a lattice expansion in-plane, as expected with a given lattice parameter mismatch of −5.1 % (see Table 1.1) in this epitaxial configuration. The simulation of the diffraction pattern reveals a strong tensile strain at the film-substrate interface that relaxes towards the Zn_3N_2 (400) literature value. Although counterintuitive, the surrounding thickness oscillations show an asymmetry similar to that of sample E, i.e. a higher intensity at smaller 2θ angles, which was interpreted before to originate from a compressive strain at the film-substrate interface. In sample G, however, an additional diffraction intensity coming from the scattering tails of the YSZ (200) substrate reflection, closely located and superimposed to the Zn_3N_2 (400) peak, leads to a similar asymmetry as observed in sample E. Including this effect in the simulation gives rise to the evolution of d_{400} as shown in Figure 3.7(d), in agreement with an in-plane tensile strain, where the YSZ substrate imposes its larger lattice parameter to the growing film. Note that the lattice mismatch is also in this case calculated using two YSZ unit cells and one Zn_3N_2 unit cell.

On the contrary, there are no finite size interference fringes observed for sample F (Zn_3N_2 (100) on MgO (100), see Figure A.4 of the Appendix for $2\theta/\omega$ scan), indicating a loss of out-of-plane x-ray scattering coherence and pointing towards a lower structural quality of this thin film, as will be demonstrated in the following.

3.2.5 Structural quality of Zn_3N_2

A good indicator for the crystalline quality of a thin film is the full width at half maximum (FWHM) of its ω rocking curve, as discussed in Section 2.2.1. The ω scans on the symmetric reflections of our epitaxial Zn_3N_2 thin films, measured with a fully open detector and fitted with pseudo-voigt functions, are presented in Figure 3.8. Note that symmetric reflections contain information about the tilt of a sample (see Figure 2.4), since only the rotational disorder of atomic planes parallel to the surface is measured.

The (111)-oriented Zn_3N_2 thin film [sample E, see Figure 3.8(a)] exhibits a narrow rocking curve with a peak width of 0.22°, proving a high parallelity of the atomic planes perpendicular to the growth direction, consistent with the occurrence of finite thickness interference fringes in Figure 3.7(a). On the contrary, sample F [Zn_3N_2 (100) on MgO (100), shown in Figure 3.8(b)] shows a broad rocking curve with an FWHM of 1.6°, indicating a strong tilt that necessarily leads to a loss of long-range x-ray scattering coherence, accompanied by vanishing thickness fringes.

Interestingly, the rocking curve of sample G, illustrated in Figure 3.8(c), consists of two components, one broad contribution with an FWHM of 1.1° and another, narrow contribution having a peak width of 0.16°. This two-component line shape gives rise to a film structure with two grain families, one being well oriented along the [100] growth direction and another one showing a relatively strong misorientation with respect to the [100] direction (tilt). In order to identify the spatial distribution of these families in the film structure, we grew a thicker Zn_3N_2 (100) thin film on YSZ (100), using the same growth conditions as for sample G. The

ω scan of the symmetric (400) reflection of this 175 nm-thick sample is shown in Figure 3.8(d). The narrow contribution disappeared completely and the rocking curve is dominated by a 1.0°-wide peak. Similar observations were found by Miyake *et al.* [175], who found two-component line shapes in symmetric ω rocking curves of their sputtered AlN layers on c-plane sapphire. They attributed the narrow contribution to a highly oriented, 10 nm-thick nucleation layer as confirmed by TEM experiments [175, 176], which is overgrown by strongly tilted AlN, causing the broad contribution. While the diffraction intensity of the nucleation layer causing the narrow peak stays constant as the film thickness increases, the intensity of the tilted grain family increases until it completely dominates the diffraction pattern, as observed in our case. We can hence assume a similar microstructure for our Zn_3N_2 (100) thin films on YSZ (100).

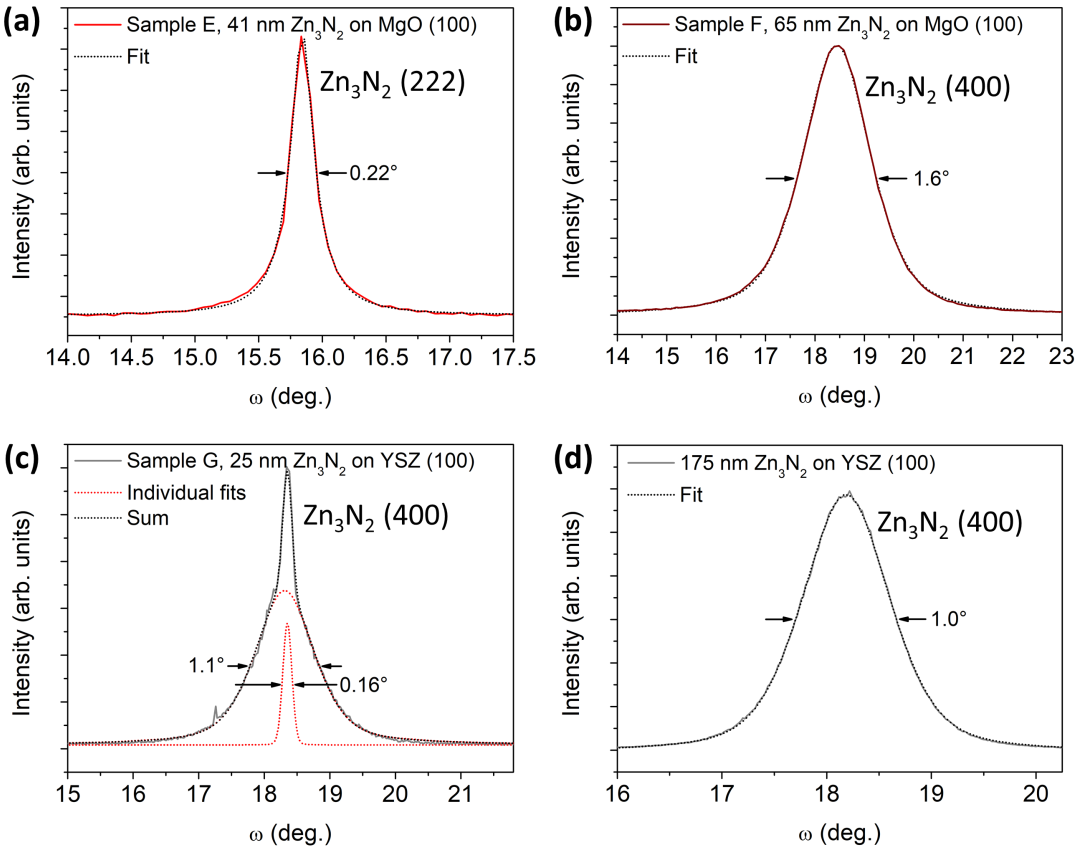

Figure 3.8: Symmetric ω scans of different Zn_3N_2 thin films. (a) Around the (222) reflection of sample E [41 nm Zn_3N_2 (111) on MgO (100)]. (b) Around the (400) reflection of sample F [65 nm Zn_3N_2 (100) on MgO (100)]. (c) Around the (400) reflection of sample G [25 nm Zn_3N_2 (100) on YSZ (100)]. (d) Around the (400) reflection on 175 nm Zn_3N_2 (100) on YSZ (100), grown at the same conditions as sample G. Note that different x-scales are used for the curves, which were all recorded using a fully open detector.

In order to obtain information about in-plane lattice rotations (twist), one has to analyze rocking curves of asymmetric reflections (see Section 2.2.1). These planes are measured by inclining the sample by an angle χ, until the desired plane to be measured fulfills the diffraction conditions (skew-geometry). While the atomic planes perpendicularly to the surface (i.e. $\chi = 90°$) allow to directly assess the twist, the planes between $0° < \chi < 90°$ contain information about both tilt and twist, which can be discriminated by subsequent modeling. In a model proposed by Lee *et al.* [177], who evaluated the crystallinity of heteroepitaxial GaN, AlN and AlGaN thin films, the FWHMs Γ_{hkl} of asymmetric reflections as a function of χ are given by

$$\Gamma_{hkl} = \sqrt{(\Gamma_y \cos\chi)^2 + (\Gamma_z \sin\chi)^2 + (2\pi/L)^2/Q^2_{hkl}}, \tag{3.5}$$

where Γ_y and Γ_z are the contributions of tilt and twist, respectively, to the width of Γ_{hkl}. The last term contains the effective coherence length L, correcting broadening due to finite grain sizes.

The FWHM extracted from the rocking curves of several asymmetric reflections as a function of χ is shown in Figure 3.9(a) for the samples E, F and G.

For all three samples an increase of Γ_{hkl} as a function of χ is observed, indicating that the film microstructure is dominated by twist, being well reproduced using Equation 3.5 and neglecting finite grain sizes. However, the absolute degree of misorientation differs strongly when considering the different samples. The samples E and G show relatively moderate misorientations with Γ_y tilt values of 0.3° and 1.0°, and Γ_z twist values of 1.1° and 1.6°, respectively, extracted from the fit. Note that we plotted the FWHM of the broad contribution for sample G, as no narrow peak was observed in any of its asymmetric reflections. Sample F, on the contrary, exhibits already an FWHM of $\Gamma_y = 1.6°$ for the tilt, which increases strongly as a function of χ to a value of $\Gamma_z = 4.9°$. This strong twist component can be also observed in the RHEED pattern of sample F, which is reprinted here from Figure 3.4 without the simulated diffraction pattern and compared to that of sample G (see Figure 3.9(b) and (c), respectively). Besides confirming again that both thin films exhibit the same epitaxial relationships, the RHEED of sample F appears blurry, exhibiting enlarged spots with respect to that of sample G, due to the strong in-plane twist present in sample F.

To account for this large misorientation in Zn_3N_2 (100) grown on MgO (100) one has to reconsider the lattice parameter mismatch of thin film and substrate. In this epitaxial configuration the lattice mismatch is +16.0 %, which is avoided by imposing a [111] growth direction to the nucleating layer, thereby reducing the average lattice mismatch to ~8 %, as mentioned before. Note that this parasitic Zn_3N_2 (111) contribution is also detected in the XRD of sample F, though with very low intensity (see left inset of Figure 3.4). Hence, the (100)-oriented Zn_3N_2 overgrows this Zn_3N_2 (111) inter-layer, probably accompanied by a reduction of structural quality in this thin film.

In summary, the crystalline properties of epitaxial Zn_3N_2 thin films have been investigated in detail using XRD and RHEED. Zn_3N_2 (100) exhibits the same in-plane orientation on MgO (100) and YSZ (100), where the cubic Zn_3N_2 thin film preserves the crystallographic directions of the respective substrate. While the Zn_3N_2 (100) thin films nucleate with a high out-of-plane crys-

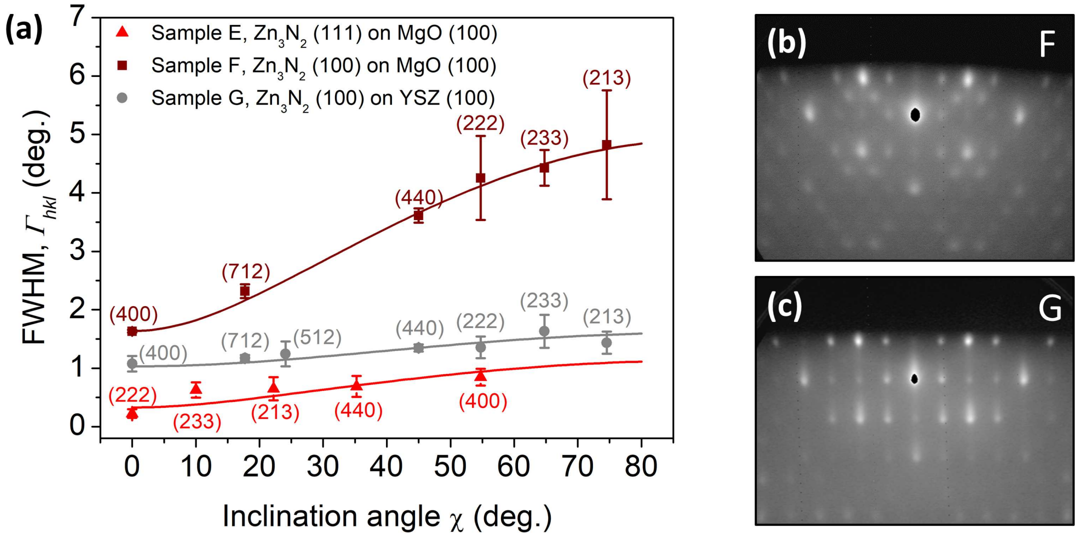

Figure 3.9: (a) FWHM as a function of χ of various asymmetric reflections for the samples E, F and G, measured with a fully open detector. The RHEED patterns along MgO [011] for the samples F and G are illustrated in (b) and (c), respectively.

talline quality on YSZ (100), which degrades as the film thickness increases, a Zn_3N_2 (111) inter-layer is introduced on MgO (100), thereby reducing the average lattice mismatch from 16 % to 8 %, at the expense of structural quality of the overgrowing (100) thin film. The thickness of the Zn_3N_2 (111) inter-layer can be varied by changing the growth conditions, as discussed in the previous section, allowing to grow thin epitaxial Zn_3N_2 (111) on MgO (100). These thin films exhibit four epitaxial domains when grown on MgO (100) due to different substrate-epilayer rotational symmetries. Nevertheless, they show small in-plane and out-of-plane misorientations before a change of film orientation towards (100) takes place, at thicknesses above ~40 nm.

3.3 Linear thermal expansion coefficient of Zn_3N_2

Since epitaxy is generally performed at temperatures higher than room temperature, the knowledge of the linear thermal expansion coefficient of thin film and substrate material in a large temperature range is extremely important in order to evaluate their lattice parameter mismatch at a given growth temperature. On the one hand, this may enable the design of heterostructures retaining pseudomorphic growth or, on the contrary, it can enable to favor a rapid plastic relaxation by maximizing the initial strain on the nucleating film. Furthermore, a mismatch of thermal expansion coefficients of thin film and substrate material can eventually yield to the formation of additional defects in the film, such as dislocations and cracks, during the cool-down to room temperature, which may be detrimental for certain applications.

In this context, we measured the out-of-plane lattice parameter of two Zn_3N_2 samples as a function of temperature by employing high-temperature XRD, as shown for one sample in

Figure 3.10(a). A clear shift of the (400) reflection towards lower diffraction angles as a function of measurement temperature is observed in the $2\theta/\omega$ scan of the Zn_3N_2 (100) thin film on YSZ (100), giving rise to an out-of-plane lattice expansion. Similar observations have been made on a Zn_3N_2 (100) grown on MgO (100), as shown in Figure A.5 of the Appendix. Note that no diffraction is detected above a temperature of 425 °C for any of the samples, indicating an evaporation or decomposition of the Zn_3N_2 thin films. This is in agreement with the low growth temperatures found for Zn_3N_2 in this work as well as in literature (≤ 400 °C) [53, 99, 103].

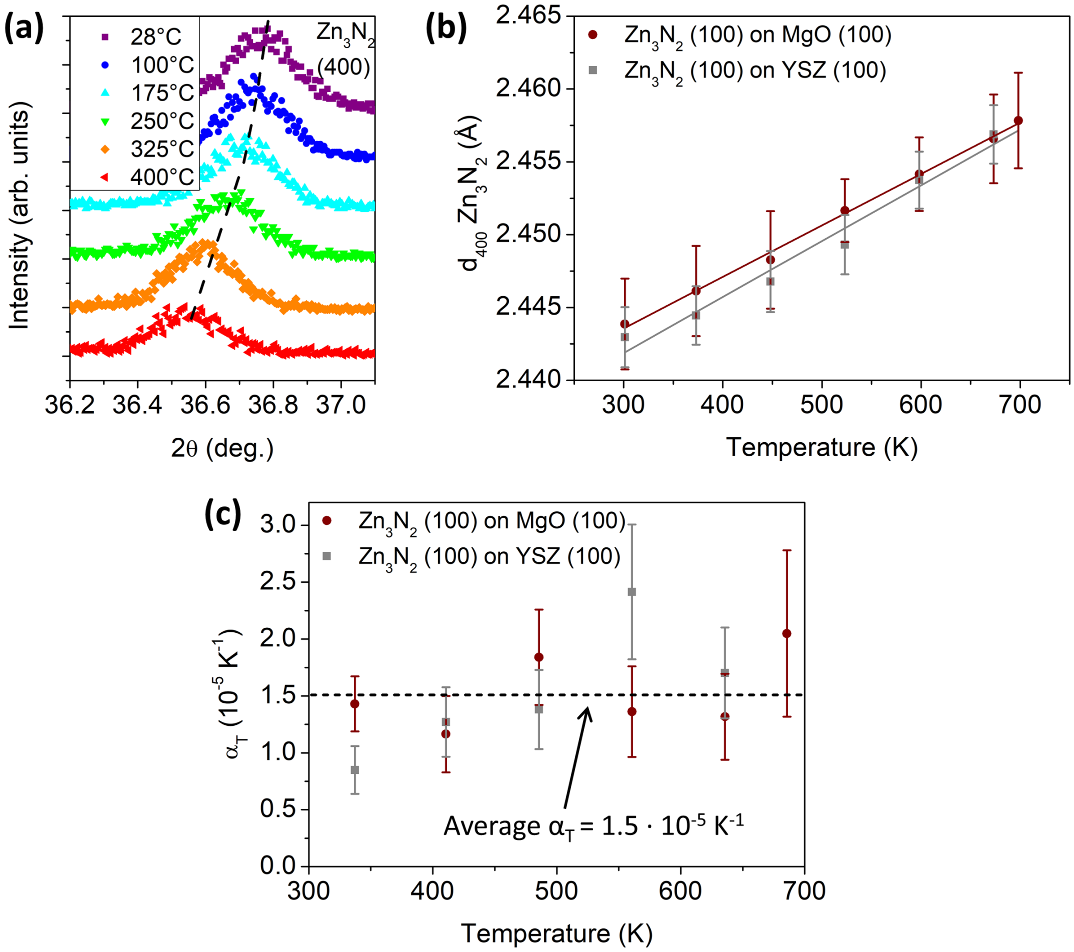

Figure 3.10: (a) High-temperature XRD on a Zn_3N_2 (100) thin film grown on YSZ (100). (b) Zn_3N_2 d_{400} inter-planar distance as a function of temperature for two Zn_3N_2 (100) thin films, the one shown in (a) and one grown on MgO (100). (c) Linear thermal expansion coefficient point by point, extracted from (b).

Using Bragg's Equation, one can extract the (400) inter-planar distance as a function of temperature, as shown in Figure 3.10(b). A linear increase of d_{400} as a function of temperature is observed. Note that in the entire temperature range, the absolute d_{400} value of Zn_3N_2 on YSZ is smaller than for the film grown on MgO. This is due to the opposite lattice parameter mismatches of Zn_3N_2 to YSZ and MgO, introducing an in-plane tensile or in-plane compressive strain to the growing thin film, respectively, as discussed in Section 3.2.3. From the slopes in Figure 3.10(b), an average linear thermal expansion coefficient of $\alpha_T = 1.5 \times 10^{-5}\,\mathrm{K}^{-1}$ is extracted, which is roughly four times higher than the linear thermal expansion coefficients of III-nitrides such as GaN or AlN [178, 179], but in the same range than the one of the iso-structural Mg_3N_2, as discussed in Section 4.5.

It is important to emphasize that we found similar slopes for both samples, even though the effect of thermal expansion from the substrates is different in the two cases. Since our thin films are epitaxially attached to their substrates, two different extreme scenarios for their thermal expansion can be considered. In case of a pseudomorphic thin film with low defect density, the thermal expansion of the layer will be mostly driven by the thermal expansion of its underlying substrate, whose influence needs to be corrected for when extracting the linear thermal expansion coefficients of the film. On the contrary, if the layer exhibits high defect densities, it eventually expands independently from the substrate, giving direct access to the linear thermal expansion coefficient without applying any further corrections. In order to investigate this effect, we extracted the linear thermal expansion coefficients [180, 181] point-by-point as a function of temperature for Zn_3N_2 on both MgO and YSZ, according to

$$\alpha_T = \frac{d_{400}(T+\Delta T) - d_{400}(T)}{\frac{1}{2}[d_{400}(T+\Delta T) + d_{400}(T)]\Delta T}, \tag{3.6}$$

where ΔT is the temperature difference between two consecutive points. Although the substrates show fairly different expansion coefficients (MgO: $\sim 1.2 \times 10^{-5}\,\mathrm{K}^{-1}$, YSZ: $\sim 8 \times 10^{-6}\,\mathrm{K}^{-1}$ [182, 183]), the linear thermal expansion coefficient for Zn_3N_2 was found to be similar on both substrates, as illustrated in Figure 3.10(c), close to the average value of $\alpha_T = 1.5 \times 10^{-5}\,\mathrm{K}^{-1}$. Hence, one can state that our films behave like in the second scenario, where the substrates have a low influence on the thermal expansion of the layers, being in agreement with their rather low structural quality (as discussed in Section 3.2.3).

Generally, the thermal expansion coefficient is not constant as a function of temperature, but shows an S-behavior, where it increases strongly at low temperatures (from 0 K to ~200 K) and saturates at higher temperatures, which is explained by a successive excitation of acoustical and optical lattice phonons [179, 184, 185]. Two materials where this behavior has been characterized are AlN and MgO, as illustrated in Figure A.6 of the Appendix. On the contrary, the linear thermal expansion coefficients increase only slightly as a function of temperature, as shown in Figure 3.10(c), indicating that they lie already in the saturation regime in the selected temperature range.

Our measurements are the first that address the linear thermal expansion coefficient of Zn_3N_2. While its knowledge is scientifically interesting from the fundamental point of view, as it affects other physical properties of a material (e.g. the temperature-dependent band gap energy), it may be important also in applied research, as it opens a way towards engineering the growth of Zn_3N_2-containing heterostructures.

3.4 Electrical properties of Zn_3N_2

When it comes to device applications of new materials, it is essential to know their electrical transport characteristics in order to evaluate which device design is most suitable. Therefore, the electrical properties of Zn_3N_2 are systematically investigated in this section. We address the effect of growth parameters, namely substrate temperature and Zn/N ratio, on the transport characteristics, and identify the scattering mechanisms limiting the electron mobility in Zn_3N_2 by employing low temperature Hall effect measurements.

3.4.1 Effect of growth conditions

All Zn_3N_2 layers grown in this PhD were found to be n-type conductive with low resistivities and high carrier concentrations, consistent with previous studies [71, 92, 96, 98, 100, 101, 103].

Figure 3.11(a) shows the results of Hall effect measurements at room temperature, on the Zn_3N_2 thin film series grown at different substrate temperatures (see Table 3.3). An electron concentration of $\sim 3 \times 10^{19}\,\mathrm{cm^{-3}}$ was found at 50 °C, which slightly increases until a value of $\sim 10^{20}\,\mathrm{cm^{-3}}$ as the growth temperature is increased, indicating degenerate Zn_3N_2. The electron mobility of the thin films stays more or less constant at a high value of $\sim 150\,\mathrm{cm^2V^{-1}s^{-1}}$, independent of the growth temperature and, interestingly, of their crystallinity [see Figure 3.4(a)]. This phenomenon may be linked to the band structure of Zn_3N_2. Since the conduction band is mainly composed of spherical Zn 4s and N 2s states (see Section 1.2.3), the electron mobility is expected to be relatively insensitive to the bond angle, enabling high mobilities also in amorphous Zn_3N_2 (as found in sample A, for instance). A counterexample is Si being composed of tetrahedral sp^3 states, where high mobilities of $\sim 1400\,\mathrm{cm^2V^{-1}s^{-1}}$ are observed in its crystalline phase, but only $\sim 1\,\mathrm{cm^2V^{-1}s^{-1}}$ in amorphous Si, where the bond angles deviate from the perfect tetrahedral angle of 109.5° [186, 187]. Overall, the increase of electron concentration while keeping a constant mobility leads to a slight reduction of film resistivity.

The effect of Zn flux on the electrical properties of Zn_3N_2 is illustrated in Figure 3.11(b). A strong increase of carrier concentration as a function of Zn flux is found, where the electron concentration increases from $2 \times 10^{19}\,\mathrm{cm^{-3}}$ to greater than $10^{21}\,\mathrm{cm^{-3}}$ at high Zn/N flux ratios, indicating a Zn-rich thin film stoichiometry in the high Zn flux regime and leading to an increased donor concentration. The change towards metal rich stoichiometries is accompanied by a morphological transition of the sample surface. For the smallest Zn fluxes, the thin films are smooth, with uniformly distributed grains of ~50 nm wide size [see AFM micrograph of sample vi in Figure 3.11(c)], displaying an RMS roughness of 1.2 nm. As the Zn flux increases, the grain distribution appears less homogeneous, accompanied by a slight reduction of grain size to ~30 nm, as shown in the AFM image of sample iii in Figure 3.11(d). Once the Zn flux is increased further, the surface consists of agglomerates with heights larger than 100 nm and lateral dimensions larger than 150 nm [see AFM micrograph of sample i in Figure 3.11(e)], which

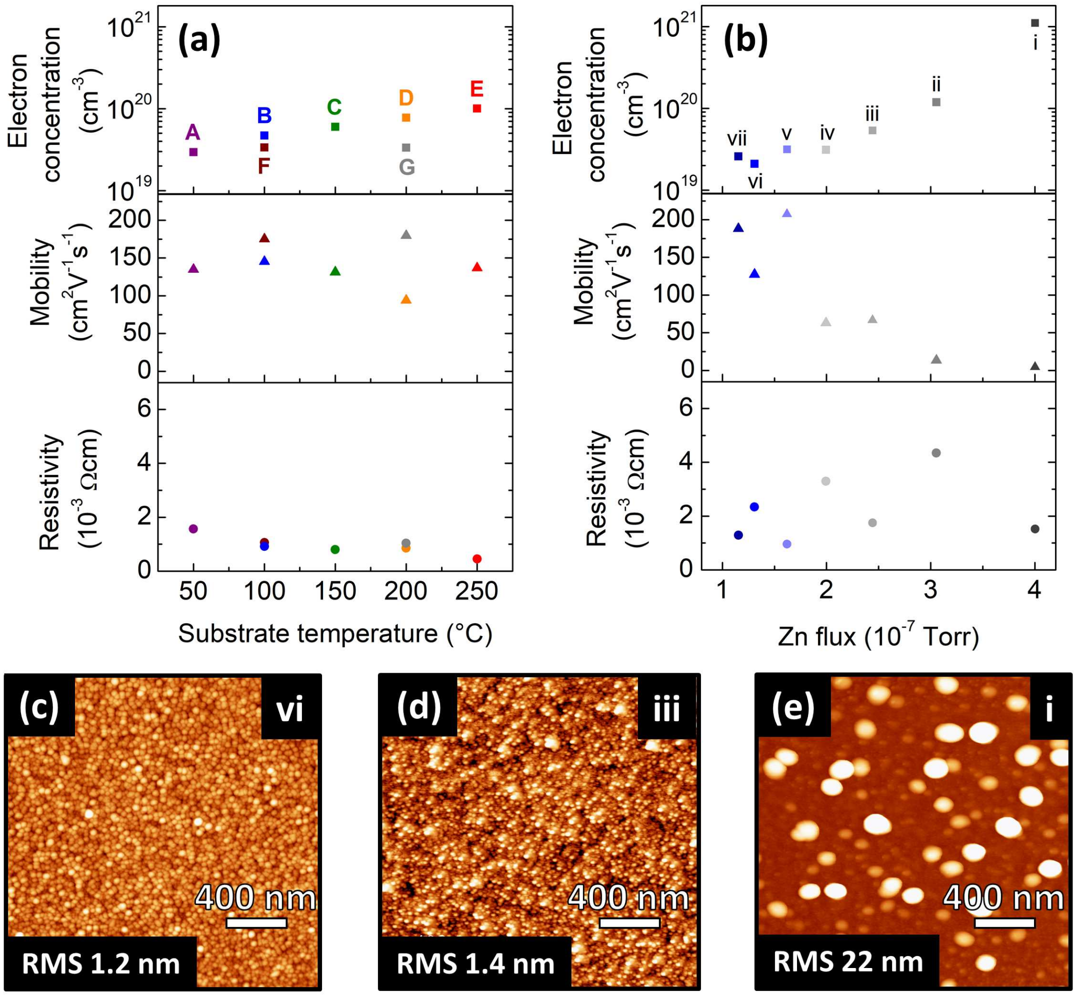

Figure 3.11: Electrical properties of Zn_3N_2 at room temperature, as a function of (a) Zn_3N_2 growth temperature and (b) Zn flux. The growth conditions for the samples in (a) and (b) are reported in the Tables 3.3 and 3.2, respectively. (c), (d) and (e) show $2 \times 2\,\mu m^2$ AFM micrographs of the samples vi, iii and i in (b), respectively.

can be interpreted as the formation of metallic Zn droplets on the surface, leading to an RMS roughness of 22 nm. Interestingly, the resistivity stays at a low level upon agglomeration, showing that the coverage is still sufficient to allow percolation conductivity. Besides agglomeration, the increase of electron concentration is accompanied by a decrease in their mobility from ~200 $cm^2V^{-1}s^{-1}$ to 3 $cm^2V^{-1}s^{-1}$, indicating that ionized impurity scattering plays a dominant role limiting the carrier mobility.

3.4.2 Scattering mechanisms in Zn_3N_2

Before investigating the scattering mechanisms occurring in Zn_3N_2 in more detail, we plotted the electron mobility of *all* Zn_3N_2 thin films grown in the context of this PhD, as a function of their electron concentration (see Figure 3.12), and compared them to previous Zn_3N_2 literature

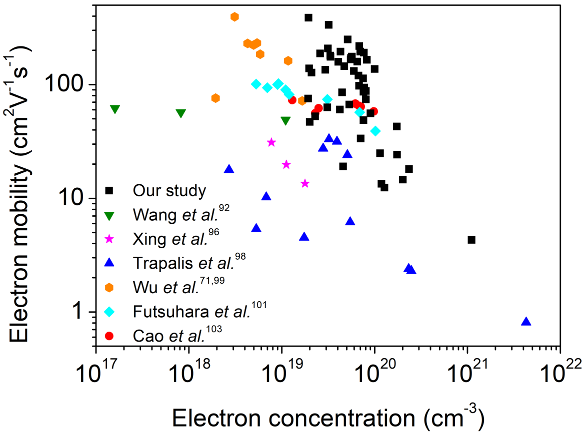

Figure 3.12: Electron mobility for all grown Zn_3N_2 thin films as a function of their concentration, compared to previous literature work.

work. Besides showing that we grew a thin film with an electron mobility of 388 $cm^2V^{-1}s^{-1}$, close to the highest reported value of 395 $cm^2V^{-1}s^{-1}$ at room temperature [99], a clear anti-correlation between the electron mobility and the electron concentration is found, underlining that ionized impurity scattering is the main mechanism limiting the mobility. Unfortunately, we were not able to grow Zn_3N_2 with carrier concentrations below 10^{19} cm^{-3}, probably due to high densities of N-vacancies and/or Zn-interstitials, as commonly observed in nitride semiconductors. Indeed, these point defects are also predicted to have low formation energies in Zn_3N_2 [72, 74, 75]. According to Figure 3.12, a decrease of the electron concentration below 10^{19} cm^{-3} can, eventually, lead to even higher electron mobilities. Therefore, we performed annealing experiments up to 450 °C under nitrogen atmosphere, in order to reduce the number of point defects and, hence, ionized impurity centers (results for one sample are shown in Figure A.7 of the Appendix). Yet, it was not possible to significantly reduce the electron concentration, which may indicate a residual amount of oxygen in the thin films, acting as a donor in Zn_3N_2 [72, 103]. For a given electron concentration, however, our thin film show the highest electron mobilities reported so far. For the low film thicknesses investigated here, scattering due to interface and surface roughness may become an increasing factor limiting the electron mobility, consistent with the AFM observations in Figure 3.11.

We measured temperature dependent Hall effect on selected Zn_3N_2 thin films (electron concentrations from 2×10^{19} cm^{-3} to 7×10^{19} cm^{-3}) in a temperature range from 30 K to 300 K, as presented in Figure 3.13. The carrier concentration is almost constant as a function of temperature, in agreement with our hypothesis of degeneracy [see Figure 3.13(a)]. Also, the electron mobility is only weakly dependent on the temperature. At temperatures below ~100 K, the mobility remains unchanged, as illustrated in Figure 3.13(b). Once the temperature is increased above ~100 K, a slight decrease of mobility is observed. By simulating this behavior with appropriate physical models, one can withdraw information about the scattering mechanisms limiting the electrical transport.

In a model applied for polycrystalline transparent conducting oxides (TCOs) [188], i.e. for degenerate semiconductors, the reciprocal mobility is given by

$$\frac{1}{\mu_H} = \frac{1}{\mu_i} + \frac{1}{\mu_l} + \frac{1}{\mu_g}, \tag{3.7}$$

where μ_i, μ_l and μ_g are the partial mobilities due to ionized impurity scattering, lattice phonon scattering and grain boundary scattering, respectively. Since our Zn_3N_2 thin films are degenerate, the Fermi level is found within the conduction band, leading to a constant temperature dependence of μ_i. On the other hand, lattice phonon excitation occurs only at high enough temperatures, leading to a $\mu_l \propto T^{-1}$ dependency. Grain boundary scattering is usually described by trap states that create potential barriers in the conduction band between the separate crystallites. Using Fermi-Dirac statistics, one obtains

$$\mu_g = cT^{-1}e^{-\frac{eV_a}{k_B T}}, \tag{3.8}$$

where V_a is the barrier energy and c a fitting constant. Inserting the dependencies of the partial mobilities in Equation 3.7 gives

$$\frac{1}{\mu_H} = \frac{1}{a} + \frac{T}{b} + \frac{T}{c\exp(-\frac{eV_a}{k_B T})}, \tag{3.9}$$

where a and b are fitting constants. Applying Equation 3.9 gives a good agreement to our experimental data, as indicated by the solid lines in Figure 3.13(b), demonstrating that the transport characteristics of our Zn_3N_2 are similar to that of TCOs. Interestingly, the barrier energy V_a is found to be in the order of a few µeV for all measured thin films, around one order of magnitude lower than $k_B T$ at room temperature, indicating that grain boundary scattering has only minor influence on the overall scattering characteristics. Indeed, omitting the term containing μ_g in Equation 3.9 leads to practically identical fits. This is rather surprising, given that the grain size in most of our Zn_3N_2 thin films is in the order of 50 nm (see AFM analysis in Figure 3.11). Nevertheless, the effect of grain boundaries in TCOs is commonly found to be negligible, as V_a is found to be smaller than $k_B T$ at room temperature by many researchers, if even measurable [188]. The knowledge of V_a can be used to deduce the barrier width of a grain boundary, which was calculated to be in the order of one mono-layer for TCOs with similar electron concentrations as present in our thin films. Hence, the grain boundaries can be easily traversed by electron tunneling. Moreover, the mean free path of electrons in degenerate TCOs is in the order of a few nm, due to the large number of ionized scattering centers, still well below the grain size observed here. Therefore, the effect of grain boundaries can be considered negligible when compared to other scattering mechanisms [188].

Our results are in agreement with a study of Cao *et al.*, who investigated the transport mechanisms in epitaxial and polycrystalline Zn_3N_2 thin films deposited by sputtering on YSZ (100) [103].

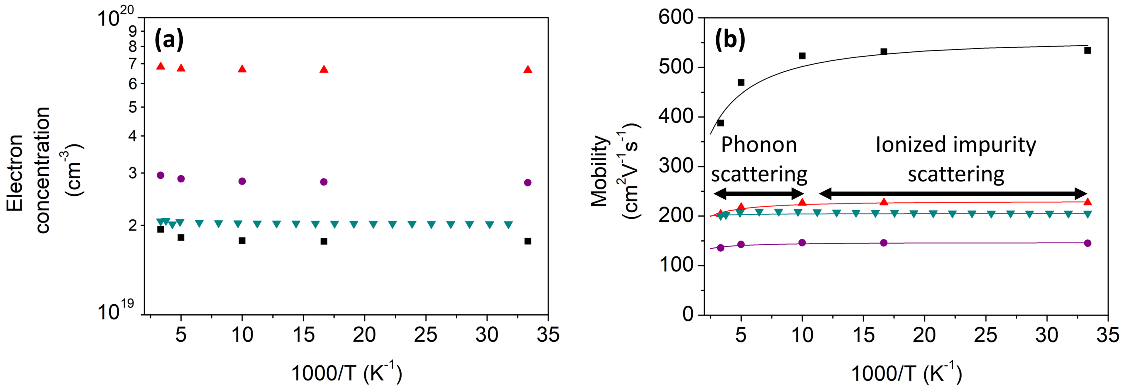

Figure 3.13: Temperature dependent Hall effect measurements of selected Zn_3N_2 thin films. (a) Electron concentration as a function of temperature. (b) Electron mobility as a function of temperature. The lines in (b) are the fits using Equation 3.9.

Similarly, they identified ionized impurity scattering as the main mechanism limiting the carrier mobility, independent of the crystallinity. Nevertheless, their optical mobilities are in the order of 110 $cm^2V^{-1}s^{-1}$, as found by Fourier transform IR spectroscopy, almost two times larger than their measured Hall mobilities of ~65 $cm^2V^{-1}s^{-1}$. They assign this discrepancy to grain boundary scattering in their polycrystalline thin films, although these exhibit grains sizes of around 100 nm, contradictory to our results. However, one should note that they did not employ temperature dependent Hall effect to verify their interpretations.

3.5 Optical properties of Zn_3N_2

The accurate knowledge of a new semiconductor's band gap is essential, especially for its application in optoelectronic devices. The determination of the optical properties of Zn_3N_2 is particularly critical due to its tendency to slowly oxidize in ambient air and the high carrier concentrations that are commonly achieved for this material, as discussed in Section 1.2.3.

We employed optical transmittance measurements from the UV to the NIR range on eight Zn_3N_2 thin films in order to reliably determine its band gap at room temperature. Figure 3.14 shows the normalized transmittance spectra of two Zn_3N_2 thin films with different electron concentrations in a wavelength range from 250 nm to 2000 nm, where the data was obtained by dividing the raw spectra by the one of the bare substrate. The thin film with a carrier concentration of 1.9×10^{19} cm^{-3} shows an absorption edge at around 1200 nm (1.0 eV). An increase of the carrier concentration by one order of magnitude leads to a significant blue shift of the absorption edge to 1030 nm (1.2 eV, see thin film with an electron concentration of 2.3×10^{20} cm^{-3}), associated with a Moss-Burstein shift. Lambert-Beer's law (see Equation 2.18) allows the extraction of the absorption coefficient α as a function of wavelength from the normalized transmittance spectra, which was found to be in the 10^5 cm^{-1} range close to the absorption edge. This large α is typical for direct band gap semiconductors, consistent with previous observations as

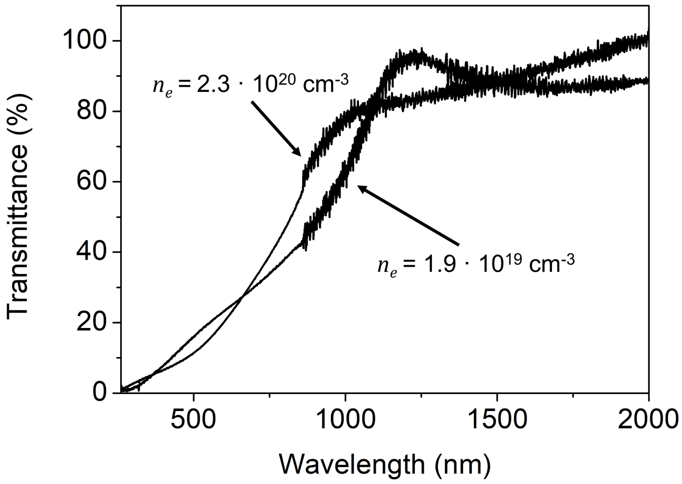

Figure 3.14: Normalized room temperature transmittance spectra of two Zn_3N_2 thin films with different electron concentrations. Note that the increase of noise at at around 850 nm is due to a change of detector.

well as theoretical calculations on Zn_3N_2 [72–77, 93, 98–101].

As explained previously, a plot of $(\alpha E)^2$ as a function of photon energy reveals a linear increase close to the band edge for a direct band gap semiconductor, where the optical band gap E_{opt} is found at the intersection with the x-axis (see Equation 2.19). This so-called Tauc plot is shown for all measured Zn_3N_2 thin films in Figure 3.15(a). The band gap energies of the measured samples lie between 1.04 eV and 1.37 eV, consistent with most of the previous literature [23, 90–101].

In order to account for this large range of band energies, one has to evaluate the effect of electron concentration on the band gap, as described by Burstein and Moss [57, 58]. As the electron concentration in a semiconductor is increased, its Fermi level is shifted upwards in energy, towards the conduction band. Once degeneracy is reached, the Fermi level lies within the conduction band, leading to an apparent blue shift of the optical band energy in absorption spectra, exactly as observed in Figure 3.15(a). Assuming a parabolic conduction band, the band gap shift ΔE as a function of carrier concentration can be described according to

$$E_{opt} = E_g + \Delta E n_e^{2/3}, \tag{3.10}$$

where E_g denotes the actual band gap energy. Plotting E_{opt} of all measured samples as a function of $n_e^{2/3}$, as presented in Figure 3.15(b), reveals a linear increase, where $E_g = 0.99$ eV and $\Delta E = 1.07 \times 10^{-14}$ eVcm^2 are extracted from the fit using Equation 3.10, which is indicated by the black line. Hence, the Fermi level is indeed shifted into the conduction band as the carrier concentration rises towards degeneracy. Although a non-parabolic conduction band was predicted for Zn_3N_2 by Kumagai *et al.* [78], Equation 3.10 agrees quite will with the experimental data. Suda *et al.* performed a similar study on MBE and MOCVD grown Zn_3N_2 thin films. Using

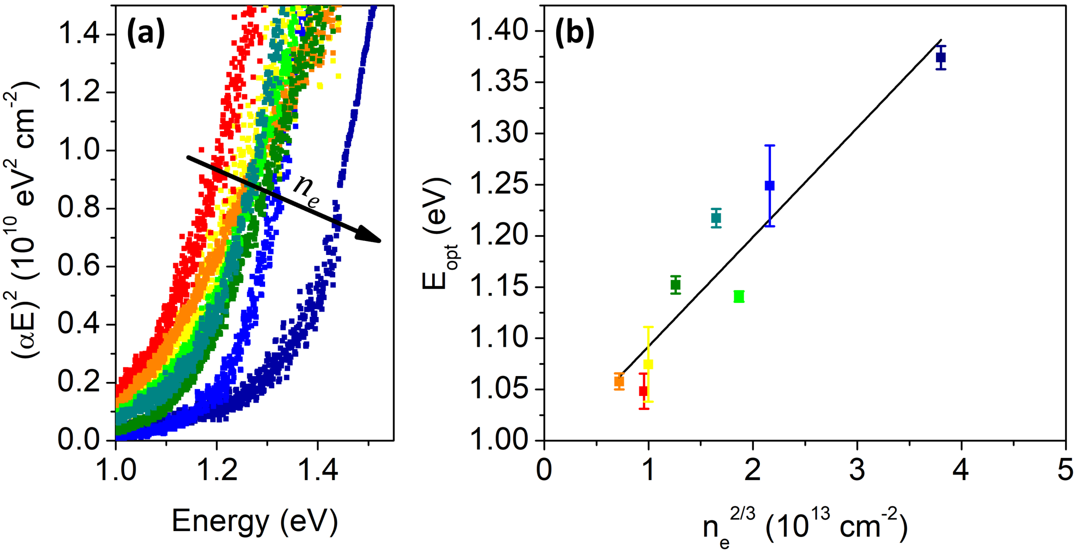

Figure 3.15: (a) Tauc plot for all measured Zn_3N_2 samples. A blue shift of the band gap is observed as the carrier concentration is increased. Note that the change of noise around 1.4 eV is due to a change of detector (b) Band gap of Zn_3N_2 thin films as a function of $n_e^{2/3}$, fitted with Equation 3.10.

the approximation of a parabolic conduction band, too, they extracted values of $E_g = 1.06$ eV and $\Delta E = 1.30 \times 10^{-14}$ eVcm^2 from their linear fit with Equation 3.10, agreeing well with out experiments [100]. Therefore, the fundamental Zn_3N_2 band gap can be declared to be ~1.0 eV.

Our measurements show that relatively large band gap shifts are indeed possible in Zn_3N_2, and are associated to Moss-Burstein shifts of the Fermi level. Nevertheless, this effect can not explain band gap energies of up to 3.4 eV, as reported in some literature studies. These can only be explained by other mechanisms, as the oxidation of Zn_3N_2 in ambient air to ZnO or $Zn(OH)_2$ [66, 87, 91, 98, 104], and it can be excluded to originate from Zn_3N_2 itself.

3.6 Summary

We demonstrated the epitaxial thin film growth of Zn_3N_2 by MBE. By achieving (111) and (100)-oriented Zn_3N_2 thin films on MgO (100), where the film orientation can be controlled by adapting the growth conditions, as well as (100)-oriented Zn_3N_2 on YSZ (100), we provide a comprehensive insight into Zn_3N_2 epitaxy, as never reported in literature, being an important step for further growth optimization in future research. The structural properties of these films were investigated in detail using XRD and RHEED. A Zn_3N_2 (111) inter-layer nucleates on the substrate when the growth is done on MgO, where its thickness can be controlled from a few mono-layers to ~40 nm. Zn_3N_2 (111) exhibits four epitaxial rotational in-plane domains, due to the different substrate and epi-layer symmetries, as expected in this epitaxial configuration. The thin

Zn_3N_2 (111) inter-layer is overgrown by (100)-oriented Zn_3N_2, probably due to the higher thermodynamic stability of (100) surfaces in cubic crystals, thereby reducing the crystalline quality of the subsequent Zn_3N_2 (100). When growing on YSZ, (100)-oriented Zn_3N_2 nucleates directly on the substrate with high crystalline quality, where the crystallographic orientation of the cubic (100) substrate is transferred to the growing film. However, as the growth proceeds, the structural quality of the growing film degrades. In future work, strategies to maintain a high-quality Zn_3N_2 over the entire film thickness need to be developed. These may consist of, for instance, temperature gradients after Zn_3N_2 nucleation, the change of substrate material or its orientation, so to reduce the initial lattice mismatch. Eventually, one can develop devices where only low film thicknesses (< 50 nm) are required.

An important step towards Zn_3N_2 growth optimization has been made by the measurement of its linear thermal expansion coefficient from room temperature to 400 °C, allowing to evaluate its lattice mismatch to a possible substrate material at any temperature where Zn_3N_2 epitaxy has been performed so far. While the knowledge of an average $\alpha_T = 1.5 \times 10^{-5}\,\mathrm{K}^{-1}$ can be practically used in epitaxy, it is also interesting from a fundamental point of view, since the thermal expansion coefficient influences some of a material's physical properties whenever temperature changes come into play.

In order to evaluate the application of our Zn_3N_2 thin films in devices, we systematically measured their electrical properties by employing Hall effect measurements. Although large electron mobilities of up to 388 $\mathrm{cm}^2\mathrm{V}^{-1}\mathrm{s}^{-1}$ are found in the n-type thin films, their carrier concentration is at a high level, from $10^{19}\,\mathrm{cm}^{-3}$ to $10^{21}\,\mathrm{cm}^{-3}$, similar to that of TCOs, indicating degenerate Zn_3N_2. Consistently, the mobility is mainly limited due to scattering by ionized impurities, which probably consist of N-vacancies or residual O-impurities. Hence, further growth optimization to decrease those is necessary if Zn_3N_2-based devices are considered, especially as channel material in TFTs. More N-rich conditions in combination with higher growth rates may favor the saturation of N-vacancies and dilution of residual oxygen in the thin films. Otherwise, the introduction of additional impurities, or even Zn_3N_2-containing ternary alloys, may help to decrease the carrier concentration further. Cu doping, for instance, was investigated by DFT calculations to possibly enable p-type Zn_3N_2 [75]. Although very recently one study on Cu addition in a range of 2.7 % to 5.7 % by sputtering presumably led to p-type Zn_3N_2 thin films, one may express some skepticism about their results, since the authors find a high band energy of 3.2 eV for their pure Zn_3N_2 thin films, that decreases to ~1.7 eV upon Cu addition, and do not give any explanation to account for these discrepancies [189].

Reliably determining a materials' band gap is crucial, especially when new semiconductors that decompose in air, such as Zn_3N_2, are measured. We investigated the band gap of Zn_3N_2 thin films with different carrier concentrations, and show that the actual Zn_3N_2 band energy lays around 1 eV, consistent with most of the previous literature, and is shifted to higher energies (here around 1.4 eV) at high carrier concentrations due to the Moss-Burstein effect.

Chapter 4

MBE growth and characterization of Mg_3N_2 thin films

In this Chapter the development of an MBE process for Mg_3N_2 epitaxy is discussed. An MgO capping layer is grown in the MBE chamber *in-situ* in order to prevent the irreversible decomposition of Mg_3N_2 in air. We present the effect of the substrate and the growth conditions on the film orientation and quality, and identify the epitaxial relationships of the grown thin films on different substrates [MgO (100), MgO (111) and YSZ (100)]. Furthermore, the crystalline properties of Mg_3N_2 (111) thin films on MgO (100) are thoroughly investigated by XRD and TEM, in order to assess the micro-structural evolution during growth. Finally, the fundamental physical properties of Mg_3N_2, such as linear thermal expansion coefficient and temperature-dependent band gap are addressed. This chapter covers:

- Development of an MgO capping: From homoepitaxy to heteroepitaxy
- Epitaxy of Mg_3N_2: Growth orientation tuning on MgO (100)
- Epitaxial relationships on different substrates: A RHEED/XRD study
- Micro-structural evolution of Mg_3N_2 (111) on MgO (100) by XRD and TEM
- Linear thermal expansion coefficients of Mg_3N_2
- Optical properties of Mg_3N_2

4.1 State of the art: Reminder

As discussed in Section 1.2.4, Mg_3N_2 epitaxy was never reported before the beginning of this PhD. Although the authors of the first attempt of Mg_3N_2 (100) growth (by MBE) claim the achievement of epitaxy, diffraction was barely measurable, even for thicknesses as large as 800 nm [82]. Consequently, the epitaxial relationships to the underlying MgO (100) substrates, as well as the structural properties, remained unknown. Furthermore, the linear expansion coefficient of Mg_3N_2 above 300 K was not reported before the beginning of this PhD. Such structural information are, however, necessary if one wants to develop strategies to improve the film quality, understand the physical properties of new materials and, eventually, apply them into devices. The low structural quality of Mg_3N_2 may be, besides its tendency to quickly decompose to $Mg(OH)_2$ in contact with humidity, one reason for the controversial determination of its band gap, which is reported to lay between 2.5 eV and 3.15 eV at room temperature.

4.2 Development of a capping layer

Bulk Mg_3N_2 is highly reactive in humid conditions, as quantified in Section 1.2.2, and irreversibly decomposes to $Mg(OH)_2$ upon air exposure within several hours. Due to their larger surface-to-volume ratio, the decomposition time scales for Mg_3N_2 thin films are even shorter, leading to a complete decomposition within a few minutes in air. Hence, the deposition of a protective layer directly after Mg_3N_2 growth (i.e. *in-situ* in the MBE chamber) is absolutely indispensable if one wants to analyze and use this II-nitride material *ex-situ*. Since the goal of this protective layer is to ensure an adequate diffusion barrier for H_2O and O_2 molecules, the layer's compactness and smoothness are the crucial parameters to be optimized.

Due to its high chemical stability and the strength of the ionic Mg-O bond (10.3 eV [190]), MgO seems a suitable candidate for an appropriate capping. Although the introduction of oxygen into the MBE chamber seems counterproductive, since it may react with the underlying Mg_3N_2 thin film, we will demonstrate a strategy that avoids Mg_3N_2 oxidation.

4.2.1 MgO homoepitaxy

Due to the wide application of MgO as refractory material, one may expect MgO homoepitaxy to be well-studied in literature. Surprisingly, there are only a few reports on MgO homoepitaxy by MBE, grown either by using separate molecular Mg and O beams, or by e-beam evaporated MgO [191, 192]. Unfortunately, in none of these studies the influence of the growth parameters on the surface morphology was deeply investigated.

We analyzed the surface morphology of MBE-grown homoepitaxial MgO (100) thin films using AFM, as shown in Figure 4.1, where the RMS roughness of the thin films is shown as a function of the growth conditions. The Mg cell temperature was kept at 410 °C throughout the

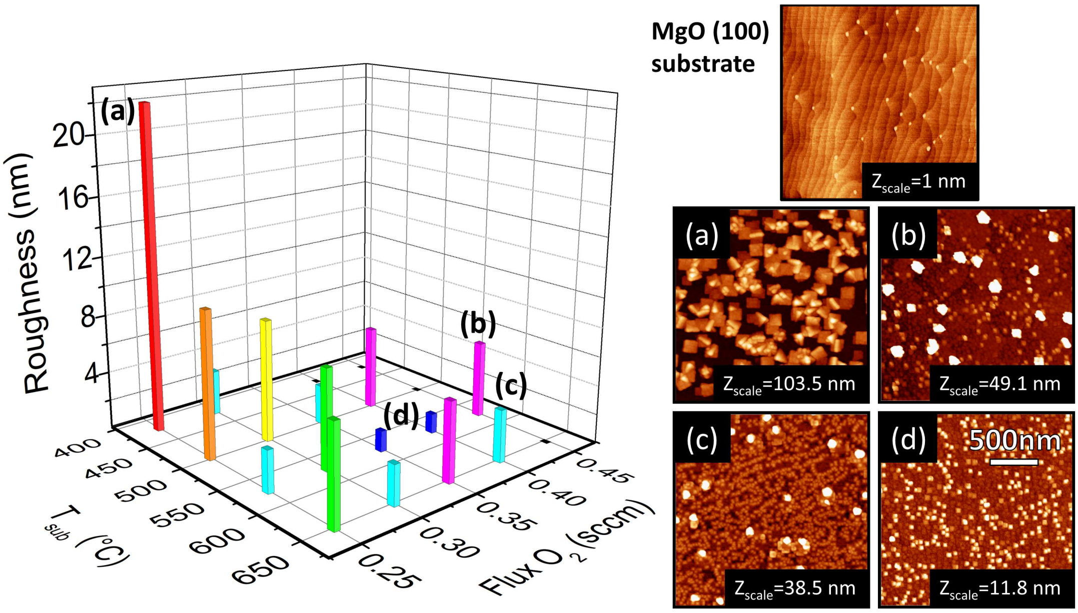

Figure 4.1: RMS roughness as a function of growth parameters for homoepitaxial MgO, extracted from $2 \times 2\,\mu m^2$ AFM images. The letters (a)-(d) correspond to the AFM micrographs given on the right-hand side, where the Z_{scale} denotes the maximum height. The Mg cell temperature was kept at 410 °C. One micrograph of an MgO substrate surface prior to growth is shown for comparison.

entire growth series, while the substrate temperature and the oxygen flow were varied from 400 °C to 650 °C and from 0.25 sccm to 0.45 sccm, respectively. An AFM micrograph of an MgO substrate surface prior to growth is shown in the upper right corner for comparison.

At the lowest temperature and oxygen flow of 420 °C and 0.25 sccm, respectively [see Figure 4.1(a)], a segregation of cubic ~100 nm large crystallites is observed. Such a rough morphology (RMS>20 nm), with an incomplete wetting, is obviously not suitable for an application as a protective capping layer. On the other hand, high oxygen flows in combination with moderate substrate temperatures (570 °C and 0.45 sccm, respectively), slows down the MgO growth, leading to small and randomly distributed, isolated agglomerates on the surface [see Figure 4.1(b)]. Also with these growth conditions, a complete wetting of the surface is not insured. At the highest growth temperature of 650 °C and moderate oxygen flow of 0.40 sccm [Figure 4.1(c)], small MgO grains nucleate along the atomic terraces of the annealed substrate, accompanied by the nucleation of some larger agglomerates. Finally, at intermediate temperatures and oxygen flows of 580 °C and 0.35 sccm, respectively, 40 nm-sized homogeneously distributed cubic grains are observed, leading to a complete wetting of the surface and a low RMS roughness of 1.4 nm. The growth rate using these optimized conditions was found to be 63 nm h^{-1}, determined by XRR on a CdO/MgO heterostructure (see Figure A.8 in the Appendix). If not indicated differently, an MgO capping with these growth parameters is deposited on top of every Mg_3N_2 thin film discussed hereafter, with a nominal thickness of 50 nm.

4.2.2 Polycrystalline MgO on Mg_3N_2

Although MgO homoepitaxy leads to smooth and apparently dense thin films, possibly suitable as a capping layer, the deposition on the material to be protected, Mg_3N_2, needs to be tested and evaluated. However, the introduction of oxygen into the chamber necessary for MgO growth may be counterproductive, as it can possibly react with the underlying Mg_3N_2 thin film. To prevent oxidation, we protect the freshly grown thin film by closing the N shutter after Mg_3N_2 growth, but leaving the Mg shutter open for further 30 s before introducing oxygen, leading to a very thin layer of metallic Mg, which is monitored in the *in-situ* reflectance curve. As illustrated in Figure 4.2(a), thickness interference oscillations occur when recording the intensity of a 650 nm laser reflected from the sample surface during Mg_3N_2 growth. These oscillations can be used to control the thickness of the growing film in real time. Additionally, a sharp rise of intensity is observed at around 145 min, indicating an increase of reflectivity due to the presence of metallic Mg. Interestingly, the intensity drops to the previous level right after the introduction of oxygen, which seems to oxidize the metallic Mg (as will be shown below). The introduction of an intermediate Mg layer was systematically used when capping Mg_3N_2 thin films by MgO.

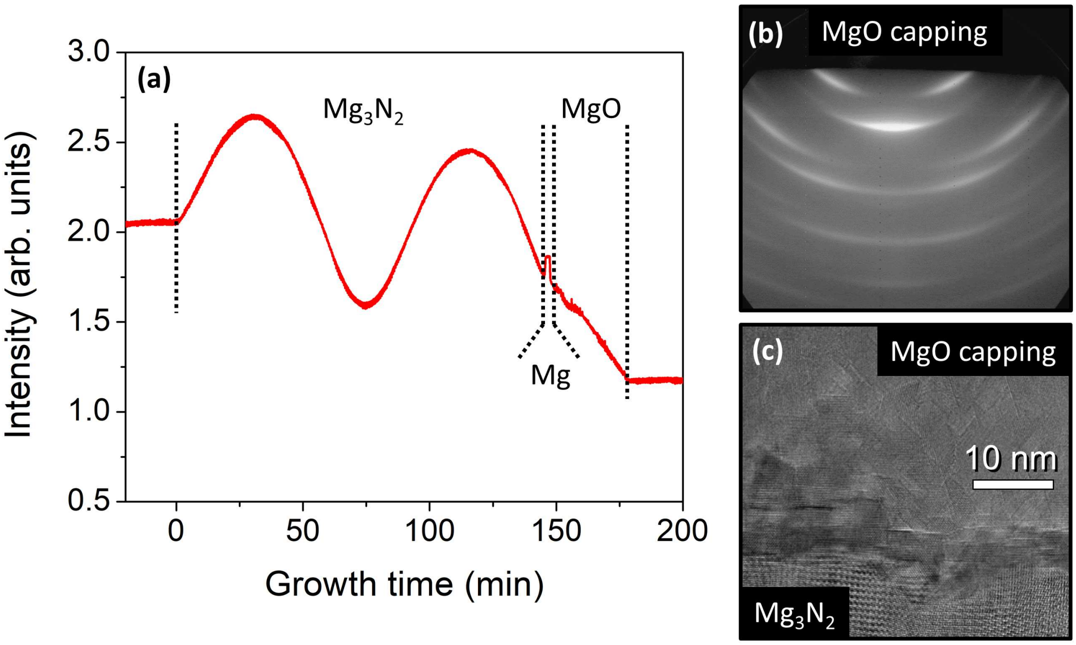

Figure 4.2: (a) *In-situ* reflectance using a 650 nm laser during MBE growth. (b) RHEED pattern of an MgO capping layer grown on Mg_3N_2. (c) HRTEM micrograph of the interface between an Mg_3N_2 (111) thin film and the MgO capping layer, along the MgO [011] substrate zone axis.

Although the MBE growth of homoepitaxial MgO at 580 °C, 0.35 sccm O_2 on MgO (100) substrates gives the best results, the same growth conditions lead, unfortunately, to poorly oriented MgO when grown on Mg_3N_2 thin films. Figure 4.2(b) shows a RHEED pattern of a growing MgO capping layer on Mg_3N_2 (111). Diffraction occurs along circular arcs, indicating a poor in-plane orientation of the growing MgO thin film. Interestingly, there are no additional MgO signals observed in the XRD patterns of Mg_3N_2 capped with MgO (see e.g. Figure 4.4), indicating that the MgO capping layer is out-of-plane oriented along the [100] direction. We performed TEM investigations at the interface between the MgO capping layer and the underlying Mg_3N_2 thin film, as shown in Figure 4.2(c). Although the HRTEM micrograph reveals a relatively rough interface, there is no inter-diffusion visible between the two materials, demonstrating that the strategy of depositing sacrificial Mg is effective to prevent Mg_3N_2 oxidation. The MgO capping layer itself appears dense, with crystallites of about 5 nm to 10 nm in diameter, and the nucleating MgO grains at the interface to the Mg_3N_2 are seen to have the same orientation as the MgO (100) substrate. This means that the metallic Mg intermediate film has been totally transformed into MgO. Once the thickness increases, the in-plane orientation is lost, leading to a polycrystalline microstructure. Using this kind of capping we were able to increase the Mg_3N_2 stability in air from a few minutes to several weeks. Still, after one month in air, a full decomposition of the Mg_3N_2 takes place. This process may be further prevented, or slowed down, by growing thicker capping layers, or employing cappings of better structural quality. Still, all the results during this PhD were obtained thanks to the use of this polycrystalline cap.

4.3 Epitaxial growth of Mg_3N_2 by MBE

In this section we discuss the development of epitaxial MBE-grown Mg_3N_2 thin films, which had never been done in CRHEA before nor anywhere else. Using MgO (100) substrates, we demonstrate the possibility to tune the Mg_3N_2 film orientation from (100) to (111) by varying the growth parameters. We identify the epitaxial relationships of Mg_3N_2 (111) to its underlying MgO (100) substrate using RHEED and XRD. Furthermore, we investigate Mg_3N_2 (111) growth on MgO (111) and YSZ (100), where we address the epitaxial relationships as well and compare the structural qualities achieved.

4.3.1 First attempts towards Mg_3N_2

In the only previous study on Mg_3N_2 MBE growth, published in 2018, the thin films are grown in a temperature range of 300 °C to 350 °C [82], which was used as a starting point for the development of our MBE process. Note that all films presented here are protected with polycrystalline ~50 nm MgO grown in the conditions described in Section 4.2.1, in order to slow down the otherwise rapid Mg_3N_2 decomposition in contact with air. Besides, between the different measurements the Mg_3N_2 thin films were stored in a vacuum desiccator, where there are stable up to several years.

Although we were able to obtain thin films in the same temperature range as Wu *et al.* [82], the thin films were amorphous, as illustrated in Figure 4.3(a). However, their yellow appearance

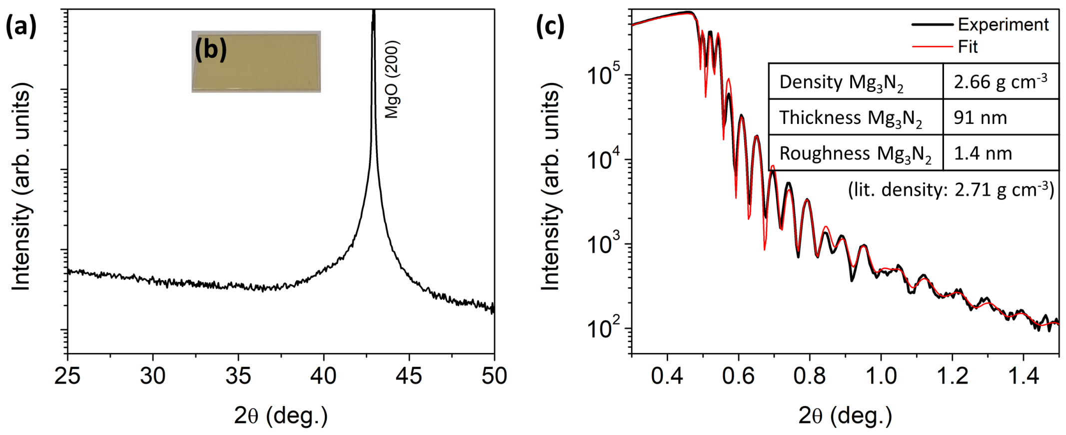

Figure 4.3: (a) $2\theta/\omega$ scan of an amorphous Mg_3N_2 thin film on MgO (100). (b) Photograph of the sample in (a). (c) XRR curve of the sample in (a).

[see Figure 4.3(b)], being a typical sign for Mg_3N_2 [82], and the XRR density of 2.66 g cm^{-3}, close to the Mg_3N_2 tabulated value of 2.71 g cm^{-3} [see Figure 4.3(c)], support that the grown material is indeed Mg_3N_2. In order to promote crystallization, we grew Mg_3N_2 at higher temperatures of up to 500 °C. Nevertheless, the obtained thin films were still amorphous or nano-crystalline (with a very low diffraction intensity). Even a large variation of the Mg/N ratio (Mg cell temperature varied from 410 °C to 430 °C and nitrogen flow from 0.35 sccm to 1.0 sccm) did not lead to crystallization, pointing towards another problem occurring during Mg_3N_2 growth. For this project, a new sample holder being capable to carry three $10 \times 20\,mm^2$ substrates simultaneously was bought. Although this configuration enables a higher throughput or the growth on different substrates at the same time, it has not been tested before on a known MBE process in CRHEA. A change of substrate holder to a commonly used one for ZnO epitaxy led, interestingly, to crystallization of the Mg_3N_2 thin films, enabling us to develop a growth process using this elder substrate holder, as discussed in the following section. We assign the occurrence of amorphous Mg_3N_2 using the new sample holder to a poor heat transfer between the molybdenum back plate and the underlying substrates.

4.3.2 From polycrystalline to epitaxial Mg_3N_2: Tuning of film orientation

Effect of Mg/N ratio:

Using a standard mono-wafer substrate holder, we studied the effect of growth conditions (substrate temperature and Mg/N ratio) on the Mg_3N_2 film growth. Figure 4.4(a) shows the $2\theta/\omega$ scans of the sample series reported in Table 4.1. At 400 °C and for the lowest Mg/N ratio (sample A) the grains are oriented along the [100] direction, as shown by the presence of a diffraction peak at ~36°, consistent with the attempt by Wu *et al.* to grow epitaxial Mg_3N_2 [82]. Nevertheless, a second, broad peak close to that of the MgO (200) substrate reflection is observed,

Table 4.1: Growth conditions of Mg_3N_2 thin films on MgO (100), capped with ~50 nm MgO.

Sample	Growth temp. (°C)	Mg cell temp. (°C)	Nitrogen flow (sccm)	Thickness (nm)	Growth rate (nm min^{-1})
A	400	410	1.0	~168	~1.6
B	400	410	0.5	~110	~1.5
C	400	410	0.35	73	1.6
D	400	420	0.35	92	2.0
E	400	430	0.35	98	2.2
F	460	430	0.35	97	2.1
G	400	440	0.35	94	2.1

which cannot be assigned to diffraction of any Mg_3N_2 plane, neither to MgO. This signal may eventually originate from a magnesium oxynitride compound, which was observed during the annealing of Mg metal in mixtures of O_2 and N_2 at 550 °C, showing a diffraction peak in the vicinity of 40° [193]. The RHEED of this sample is streaky at the initial growth stage until the first ~20 nm, as illustrated in Figure 4.4(d). However, as the growth proceeds, the pattern converts into a spotty one, the spots elongating along circular arcs as the thickness increases, indicating a decrease of in-plane structural quality. The in-plane Mg_3N_2 (020) inter-planar distance was extracted to be 4.65 ± 0.24 Å from the RHEED pattern in Figure 4.4(d), indicating a strong in-plane compressive strain (the fully relaxed inter-planar Mg_3N_2 (020) distance is 4.976 Å), which is indeed expected with a lattice mismatch of +18 %.

With a decrease of N_2 flow, the additional peak around 40° disappears, accompanied by a decrease in crystallinity of the Mg_3N_2 films (see sample B), although the (100) orientation is still conserved. A further decrease of N_2 flow leads to the appearance of Mg_3N_2 (111) grains, concomitantly present with the Mg_3N_2 (100) ones, which become dominant as the Mg/N ratio is increased further (this time by an increase of Mg cell temperature), as observed for the samples C and D.

Interestingly, a further increase of Mg/N ratio (see sample E) leads to a crystallization uniquely along the [111] direction, giving rise to single-orientated Mg_3N_2. The associated RHEED pattern shown in Figure 4.4(e) is spotty and can be simulated with diffraction of three different crystallographic planes, as denoted by the colored dots. The epitaxial relations giving rise to such a diffraction pattern are discussed in Figure 4.7 of the following section. We can hence tune the film orientation of Mg_3N_2 from (100) to (111) by adjusting the growth conditions.

Interestingly, an increase of temperature using the growth conditions of sample E leads to the same RHEED pattern, but streaky, as shown in Figure 4.4(f), indicating a smooth Mg_3N_2 (111) surface, consistent with an RMS roughness found by XRR of 1 nm (sample F), whereas the Mg_3N_2 thin film of sample E exhibits an XRR roughness of 2.2 nm. The streaky pattern found for sample F is very similar to that found for the iso-structural Zn_3N_2 (111) grown on MgO (100) [see Figure 3.4(b)], indicating that both thin films grow with the same epitaxial relationships.

The growth rates as a function of the Mg cell temperatures for selected samples are shown in Figure 4.4(b). Contrary to Zn_3N_2, where we found a linear dependence of the growth rate as a function of Zn flux, a typical shape is obtained here for Mg_3N_2. From 410 °C to 420 °C, an increase of growth rate is observed as a function of Mg cell temperature, indicating that the growth rate is limited by the amount of Mg that arrives at the surface (i.e. the growth is N-rich). Above 420 °C, a saturation takes place, showing that the additional Mg is no longer incorporated into the film (i.e. the growth is Mg rich).

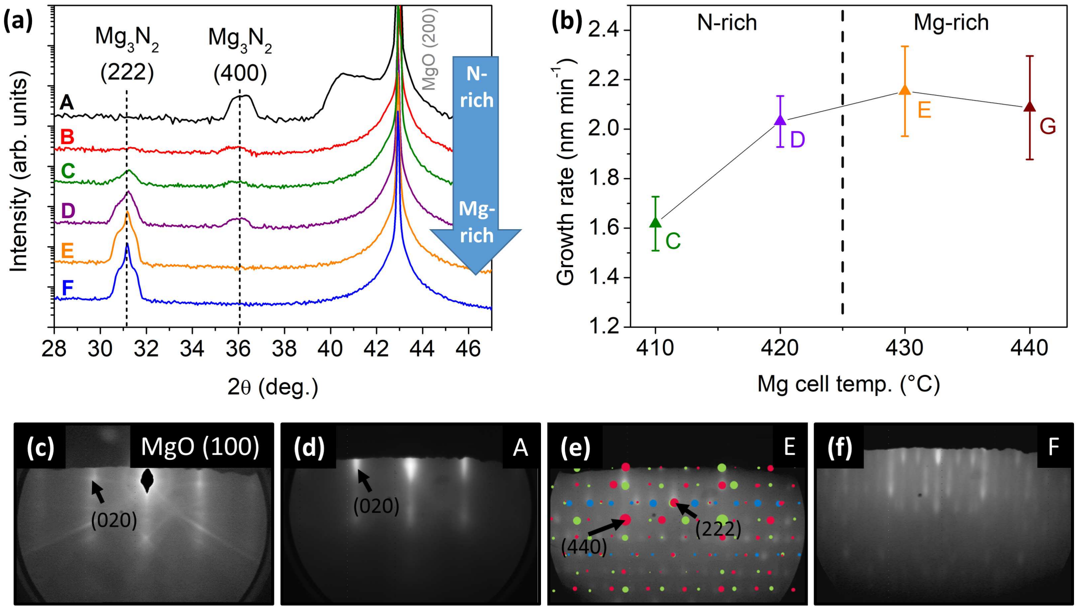

Figure 4.4: (a) $2\theta/\omega$ scans of Mg_3N_2 thin films grown at different growth conditions, which are reported in Table 4.1. (b) Growth rates as a function of Mg cell temperature for some selected samples. (c) and (d) show the RHEED patterns of the MgO (100) substrate and of sample A along the MgO [010] axis, respectively. (e) and (f) show the RHEED patterns of sample E and sample F, along the MgO [011] substrate axis, respectively. The colored dots in (e) correspond to diffraction patterns coming from three different families of planes (see Figure A.11 of the Appendix).

Effect of the substrate:

We further investigated growth on two other substrates, YSZ (100) and MgO (111), in order to evaluate Mg_3N_2 epitaxy in different configurations. The growth conditions of the best samples are reported in Table 4.2. In the XRD of sample H [Mg_3N_2 on YSZ (100), see Figure 4.5(a)], only one signal at 31° originating from Mg_3N_2 is observed, which can be assigned to diffraction of (222) planes, indicating single-oriented films. Besides the YSZ (200) substrate peak, a small contribution at ~42.5° is found, which can be assigned to MgO (200) originating from the capping layer. The RHEED of this sample, shown in Figure 4.5(c) and taken along the YSZ [010] direction, resembles that of Mg_3N_2 (111) grown on MgO (100) [see Figure 4.4(f)], indicating that the two films grow with the same in-plane and out-of plane orientations, although the pattern here is taken at an azimuthal angle rotated by 45° with respect to Mg_3N_2 (111) grown

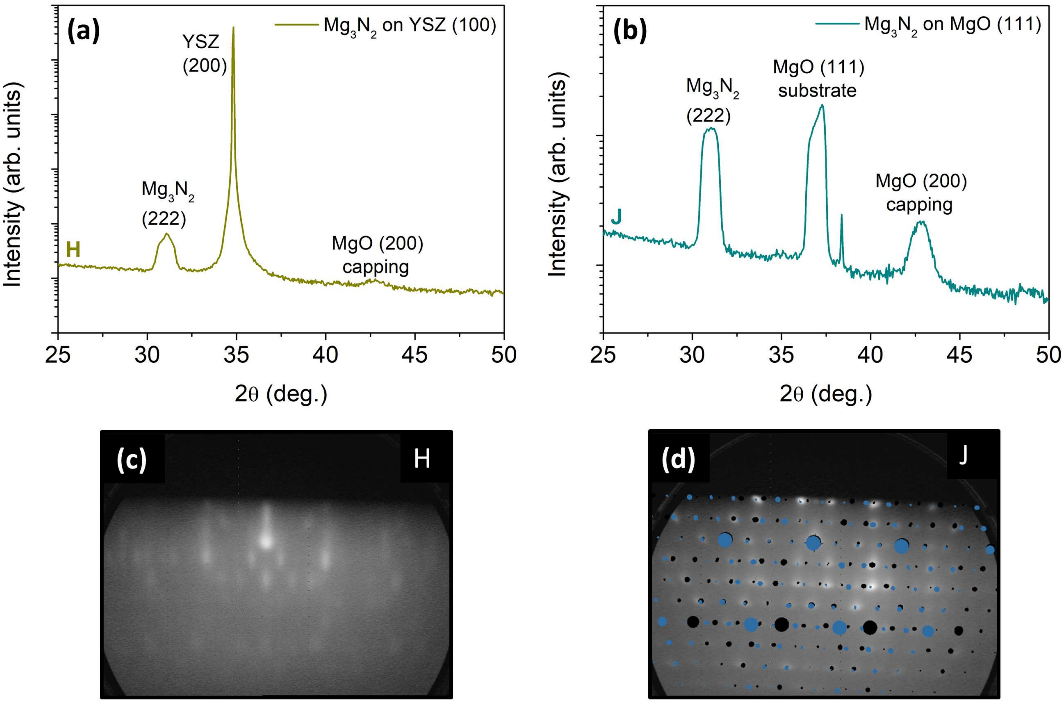

Figure 4.5: $2\theta/\omega$ scans of (a) sample H [Mg_3N_2 (111) on YSZ (100)] and (b) sample J [Mg_3N_2 (111) on MgO (111)]. (c) RHEED pattern of sample H, taken along the YSZ [010] direction. (d) RHEED pattern of sample J, taken along the MgO [$1\bar{1}0$] direction.

on MgO (100), which will be discussed in more detail in the following section. However, as the film thickness increases, the pattern turns spotty and the spots elongate along circular arcs, indicating a decrease of structural quality as the growth proceeds.

The XRD of Mg_3N_2 on MgO (111) (sample J) is shown in Figure 4.5(b). Also in this XRD pattern, diffraction from Mg_3N_2 (222) planes, the MgO (200) capping layer, as well as the substrate [MgO (111)] is observed, indicating single-oriented Mg_3N_2 films along the [111] direction. However, the intensity of the substrate reflection is significantly lower when compared to the previous case (sample H), due to a poor adjustment in ω on the substrate reflection, as also confirmed by the presence of a source/analyzer streak at around 38°. Readjusting the ω offset reveals a high MgO (111) intensity, as expected for a substrate reflection (curve not shown), but at the expense of Mg_3N_2 (222) intensity, showing that the Mg_3N_2 lattice is inclined with respect to the MgO substrate one. This inclination is even visible in the RHEED pattern of this sample, shown in Figure 4.5(d). Besides showing that we can correctly simulate the diffraction pattern by using two families of Mg_3N_2 planes (see Figure A.12 of the Appendix), a ~2° inclination of the diffraction pattern with respect to the growth axis is observed, indicating that the symmetric Mg_3N_2 planes are indeed not parallel to the sample surface.

In order to investigate the maximum inclination angle of the atomic Mg_3N_2 planes with respect to the MgO (111) substrate ones, we measured the ω offset of the symmetric Mg_3N_2 (222)

Table 4.2: Optimized growth conditions of Mg_3N_2 thin films on YSZ (100) and MgO (111), capped with ~50 nm MgO.

Sample	Substrate	Growth temp. (°C)	Mg cell temp. (°C)	Nitrogen flow (sccm)	Thickness (nm)	Growth rate (nm min^{-1})
H	YSZ (100)	475	410	1.0	~105	~0.92
J	MgO (111)	600	410	1.0	63	0.53

reflection as a function of azimuthal angle Φ, as shown in Figure 4.6(a). A sinus function is observed for a 360° rotation around Φ. At $\Phi = 0°$ [i.e. parallel to the MgO [$1\bar{1}0$] direction, see Figure 4.6(b)], the ω offset is 2°, in agreement with the RHEED observations in Figure 4.5(d), taken in the same direction. The maximum inclination angle with respect to the substrate is 3°, occurring at $\Phi = 60°$ (and $\Phi = -120°$) parallel to the MgO [$\bar{1}01$], as indicated in Figure 4.6(c). Hence, the rotational axis around which the inclination is observed lies in the perpendicular [$1\bar{2}1$] direction. This is rather surprising, given that the three $\langle 11\bar{2}\rangle$-type directions along the diagonals of the MgO (111) planes are crystallographically equivalent. Due to their triangular symmetry, an inclination around only one of these axis should be, in principle, energetically unfavorable.

Although usually little attention is paid to this effect, tilted heteroepitaxy is quite commonly observed. Nagai showed in 1974 that the inclination angle of heteroepitaxial $Ga_xIn_{1-x}As$ on GaAs (100) and (110) substrates increases as a function of the substrate's miscut angle, due to the change of the atomic step length in combination with the lattice mismatch [194]. In our case, however, no miscut angle was introduced, and the MgO (111) substrates do not show atomic steps, as shown in Figure A.9 of the Appendix. Another possible mechanism to explain tilted heteroepitaxy are arrays of misfit dislocations, preferentially oriented along certain crystallographic directions, as e.g. observed in the heteroepitaxial growth of semipolar III-nitrides. Interfacial misfit dislocations with inclined burgers vectors were, for instance, observed in $In_xGa_{1-x}N$ and $Al_xGa_{1-x}N$ layers on GaN ($11\bar{2}2$) substrates [195–198]. Since in hexagonal wurtzite materials, the (0001) *c*-plane is the most favorable glide system, interfacial misfit dislocation lines tend to be created in this plane, leading to a film relaxation by lattice tilt due to the introduction of inclined extra half-planes. Nevertheless, this mechanism fails for the cubic Mg_3N_2 (111), because the crystallographic directions lying in the MgO (111) plane are symmetric, excluding the occurrence of a preferred inclination around one of these axis, as mentioned before. Although the exact mechanisms explaining inclined Mg_3N_2 (111) growth on MgO (111) remain unclear, the large lattice mismatch of ~18 % present in our thin films and some slight unintentional substrate miscut may eventually play a role to explain the ω offset between the atomic Mg_3N_2 and MgO planes.

In summary, we established Mg_3N_2 epitaxy by MBE in CRHEA and slowed down sufficiently the irreversible decomposition to $Mg(OH)_2$ in air by depositing an MgO cap *in-situ*, enabling to carry out deeper analyses. Although Mg_3N_2 can be grown in two orientations by varying

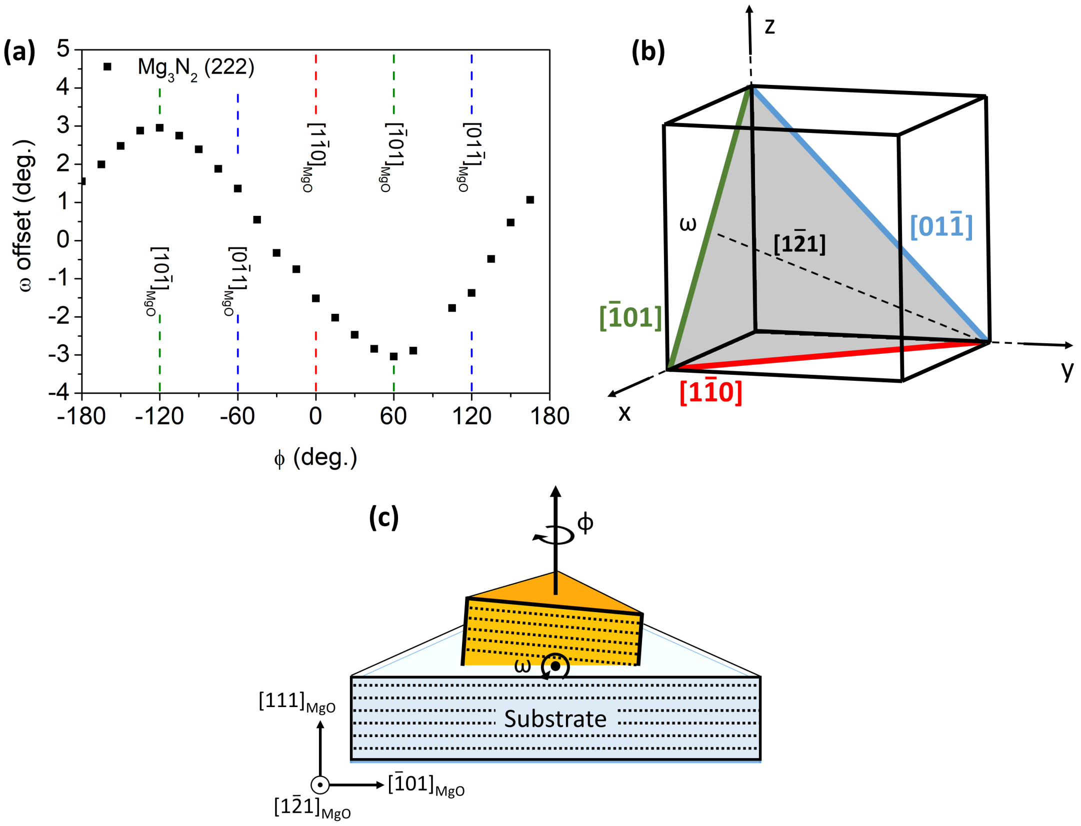

Figure 4.6: (a) ω offset between symmetric planes of Mg_3N_2 (111) on MgO (111) as a function of the azimuthal angle Φ, showing that the maximum angle of inclination between them is 3° and the rotational axis lies in the $[1\bar{2}1]$ direction. (b) Schematic MgO unit cell with an inserted triangular (111) plane. The colors of the edges denote the $\langle 1\bar{1}0\rangle$-type directions, which are indicated in (a). (c) Schematic arrangement of Mg_3N_2 (111) on MgO (111). The atomic (222) and (111) planes of the thin film and substrate, respectively, represented by dotted lines, show a relative ω offset.

the growth conditions [(100) and (111)], the conditions found so far for (100)-oriented thin films lead to a poor in-plane orientation on MgO (100) once the thickness exceeds ~20 nm. On the other hand, Mg_3N_2 (111) epitaxy is maintained for higher film thicknesses when grown on MgO (100), MgO (111) as well as YSZ (100), where the RHEED patterns can be simulated using the epitaxial relationships discussed in the following section. While the Mg_3N_2 (222) planes are parallel to the substrate surface when growth carried out on YSZ (100) and MgO (100), tilted heteroepitaxy is observed on MgO (111), where the Mg_3N_2 (222) planes show a 3° inclination with respect to the MgO (111) planes.

4.3.3 Epitaxial relationships of Mg_3N_2 on different substrates

To identify the epitaxial relationships of Mg_3N_2 (111) on the different substrates [MgO (100), YSZ (100) and MgO (111)], we performed Φ scans on asymmetric Mg_3N_2 and the respective substrate reflections. The Φ scan on Mg_3N_2 440 planes of sample F [Mg_3N_2 (111) on MgO (100)] is shown in Figure 4.7(a). Similarly to Zn_3N_2 (111) on MgO (100) [see Figure 3.5(a)], 12 peaks are observed for a rotation of $\Phi = 360°$, although three peaks would have been expected for a cubic (111)-oriented layer. This indicates the presence of four in-plane rotational domains, due to the different rotational symmetries of thin film and substrate, as discussed in Section 1.1.1. Also this time, the peaks of the Mg_3N_2 (440) occur at different azimuthal angles than the MgO (220) substrate ones, showing a 45° rotation of the entire domain structure around the growth direction [see Figure 4.7(b)], exactly as found for Zn_3N_2 (111) on MgO (100). The epitaxial relationships are thus given by

$$[1\bar{1}0]\ Mg_3N_2 \parallel [011]\ MgO \tag{4.1a}$$

$$[11\bar{2}]\ Mg_3N_2 \parallel [01\bar{1}]\ MgO \tag{4.1b}$$

plus the three additional epitaxial domains obtained by 90°, 180°, and 270° rotations of one triangular Mg_3N_2 domain around the [111] growth axis.

On the other hand, the Φ scan on Mg_3N_2 440 planes of sample H [Mg_3N_2 (111) on YSZ (100)] is shown in Figure 4.7(c). While the presence of 12 peaks highlights again that the thin film consists of four rotational in-plane domains, the azimuthal angles of the Mg_3N_2 (440) planes coincide this time with the asymmetric YSZ (220) ones. Hence, the Mg_3N_2 domains show epitaxial relationships as illustrated in Figure 4.7(d) and given by

$$[1\bar{1}0]\ Mg_3N_2 \parallel [010]\ YSZ \tag{4.2a}$$

$$[11\bar{2}]\ Mg_3N_2 \parallel [001]\ YSZ. \tag{4.2b}$$

plus the three additional epitaxial rotational domains obtained by 90°, 180°, and 270° rotations of one triangular Mg_3N_2 domain around the [111] growth axis.

In order to avoid the formation of several rotational Mg_3N_2 domains, we performed growth on MgO (111) substrates, as discussed before. When Mg_3N_2 (111) is grown on MgO (111), the occurrence of additional domains should be in principle suppressed according to the theory discussed in Section 1.1.1. Nevertheless, instead of three peaks, expected for a Φ scan around 360°, we experimentally find six peaks for sample J [see Figure 4.7(e)], giving rise to one additional in-plane rotational domain, rotated by 180° around the growth axis with respect to the first one. Although the occurrence of additional domains in epitaxy is possible, their formation is energetically unfavorable. Therefore, the ratio of two energetically non-equivalent domains should be in principle influenceable by varying the growth conditions. However, we did not succeed to change this ratio, although we grew more samples at different growth temperatures and Mg/N ratios (not shown here), indicating that the two domains are equally stable at the investigated growth conditions. To account for this additional domain, one has to distinguish between the symmetry of the substrate surface and the substrate volume, as shown in Figure A.10 of the Appendix. If the nucleation is mainly determined by the substrate vol-

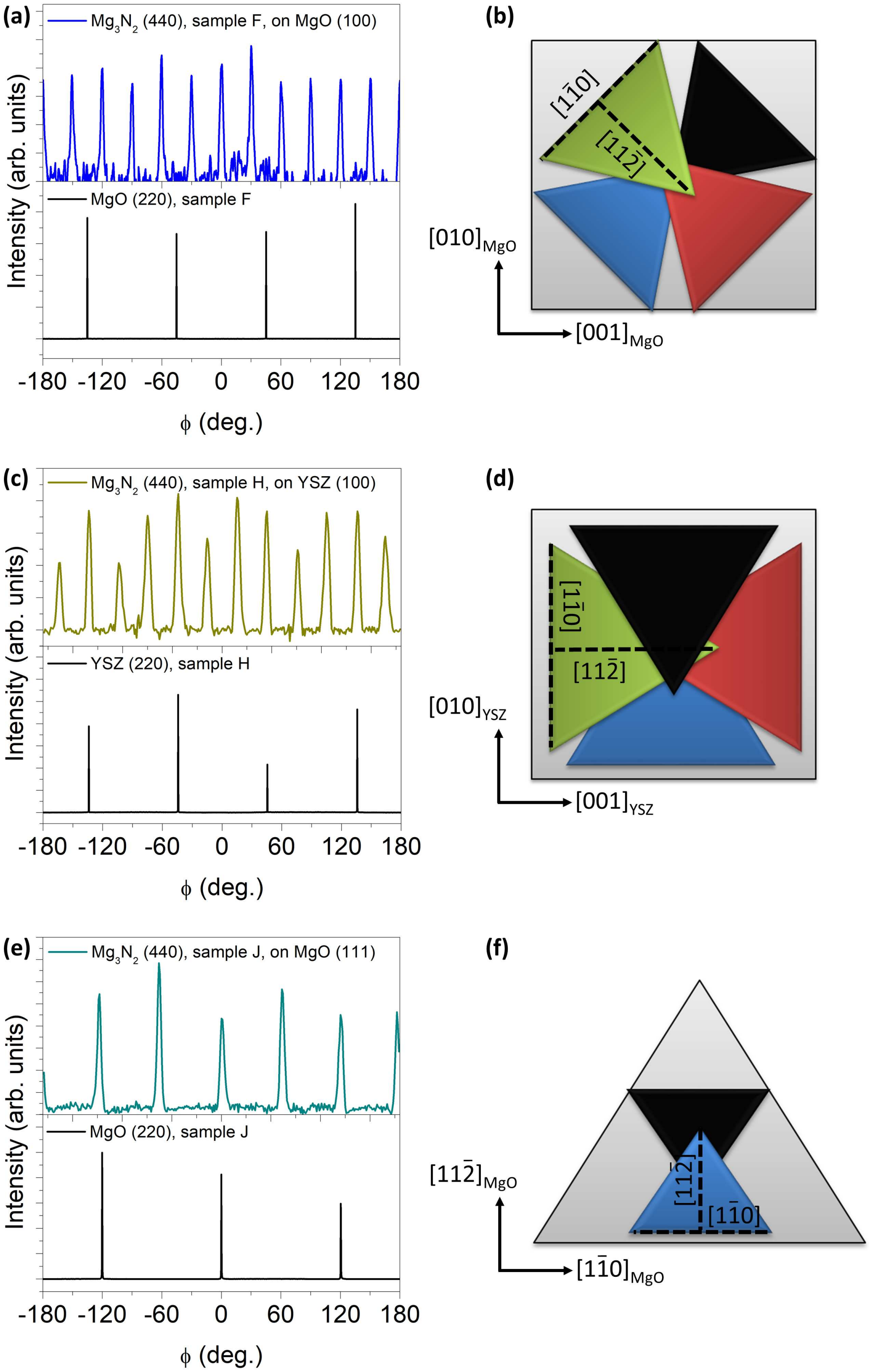

Figure 4.7: Φ scans on asymmetric Mg_3N_2 (440) planes. (a) On sample F [Mg_3N_2 (111) on MgO (100)], with (b) the extracted schematic epitaxial relationships. (c) On sample H [Mg_3N_2 (111) on YSZ (100)], with (d) the extracted schematic epitaxial relationships. (e) On sample J [Mg_3N_2 (111) on MgO (111)], with (f) the extracted schematic epitaxial relationships.

ume (also referred to as substrate half space) having three-fold symmetry, a single domain is expected. This is observed for example for Ge (111) on Si (111) [199], C (111) on Si (111) [200] or HfN (111) on Si (111) [201]. On the other hand, if the nucleation is mainly determined by the topmost atomic (111) surface layer (having in our case a six-fold symmetry, see Figure .10), two rotational domains are expected, as reported for ScN (111) on Si (111) [202] or TiN (111) on Si (111) [203]. The fact that we observe two Mg_3N_2 (111) domains on MgO (111) points, hence, towards a nucleation mainly determined by the first atomic layer. Note that the occurrence of this additional domain was considered in the context of Figure 4.6, where we discussed the lattice inclination occurring in this sample, although omitted for clarity in Figure 4.6(c). From Figure 4.7(e), the in-plane epitaxial relationships of Mg_3N_2 (111) on MgO (111) are thus

$$[1\bar{1}0]\ \mathrm{Mg_3N_2} \parallel [1\bar{1}0]\ \mathrm{MgO} \tag{4.3a}$$

$$[11\bar{2}]\ \mathrm{Mg_3N_2} \parallel [11\bar{2}]\ \mathrm{MgO} \tag{4.3b}$$

plus the additional domain obtained by rotating one triangular Mg_3N_2 domain by 180°, as shown in Figure 4.7(f).

Note that all the epitaxial relationships found here are in agreement with the RHEED observations discussed in Section 4.3.2. The RHEED pattern of Mg_3N_2 (111) on MgO (100), taken along the MgO [011] axis [see sample E in Figure 4.4(e)] was simulated using the epitaxial relations found here, where the colors of the diffraction spots correspond to the colors of the epitaxial domains indicated in Figure 4.7(b): Blue spots correspond to the diffraction of $(11\bar{2})$ planes (blue and black domains) and red and yellow spots correspond to diffraction of $(1\bar{1}0)$ planes in twin relation. By superimposing the simulated diffraction patterns of the different domains, one can reproduce the experimental RHEED pattern. The exact reproduction of the simulated diffraction is shown in Figure A.11 of the Appendix. Note that a similar RHEED pattern is observed for Mg_3N_2 (111) on YSZ (100) (sample H), as shown in Figure 4.5(c), despite 45°-rotated epitaxial relationships with respect to Mg_3N_2 (111) on MgO (100) (samples E and F). However, this RHEED is taken along the YSZ [010] direction, having a 45° angle to the [011] direction, too (used to record the RHEED pattern of sample E), leading therefore to similar diffraction.

The RHEED simulations done here are also consistent with the experimental pattern found for Zn_3N_2 (111) thin films grown on MgO (100) [see Figure 3.4(b)]. Since these thin films crystallize in the same structure and show the same epitaxial relationships as Mg_3N_2 (111) on MgO (100), the observed pattern along the MgO [011] axis is practically identical.

Also the epitaxial relationships of Mg_3N_2 (111) on MgO (111) shown in Figure 4.7(f) can be used to reproduce the experimental RHEED pattern of this sample [see Figure 4.5(d)]. Taken along the MgO $[1\bar{1}0]$ direction, diffraction from the $(1\bar{1}0)$ planes of the two twins are expected. Simulating those leads to a good agreement with the experimental pattern, where blue and black dots correspond to the diffraction of the $(1\bar{1}0)$ planes of the blue and the black domain, respectively. The superposition of the simulated diffraction patterns is shown in more detail in Figure A.12 of the Appendix.

In summary, the epitaxial relationships of crystalline Mg_3N_2 (111) thin films on three different substrates were identified. On MgO (100) and YSZ (100), the Mg_3N_2 (111) thin films exhibit four rotational in-plane domains, as expected due to unequal thin film and substrate rotational symmetries, where the different domains are obtained by a 90°, 180° and 270° rotation around the growth axis. However, on MgO (100) the four domains are inclined by an angle of 45° with respect to the domains on YSZ (100). To avoid the occurrence of rotational domains, we tried growth on MgO (111) substrates. Nevertheless, the Mg_3N_2 (111) thin films consist still of two epitaxial domains, rotated by 180° with respect to each other, due to the atomic structure of the (111) substrate surface plane being six-fold symmetric. All the epitaxial relations found are consistent with RHEED observations shown in the previous section.

4.3.4 Epitaxial MgO on Mg_3N_2

By the end of this PhD we succeeded to grow epitaxial MgO (111) on Mg_3N_2 (111), as illustrated in Figure 4.8. Using the same conditions for the MgO capping discussed in Section 4.2.2 (580 °C, 0.35 sccm O_2, Mg cell temperature 410 °C), but keeping the N_2 plasma ignited during the temperature ramping and during MgO growth (i.e. growing the capping layer under oxygen *and* nitrogen) leads, interestingly, to the crystallization of MgO (111).

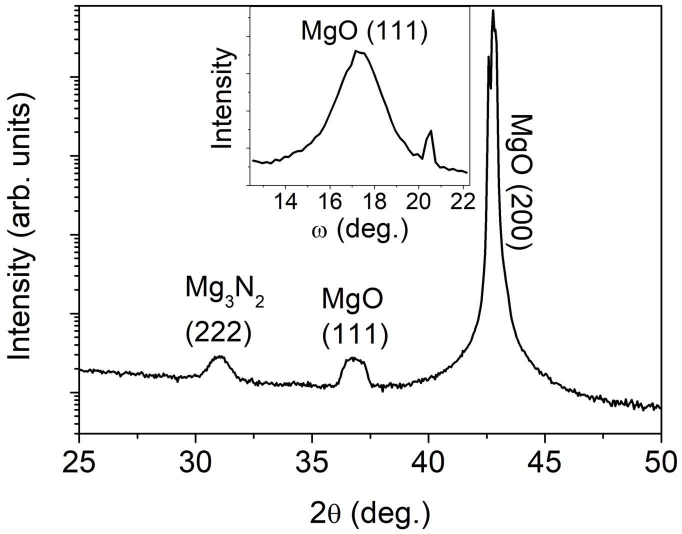

Figure 4.8: $2\theta/\omega$ scan of an Mg_3N_2 (111) thin film with epitaxial MgO (111) capping layer, grown on MgO (100). The inset shows the ω scan of the MgO (111) reflection. Note that the additional peak of $\omega = 20.5°$ is due to the detector/analyzer streak.

The XRD of the MgO (111)-capped Mg_3N_2 thin film reveals two signals (besides the MgO (200) substrate reflection). While the signal around 31° corresponds to the diffraction of Mg_3N_2 (222) planes, the peak at 37° can be assigned to diffraction of MgO (111). However, an ω scan on the

MgO (111) reveals a broad peak with an FWHM of ~2.5°, indicating a strong tilt present in the MgO capping.

In order to investigate the epitaxial relationships of the epitaxial MgO capping to its underlying Mg_3N_2 layer we performed Φ scans on the asymmetric MgO (200) reflections, which we compared to the one of Mg_3N_2 (400), as shown in Figure 4.9. 12 peaks are found for a rotation of Φ around 360° [see Figure 4.9(a)], indicating that the four rotational domains present in Mg_3N_2 (111) serve as growth template [see Figure 4.9(b)] and transfer their orientation to the capping layer. The peak positions of the Mg_3N_2 (400) and the MgO (200) planes coincide, showing that the MgO capping layer grows coherently on the Mg_3N_2 domains. The epitaxial relationships of the MgO capping to the underlying Mg_3N_2 rotational domains are hence

$$[1\bar{1}0]\ \mathrm{MgO_{cap}} \parallel [1\bar{1}0]\ \mathrm{Mg_3N_2} \tag{4.4a}$$

$$[11\bar{2}]\ \mathrm{MgO_{cap}} \parallel [11\bar{2}]\ \mathrm{Mg_3N_2}. \tag{4.4b}$$

Note that the Φ scan of the MgO (100) substrate is not shown. Using the epitaxial relationships of the capping layer, we can simulate its RHEED pattern, as shown in Figure 4.9(c). Similarly to Mg_3N_2 (111) on MgO (111), simulation of three different crystallographic planes is necessary. Note that the color of the dots represent the color of the epitaxial domains shown in Figure A.13 of the Appendix, where purple denotes diffraction from MgO $(11\bar{2})$ planes, and orange and green denote diffraction from MgO $(1\bar{1}0)$ planes in twin relation.

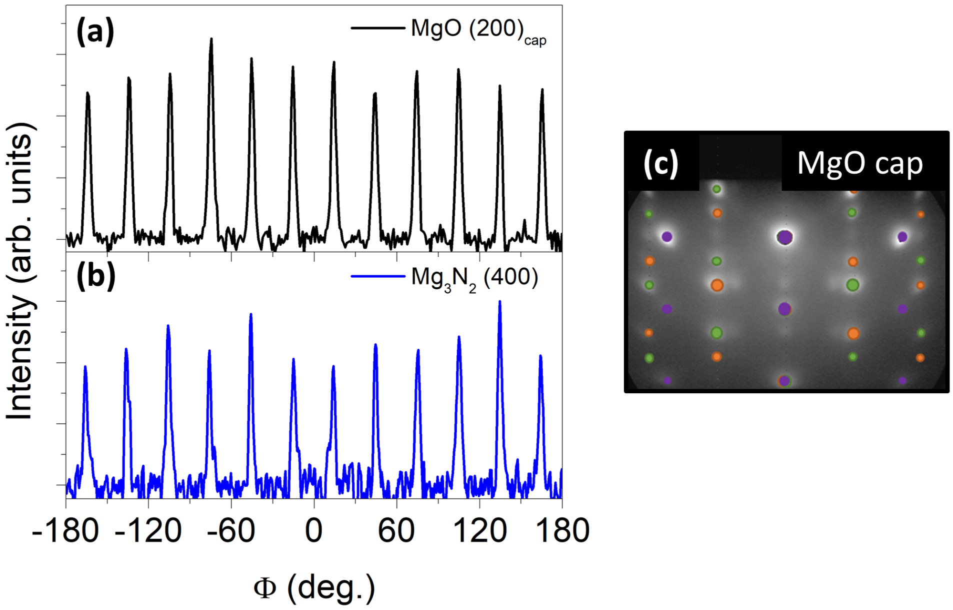

Figure 4.9: (a) Φ scans on asymmetric MgO (200) planes of the capping layer compared to (b) Φ scans on asymmetric (400) planes of the underlying Mg_3N_2 (111) layer. The Φ scan of the MgO (100) is not shown. (c) RHEED pattern of the MgO capping, taken along the MgO [011] substrate direction.

Experiments about the protective effect of the epitaxial MgO (111) capping with respect to its polycrystalline alternative are still ongoing. The growth of heteroepitaxial MgO on Mg_3N_2, which has never been reported previously, is a first step towards Mg_3N_2/MgO heterostructures.

4.3.5 Structural quality of Mg_3N_2

To evaluate the crystalline quality of our epitaxial Mg_3N_2 (111) thin films we evaluated the FWHMs of their ω rocking curves. The ω scans measured on the symmetric Mg_3N_2 (222) reflections of the samples F [Mg_3N_2 (111) on MgO (100)], H [Mg_3N_2 (111) on YSZ (100)] and J [Mg_3N_2 (111) on MgO (111)], fitted with pseudo-voigt functions, are presented in Figure 4.10. Note that the curves were recorded using a 1/4° slit in the diffraction path to better deconvolute the two different contributions occurring in some of the films.

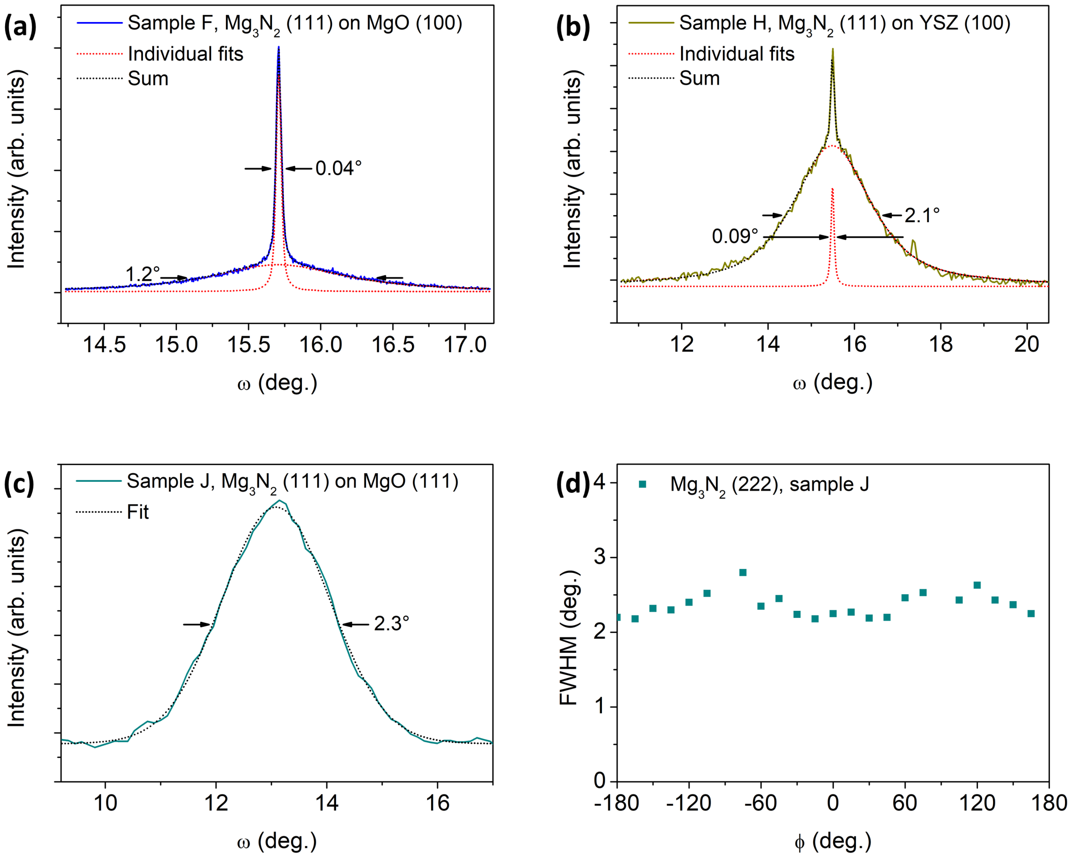

Figure 4.10: Symmetric ω scans of Mg_3N_2 (111) thin films on different substrates. (a) Around the (222) reflection of sample F [Mg_3N_2 (111) on MgO (100)]. (b) Around the (222) reflection of sample H [Mg_3N_2 (111) on YSZ (100)]. (c) Around the (222) reflection of sample J [Mg_3N_2 (111) on MgO (111)]. Note that different x-scales are used for the curves, which were all recorded using a 1/4° slit in the diffraction path. (d) FWHM of the Mg_3N_2 (222) reflection as a function of azimuthal angle Φ on sample J.

For sample F [Mg_3N_2 (111) on MgO (100)], an extremely narrow rocking curve with an FWHM of 0.04° is observed, superimposed to a low-intensity, 1.2°-wide peak, as shown in Figure 4.10(a). A similar behavior was observed for Zn_3N_2 (100) on YSZ (100) [see Figure 3.8(c)], where we assigned the narrow contribution to a thin, highly oriented nucleation layer, overgrown by tilted Zn_3N_2. However, the Mg_3N_2 thin film measured here is roughly four times thicker than the Zn_3N_2 thin film discussed in Figure 3.8(c). Still, the ratio of the narrow to the broad contribution is significantly larger in the Mg_3N_2 case, indicating that the grains present here are also highly oriented, but over a larger thickness range. While the extremely narrow FWHM of 0.04° may be interpreted as a parameter for outstanding structural quality, we will demonstrate in the following section that it occurs due to the correlation of defects, homogeneously distributed during the initial growth stage and, thus, can not be taken as a sign of good structural quality.

Likewise, the rocking curve of sample H [Mg_3N_2 (111) on YSZ (100)], shown in Figure 4.10(b) consists of a two component line shape. This time the broad contribution is more intense than in sample F (despite similar film thicknesses), indicating that tilt is introduced to the film at a lower thickness. Furthermore, the degree of tilt is larger, with the broad contribution having a larger FWHM of 2.1°.

For Mg_3N_2 (111) on MgO (111) (sample J), on the contrary, only one single peak, as commonly observed in heteroepitaxial systems, is found. Its width, 2.3°, indicates a strongly tilted thin film [Figure 4.10(c)]. Given the anisotropy of the symmetric Mg_3N_2 (222) planes (inclined by 3° with respect to the MgO (111) substrate planes, see Figure 4.6), we investigated their FWHM as a function of azimuthal angle Φ, as illustrated in Figure 4.10(d). Although one may expect an influence of the tilt anisotropy on the FWHM, the latter one stays roughly constant as a function of Φ.

4.4 Advanced structural characterization of Mg_3N_2 (111) on MgO (100)

Understanding the microstructure of thin films is important to improve their crystalline quality by adapting the growth conditions, as well as to understand their physical properties. To give a comprehensive insight into the microstructure of epitaxial Mg_3N_2, we grew a series of Mg_3N_2 (111) thin films on MgO (100) with different thicknesses in order to investigate the micro-structural evolution taking place during film growth. The growth conditions of these samples are the same as used for sample E of the previous section (see Table 4.3).

We thoroughly analyzed the two-component line shapes occurring in the ω rocking curves of these thin films, allowing us to extract detailed information of the film microstructure as a function of thickness. The measurement of asymmetric reflections allowed us, furthermore, to investigate the in-plane crystallinity in the investigated Mg_3N_2 (111) thin films (twist). Our results are in agreement with plan-view and cross-section TEM observations, never done before on Mg_3N_2 thin films, and enable us to develop a structural growth model for Mg_3N_2 (111) thin films on MgO (100).

Table 4.3: Growth conditions and thicknesses of Mg_3N_2 (100) thin films on MgO (100), capped with ~50 nm MgO. Note that the growth conditions given here are the same as for sample E of the previous section.

Sample	Growth temp. (°C)	Mg cell temp. (°C)	Nitrogen flow (sccm)	Thickness (nm)
I	400	430	0.35	15
II	400	430	0.35	69
III	400	430	0.35	90
IV	400	430	0.35	131
V	400	430	0.35	~302
VI	400	430	0.35	~547

4.4.1 Background

In heteroepitaxy the defect densities occurring can be particularly high due to the numerous differences that the thin film and the substrate might have, including crystal structure, orientation, lattice parameter and chemical composition (see Section 1.1.2). These differences can give rise to the build-up of strain, which can be released by the formation of defects (e.g. dislocations) as well as misorientations between neighboring grains (tilt and twist).

As demonstrated in the previous sections, XRD is a powerful, non-destructive technique to evaluate accurately a materials' microstructure, as it allows to determine the lattice parameters and crystalline quality over large spatial scales. Defects occurring in thin films lead to rotations and distortions of its crystalline lattice. Hence, the diffraction characteristics of a thin film depend on the defect types and on their concentrations. Generally, defects lead to peak broadening in ω rocking curves, where the FWHM increases as a function of defect density. More specifically, the lattice rotations and distortions, described by a vector $\boldsymbol{u}(\boldsymbol{r})$ (representing the sum of all displacements caused by defects in the point $\boldsymbol{r}$), directly influence the diffraction intensity, which can be represented by a Fourier transform

$$I(\boldsymbol{q}) = \int e^{i\boldsymbol{q}\boldsymbol{r}} G(\boldsymbol{r})\, d\boldsymbol{r} \tag{4.5a}$$

of the correlation function

$$G(\boldsymbol{r}) = \langle \exp(i\boldsymbol{Q}[\boldsymbol{u}(\boldsymbol{r}) - \boldsymbol{u}(0)]) \rangle. \tag{4.5b}$$

Here $\boldsymbol{q}$ denotes a small deviation from the reciprocal lattice vector $\boldsymbol{Q}_{hkl}$, where the average $\langle\rangle$ is performed over all possible origins. The dependence of $G(\boldsymbol{r})$ on the type and arrangement of the defects causing displacements is rather complex, making it difficult (although not impossible) to solve Equation 4.5a analytically [204–208].

However, there are two cases where $G(\boldsymbol{r})$ becomes unity, leading to $I(\boldsymbol{q}) = \delta(\boldsymbol{q})$ and, hence, an extremely narrow diffraction peak (with $\delta(\boldsymbol{q})$ denoting the Dirac delta function). The first one is a perfectly crystalline thin film without any defects, i.e. a complete absence of displacements with respect to the ideal atomic positions. While this case is often used to describe the basic theory of diffraction, it will never be achievable, since even bulk crystals contain imperfections. In the second case, on the other hand, defects are still present in the layer, but with an average net displacement that is zero over large spatial areas, hence, Equation 4.5b becomes unity. This so-called *correlation* of defects defines an associated correlation length, determining the area of zero average net displacement. Even with relatively high defect densities, coherent x-ray scattering can be preserved if the position and, eventually, the orientation of the defects are correlated, leading to very narrow FWHMs in ω rocking curves [204–217]. Besides defects, also the finite size of crystallites lead to peak broadening. It is hence necessary to separate both effects.

While XRD offers a global view of the microstructure in crystalline thin films, TEM enables a direct local insight and can allow therefore the identification of the defect type and spatial arrangement, as well as the crystallite size. In this sense, both techniques are complementary. Unfortunately, TEM is a destructive technique, requiring long sample preparation times when done by classical polishing techniques, which becomes problematic when dealing with Mg_3N_2, whose decomposition time constant is in the order of some minutes in air. For our samples, a preparation and latter transfer to the TEM under vacuum is therefore strictly necessary.

4.4.2 Out-of-plane lattice parameter

In order to investigate the out-of plane inter-planar distance we measured HRXRD on the symmetric Mg_3N_2 reflections of all samples reported in Table 4.3. The $2\theta/\omega$ scans around Mg_3N_2 (222) of the thickness series are shown in Figure 4.11(a).

The samples I to IV show finite size interference fringes, indicating a high out-of plane x-ray scattering coherence due to a high parallelity of (222) planes perpendicular to the growth direction. The thicknesses of these samples were obtained using Equation 3.3, as discussed earlier for Zn_3N_2, and are in agreement with XRR measurements (see Figure A.14 of the Appendix). As the film thickness increases further (samples V and VI), the interference pattern vanishes, although they should be in principle visible according to Equation 3.3 (for the simulated diffraction pattern of Sample V see Figure A.15 of the Appendix). This indicates hence a loss of x-ray coherence induced by an increase in roughness and/or a decrease in structural quality, as will be explained in the following. The thickness of these two last samples was obtained by extrapolating the growth rate of the previous ones.

Similarly to Zn_3N_2 (111) on MgO (100), an asymmetry of the interference pattern surrounding the Mg_3N_2 main peak is observed between the higher/lower 2θ angles, indicating a gradual change of d_{222} as a function thickness. By performing numerical simulations using Equation 3.4, this asymmetry can be reproduced (fits indicated by black dotted lines), allowing for the extraction of the (222) inter-planar distance variation as a function of thickness, as illustrated in Figure 4.11(b). The additional interference fringes occurring in sample I are due to the ~50 nm capping layer, which is included in the simulations. Close to the film-substrate interface, d_{222} is larger than the literature value for relaxed Mg_3N_2 (2.873 Å), indicating the presence of compressive strain in the samples I to IV. Indeed, the calculation of the lattice mismatch for

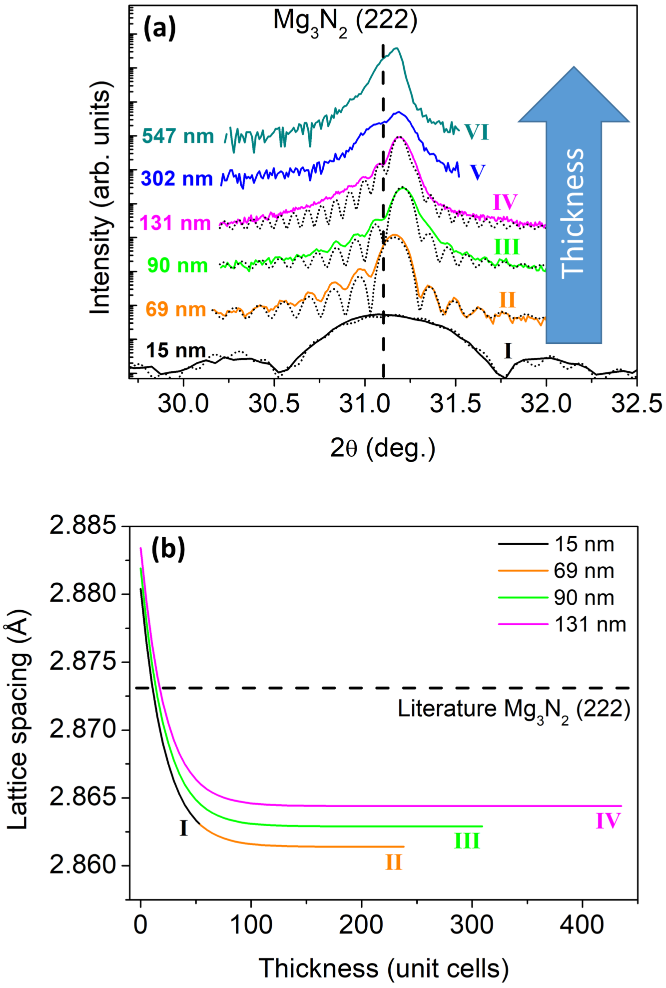

Figure 4.11: (a) High-resolution $2\theta/\omega$ scans around the symmetric Mg_3N_2 (222) reflections for the samples I to VI, i.e. of different film thickness. The curves were measured with a crystal analyzer detector and vertically shifted for clarity. The numerical fits using the Equations 3.3 and 3.4 are indicated by black, dotted lines. (b) Inter-planar (222) distance as a function of thickness, resulting from the fits in (a).

Mg_3N_2 to MgO using the epitaxial relationships found earlier [see Figure 4.7(b)] reveals +2.3 % along the Mg_3N_2 $[11\bar{2}]$ direction and +18.2 % along its $[1\bar{1}0]$ direction. Hence, the substrate imposes its smaller lattice to the nucleating layer, leading to an out-of plane lattice expansion. As the thickness increases, d_{222} decreases, indicating a relaxation of the thin film.

Interestingly, d_{222} does not only relax to the Mg_3N_2 (222) literature value, but decreases further for thicknesses larger than ~20 unit cells (~5 nm), evolving to a tensile strain. A reason for this may be the grain coalescence, frequently introducing tensile strain into growing thin films [218–220], and leading to a shift towards higher 2θ angles with respect to the bulk [literature value of Mg_3N_2 (222) indicated by the dashed line in Figure 4.11(a)].

4.4.3 Grain size and lattice rotations: XRD characterization

Normalized high-resolution transverse ω scans on the same sample series, measured on the symmetric Mg_3N_2 (222) reflection, are presented in Figure 4.12(a). All curves consist of a narrow (coherent) and a broad (diffuse) contribution, giving rise to a two-component line shape. The narrow peaks have approximately the same FWHM than the symmetric MgO (200) reflection of the substrate, as shown in the inset of Figure 4.12(a). At this stage, we assume that this narrow peak is linked to a coherent scattering phenomenon with a homogeneous spatial distribution of some crystalline defects displaying long correlation distances, as explained in the previous section, and as observed previously in other material systems [204–217]. Interestingly, the peak area of the broad contribution increases as a function of thickness with respect to the narrow one, indicating that this contribution has an origin independent of the correlated defects.

Using two pseudo-voigt functions we fitted the transverse ω scans of all samples before normalization in order to evaluate the absolute intensities of both contributions. As shown in Figure 4.12(b), the peak area of the narrow contribution stays constant, while the area of the broad contribution increases linearly as the function of thickness, pointing towards the origin of coherent scattering being located close to the film-substrate interface. Initially exhibiting correlated defects, the thin film is overgrown by Mg_3N_2 showing much shorter correlation distances (if correlation is even present). Such two-component line shapes are observed in various heteroepitaxial systems and are usually interpreted to stem from correlated threading dislocations [205, 206, 209–211], misfit dislocations at the film-substrate interface [204, 206–208, 213–216], misorientations [209, 215, 216] or grain boundaries [212, 217].

When it comes to peak broadening of XRD patterns, Williamson and Hall [221] analyzed already in 1953 the line widths of diffraction peaks in $2\theta/\omega$ scans as a function of their diffraction order, allowing them to separate broadening due to out-of plane finite crystallite size and lattice strain.

Similarly, this procedure can be transferred to the investigation of symmetric transverse ω scans, allowing this time the separation of in-plane finite size effects and lattice rotations around an in-plane axis (tilt). In their two-component ω scans, Miceli *et al.* [215, 216] observed that the FWHM of the broad contribution stays constant (in units of in-plane reciprocal space units Q_x) as a function of diffraction order when finite size effects are the origin of broadening. On the other hand, if lattice rotations cause peak broadening, the line width is proportional to the length of the scattering vector $\boldsymbol{Q}$, i.e. it increases in units of Q_x, but stays constant in units of ω.

We analyzed the peak width of the symmetric Mg_3N_2 (222) and (444) reflections (i.e. of different diffraction orders), as presented in Figure 4.13 for the samples II and V in logarithmic scale. For both samples the coherent scattering intensity decreases significantly when going from the (222) to the (444) reflection, consistent with the literature cited above. More importantly, the line width of the broad peak of sample II (69 nm-thick Mg_3N_2 film) is constant when plotted as a function of Q_x, indicating that finite size effects are the main origin of peak broadening, as

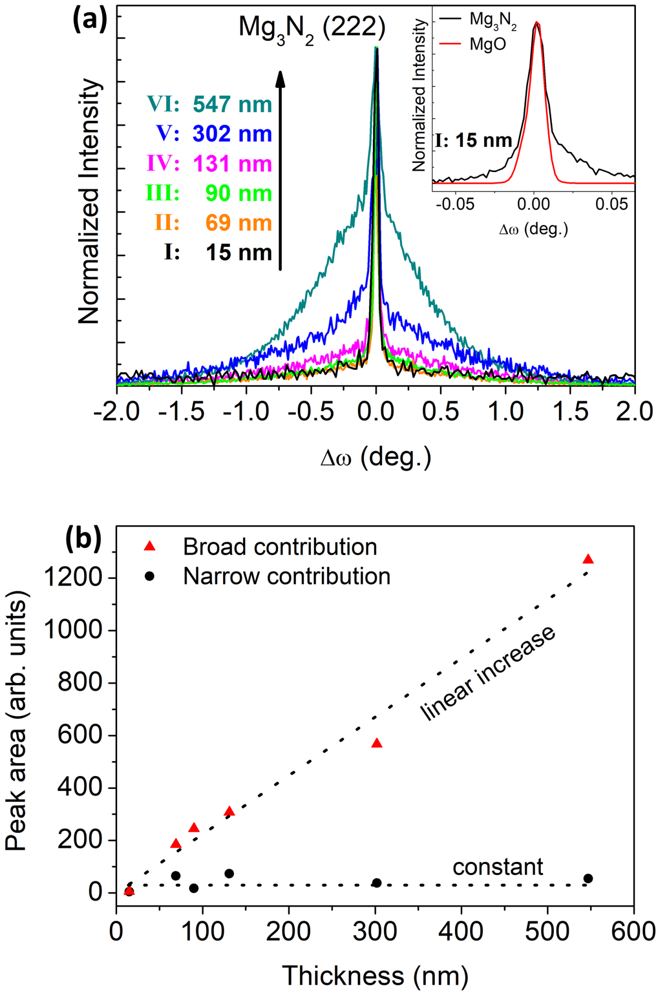

Figure 4.12: (a) Normalized high-resolution transverse ω scans on Mg_3N_2 (222) for the samples I to VI, measured with a crystal analyzer detector. The inset shows the magnified normalized scan of sample I in comparison with the symmetric MgO (200) substrate reflection. (b) Peak area under the peaks in (a), consisting of a narrow and a broad contribution.

shown in Figure 4.13(a). In this case, the FWHM ΔQ_x is inversely proportional to the lateral length l causing the peak broadening ($l = 2\pi/\Delta Q_x$), which can be interpreted as the lateral

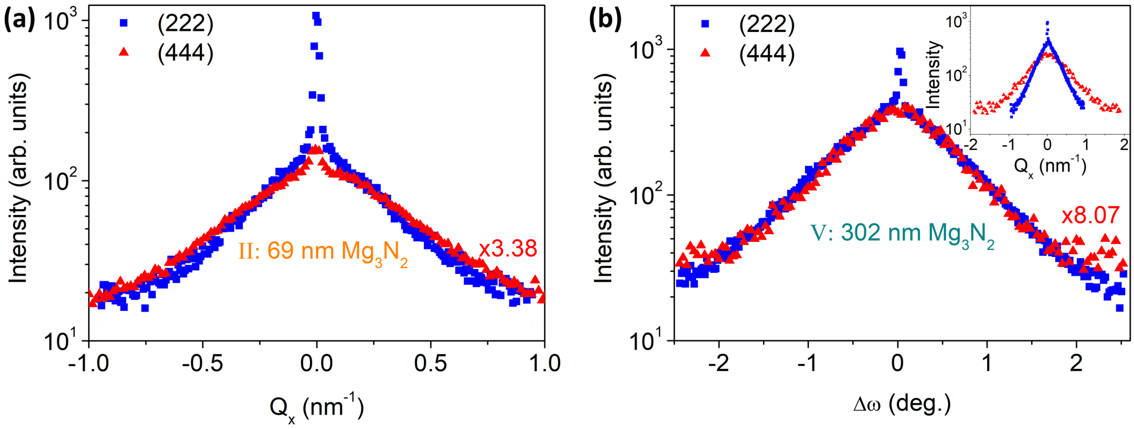

Figure 4.13: ω rocking curves on the symmetric Mg_3N_2 (222) and (444) reflections, measured by an open detector with a 1/4° slit in the diffraction path. A multiplicative factor k (shown in red) is used to rescale the (444) rocking curve, having a lower diffraction intensity. (a) Sample II (69 nm-thick Mg_3N_2 film), as a function of in-plane reciprocal space units Q_x. (b) Sample V (302 nm-thick Mg_3N_2 film), as a function of angular units ω. The inset in (b) shows the same curves, but as a function of in-plane reciprocal space units Q_x.

grain size. Doing this analysis one can extract a lateral grain size of $l \approx 13$ nm for the 69 nm-thick Mg_3N_2 film.

On the other hand, Figure 4.13(b) shows the rocking curves of the (222) and (444) reflection of sample V, this time as a function of angular units. For the 302 nm-thick film the line shape seems similar to that of sample II. However, rescaling the (444) rocking curve by a multiplicative factor k shows that the line width of the broad peak is constant in ω and hence, increases as a function of diffraction order [as shown in the inset of Figure 4.13(b)]. This demonstrates that lattice rotations are the main origin of peak broadening in the thicker thin films, giving rise to a two-layer structure occurring during film growth. The FWHM of the broad contribution is 1.3°, which is the degree of tilt present in this sample.

Note that the curves shown in Figure 4.13 have been recorded with a 1/4° slit in the diffraction path in order to ensure a sufficiently high intensity of the (444) reflection, but still enabling to separate the narrow from the broad contribution. Indeed, while the FWHM of the diffuse contribution stays roughly constant as a function of detector configuration ($1.3 \pm 0.1°$), it increases for the coherent peak from 100 arcsec, via 196 arcsec to 238 arcsec when changing from the crystal analyzer, via 1/4° slit, to a completely open configuration (see Figure A.16 of the Appendix).

Using this relatively simple XRD analysis, we were able to define two different micro-structural regions in our samples: Finite size broadening dominates the x-ray scattering characteristics for thin Mg_3N_2, whereas lattice rotations (tilt) dominate the peak broadening for thicker Mg_3N_2 layers. In order to define the *critical* thickness, where the transition between the two limiting behaviors occurs, we calculated the difference Δ between the (222) and (444) diffuse scattering

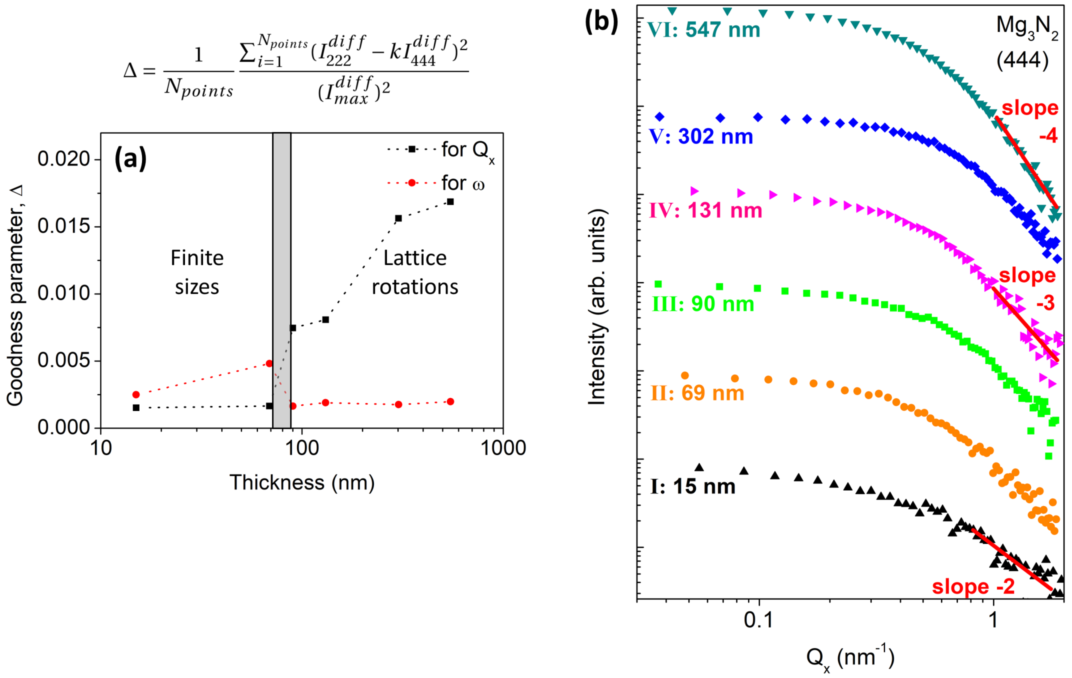

Figure 4.14: (a) Goodness parameter Δ for the samples I to VI, calculated as a function of in-plane reciprocal space units Q_x as well as of angular units ω. The area indicated in gray denotes the the transition from finite size limited to tilt limited structural quality. (b) Diffraction tail analysis of the ω rocking curves around the Mg_3N_2 (444) reflection in log-log scale, as a function of film thickness, measured with a fully open detector.

curves for all samples, when plotted as a function of Q_x as well as ω

$$\Delta = \frac{1}{N_{points}} \frac{\sum_{i=1}^{N_{points}} (I_{222}^{diff} - k I_{444}^{diff})^2}{(I_{max}^{diff})^2}. \tag{4.6}$$

Here N_{points} is the number of measured points in the curve and I_{222}^{diff} and I_{444}^{diff} denote the scattering intensity values for each point in the Mg_3N_2 (222) and (444) curves, respectively. Minimizing Equation 4.6 enables to extract the curve difference Δ when plotted as a function of Q_x or ω, as well as the multiplicative factor k required to rescale the diffuse intensity of the (444) reflection (used in Figure 4.13). In order to quantitatively compare the goodness parameter Δ between the different thin films, we normalized the result by the maximum value of the diffuse scattering intensity I_{max}^{diff}. If Δ is smaller when calculated as a function of Q_x (i.e. the difference between the (222) and (444) curves is smaller when plotted as a function of Q_x), the peak broadening is dominated by finite size effects. On the contrary, if Δ is smaller when calculated as a function of ω, lattice rotations (tilt) dominate the peak broadening.

Figure 4.14(a) shows the goodness parameter as a function of Mg_3N_2 film thickness, in units of Q_x as well as of ω. Consistent with the observations in Figure 4.13, Δ is small when calculated in units of Q_x for the thinnest samples (I and II), indicating that finite size effects with lateral grain sizes of 9 nm to 13 nm are the main source of peak broadening (depending on the sample). For the thicker samples (III to VI), however, its value increases, indicating a mismatch between the Mg_3N_2 (222) and (444) rocking curves in units of Q_x. Indeed, all samples thicker than 69 nm exhibit a smaller Δ when calculated in units of ω, indicating that a ~1.3° tilt dominates their microstructure. The crossing of these behaviors is found at a thickness of 70 nm to 90 nm, indicating the critical thickness where the transition occurs.

Another way to determine the origin of peak broadening is to analyze the diffraction tails of ω rocking curves for sufficiently large Q_x. A model to fit ω scans measured with a fully open detector was developed by Kaganer *et al.* [205], who calculated the intensity decay as a function of Q_x. More precisely, they found a Q_x^{-2} decay in thin films dominated by finite size broadening, whereas a Q_x^{-3} decay was attributed to stem from lattice defects, in their case randomly distributed threading dislocations. Figure 4.14(b) shows such an analysis on our sample series, where we plot the intensity decay of the symmetric Mg_3N_2 (444) reflection as a function of film thickness in a log-log scale. This representation has the advantage that curves obeying a power law are converted to straight lines, where slopes of -2 and -3 symbolize Q_x^{-2} and Q_x^{-3} dependencies, respectively.

For the samples I and II (15 nm and 69 nm, respectively), a slope of -2 is observed, denoting a Q_x^{-2} decay, which indicates a finite size limited structural quality. An increase of Mg_3N_2 film thickness (samples III to V) leads to a gradual change of tail slope towards -3, hence, Q_x^{-3} dependence, indicating a microstructure that is dominated by defects and consistent with the observations of Figure 4.14(a). Interestingly, a slope of -4 is found in the diffraction tail of the sample VI (547 nm), exhibiting therefore an intensity decay following a Q_x^{-4} law. This tail slope was not predicted by the model of Kaganer *et al.* and points towards other mechanisms limiting the overall structural quality for thicker Mg_3N_2 films. To complete the picture of the Mg_3N_2 films' microstructure, we performed TEM analysis on cross-section and plan-view specimens, as discussed in the following.

4.4.4 Grain size and lattice rotations: TEM characterization

To analyze lattice defects, in particular their type and spatial arrangement, TEM is the method of choice since it gives a direct insight into the microstructure of a thin film.

Note that in the case of Mg_3N_2 special attention needs to be payed in order to avoid the degradation of the material in contact with air, which probably explains why there are no prior TEM studies on this material. Consequently, the preparation of the TEM specimen necessarily needs to be done under vacuum, i.e. using FIB sectioning. Once the specimen is prepared, the Mg_3N_2 layer is not anymore protected by its MgO capping layer. To reduce the exposure time of the unprotected specimen to air, we transferred it to a vacuum container right after the FIB preparation, and, transported it to the TEM. A fast transfer to the microscope ensured that the total air exposure of the specimen did not exceed 1 min, sufficiently small to allow the observation of Mg_3N_2 thin films. This procedure was applied for all the TEM samples shown in the following.

4.4.4.1 Cross-section TEM analysis of Mg_3N_2

We prepared cross-section specimens of sample V [302 nm-thick Mg_3N_2 (111) grown at 400 °C on MgO (100)] and of sample F of the previous section for comparison [97 nm-thick Mg_3N_2 (111) grown at 460 °C on MgO (100)].

The film structure of sample V, prepared along an MgO ⟨011⟩ zone axis, is shown in the TEM multi-beam micrograph in Figure 4.15(a). The MgO capping layer shows a brighter contrast than the substrate consisting of the same material due to its lower crystallinity (see Figure 4.2).

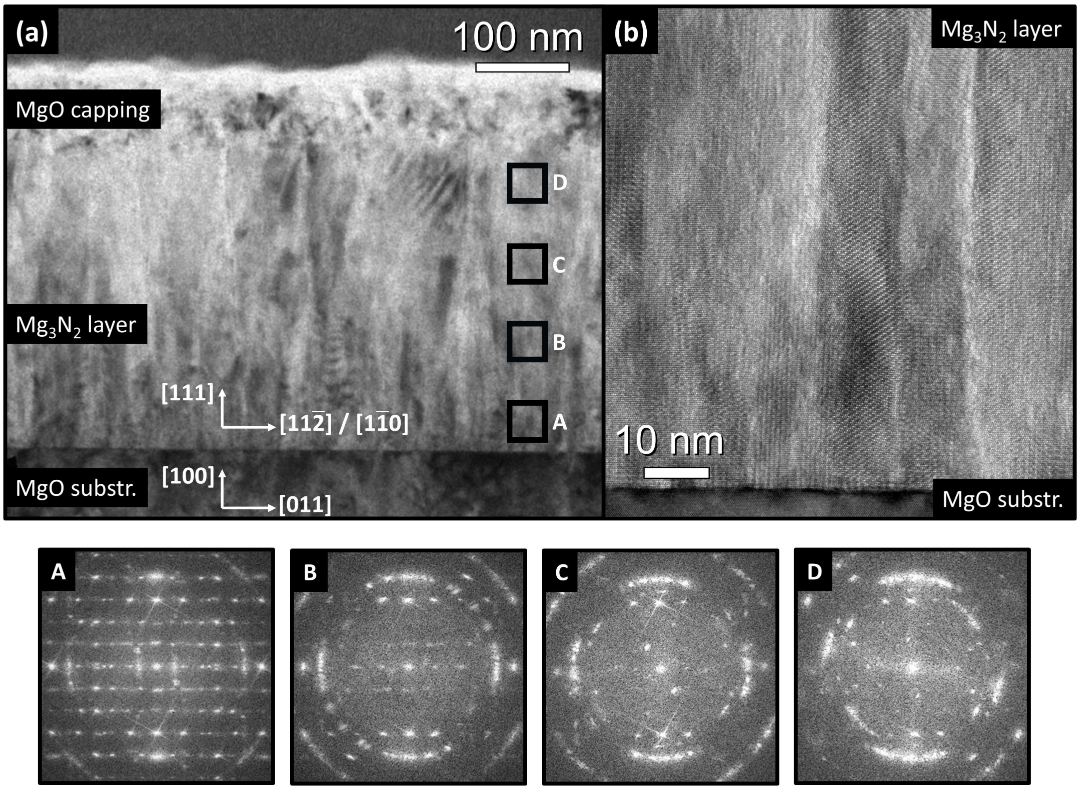

Figure 4.15: (a) Cross-section TEM micrograph of sample V (302 nm-thick Mg_3N_2), along an MgO ⟨011⟩ zone axis. A columnar structure is revealed for the Mg_3N_2 (111) thin film close to the film-substrate interface, disappearing at higher film thickness. (b) High-resolution TEM micrograph of the film-substrate interface. A to D show Fourier transform images generated from high-resolution images at the corresponding positions indicated in (a).

The Mg_3N_2 thin film itself exhibits a columnar structure close to the film-substrate interface, with a lateral grain size of ~10 nm, consistent with the results obtained by XRD in the previous section. The film is clearly crystalline in the initial growth stage, showing an abrupt interface to the underlying MgO substrate, confirmed by the high-resolution TEM micrograph shown in Figure 4.15(b). Note that this image consists of Moiré patterns due to the relatively small column diameter with respect to the specimen thickness (~10 nm vs. several tens of nm). Interestingly, some of the column boundaries are linked to steps occurring in the MgO substrate (see Figure A.17 of the Appendix), although this is not systematically observed.

Once the Mg_3N_2 film thickness increases, the columnar structure is lost, accompanied by an increase in bright contrast, hence, a decrease in crystallinity. Using Fourier transform analysis of high-resolution images (micrographs not shown here) taken at the positions indicated in Figure 4.15(a), we can investigate the change in crystallinity as a function of Mg_3N_2 film thickness. Close to the film-substrate interface (see image A), the thin film is crystalline as indicated by the presence of various diffraction spots in the Fourier transform. As the growth proceeds, circular arcs appear (see image B), giving rise to an increased tilt present in this sample. Finally, these arcs dominate the Fourier transform at large thicknesses (see image C and D), indicating a tilt-limited microstructure. The micro-structural evolution during growth is in agreement with RHEED observations (see Figure A.18 of the Appendix), where circular arcs develop as the Mg_3N_2 film becomes thicker.

To identify the in-plane orientations of the columns, we recorded selective area electron diffraction (SAED) patterns of the cross-section specimen of sample V, as shown again in Figure 4.16(a). The diffraction of the thin film can be perfectly reproduced using the simulated diffraction patterns in Figure A.11 of the Appendix, confirming the epitaxial relationships found earlier and shown in Figure 4.16(b). Note in the SAED pattern of Figure 4.16(a) diffraction of the MgO substrate is present (indicated by the gray dots) besides the ones of the four rotational Mg_3N_2 domains (indicated by the color of each respective domain).

In order to identify the nature of the columnar grains we performed two beam observations using $g = (044)$ of two different rotational domains [see Twin I and Twin II in Figure 4.16(a) and (b)]. Only some of the columns appear bright when collecting the $g = (044)$ diffraction of one individual domain family (Twin I), as displayed in Figure 4.16(c), showing that the columns themselves correspond to the epitaxial rotational domains the Mg_3N_2 film consists of. Besides, the columns show an average height of ~70 nm. This result is in agreement with the XRD observations discussed in the previous section, where we found a transition from finite-size limited structural quality to tilt-limited structural quality in the same thickness range. Above this thickness, the columnar structure disappears as attested by the loss of diffraction conditions, indicating an increased film twist.

Interestingly, an increase of growth temperature from 400 °C to 460 °C leads to an increase of column height, as shown in the dark field images of sample F [see Figure 4.16(d)]. While the column width is also found to be ~10 nm, similarly to that of Sample V, the columns stay intact over the entire film thickness, leading to a height of 97 nm. Similarly to Figure 4.16(c), by selecting the $g = (044)$ of the other rotational domain (Twin II) diffraction of complementary columns is obtained [Figure 4.16(e)]. However, the small Mg_3N_2 grain size with respect to the specimen thickness prevented the observation of perfectly complementary images.

The microstructure of our Mg_3N_2 (111) thin films on MgO (100) is similar to that found by Heinke *et al.* for GaN (0001) on c-plane sapphire. They found ~24 nm wide GaN columns that were identified as inversion domain boundaries with inversed GaN polarity. The regular distribution of the column boundaries led, in their case, to the occurrence of a narrow diffraction peak in XRD too. We can therefore assume that our narrow diffraction peaks in XRD originate from the regular distribution of our rotational Mg_3N_2 domains, leading to a correlation of the domain boundaries separating them, with a correlation length in the order of 10 nm.

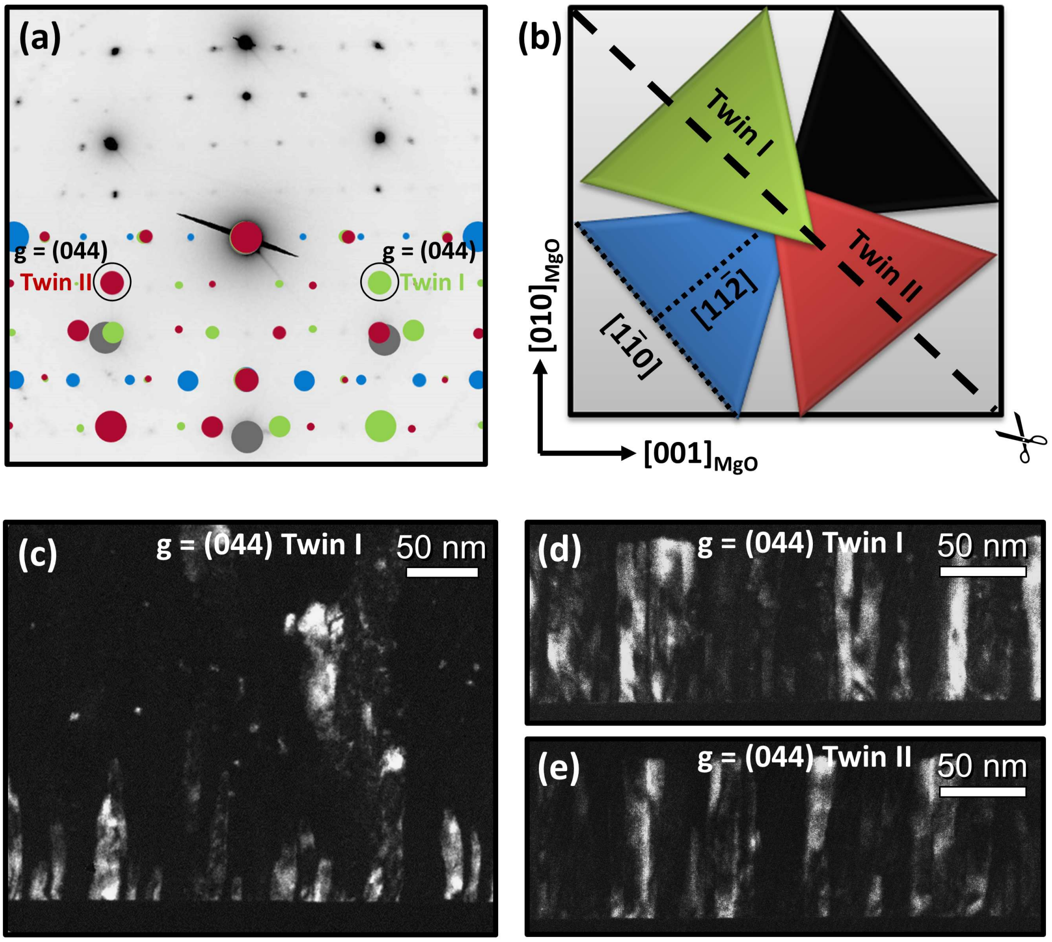

Figure 4.16: (a) SAED pattern of sample V, where half of the pattern is reproduced using the simulations shown in Figure .11, confirming the epitaxial relations found earlier. (b) Schematic epitaxial relationships of Mg_3N_2 (111) on MgO (100). The dashed line denotes one MgO ⟨011⟩ zone axis, along which sample preparation was performed. (c) Cross-section dark field TEM micrograph of sample V (302 nm Mg_3N_2 (111) on MgO (100) grown at 400 °C) using g = (044) of one rotational domain (Twin I). (d) and (e) display the same experiment on sample F (97 nm Mg_3N_2 (111) on MgO (100) grown at 460 °C) using g = (044) of Twin I and Twin II, respectively, showing that the column height can be controlled by the growth conditions.

4.4.4.2 Plan-view TEM analysis of Mg_3N_2

In order to investigate the rotational domain boundaries, we prepared a plan-view TEM specimen of sample III [90 nm Mg_3N_2 (111) grown at 400 °C on MgO (100)]. This sample was chosen due to its low Mg_3N_2 thickness, in order to exclusively observe the correlated, columnar Mg_3N_2 structure. It is worth emphasizing that the preparation of such thin plan view specimen is challenging, since it also involves the removal of the MgO substrate, as well as the protective MgO capping layer. Hence, it is quite difficult to control the right moment where to stop the ion etching. If too much of the MgO substrate and/or capping layer is removed, one risks to etch the thin Mg_3N_2 film. On the contrary, if the etching is stopped too early, the Mg_3N_2 thin film will overlap with the MgO substrate and/or capping layer, hindering a proper observation. Therefore, we applied a sample preparation involving several etching levels in order to increase the chance of having exclusively Mg_3N_2.

Figure 4.17(a) shows the SAED pattern of sample III. The observed diffraction agrees well with the simulations, based on the epitaxial relationships found for Mg_3N_2 (111) on MgO (100) (for simulations see Figure A.19 of the Appendix). However, diffraction of the MgO substrate is still present [indicated by the dashed square in Figure 4.17(a)], leading to additional diffraction spots due to the overlap with the Mg_3N_2 thin film due to multiple diffraction (dynamical theory of diffraction). For the diffraction coming from Mg_3N_2 itself, a lateral elongation of the diffraction spots is observed, pointing towards a 4-5° twist present in the Mg_3N_2 columns.

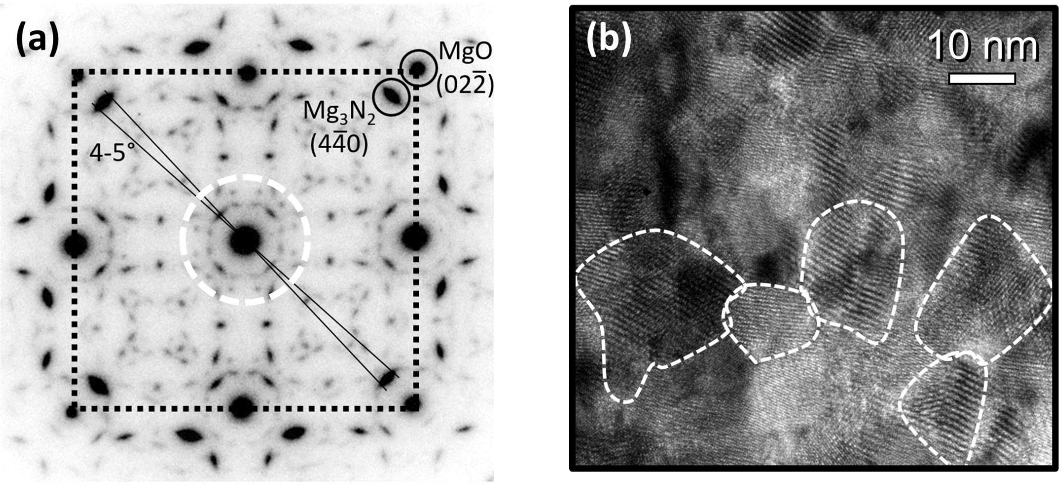

Figure 4.17: (a) Cross-section SAED pattern of sample III [90 nm Mg_3N_2 (111) on MgO (100)]. Diffraction coming from the MgO substrate is indicated by the dotted square. (b) High-resolution TEM micrograph of the plan-view specimen, recorded using the diffraction spots situated inside the dashed white circle in (a).

Furthermore, we recorded high-resolution images by selecting electrons coming mainly from Mg_3N_2 [selected area indicated by the dashed white circle in Figure 4.17(a)]. Although the high-resolution micrograph in Figure 4.17(b) reveals ~10 nm-sized grains (some of them indicated by white dashed lines), the exact arrangement of the Mg_3N_2 columns, as well as the structure of their boundaries, remains unclear due to the occurrence of Moiré patterns.

4.4.5 XRD of asymmetric reflections

In order to quantify the twist occurring in the Mg_3N_2 domains, we performed XRD on asymmetric Mg_3N_2 reflections, as shown for sample IV (131 nm Mg_3N_2) in Figure 4.18(a). The FWHM increases clearly as a function of the inclination angle χ to the sample surface, indicating that the microstructure is dominated by twist. To fit the FWHMs of these reflections one has to recall the model of Lee *et al.* that we already used in Section 3.2.5 to analyze the asymmetric reflections in Zn_3N_2 thin films. Using the equation given in Figure 4.18(a) we can reproduce well the experimental results, with values of Γ_y and Γ_z of 1.3° and 2.5°, respectively.

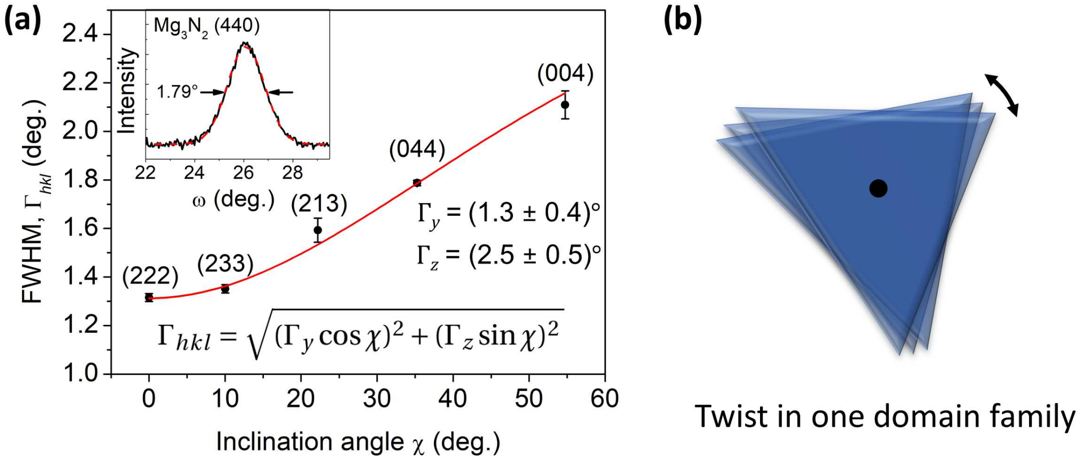

Figure 4.18: (a) FWHM as a function of inclination angle χ. (b) Schematic twist present in one rotational domain family.

Since we did not observe a narrow, coherent scattering peak in any of the asymmetric reflections, as shown in the inset of Figure 4.18(a), we used the FWHM of the broad contribution for the symmetric Mg_3N_2 (222) reflection at $\chi = 0°$. Note that the twist of $\Gamma_z = 2.5°$ is measured for one rotational domain family, as schematically shown in Figure 4.18(b). Although counterintuitive, this value is in agreement with the plan-view TEM observations of the previous section, where we found a ~5° twist, given that XRD provides the FWHM of the peak, whereas in TEM the entire spot size is measured. Note that, although we measured the XRD on one rotational domain family, all four domain families experience the same twist for their diffraction spots, as a lateral spot elongation is observed in the SAED pattern of Figure 4.17(a).

4.4.6 Growth model

Thanks to XRD analyses on symmetric and asymmetric Mg_3N_2 reflections, as well as TEM observations on cross-section and plan-view specimens, we could unravel the microstructure of

Mg_3N_2 (111) on MgO (100), which is illustrated in Figure 4.19. A columnar structure is revealed in the initial growth stage, where the columns are assigned to four rotational domains occurring due to different thin film and substrate rotational symmetries. Although these columns exhibit an in-plane twist component, they are well aligned along the [111] growth direction, causing an extremely narrow diffraction peak in symmetric transverse ω scans, superimposed to a broad, low-intensity contribution due to the finite column diameter of ~10 nm. These scattering characteristics are accompanied by finite size interference fringes occurring in longitudinal $2\theta/\omega$ scans. As the growth proceeds, the correlated columns are overgrown by strongly disordered Mg_3N_2, causing the broad contribution to increase in intensity, accompanied by a change of scattering characteristics from finite size broadening to tilt limited broadening in symmetric Mg_3N_2 reflections, and a loss of diffraction conditions in cross-section dark field TEM.

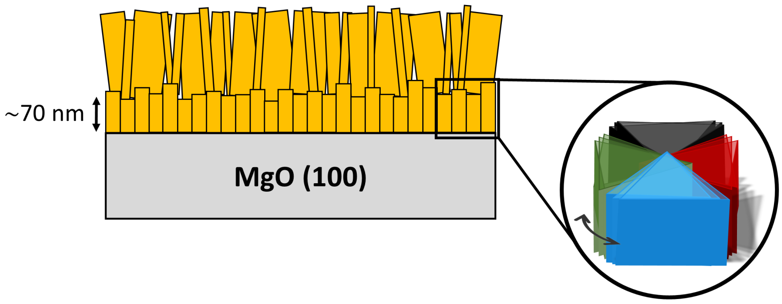

Figure 4.19: Schematic film structure found for Mg_3N_2 (111) on MgO (100). A two-layer structure is revealed, where the first ~70 nm consist of columnar rotational domains, well aligned along the [111] growth direction, but showing an in-plane twist. These columns are overgrown by strongly misoriented Mg_3N_2 as the growth proceeds.

The microstructure of our Mg_3N_2 thin films is similar to that of sputtered AlN (0001) thin films found by Miyake *et al.* on *c*-plane sapphire [175, 176]. In their case, a columnar, ~10 nm-thick AlN nucleation layer was observed by the authors, where the column diameter was found to be in the order of a few nm. This nucleation layer, well oriented along the [0001] growth direction and showing a twist of ~2°, is overgrown by misoriented, ca. 25 nm wide columns, leading to two-component line shapes in their ω rocking curves, similarly to our thin films (although our column height was found to be ~70 nm).

The large twist component observed in the nucleation layer in both material systems can be linked to the large lattice mismatch of the thin films to their crystalline substrate [13 % in AlN on sapphire and up to 18 % in Mg_3N_2 (111) on MgO (100)]. Mante *et al.* [222] developed a model that explains the twist occurring in highly-mismatched heteroepitaxial systems, the twist value being proportional to the mismatch. In their model AlN (0001) on Si (111) system (with a 19 % lattice mismatch), they found a twist of 3.3° between the nucleating AlN islands, as measured by grazing incidence XRD. TEM investigations revealed that, in this case, the mismatch is introduced by 60° misfit dislocations at the film-substrate interface, compensating for the high lattice mismatch. Similarly, the twist observed in our system could be an intrinsic property linked to the film-substrate combination that we chose, exhibiting a high lattice mismatch, too.

Interestingly, both works propose strategies to improve the film quality. While Miyake *et al.* performed high temperature annealing at up to 1700 °C thereby coalescing the misoriented columns [175, 176], Mante *et al.* were able to overgrow the tilted AlN nucleation layer with coalesced AlN of higher quality by increasing the growth temperature after the nucleation step [222]. These, or similar strategies might be a means of improving the structural quality of our thin films, although the limited stability of Mg_3N_2 restricts us to lower annealing temperatures (see following section).

4.5 Linear thermal expansion coefficient of Mg_3N_2

As discussed in Section 3.3, the knowledge of the linear thermal expansion coefficient of a material is important to optimize its epitaxial growth and to understand its fundamental physical properties. Hence, we measured the out-of plane lattice distance in Mg_3N_2 (111) thin films grown on MgO (100) using high-temperature XRD in order to evaluate the lattice expansion as a function of temperature. Although the linear thermal expansion coefficient for Mg_3N_2 was investigated for temperatures below 300 K [223], there is no report for higher temperatures.

Figure 4.20(a) shows the $2\theta/\omega$ scans on the symmetric Mg_3N_2 (222) reflection at temperatures from room temperature to 600 °C. A shift towards lower 2θ angles is observed as the temperature increases, indicating an out-of plane lattice expansion. Note that the diffraction at 600 °C is weakened with respect to the peaks at lower temperature, indicating the beginning of Mg_3N_2 decomposition/evaporation. Indeed, at higher temperatures, no diffraction is observed (diffractograms not shown here), showing that the film is entirely decomposed/evaporated. Given that the Mg_3N_2 thin film was capped with MgO and the measurements were done under nitrogen, this points towards a pure thermal stability problem of the material.

Using Bragg's Equation, one can extract the (222) inter-planar distance as a function of temperature, as shown in Figure 4.20(b). A linear increase is observed, where an average thermal expansion coefficient of $\alpha_T = 1.1 \times 10^{-5}\,\mathrm{K}^{-1}$ can be extracted from the slope of the fit.

As shown in Figure 4.20(c), we extracted the linear thermal expansion coefficient point-by-point, as a function of temperature using

$$\alpha_T = \frac{d_{222}(T+\Delta T) - d_{222}(T)}{\frac{1}{2}[d_{222}(T+\Delta T) + d_{222}(T)]\Delta T}. \tag{4.7}$$

The extracted points complement well the data of Paszkowicz *et al.* [223], leading to the well-known S-behavior of the temperature-dependent thermal expansion coefficient (see Figure A.6 of the Appendix), which is due to the successive occupation of acoustic and optical phonon states, as discussed in Section 3.3.

While the data of Paszkowicz *et al.* reproduce well the low-temperature regime, our data lies already in the saturation regime, where the expansion coefficient changes only slightly as the temperature is increased. Note that we did not apply any correction for the calculation using Equation 4.7, even though the average thermal expansion coefficient of the MgO substrate ($\alpha_T = 1.2 \times 10^{-5}\,\mathrm{K}^{-1}$ [182]) is close to that found for Mg_3N_2. In contrast to pseudomorphic layers, whose thermal expansion is mainly governed by the underlying substrate, our Mg_3N_2 thin films exhibit high defect densities (see Section 4.4), supporting the assumption that they expand mostly independent of the substrate.

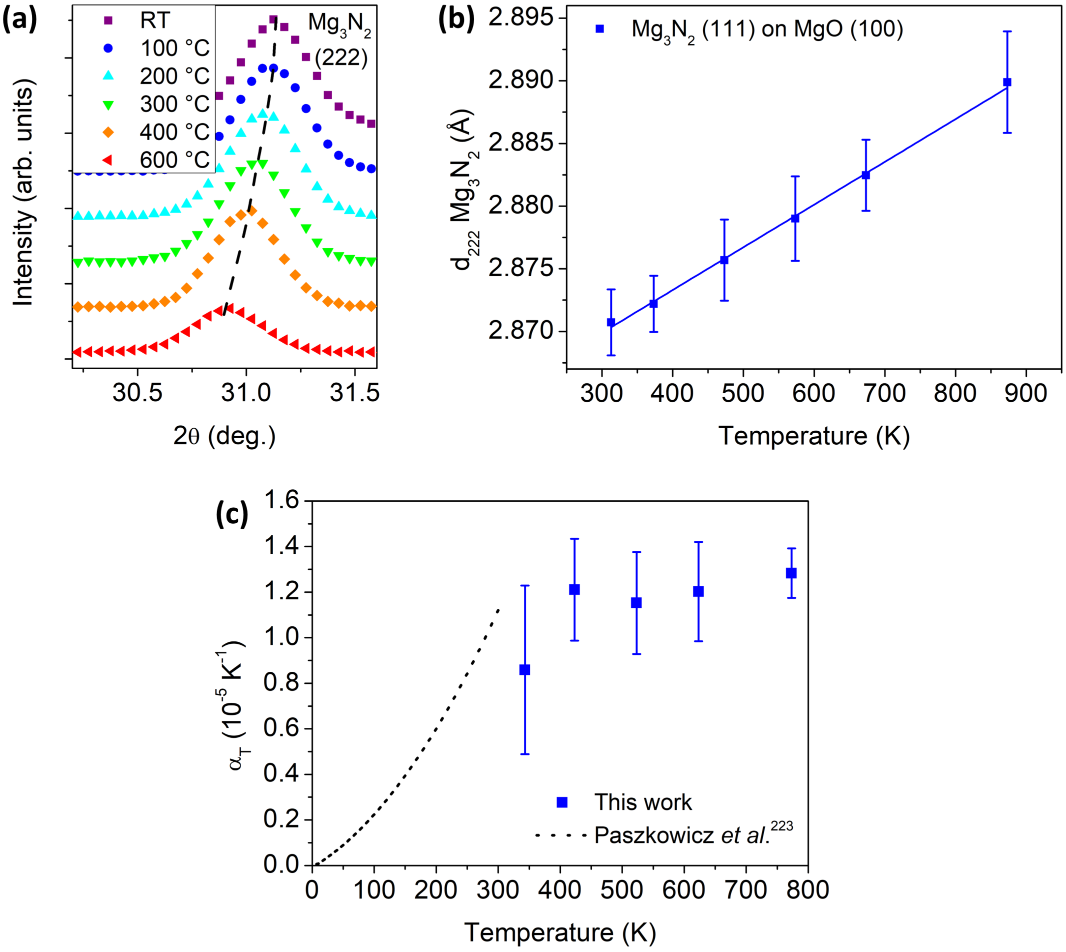

Figure 4.20: (a) High-temperature XRD on a Mg_3N_2 (111) grown on MgO (100), from room temperature (RT) to 600 °C. (b) Mg_3N_2 d_{222} inter-planar distance as a function of temperature, revealing an average of $\alpha_T = 1.1 \times 10^{-5}\,\mathrm{K}^{-1}$. (c) Linear thermal expansion coefficient point by point, extracted from (b).

While the knowledge of the linear thermal expansion coefficient of Mg_3N_2 is interesting from the fundamental point of view, it will be valuable from a practical point of view when we will introduce Mg_3N_2 into heterostructures, as it will allow us to evaluate the lattice mismatch of different materials at growth temperature.

4.6 Optical properties of Mg_3N_2

The measurement of a semiconductor's optical properties is a first step to evaluate its electronic structure. Particularly, the knowledge of the band gap nature (direct or indirect), what is the exact band gap energy and how does the lattice of a crystalline semiconductor influences its luminescent properties is important when it comes to the application in opto-electronics.

Photoluminescence (PL) measurements rely on the spectroscopy of emitted photons after optical pumping, as explained in Section 2.4. These photons are created in the semiconductor itself, hence containing information about its electronic structure. Their creation may include recombinations of free excitons (bound electron-hole pairs due to their coulomb interaction), recombinations involving excitons bound to lattice defects or recombinations after exciton-phonon interactions. Hence, PL is an ideal technique to assess the band structure of a material and to evaluate the type and density of some of the defects present therein.

In transmittance spectroscopy, the light passing through a material is recorded. Due to the absorption of light at higher energies than the optical band gap, one can relatively easily deduce the band gap energy from its absorption coefficient. The advantage of transmittance with respect to PL is that the material to be analyzed does not need to be crystalline and with low defect densities in order to allow radiative emission.

In this chapter we discuss the optical properties of Mg_3N_2 measured by PL and transmittance spectroscopy. Commercial Mg_3N_2 powder (purchased from AlfaAesar, nominal particle size 44 μm) was investigated using PL and diffuse reflectance spectroscopy, and its emission characteristics were compared to that of Uenaka *et al.* [85], who published the only work on Mg_3N_2 PL so far. On the other hand, the optical properties of Mg_3N_2 thin films were determined using transmittance spectroscopy.

4.6.1 Optical properties of commercial Mg_3N_2 micro-particles

The PL spectra measured on Mg_3N_2 micro-particles were analyzed in a temperature range from 9 K to 300 K, where selected PL spectra taken in a large range are presented in Figure 4.21(a). At low temperature, a sharp emission at 3.04 eV is observed, suggesting a direct band gap semiconductor. This emission can be assigned to an excitonic recombination in Mg_3N_2, as will be shown in the following. At lower energy, between 2.7 eV to 3.0 eV, an emission pattern of several equally-spaced peaks is observed, showing an energy separation of ~81 meV. These peaks are assigned to phonon replicas. In the case of Mg_3N_2, they correspond to longitudinal optical (LO) phonon replicas, as determined by Uenaka *et al.* [85]. Finally, around 1.9 eV, a broad peak originating from defect emission occurs. Uenaka *et al.* assumed the defect emission around 1.9 eV to originate from N vacancies, in agreement with DFT calculations predicting them as the most stable defect in Mg_3N_2 [78].

As the temperature is increased, the excitonic peak and the phonon replicas broaden, accompanied by a strong loss in intensity by around two orders of magnitude. This is probably due to a large density of defects, leading to non-radiative recombination at higher temperatures.

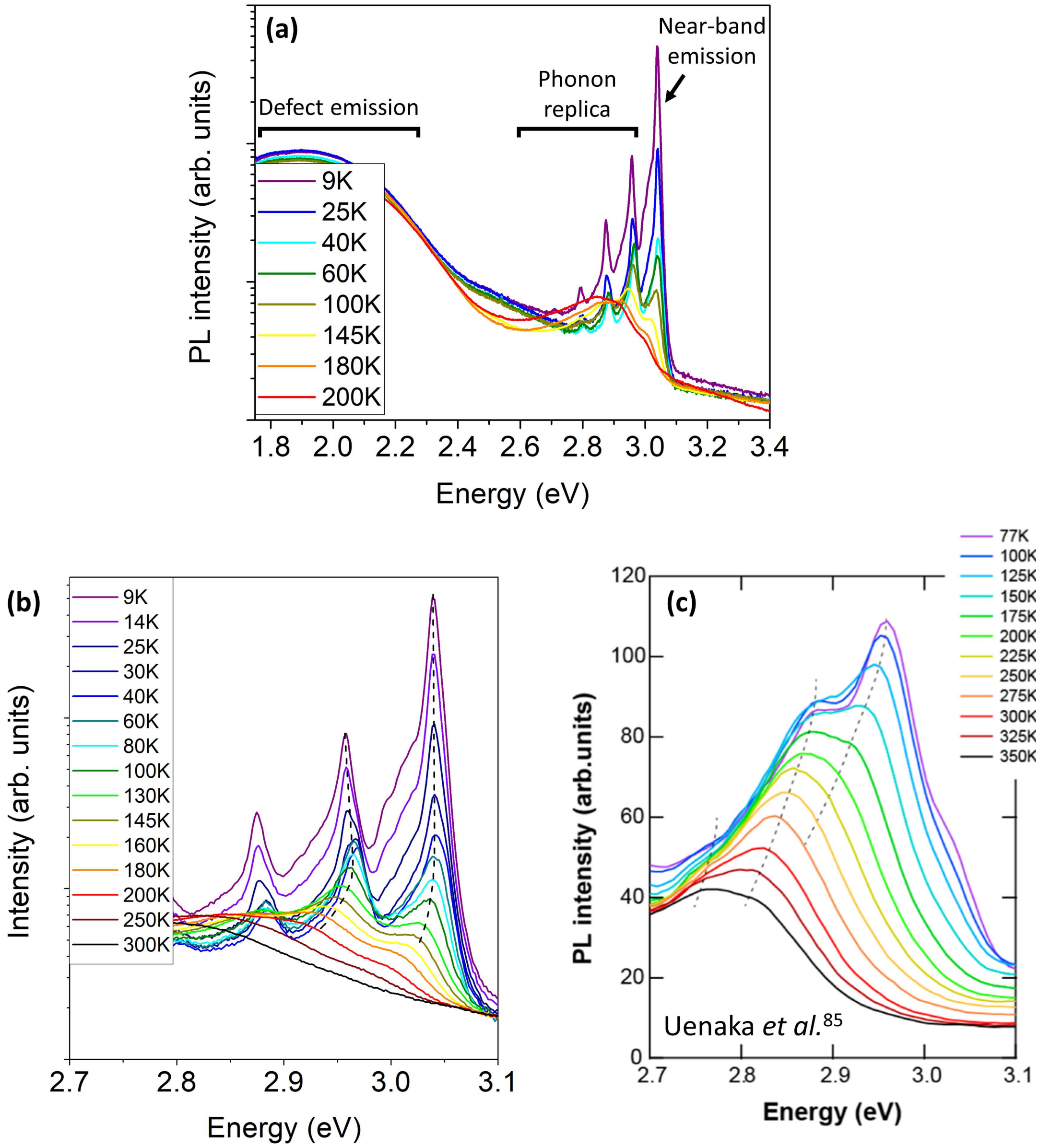

Figure 4.21: (a) Temperature-dependent PL spectra of Mg_3N_2 powder from 9 K to 200 K. (b) Zoom on the luminescence close to the near-band emission, 9 K to 300 K. (c) Literature PL spectra on Mg_3N_2 powder in a temperature range of 77 K to 350 K, reprinted from Uenaka *et al.* [85].

Our results are qualitatively similar to that of Uenaka *et al.*, who found band-to-band emission around 2.95 eV at 77 K, and a defect emission band around ~2 eV. However, when having a closer look [both spectra shown in the same scale in Figure 4.21(b) and (c)], our spectra seem slightly blue-shifted with respect to their PL, from which they extracted a band gap energy of 2.96 eV at zero temperature. To account for this difference (our data leads to 3.04 eV at zero temperature), one has first to consider the different minimum temperatures applied in the measurements. While Uenaka *et al.* measured until a minimum of 77 K (i.e. liquid nitrogen temperature), our data was collected down to 9 K. Hence, their emission spectra, even at the lowest measurement temperature, comprise already significant intensity losses, making it more difficult to interpret the data. Uenaka *et al.* assigned the highest-intensity peak at around 2.95 at 77 K to the free exciton transition, although a low-intensity shoulder at around 3.03 eV is present in their spectra. We observe similar emission in our PL at comparable temperatures (see for instance spectrum at 100 K), although the high-energy shoulder is slightly more pronounced. It turns out that a decrease in temperature below that of liquid nitrogen leads to an increase in intensity of this shoulder, which finally dominates the entire PL. Thus, contrary to Uenaka *et al.*, we assign the peak at 2.95 eV (at 9 K) to the first phonon replica, as discussed below (but not only).

To support this hypothesis, we measured diffuse reflectance in the same temperature range on the Mg_3N_2 powder. In Figure 4.22(a) the spectra at 12 K, 100 K and 200 K are displayed and compared to the PL spectra taken at the same temperatures, reprinted in dashed lines.

A step in reflectance is observed, with the minimum being close to the highest-energy PL peak. This step is linked to the absorption of the Mg_3N_2 by the Kubelka-Munk [224] approximation

$$\frac{\alpha(\lambda)}{S} = \frac{(1-R(\lambda))^2}{2R(\lambda)}, \tag{4.8}$$

where $\alpha(\lambda)$ is the absorption coefficient, $R(\lambda)$ the reflectance and S is the diffuse scattering coefficient.

Hence, a minimum in $R(\lambda)$ corresponds to a maximum in absorption. The fact that the minimum in reflectance coincides with the highest-energy peak found in our PL indicates that this PL emission corresponds to the free exciton transition.

We investigated the evolution of the peak positions in the PL spectra as a function of temperature, together with the data obtained from the diffuse reflectivity measurements, as displayed in Figure 4.22(b). Besides revealing a phonon energy of ~81 meV at low temperature, a clear red-shift is observed for the excitonic transition energy once the temperature exceeds ~75 K. This temperature-dependence of the band gap energy is commonly observed in semiconductors, which is due to the lattice dilatation as well as electron-phonon interactions, as discussed in the following.

Let us now focus on the phonon energy of ~81 meV. If we assume the data of Uenaka *et al.* to correspond to the first LO phonon instead of the free exciton transition, an addition of 81 meV to their temperature-dependent data should lead to an agreement with our results. Indeed, a good match is obtained when shifting the literature results by 81 meV, as indicated by the red dashed line. Furthermore, photoluminescence excitation (PLE) measurements performed too by Uenaka *et al.* lie in the same range, as indicated by red dots, confirming our interpretation.

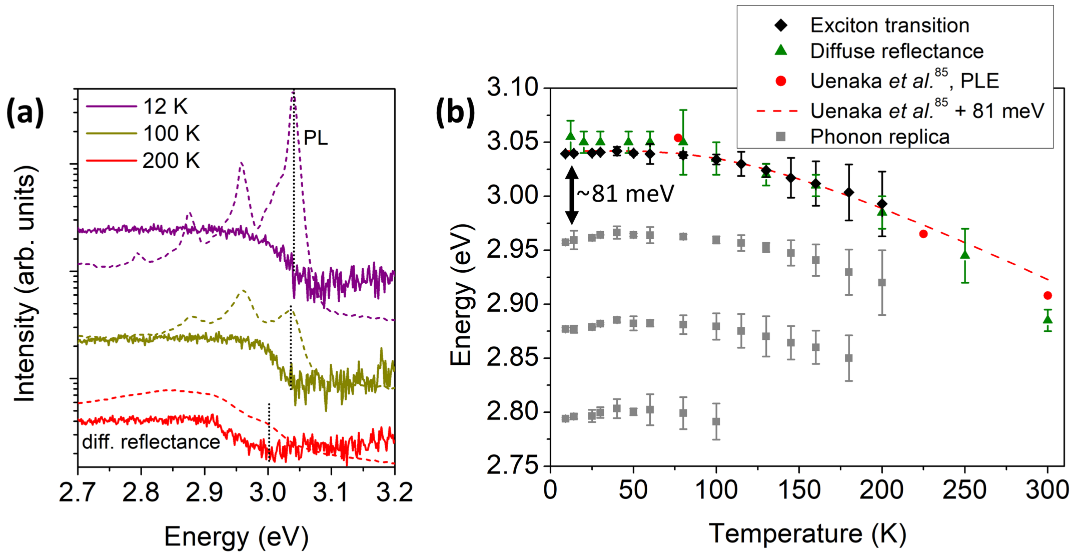

Figure 4.22: (a) Diffuse reflectance spectra on Mg_3N_2 powder at 12 K, 100 K and 200 K, vertically shifted for clarity. The PL spectra recorded at the same temperatures are reprinted as dashed lines for comparison. (b) Temperature dependent peak positions, extracted from PL and diffuse reflectivity spectra and compared to the work of Uenaka *et al.* [85].

4.6.2 Optical properties of Mg_3N_2 thin films

To evaluate the luminescence properties in our thin films, we performed PL measurements at 10 K, as shown in Figure 4.23(a), where we compare the PL of a Mg_3N_2 thin film to the one of commercial Mg_3N_2 micro-particles discussed in the previous section. While the Mg_3N_2 powder shows a sharp luminescence at 3.04 eV, the thin film shows unfortunately only a broad, low-intensity emission located around ~2.8 eV, accompanied by an intense defect emission around 1.8 eV. This poor luminescence, occurring in all measured Mg_3N_2 thin films, attests of a large density of non-radiative recombination centers. These could be point defects (e.g. N vacancies) or grain boundaries, as the grain size in our thin films is in the order of ~10 nm.

To determine the band gap of the material, independent of its crystallinity, we deduced the absorption coefficient from transmittance measurements, as discussed also for Zn_3N_2 in Section 3.5. The transmittance spectra of two Mg_3N_2 thin films recorded at room temperature are displayed in Figure 4.23(b). Above ~3 eV, the transmittance is close to zero, indicating a strong absorption in this spectral range. On the other hand, the transmittance increases below ~3 eV for both thin films, indicating a high transparency in the visible-NIR range and a band edge around this value. Thickness fringes are observed, the transmitting light interfering between the film-substrate interface and the interface of the thin film to air. Using Equation 2.18 allows us to determine the absorption coefficient from the transmittance data, which lies in the 10^5 cm^{-1} range close to the band edge, typical for a direct band gap semiconductor. Hence, $(\alpha E)^2$ as a function of photon energy should reveal a linear increase close to the band edge. An extrapolation of the linear region reveals the optical band gap E_{opt} at the intersection with the horizontal axis.

The Tauc plots for the two Mg_3N_2 thin films are shown in Figure 4.23(c). Two different optical band gaps of 2.75±0.05 eV and 2.84±0.05 eV are observed for the two thin films, slightly lower than the value of 2.90 eV at room temperature found on the micro-particles. Although the large error bars may already account for the slightly different optical band gaps, the difference may be due to some physical mechanisms, as discussed in the following.

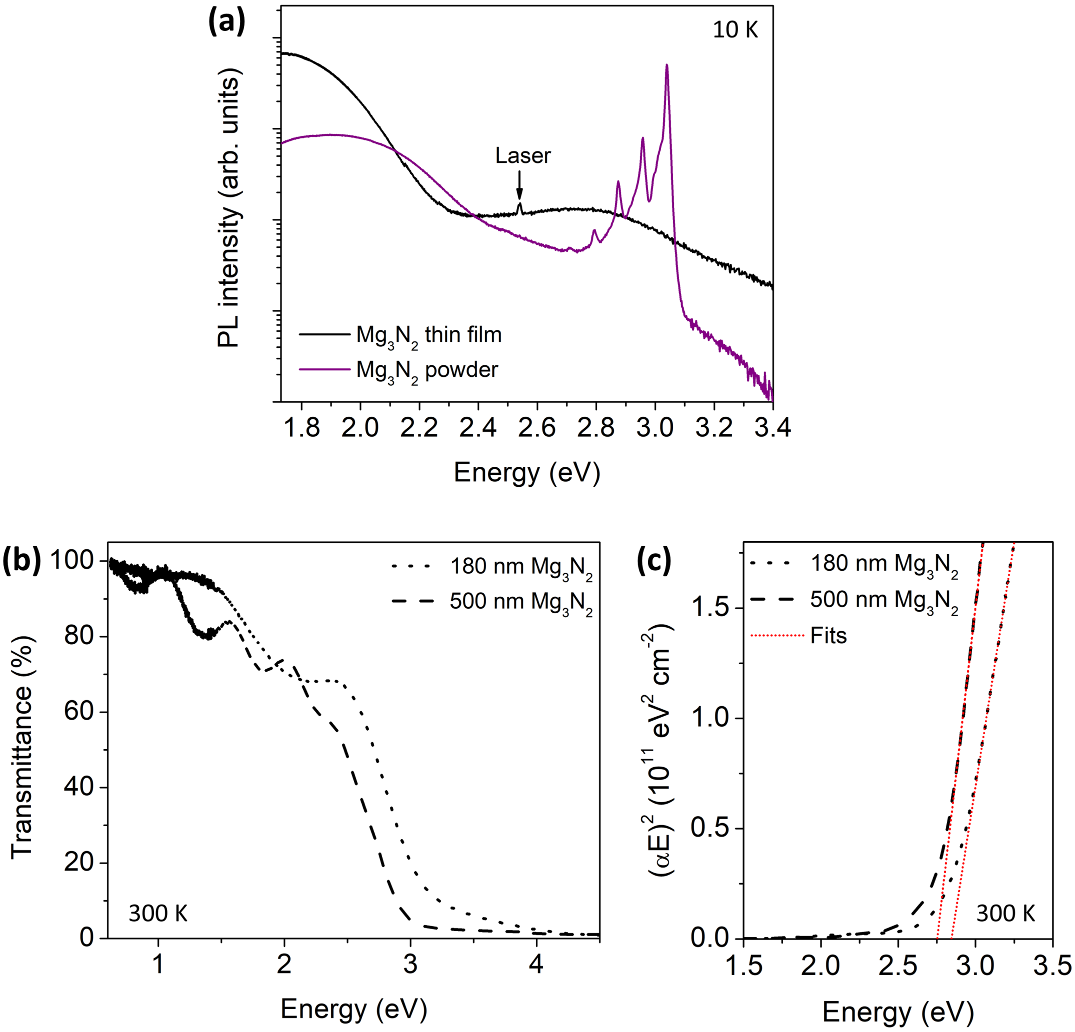

Figure 4.23: (a) PL spectra of an Mg_3N_2 thin film recorded at 10 K and compared to the PL of Mg_3N_2 powder. (b) Transmittance spectra recorded at room temperature on Mg_3N_2 thin films with different thicknesses. The change of noise around 1.4 eV is due to a change of detector (c) Tauc plots extracted from (b), indicating a 2.75 eV band energy for the 180 nm-thick Mg_3N_2 film and a 2.84 eV band energy for the 500 nm-thick Mg_3N_2 film.

We employed temperature dependent transmittance measurements on our epitaxial Mg_3N_2

thin films in order to investigate the evolution of the optical band gap between 10 K and 300 K. Using the same procedure as in Figure 4.23, the optical band gap was extracted from three selected thin films and compared to that of Mg_3N_2 micro-particles, as shown in Figure 4.24. Similarly to the Mg_3N_2 micro-particles, a band gap shrinkage is revealed as the temperature is increased. This behavior is commonly observed in semiconductors and can be reproduced with the empirical Varshni formula [225]

$$E_g(T) = E_0 - \frac{\delta T^2}{T+\beta}, \tag{4.9}$$

where E_0 denotes the band gap energy at 0 K and δ and β are fitting constants.

Using the diffuse reflectivity measurements, we obtain a good agreement to the experiments with values of 3.06 eV, 4.03×10^{-3} eV K^{-1} and 1882 K for E_0, δ and β, respectively. Unfortunately, the values found for the thin films show a large spread and deviate from the ones obtained on the micro-particles. Several reasons for this deviation may be feasible.

As mentioned before, the temperature dependence of the band gap occurs due to electron phonon interactions as well as lattice dilatations. In most cases, the first term dominates the band gap shrinkage, while the second term usually accounts only for a small fraction (e.g. 15 % in ZnO [226]) and is therefore often neglected. Nevertheless, Mg_3N_2 exhibits a large thermal expansion coefficient when compared to other semiconductors (see Section 4.5). Therefore, one may hypothesize that the lattice expansion might account for a non-negligible contribution of the band gap shrinkage. Since the thermal expansion in our thin films might be, despite high defect densities, still influenced by its underlying substrate, this could in principle give rise to a different band gap shrinkage behavior as as compared to the Mg_3N_2 micro-particles. However, if this was the sole reason for the discrepancy, one would expect a systematic deviation in one direction. This is clearly not the case, as shown in Figure 4.24, where we find two thin films with a smaller shrinkage compared to the ~150 meV observed in Mg_3N_2 micro-particles, but also one thin film with a larger band gap shrinkage.

Another possible origin for the discrepancy between Mg_3N_2 thin film and powder samples may arise from Moss-Burstein shifts, as characterized in Section 3.5, the absorption edge being dominated by the actual position of the Fermi level within the conduction band (due to large electron concentrations), leading to an apparent increase of the optical band gap. In Zn_3N_2, for instance, we experimentally observed a band gap spread of ~400 meV due to this phenomenon (see Section 3.5). To investigate this effect on Mg_3N_2 one needs to measure its electrical properties. However, although we deposited contacts on Mg_3N_2 after etching the MgO capping layer (see Figure A.20 of the Appendix), as well as prior to Mg_3N_2 growth, no reliable measurements could be performed, all thin films displaying a very large resistivity. These observations are in agreement with contactless resistivity analyses using inductive RF coils performed with a 20J3 sensor from DELCOM Instruments. While the measurements on Zn_3N_2 layers give values consistent with the resistivity obtained by Hall effect measurements (see Figure A.21 of the Ap-

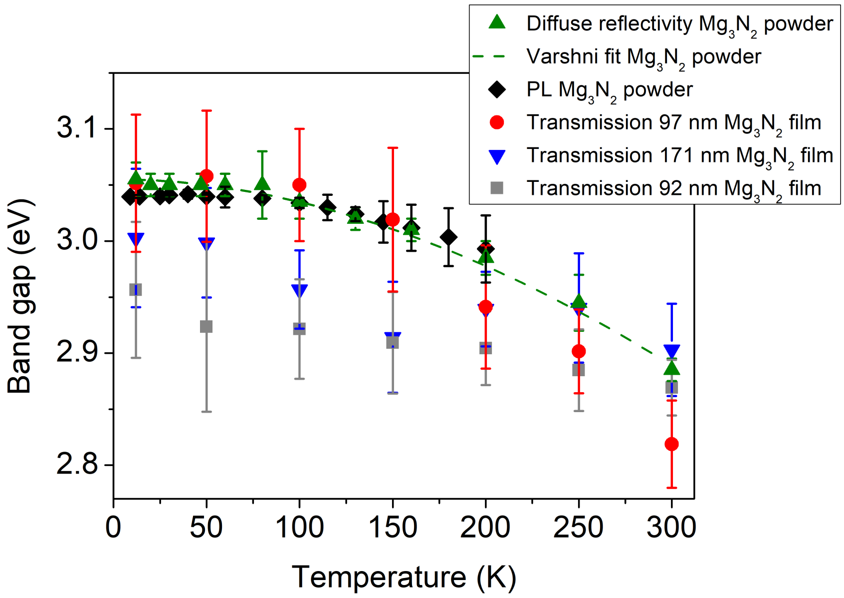

Figure 4.24: Temperature dependence of the optical band gap in Mg_3N_2, extracted from transmittance measurements on thin films and from diffuse reflectance and PL measurements on Mg_3N_2 micro-particles.

pendix), the resistivity in Mg_3N_2 is too high to be measured, giving rise to the assumption that our Mg_3N_2 thin films are insulating. Consequently, the influence of carrier concentration on the optical band gap should be negligible. Still, even if one would assume an influence due to Moss-Burstein shifts in Mg_3N_2, the band gap found in the thin films would be systematically higher than that of the bulk powder, which is not the case either (unless the microparticles themselves are highly doped).

It is well-known that the presence of defects influence the electronic structure of semiconductors and hence, the band gap, since they lead to deformations of the crystalline lattice. Detailed structural investigations (see Section 4.4) revealed high defect densities in our Mg_3N_2 thin films, that led to a complete vanishing of excitonic luminescence [see Figure 4.23(a)]. It seems therefore likely, that these defects also influence the absorption properties of Mg_3N_2, which were accessed indirectly by transmittance measurements. However, such an influence is difficult to quantify and requires further work in this direction.

Overall, our study allows to establish the direct band gap of Mg_3N_2 to lay around 2.9 eV at room temperature using PL and diffuse reflectance measurements on Mg_3N_2 micro-particles. Mg_3N_2 shows LO phonon replica with an energy of 81 meV and relatively strong defect emission around 1.9 eV, possibly attributed to N vacancies. The optical quality of Mg_3N_2 thin films prevents any excitonic luminescence. Hence, further experimental work is required to optimize their optical quality and to unravel the precise electronic structure of Mg_3N_2, including effective masses, band offsets, excitonic properties (e.g. binding energy), as well as vibrational properties.

4.7 Summary

We succeeded to grow epitaxial Mg_3N_2 thin films for the first time in the literature. The reactivity of the thin films in air could be successfully slowed down using polycrystalline MgO capping layers, thereby increasing the thin films' lifetime from a few minutes to several weeks in air. Recently, epitaxial MgO (111) capping layers were grown on the Mg_3N_2 thin films, which may increase their stability further and open a pathway towards MgO/Mg_3N_2 heterostructures.

By changing the MBE growth conditions we could tune the Mg_3N_2 film orientations on MgO (100) substrates, and obtain (100) and (111). Furthermore, Mg_3N_2 (111) thin films were grown on MgO (111) and YSZ (100). These results provide a comprehensive insight into Mg_3N_2 epitaxy. The epitaxial relationships of Mg_3N_2 (111) on MgO (100), YSZ (100) as well as on MgO (111) were identified using various diffraction techniques. Four rotational in-plane domains are observed in Mg_3N_2 (111) films grown on MgO (100) and YSZ (100), as expected due to the different film-substrate rotational symmetries. Interestingly, the domain structure is rotated by 45° when changing the substrate from MgO (100) to YSZ (100). On the other hand, two rotational domains are found for Mg_3N_2 (111) on MgO (111), where the Mg_3N_2 (222) planes are inclined by 3° with respect to the MgO (111) substrate planes.

The structural properties of Mg_3N_2 (111) thin films grown on MgO (100) were analyzed in detail using XRD, as well as plan-view and cross-section TEM. The films consist of well-aligned 10 nm-wide columns at the film-substrate interface, displaying a significant in-plane twist of 2.5°. These columns, identified as the four rotational domains present in these layers, lead to extremely narrow peak widths in XRD rocking curves until a film thickness of 70 nm. As the growth proceeds further, they are overgrown by strongly misoriented Mg_3N_2, giving rise to a concomitant broad contribution in XRD, superimposed to the narrow one and increasing linearly as a function of film thickness. While further optimizations have to be made in order to grow Mg_3N_2 with improved quality, in-depth structural characterization is a necessary tool to understand the microstructure of new semiconductors and, consequently, to develop strategies for achieving such qualities. Among them, the use of different substrate materials, the implementation of buffer layers and/or high-temperature annealing may prevent the formation of multiple rotational domains and reduce the defect density, as observed for other semiconductors displaying similar microstructures.

Another important step towards Mg_3N_2 growth optimization has been made by determining the linear thermal expansion coefficient in a temperature range from 300 K to 800 K, allowing to evaluate its lattice mismatch to possible substrate materials at the actual growth temperatures. While the knowledge of an average thermal expansion coefficient of $\alpha_T = 1.1 \times 10^{-5}\,\mathrm{K}^{-1}$ can be practically used in epitaxy, e.g. in the design of heterostructures, it is also interesting from a fundamental point of view, since lattice dilatation influences the physical properties of Mg_3N_2 whenever temperature variations occur.

The correct determination of the optical properties is important in new materials in order to evaluate their potential application in devices. Furthermore, the luminescence properties of materials are a good indicator for its quality. The optical band gap of Mg_3N_2 was not reported reliably before the beginning of this PhD, which may be linked to its sensitivity to air, complicating its determination. PL and diffuse reflectance measurements on Mg_3N_2 microparticles, for the first time performed close to liquid helium temperature, enabled to establish the Mg_3N_2 band gap in the blue-violet spectral region. A band gap around 3.05 eV was observed at low temperatures, that shrinks down to 2.90 eV at room temperature. Hence, alloying Mg_3N_2 with Zn_3N_2 (having a band gap in the NIR around 1 eV) would allow to cover almost the entire visible wavelength range.

Conclusions and future work

EPITAXY of two earth abundant II-nitride semiconductors, Zn_3N_2 and Mg_3N_2, was achieved by MBE and the structural properties of the thin films were thoroughly investigated. Besides demonstrating the first ever epitaxial Mg_3N_2 thin films, we investigated Mg_3N_2 and Zn_3N_2 epitaxy on several substrates and with two different orientations, (100) and (111). We further performed the first ever TEM measurements on Mg_3N_2, allowing us to deeply understand the film microstructure of MgN_2 (111) thin films on MgO (100) and develop strategies for further improvements of its crystalline quality.

While this work paves the way to more complex heterostructures, such as Zn_3N_2/Mg_3N_2, it also enabled the determination of some of the fundamental physical properties of these materials, whose knowledge is indispensable for the future application in devices. Among them are the linear thermal expansion coefficients of both Zn_3N_2 and Mg_3N_2, which were never measured before above room temperature, as well as their band gap energies, a matter of controversial discussion in the literature.

Besides, we demonstrated that the growth and analysis of highly air-sensitive materials is possible by employing appropriate protective thin films. While MgO capping layers successfully increase the Mg_3N_2 lifetime from a few minutes to a few weeks in air, there is still is room for further improvement, e.g. by changing the capping layer material, its thickness or crystallinity.

From the materials science and the application point of view, it is interesting to investigate the ternary $(Zn_{1-x}Mg_x)_3N_2$ alloy by combining both Zn_3N_2 and Mg_3N_2, due to the possibility to access almost the entire visible spectral range. Preliminary results seem promising: epitaxial $(Zn_{1-x}Mg_x)_3N_2$ growth is currently developed and first thin films in a compositional range up to $x = 0.61$ were already obtained, as shown in Figure 4.25. Their possible integration in II-nitride based semiconductor devices is currently under evaluation.

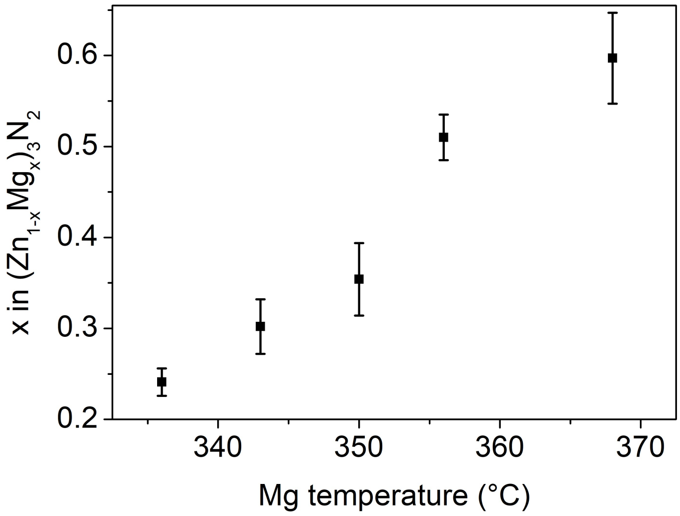

Figure 4.25: Mg concentration x in $(Zn_{1-x}Mg_x)_3N_2$ thin films on MgO (100) determined by x-ray photoelectron spectroscopy, as a function of Mg cell temperature.The Zn temperature was kept constant at 216 °C and films were grown at a substrate temperature of 250 °C, with a nitrogen flow of 1.0 sccm.

In parallel, the growth of ternary ZnO_xN_y and MgO_xN_y alloys by adding oxygen during the Zn_3N_2 or Mg_3N_2 growth is examined. While ternary ZnO_xN_y is already reported in amorphous and polycrystalline phases and applied in TFTs, there is no study on epitaxial ZnO_xN_y. On the other hand, MgO_xN_y thin films are completely unknown up to date. One problem in the epitaxy of these ternary oxynitride materials may be the different anion valence of oxygen and nitrogen, as well as the different crystal structures and lattice parameters of their corresponding binaries, as shown in Figure 4.26. On they other hand, they may offer a higher stability in air than the binary nitrides, since they can be considered as partially oxidized Zn_3N_2 or Mg_3N_2.

Furthermore, the growth of the quarternary $Zn_{1-x}Mg_xO_yN_z$ compound by combining all the binaries MgO, Mg_3N_2, ZnO and Zn_3N_2 is currently evaluated and will be, eventually, further investigated. Although the growth of epitaxial $Zn_{1-x}Mg_xO_yN_z$ may be challenging to achieve due to the different crystal structures of the binaries it consists of, this quarternary compound offers many interesting possibilities for crystal structure engineering. Depending on its stoichiometry, $Zn_{1-x}Mg_xO_yN_z$ may crystallize in one of the three crystal structures shown in Figure 4.26, or even in other, completely different structures. Moreover, a change of composition determines its physical properties. Owing to the large band gap of MgO in the deep-UV range, it should be in principle possible to cover the entire visible spectral range, as well as part of the UV range using $Zn_{1-x}Mg_xO_yN_z$. Besides, the different electrical properties of the binaries shown in Figure 4.26 (MgO and Mg_3N_2 are insulators, ZnO and Zn_3N_2 semiconductors) suggest that compositional changes in $Zn_{1-x}Mg_xO_yN_z$ may enable to control its electrical properties in a large range.

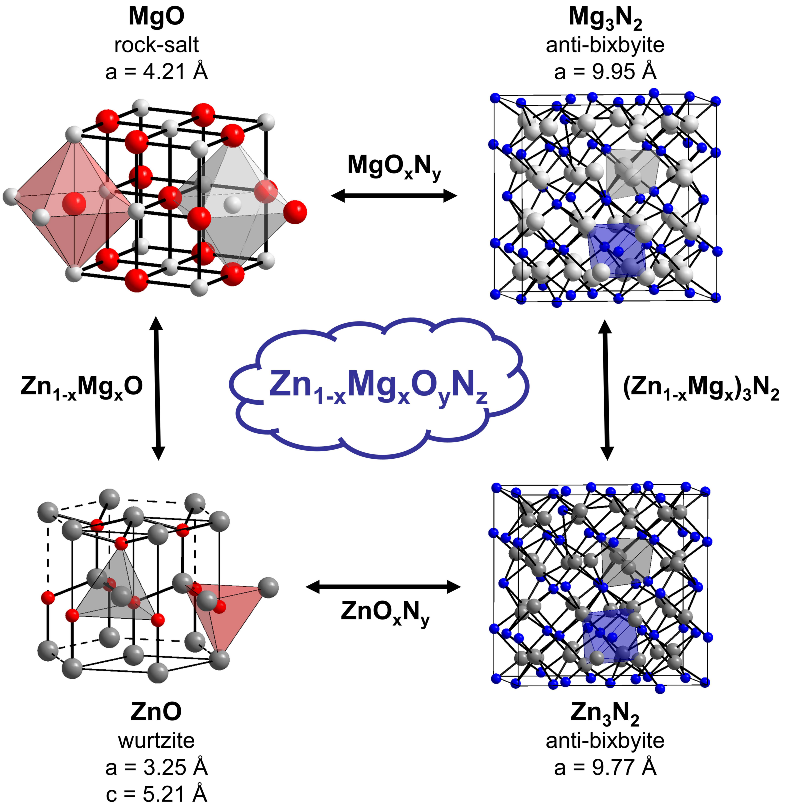

Figure 4.26: Comparison of the crystal structure and lattice parameter of MgO, Mg_3N_2, ZnO and Zn_3N_2. Their potential ternary and quaternary compounds are indicated between the binaries.

Overall, this work demonstrates that research in new semiconductors, such as II-nitrides, includes several optimization steps before reaching high-quality crystalline materials. One of them consists in the development of their epitaxial growth, necessary to investigate precisely their fundamental physical properties in the context of material science, but also to evaluate their application in devices.

Appendix

Fig. A.1: Symmetry properties of Mg_3N_2 and Zn_3N_2.
Fig. A.2: RHEED pattern of a poorly in-plane oriented Zn_3N_2 thin film.
Fig. A.3: Φ scan on asymmetric Zn_3N_2 (440) planes of a (100)-oriented thin film on MgO (100).
Fig. A.4: HRXRD around the Zn_3N_2 (400) reflection grown on MgO (100) (sample F).
Fig. A.5: High-temperature XRD on a Zn_3N_2 (100) thin film on MgO (100).
Fig. A.6: Linear thermal expansion coefficients of MgO and AlN as a function of temperature.
Fig. A.7: Electrical properties of annealed Zn_3N_2 thin films.
Fig. A.8: XRR on a CdO/MgO heterostructure.
Fig. A.9: AFM micrograph of an MgO (111) substrate surface.
Fig. A.10: Schematic atomic structure of an atomic MgO (111) plane.
Fig. A.11: Diffraction pattern simulation of Mg_3N_2 (111) on MgO (100).
Fig. A.12: Diffraction pattern simulation of Mg_3N_2 (111) on MgO (111).
Fig. A.13: Diffraction pattern simulation of MgO (111) on Mg_3N_2 (111).
Fig. A.14: XRR on Mg_3N_2 thin films with different thicknesses, capped with ~50 nm MgO.
Fig. A.15: XRD thickness fringes simulation for 302 nm Mg_3N_2 (222).
Fig. A.16: Comparison of different XRD detector configurations.
Fig. A.17: High-resolution TEM micrographs of the film-substrate interface between Mg_3N_2 (111) and MgO (100).
Fig. A.18: Evolution of the RHEED pattern during Mg_3N_2 (111) growth on MgO (100).
Fig. A.19: Simulation of a plan-view SAED pattern of Mg_3N_2 (111) on MgO (100).
Fig. A.20: Optical microscope images of electrical contacts on Mg_3N_2 thin films.
Fig. A.21: Comparison of Zn_3N_2 resistivity values obtained by Hall effect and by contactless measurements.

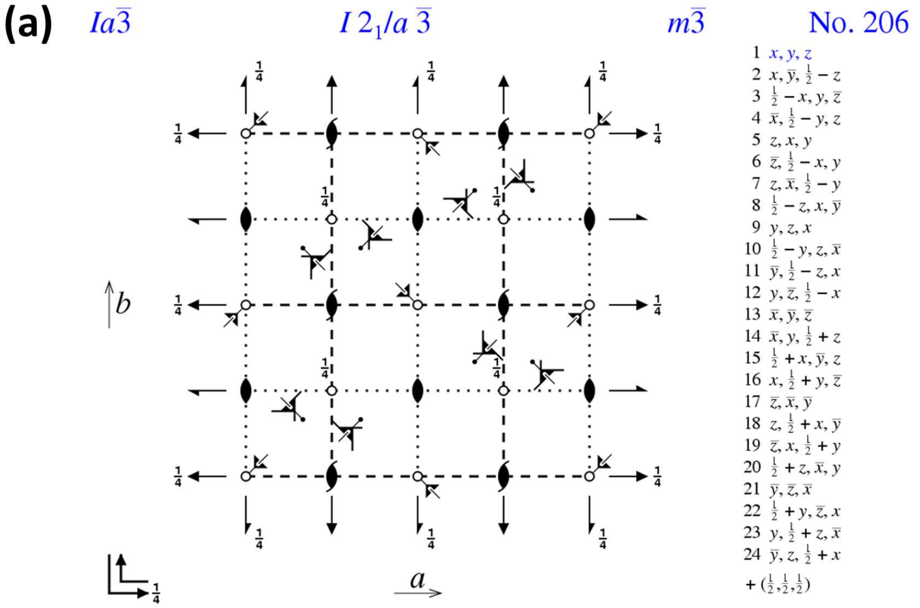

1 x, y, z
2 $x, \bar{y}, \frac{1}{2}-z$
3 $\frac{1}{2}-x, y, \bar{z}$
4 $\bar{x}, \frac{1}{2}-y, z$
5 z, x, y
6 $\bar{z}, \frac{1}{2}-x, y$
7 $z, \bar{x}, \frac{1}{2}-y$
8 $\frac{1}{2}-z, x, \bar{y}$
9 y, z, x
10 $\frac{1}{2}-y, z, \bar{x}$
11 $\bar{y}, \frac{1}{2}-z, x$
12 $y, \bar{z}, \frac{1}{2}-x$
13 $\bar{x}, \bar{y}, \bar{z}$
14 $\bar{x}, y, \frac{1}{2}+z$
15 $\frac{1}{2}+x, \bar{y}, z$
16 $x, \frac{1}{2}+y, \bar{z}$
17 $\bar{z}, \bar{x}, \bar{y}$
18 $z, \frac{1}{2}+x, \bar{y}$
19 $\bar{z}, x, \frac{1}{2}+y$
20 $\frac{1}{2}+z, \bar{x}, y$
21 $\bar{y}, \bar{z}, \bar{x}$
22 $\frac{1}{2}+y, \bar{z}, x$
23 $y, \frac{1}{2}+z, \bar{x}$
24 $\bar{y}, z, \frac{1}{2}+x$
$+ (\frac{1}{2}, \frac{1}{2}, \frac{1}{2})$

(b)

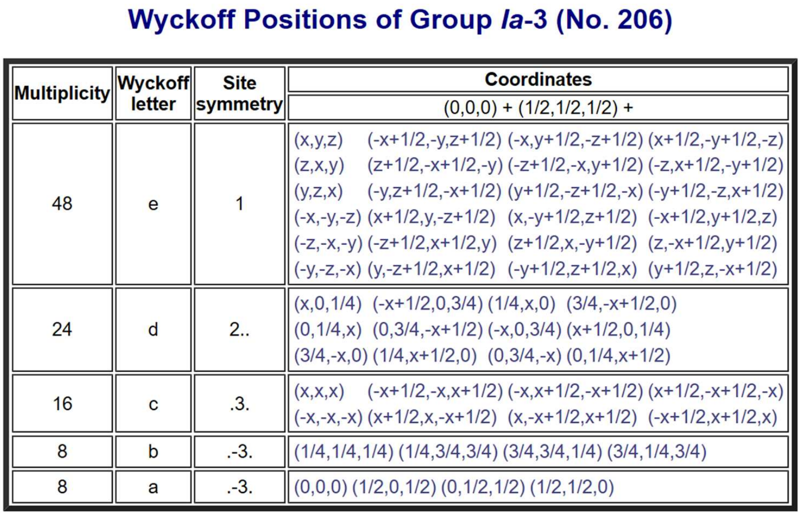

Wyckoff Positions of Group *Ia*-3 (No. 206)

Multiplicity	Wyckoff letter	Site symmetry	Coordinates
			(0,0,0) + (1/2,1/2,1/2) +
48	e	1	(x,y,z) (-x+1/2,-y,z+1/2) (-x,y+1/2,-z+1/2) (x+1/2,-y+1/2,-z) (z,x,y) (z+1/2,-x+1/2,-y) (-z+1/2,-x,y+1/2) (-z,x+1/2,-y+1/2) (y,z,x) (-y,z+1/2,-x+1/2) (y+1/2,-z+1/2,-x) (-y+1/2,-z,x+1/2) (-x,-y,-z) (x+1/2,y,-z+1/2) (x,-y+1/2,z+1/2) (-x+1/2,y+1/2,z) (-z,-x,-y) (-z+1/2,x+1/2,y) (z+1/2,x,-y+1/2) (z,-x+1/2,y+1/2) (-y,-z,-x) (y,-z+1/2,x+1/2) (-y+1/2,z+1/2,x) (y+1/2,z,-x+1/2)
24	d	2..	(x,0,1/4) (-x+1/2,0,3/4) (1/4,x,0) (3/4,-x+1/2,0) (0,1/4,x) (0,3/4,-x+1/2) (-x,0,3/4) (x+1/2,0,1/4) (3/4,-x,0) (1/4,x+1/2,0) (0,3/4,-x) (0,1/4,x+1/2)
16	c	.3.	(x,x,x) (-x+1/2,-x,x+1/2) (-x,x+1/2,-x+1/2) (x+1/2,-x+1/2,-x) (-x,-x,-x) (x+1/2,x,-x+1/2) (x,-x+1/2,x+1/2) (-x+1/2,x+1/2,x)
8	b	.-3.	(1/4,1/4,1/4) (1/4,3/4,3/4) (3/4,3/4,1/4) (3/4,1/4,3/4)
8	a	.-3.	(0,0,0) (1/2,0,1/2) (0,1/2,1/2) (1/2,1/2,0)

Figure A .1: (a) Symmetry operations of the Ia$\bar{3}$ space group (from http://img.chem.ucl.ac.uk/sgp/large/206az1.htm). (b) Wyckoff positions in the Ia$\bar{3}$ space group (from https://www.cryst.ehu.es/cgi-bin/cryst/programs/nph-wp-list).

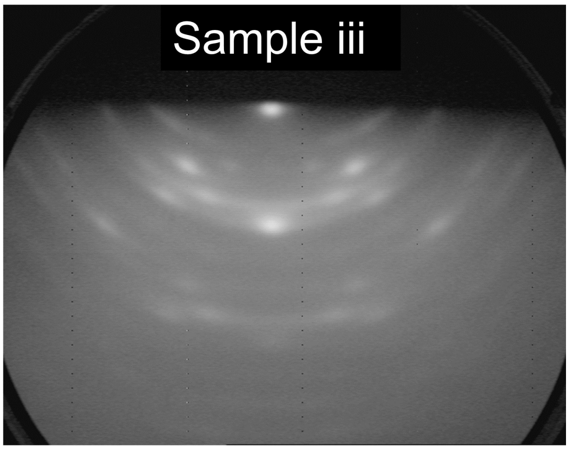

Figure A .2: RHEED pattern of sample iii (44 nm Zn_3N_2 (100) on MgO (100), see Section 3.2.2), showing a poor in-plane orientation of the growing Zn_3N_2 (100) thin film on MgO (100). The growth conditions of this sample are reported in Table 3.2.

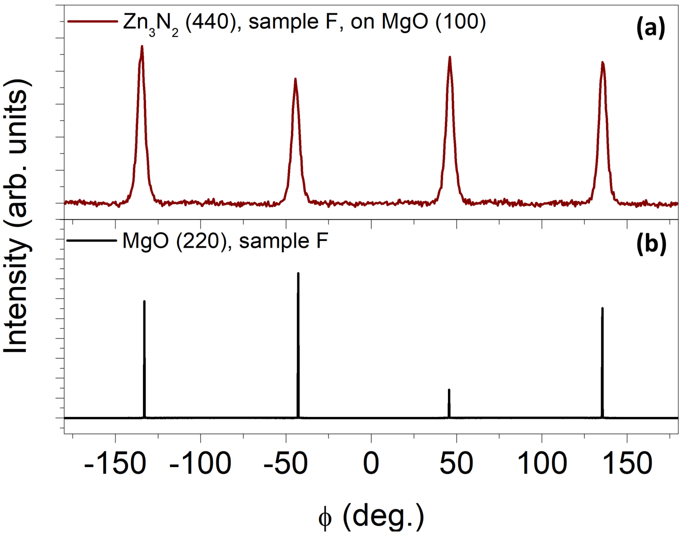

Figure A .3: Φ scan of sample F (Zn_3N_2 (100) on MgO (100), see Section 3.2.3) on (a) Zn_3N_2 (440) planes and (b) MgO (220) planes, measured with a fully open detector. The growth conditions of this sample are reported in Table 3.3.

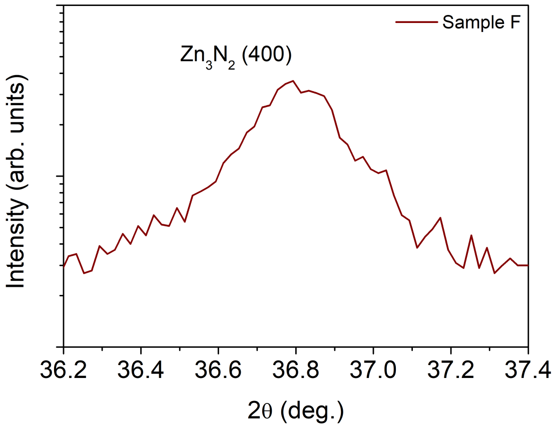

Figure A .4: HRXRD on the symmetric Zn_3N_2 (400) reflection of sample F (Zn_3N_2 (100) on MgO (100), see Section 3.2.4).

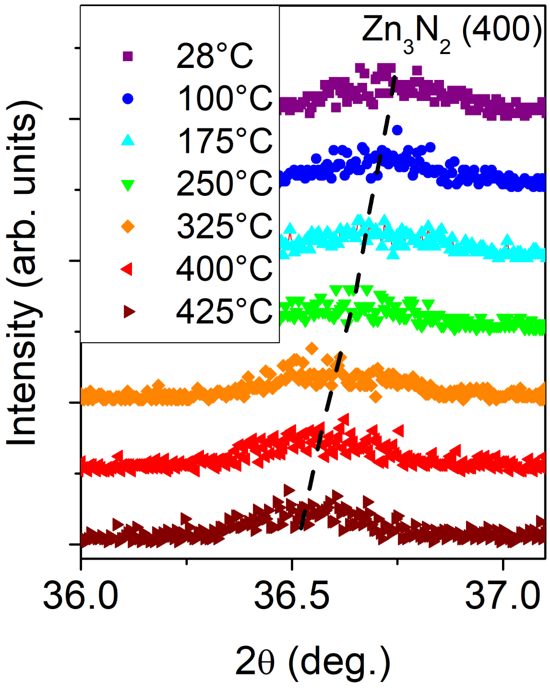

Figure A .5: High-temperature XRD on a Zn_3N_2 (100) thin film grown on MgO (100), as discussed in Section 3.3.

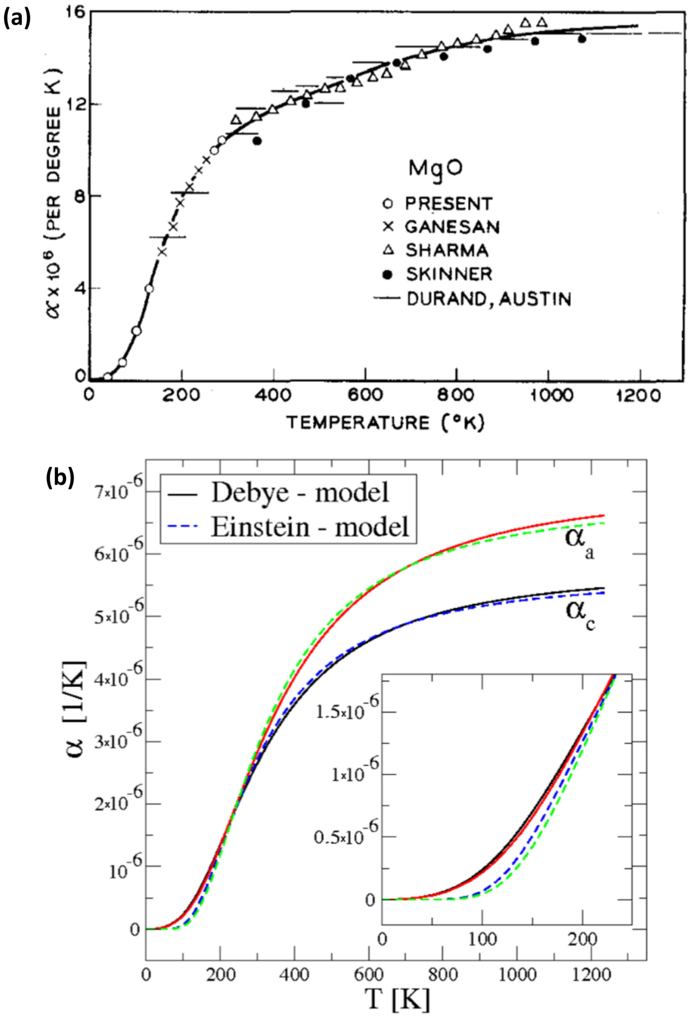

Figure A .6: Linear thermal expansion coefficients of (a) MgO and (b) AlN, showing the well-known S-behavior, as discussed in Section 3.3. Note that the two curves for AlN show the expansion in the crystallographically non-equivalent *a*- and *c*-directions. (a) and (b) are reprinted from [182] and [179], respectively.

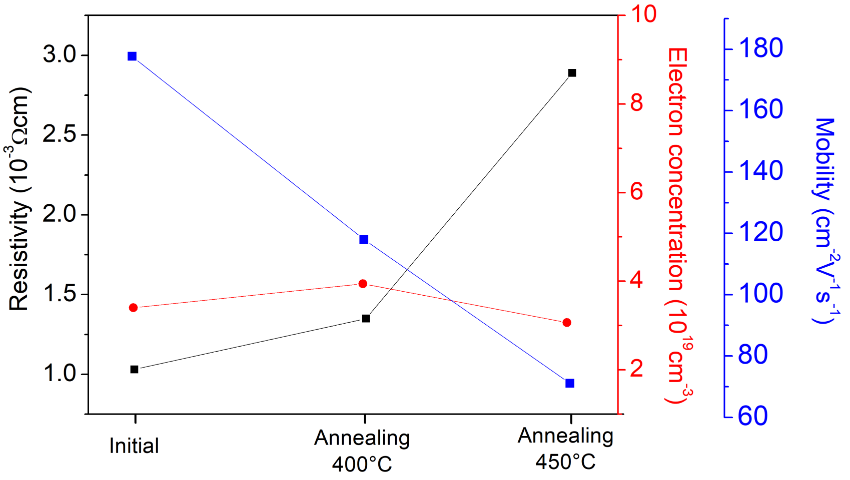

Figure A .7: Hall effect measurements on a Zn_3N_2 thin film annealed for 2 min under nitrogen atmosphere, as discussed in Section 3.4.

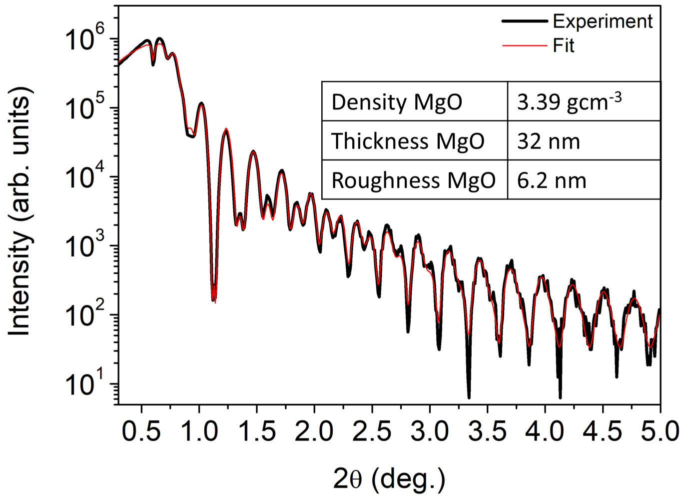

Density MgO	3.39 gcm^{-3}
Thickness MgO	32 nm
Roughness MgO	6.2 nm

Figure A .8: XRR curve of an MgO thin film on CdO on MgO (100), as discussed in Section 4.2.1. The thickness, roughness and density obtained from the fit are indicated for MgO in the inset table. Note that the MgO literature density is 3.58 gcm^{-3}.

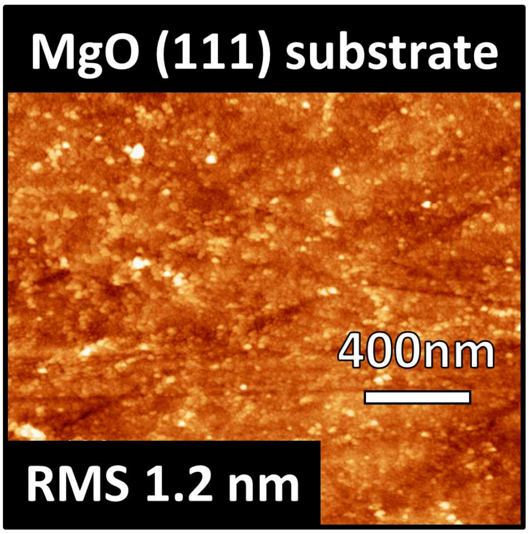

Figure A .9: $2 \times 2\,\mu m^2$ AFM micrograph of an MgO (111) substrate surface, annealed for 2 min at 1150 °C under oxygen atmosphere, as discussed in Section 4.3.2.

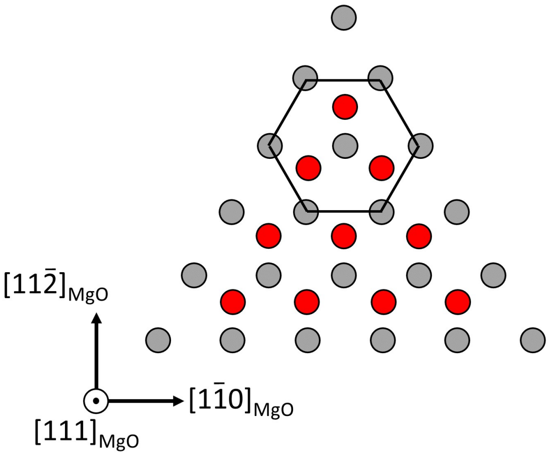

Figure A .10: Schematic atomic structure of an atomic MgO (111) plane, as discussed in Section 4.3.2. The gray dots represent the surface layer (Mg) and the red ones the underlying second atomic layer (O). Although a three-fold symmetry is observed for the substrate half space, the first atomic layer shows six-fold symmetry, as indicated by the black hexagon, leading in our case to the occurrence of two rotational Mg_3N_2 (111) domains.

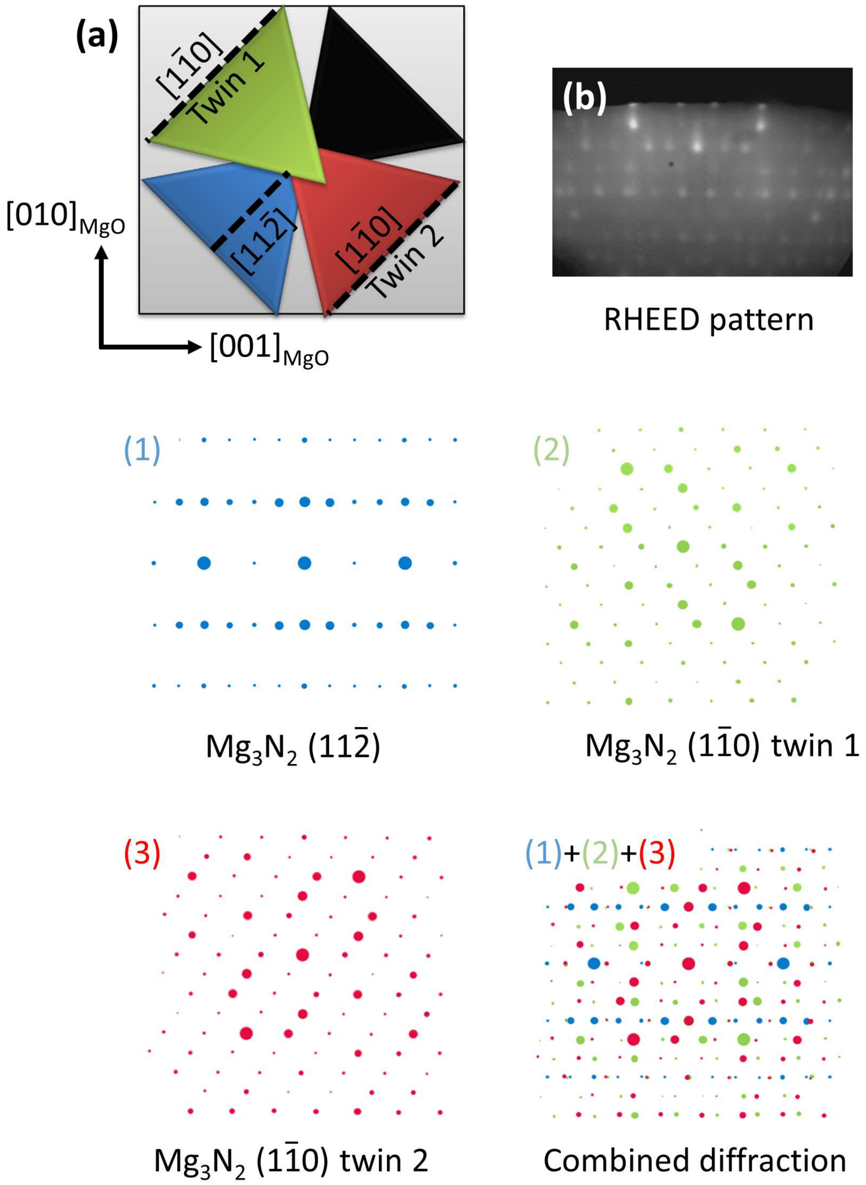

Figure A .11: (a) Schematic representation of the four rotational domains occurring in epitaxial Mg_3N_2 (111) on MgO (100). (b) RHEED pattern of the growing Mg_3N_2 (111) thin film. (1)-(3) denote the simulated diffraction patterns of the different domains indicated in (a). Note that the pattern of the black triangle (not shown here) is the same as that shown in (1). The RHEED is taken along the MgO [011] substrate zone axis. For the discussion see Section 4.3.3.

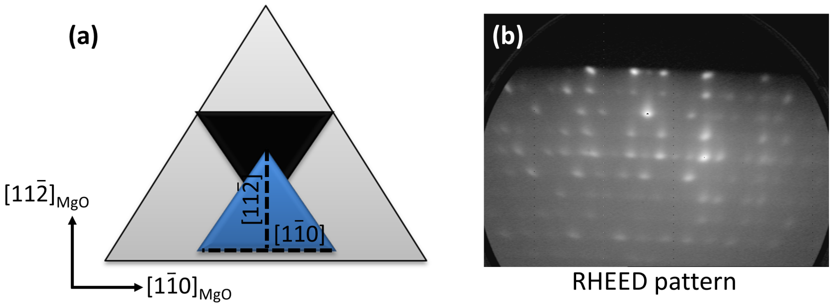

RHEED pattern

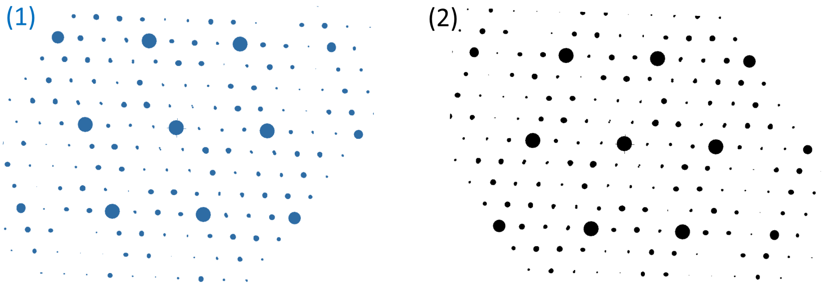

Mg_3N_2 $(1\bar{1}0)$ twin 1

Mg_3N_2 $(1\bar{1}0)$ twin 2

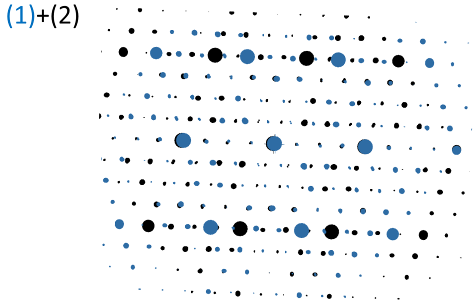

Combined diffraction

Figure A .12: (a) Schematic representation of the two rotational domains occurring in epitaxial Mg_3N_2 (111) on MgO (111). (b) RHEED pattern of the growing Mg_3N_2 (111) thin film. (1) and (2) denote the simulated diffraction patterns of the different domains indicated in (a). The RHEED is taken along the MgO $[0\bar{1}1]$ substrate zone axis. For the discussion see Section 4.3.3.

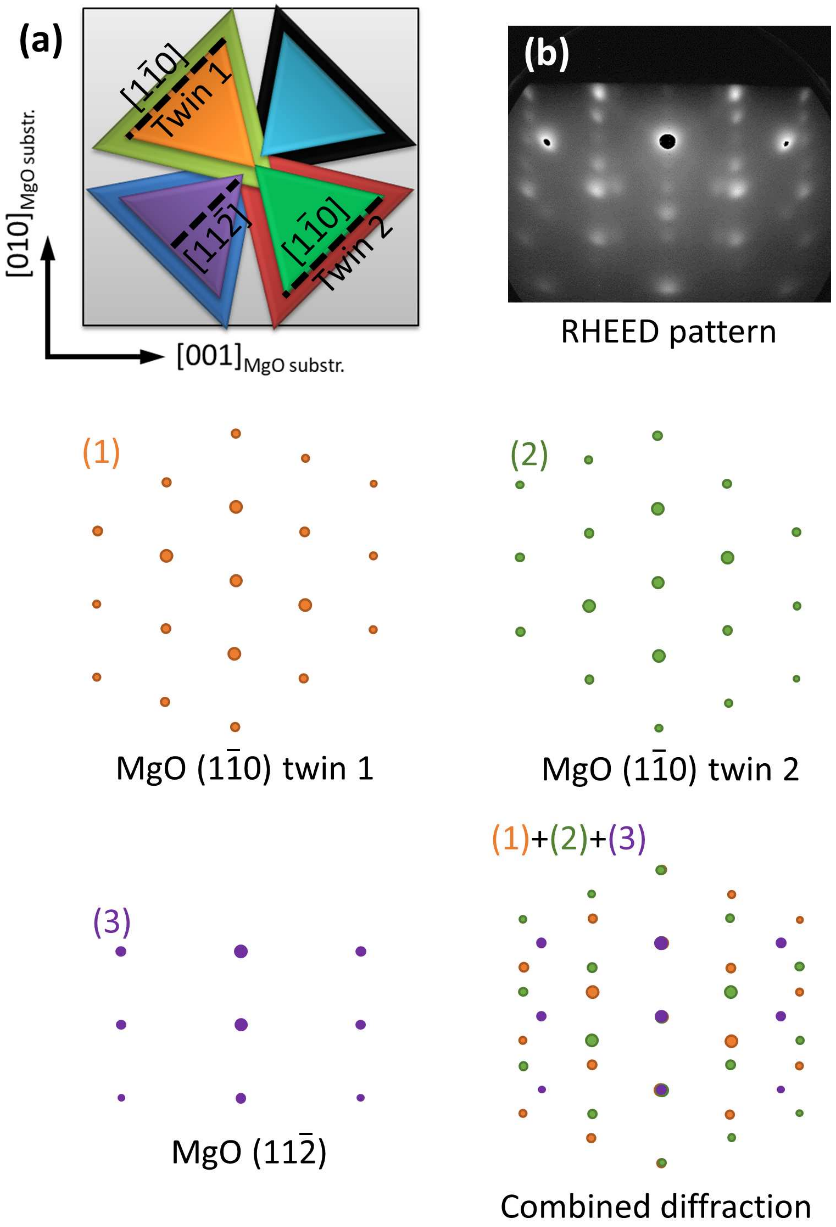

Figure A .13: (a) Schematic representation of the four rotational domains occurring in the epitaxial MgO (111) capping layer, growing coherently on Mg_3N_2 (111). (b) RHEED pattern of the growing MgO (111) thin film. (1)-(3) denote the simulated diffraction patterns of the different domains indicated in (a). Note that the RHEED is taken along the MgO [011] substrate zone axis. For the discussion see Section 4.3.4.

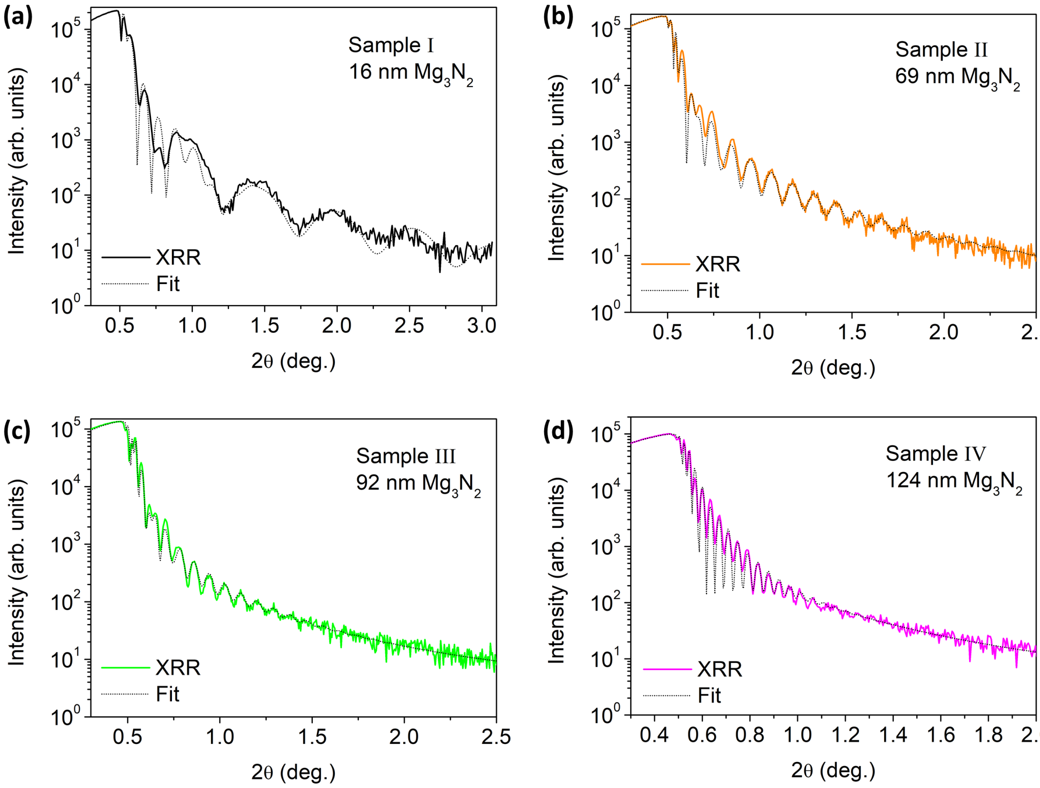

Figure A .14: XRR measurements of Mg_3N_2 (111) thin films grown on MgO (100) with different thicknesses, capped with ~50 nm MgO on (a) sample I, (b) sample II, (c) sample III and (d) sample IV, as indicated in Section 4.4.2.

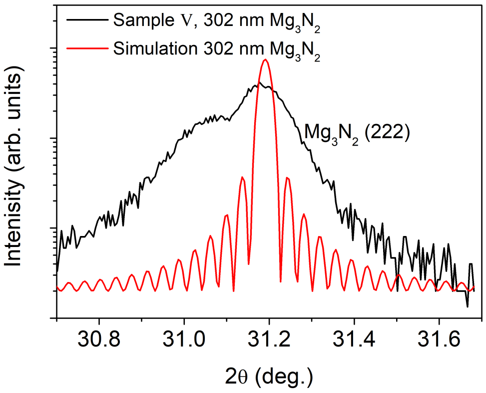

Figure A .15: High-resolution $2\theta/\omega$ scan of sample V (302 nm Mg_3N_2 (111), see Section 4.4.2) compared to a simulated pattern using Equation 3.3.

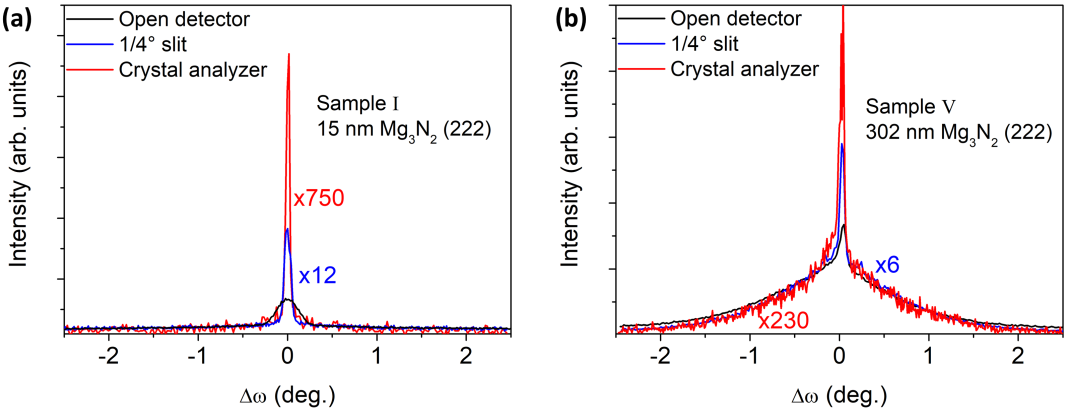

Figure A .16: (a) ω rocking curve around the symmetric (222) reflection of Mg_3N_2 (111) thin films grown on MgO (100). (a) A shows the measurement on sample I (15 nm Mg_3N_2) and (b) on sample V (302 nm Mg_3N_2) using different detector configurations. The FWHM of the narrow contribution increases with a decrease in detector resolution, while the FWHM of the broad contribution stays constant, as discussed in Section 4.4.3.

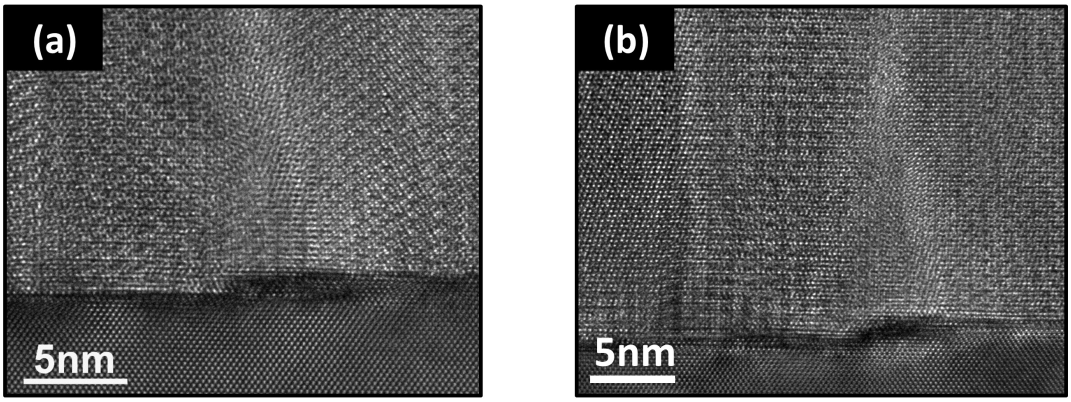

Figure A .17: High-resolution TEM multi-beam micrograph of sample F [Mg_3N_2 (111) on MgO (100)] showing that some of the column boundaries occurring in Mg_3N_2 are linked to steps present in the MgO substrate, as discussed in Section 4.4.4.

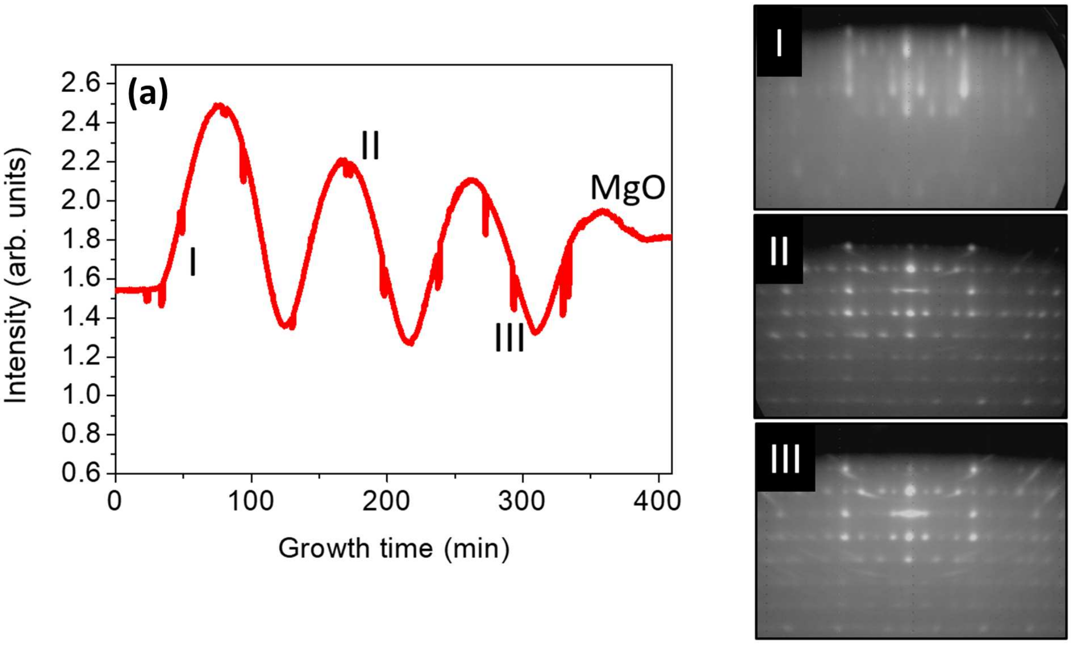

Figure A .18: (a) *In-situ* reflectance using a 650 nm laser during MBE growth of Mg_3N_2 (111) on MgO (100), where I to III indicate the growth times, where the corresponding RHEED patterns I to III (shown on the right-hand side) were recorded. For the discussion see Section 4.4.4.

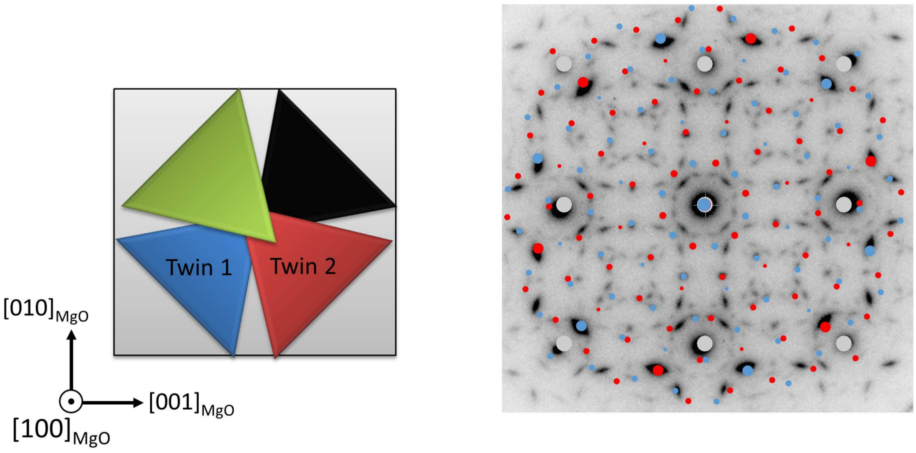

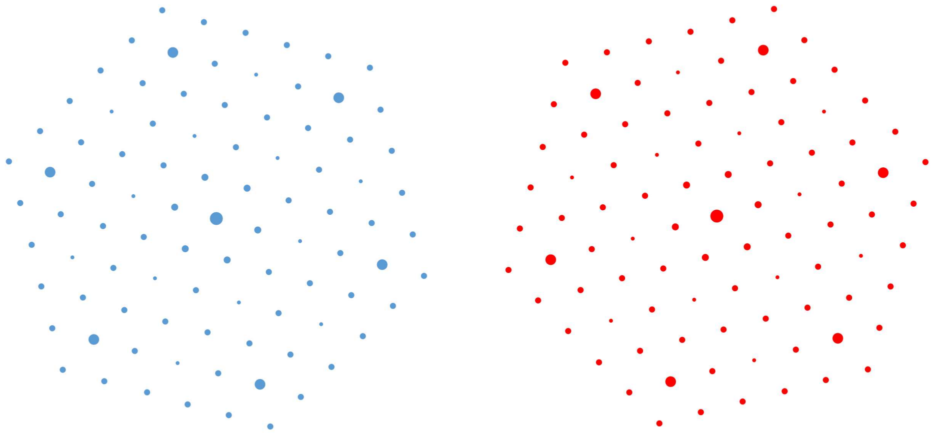

Mg_3N_2 (111) twin 1

Mg_3N_2 (111) twin 2

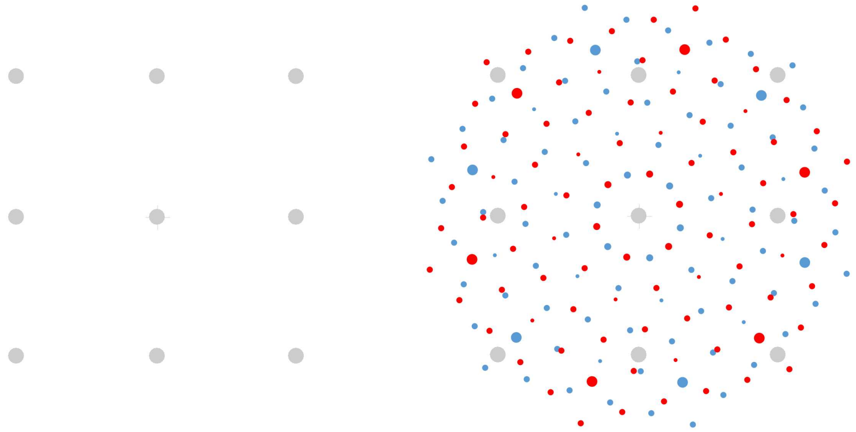

MgO (100)

Combined diffraction

Figure A .19: (a) Schematic representation of the four rotational domains occurring in Mg_3N_2 (111) on MgO (100).(b) Plan-view SAED pattern of sample III [90 nm Mg_3N_2 (111) on MgO (100)], superimposed to the simulated diffraction pattern based on the considerations in (a). (1)-(3) denote the simulated diffraction patterns of the domains indicated in (a) and of the MgO (100) substrate. Note that the diffraction patterns of the rotational domains are identical when rotated around 180°. We show therefore only the simulations of two domains. The experimental pattern contains additional spots due to the overlapping of the Mg_3N_2 thin film and the MgO substrate, causing dynamic diffraction effects. For the discussion see Section 4.4.4.

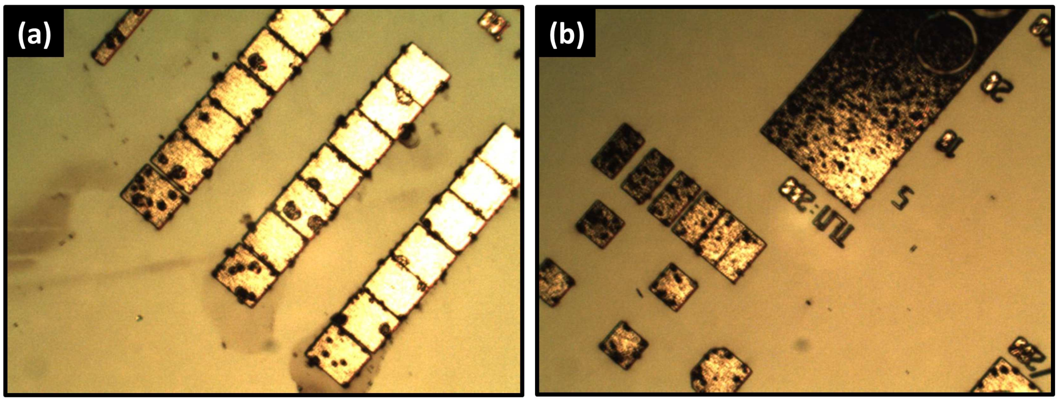

Figure A .20: Optical microscope images of electrical contacts on Mg_3N_2 thin films, as discussed in Section 4.6.

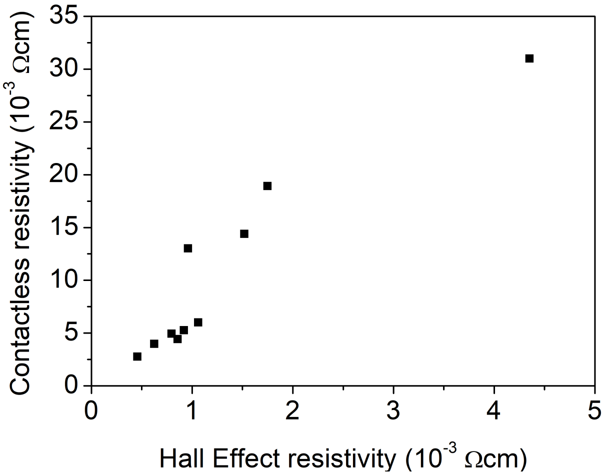

Figure A .21: Contactless resistivity on Zn_3N_2 thin films compared to values obtained by Hall effect measurements, as discussed in Section 4.6. The factor of ~6 between the values is due to the small sample size of 10×20 mm^2, although the instrument to measure the contactless resistivity is designed for minimum 2” samples.

Bibliography

[1] K. Zuse, *The Computer - My Life.* Springer, Berlin, Heidelberg, 1993.

[2] S. W. Oliver Stengel, Alexander van Looy, *Digitalzeitalter - Digitalgesellschaft: Das Ende des Industriezeitalters und der Beginn einer neuen Epoche.* Springer Fachmedien Wiesbaden, 2017.

[3] T. Berners-Lee, "Information management: A proposal."

[4] NobelPrize.org, "The nobel prize in physics 1956."

[5] B. Streetman and S. Banerjee, *Solid state electronic devices.* Boston : Pearson, seventh edition ed., 2016. Includes bibliographical references and index.

[6] W. Adcock, M. Jones, J. Thornhill, and E. Jackson, "Silicon transistor," *Proceedings of the IRE*, vol. 42, p. 1192, 1954.

[7] NobelPrize.org, "The nobel prize in physics 2014."

[8] M. T. Hardy, D. F. Feezell, S. P. DenBaars, and S. Nakamura, "Group III-nitride lasers: a materials perspective," *Materials Today*, vol. 14, no. 9, pp. 408–415, 2011.

[9] A. David and L. A. Whitehead, "LED-based white light," *Comptes Rendus Physique*, vol. 19, no. 3, pp. 169–181, 2018. LEDs: The new revolution in lighting / Les LED : la nouvelle révolution de l'éclairage.

[10] B. N. P. Tyler J. Flack and S. B. Bayne, "GaN technology for power electronic applications: A review," *Journal of Electronic Materials*, vol. 45, pp. 2673–2682, 2016.

[11] A. Zafeiropoulos, A. Gavras, A. Tzanakaki, A. Albanese, A. Kousaridas, A. Weit, B. Sayadi, B. Jou, C. Bernardos, C. Benzaid, C. Mannweiler, D. Camps-Mur, D. Breitgand, D. Estevez, D. Navratil, D. Mi, D. Lopez, D. Klonidis, E. Mutafungwa, E. Fotopoulou, E. Kafetzakis, E. Pateromichelakis, E. Biton, F. Tesema, G. Kalfas, H. Karl, J. Bartelt, J. Gutiérrez, J. Cosmas, J. Thomson, J. Giménez, J. Alcaraz Calero, J. Mangues-Bafalluy, K. Katsalis, L. Gallo, M. Gramaglia, M. Spada, M. Salih, N. Nikaein, N. Jawad, N. Maletic, Ö. Bulakci, P. Demestichas, P. Hasselmeyer, Q. Wang, Q. Wei, R. Ustok, R. Blom, S. Pontarelli, S. Keskin,

S. Salsano, S. Parker, T. Deiss, U. Acar, X. Li, and Y. Zhang, *5G PPP Architecture Working Group: View on 5G Architecture*, vol. Version 3.0. Belgium: European Commission, June 2019.

[12] J. Karlgren, L. E. Fahlén, A. Wallberg, P. Hansson, O. Ståhl, J. Söderberg, and K.-P. Åkesson, "Socially intelligent interfaces for increased energy awareness in the home," in *The Internet of Things* (C. Floerkemeier, M. Langheinrich, E. Fleisch, F. Mattern, and S. E. Sarma, eds.), (Berlin, Heidelberg), pp. 263–275, Springer Berlin Heidelberg, 2008.

[13] M. Auf der Maur, A. Pecchia, G. Penazzi, W. Rodrigues, and A. Di Carlo, "Efficiency drop in green InGaN/GaN light emitting diodes: The role of random alloy fluctuations," *Physical Review Letters*, vol. 116, p. 027401, 2016.

[14] S. Zhang, J. Zhang, J. Gao, X. Wang, C. Zheng, M. Zhang, X. Wu, L. Xu, J. Ding, Z. Quan, and F. Jiang, "Efficient emission of InGaN-based light-emitting diodes: toward orange and red," *Photonics Research*, vol. 8, no. 11, pp. 1671–1675, 2020.

[15] D. Schiavon, M. Binder, M. Peter, B. Galler, P. Drechsel, and F. Scholz, "Wavelength-dependent determination of the recombination rate coefficients in single-quantum-well GaInN/GaN light emitting diodes," *physica status solidi (b)*, vol. 250, no. 2, pp. 283–290, 2013.

[16] Y. Zhao, S. H. Oh, F. Wu, Y. Kawaguchi, S. Tanaka, K. Fujito, J. S. Speck, S. P. DenBaars, and S. Nakamura, "Green semipolar (202-1) InGaN light-emitting diodes with small wavelength shift and narrow spectral linewidth," *Applied Physics Express*, vol. 6, no. 6, p. 062102.

[17] S. Schulz, M. A. Caro, C. Coughlan, and E. P. O'Reilly, "Atomistic analysis of the impact of alloy and well-width fluctuations on the electronic and optical properties of InGaN/GaN quantum wells," *Physical Review B*, vol. 91, p. 035439, 2015.

[18] S. Karpov, "ABC-model for interpretation of internal quantum efficiency and its droop in III-nitride LEDs: A review," *Optical and Quantum Electronics*, vol. 47, pp. 1293–1303, 2015.

[19] R. Eggert, "Minerals go critical," *Nature Chemistry*, vol. 3, pp. 688–691, 2011.

[20] A. Hurd, R. Kelley, R. Eggert, and M. Lee, "Energy-critical elements for sustainable development," *MRS Bulletin*, vol. 37, 04 2012.

[21] H. Deville and H. Caron, "Du magnésium, de sa préparation et de sa volatilisation," *Comptes Rendus*, vol. 47, pp. 394–396, 1857.

[22] P. Vennéguès, M. Leroux, S. Dalmasso, M. Benaissa, P. De Mierry, P. Lorenzini, B. Damilano, B. Beaumont, J. Massies, and P. Gibart, “Atomic structure of pyramidal defects in Mg-doped GaN,” *Physical Review B*, vol. 68, p. 235214, 2003.

[23] B. S. Li, Y. C. Liu, Z. Z. Zhi, D. Z. Shen, Y. M. Lu, J. Y. Zhang, X. W. Fan, R. X. Mu, and D. O. Henderson, “Optical properties and electrical characterization of p-type ZnO thin films prepared by thermally oxiding Zn_3N_2 thin films,” *Journal of Materials Research*, vol. 18, no. 1, p. 8–13, 2003.

[24] C. Wang, Z. Ji, K. Liu, Y. Xiang, and Z. Ye, “p-type ZnO thin films prepared by oxidation of Zn_3N_2 thin films deposited by dc magnetron sputtering,” *Journal of Crystal Growth*, vol. 259, no. 3, pp. 279–281, 2003.

[25] Y. Nakano, T. Morikawa, T. Ohwaki, and Y. Taga, “Electrical characterization of p-type N-doped ZnO films prepared by thermal oxidation of sputtered Zn_3N_2 films,” *Applied Physics Letters*, vol. 88, no. 17, p. 172103, 2006.

[26] E. Kaminska, E. Przezdziecka, A. Piotrowska, J. Kossut, P. Boguslawski, I. Pasternak, R. Jakiela, and E. Dynowska, “Properties of p-type ZnO grown by oxidation of Zn-group-V compounds,” *MRS Proceedings*, vol. 957, pp. 0957–K08–04, 2006.

[27] C.-W. Lin, Y.-P. Song, and S.-C. Chang, “Rapid thermal oxidation of zinc nitride film,” *Japanese Journal of Applied Physics*, vol. 54, no. 4S, p. 04DH06, 2015.

[28] Y. F. Wang, D. Y. Song, L. Li, B. S. Li, A. Shen, and Y. Sui, “Improvement of thermal stability of p-type ZnO:(Al,N) fabricated by oxidizing Zn_3N_2:Al thin films,” *physica status solidi c*, vol. 13, no. 7-9, pp. 585–589, 2016.

[29] B.-S. Li, Z.-Y. Xiao, J.-G. Ma, and Y.-C. Liu, “The p-type ZnO thin films obtained by a reversed substitution doping method of thermal oxidation of Zn_3N_2 precursors,” *Chinese Physics B*, vol. 26, no. 11, p. 117101, 2017.

[30] Y. Jin, N. Zhang, and B. Zhang, “Fabrication of p-type ZnO:N films by oxidizing Zn_3N_2 films in oxygen plasma at low temperature,” *Materials*, vol. 10, no. 3, 2017.

[31] Y. Jin, N. Zhang, H. Xu, and B. Zhang, “Room-temperature ferromagnetism in p-type ZnO:N films prepared by oxidizing Zn_3N_2 in oxygen plasma,” *Applied Physics Letters*, vol. 113, no. 20, p. 202401, 2018.

[32] A. Allenic, W. Guo, Y. Chen, G. Zhao, X. Pan, Y. Che, Z. Hu, and B. Liu, “Synthesis and properties of p-type nitrogen-doped ZnO thin films by pulsed laser ablation of a Zn-rich Zn_3N_2 target,” *Journal of Materials Research*, vol. 22, no. 8, p. 2339–2344, 2007.

[33] E. Aperathitis, V. Kambilafka, and M. Modreanu, “Properties of n-type ZnN thin films as channel for transparent thin film transistors,” *Thin Solid Films*, vol. 518, no. 4, pp. 1036–1039, 2009. Transparent Conductive Oxides.

[34] C. García Núñez, J. L. Pau, E. Ruíz, and J. Piqueras, “Thin film transistors based on zinc nitride as a channel layer for optoelectronic devices,” *Applied Physics Letters*, vol. 101, no. 25, p. 253501, 2012.

[35] S. R. Bhattacharyya, R. Ayouchi, M. Pinnisch, and R. Schwarz, “Transfer characteristic of zinc nitride based thin film transistors,” *physica status solidi c*, vol. 9, no. 3-4, pp. 469–472, 2012.

[36] M. A. Dominguez, J. L. Pau, M. Gómez-Castaño, J. A. Luna-Lopez, and P. Rosales, “High mobility thin film transistors based on zinc nitride deposited at room temperature,” *Thin Solid Films*, vol. 619, pp. 261–264, 2016.

[37] M. A. Dominguez, J. L. Pau, and A. Redondo-Cubero, “Flexible zinc nitride thin-film transistors using spin-on glass as gate insulator,” *IEEE Transactions on Electron Devices*, vol. 65, no. 3, pp. 1014–1017, 2018.

[38] M. Dominguez, J. Pau, O. Obregon, A. Luna, and A. Redondo-Cubero, “Characterization of high mobility inverted coplanar Zinc Nitride thin-film transistors,” *Revista mexicana de fisica*, vol. 65, pp. 10 – 13, 2019.

[39] M. A. Dominguez, J. L. Pau, and A. Redondo-Cubero, “Unusual ambipolar behavior in zinc nitride thin-film transistors on plastic substrates,” *Semiconductor Science and Technology*, vol. 34, no. 5, p. 055002, 2019.

[40] M. Dominguez, J. Pau, A. Orduña-Diaz, and A. Redondo-Cubero, “Comparison of source/drain electrodes in thin-film transistors based on room temperature deposited zinc nitride films,” *Solid-State Electronics*, vol. 156, pp. 12–15, 2019. Publisher Copyright: © 2019 Elsevier Ltd Copyright: Copyright 2019 Elsevier B.V., All rights reserved.

[41] M. A. Dominguez, J. L. Pau, and A. Redondo-Cubero, “Stability of zinc nitride thin-film transistors under positive and negative bias stress,” *Solid-State Electronics*, vol. 171, p. 107841, 2020.

[42] M. Ryu, T. S. Kim, K. S. Son, H. Kim, J. S. Park, J. Seon, S. Seo, S. Kim, E. Lee, H. Lee, S. H. Jeon, S. Han, and S. Y. Lee, “High mobility zinc oxynitride-TFT with operation stability under light-illuminated bias-stress conditions for large area and high resolution display applications,” in *2012 International Electron Devices Meeting*, pp. 5.6.1–5.6.3, 2012.

[43] E. Lee, T. Kim, A. Benayad, J. Hur, G.-S. Park, and S. Jeon, “High mobility and high stability glassy metal-oxynitride materials and devices,” *Scientific Reports*, vol. 6, no. 1, p. 23940, 2016.

[44] E. Lee, A. Benayad, T. Shin, H. Lee, D.-S. Ko, T. S. Kim, K. S. Son, M. Ryu, S. Jeon, and G.-S. Park, "Nanocrystalline ZnON; high mobility and low band gap semiconductor material for high performance switch transistor and image sensor application," *Scientific Reports*, vol. 4, no. 1, p. 4948, 2014.

[45] H.-S. Kim, S. H. Jeon, J. S. Park, T. S. Kim, K. S. Son, J.-B. Seon, S.-J. Seo, S.-J. Kim, E. Lee, J. G. Chung, H. Lee, S. Han, M. Ryu, S. Y. Lee, and K. Kim, "Anion control as a strategy to achieve high-mobility and high-stability oxide thin-film transistors," *Scientific Reports*, vol. 3, no. 1, p. 1459, 2013.

[46] R. D. Shannon, "Revised effective ionic radii and systematic studies of interatomic distances in halides and chalcogenides," *Acta Crystallographica Section A*, vol. 32, no. 5, pp. 751–767, 1976.

[47] M. Grundmann, "Formation of epitaxial domains: Unified theory and survey of experimental results," *physica status solidi (b)*, vol. 248, no. 4, pp. 805–824, 2011.

[48] J. Narayan and B. C. Larson, "Domain epitaxy: A unified paradigm for thin film growth," *Journal of Applied Physics*, vol. 93, no. 1, pp. 278–285, 2003.

[49] R. M. Hazen, "Effects of temperature and pressure on the cell dimension and X-ray temperature factors of periclase," *American Mineralogist*, vol. 61, no. 3-4, pp. 266–271, 1976.

[50] D. Partin, D. Williams, and M. O'Keeffe, "The crystal structures of Mg_3N_2 and Zn_3N_2," *Journal of Solid State Chemistry*, vol. 132, no. 1, pp. 56–59, 1997.

[51] W. M. Yim and R. J. Paff, "Thermal expansion of AlN, sapphire, and silicon," *Journal of Applied Physics*, vol. 45, no. 3, pp. 1456–1457, 1974.

[52] M. B. Pomfret, C. Stoltz, B. Varughese, and R. A. Walker, "Structural and compositiona characterization of yttria-stabilized zirconia: Evidence of surface-stabilized, low-valence metal species," *Analytical Chemistry*, vol. 77, no. 6, pp. 1791–1795, 2005.

[53] T. Oshima and S. Fujita, "(111)-oriented Zn_3N_2 growth on a-plane sapphire substrates by molecular beam epitaxy," *Japanese Journal of Applied Physics*, vol. 45, no. 11, pp. 8653–8655, 2006.

[54] D. Hull and D. Bacon, "Chapter 1 - defects in crystals," in *Introduction to Dislocations (Fifth Edition)* (D. Hull and D. Bacon, eds.), pp. 1–20, Oxford: Butterworth-Heinemann, fifth edition ed., 2011.

[55] S. K. Kamani, "Influence of defects on thermal and mechanical properties of metals," 2009.

[56] S. Joonwichien, S. Matsushima, and N. Usami, “Effects of crystal defects and their interactions with impurities on electrical properties of multicrystalline Si,” *Journal of Applied Physics*, vol. 113, no. 13, p. 133503, 2013.

[57] T. S. Moss, “The interpretation of the properties of indium antimonide,” *Proceedings of the Physical Society. Section B*, vol. 67, no. 10, pp. 775–782, 1954.

[58] E. Burstein, “Anomalous optical absorption limit in InSb,” *Physical Review*, vol. 93, pp. 632–633, 1954.

[59] L. Priester, *Les joints de grains - De la théorie à l’ingénierie*. EDP Sciences, 2006.

[60] C. Darwin, “XXXIV. the theory of x-ray reflexion,” *The London, Edinburgh, and Dublin Philosophical Magazine and Journal of Science*, vol. 27, no. 158, pp. 315–333, 1914.

[61] C. Darwin, “LXXVIII. the theory of x-ray reflexion. part II,” *The London, Edinburgh, and Dublin Philosophical Magazine and Journal of Science*, vol. 27, no. 160, pp. 675–690, 1914.

[62] M. v. Stackelberg and R. Paulus, “Untersuchungen über die Kristallstruktur der Nitride und Phosphide zweiwertiger Metalle,” *Z. Phys. Chem. B*, vol. 22, p. 305, 1933.

[63] S. R. Römer, T. Dörfler, P. Kroll, and W. Schnick, “Group II element nitrides M_3N_2 under pressure: a comparative density functional study,” *physica status solidi (b)*, vol. 246, no. 7, pp. 1604–1613, 2009.

[64] B. Lange, C. Freysoldt, and J. Neugebauer, “Native and hydrogen-containing point defects in mg_3n_2: A density functional theory study,” *Physical Review B*, vol. 81, p. 224109, 2010.

[65] P. John, H. Rotella, C. Deparis, G. Monge, F. Georgi, P. Vennéguès, M. Leroux, and J. Zuniga-Perez, “Crystalline magnesium nitride (Mg_3N_2): From epitaxial growth to fundamental physical properties,” *Physical Review Materials*, vol. 4, p. 054601, 2020.

[66] A. Redondo-Cubero, M. Gomez-Castaño, C. García Núñez, M. Dominguez, L. Vázquez, and J. Pau, “Zinc nitride thin films: basic properties and applications,” p. 101051B, 2017.

[67] “The vibrational spectra and decomposition of α-Calcium Nitride (α-Ca_3N_2) and Magnesium Nitride (Mg_3N_2), journal = Journal of Solid State Chemistry, volume = 137, number = 1, pages = 33-41, year = 1998, issn = 0022-4596, doi = https://doi.org/10.1006/jssc.1997.7672, url = https://www.sciencedirect.com/science/article/pii/S0022459697976726, author = Anton M. Heyns and Linda C. Prinsloo and Klaus-Jürgen Range and Martin Stassen, abstract = alpha-Ca3N2 has been characterized by X-ray powder diffraction and its structure confirmed by a crystal structure refinement with the Rietveld method. Ca3N2and the isostructural Mg3N2crystallize in the anti-bixbyite structure of the mineral (Mn,

Fe)2O3in the body-centered space group ofIa3(T7h), and the general appearance of their infrared and Raman spectra resembles that of the sesquioxides belonging to the same space group. The decomposition ofM3N2(M=alpha-Ca, Mg) intoM(OH)2and NH3, when exposed to the atmosphere, is reported. The presence of NH+4vibrational bands in the decomposition products is explained in terms of the existence of Brønsted acid centers on the surface of the solid. During the initial stages of decomposition, infrared bands characteristic of adsorbed NH3were observed, showing that Lewis centers also exist on the surface. The decomposition product Mg(OH)2has weaker proton-donating centers than Ca(OH)2. The kinetics of the decomposition of Mg3N2, which is a much slower reaction than that of alpha-Ca3N2, has been studied with FT-IR microspectrometry, and it is shown that the formation of Mg(OH)2is a three-dimensional diffusion process while the proton donation by the hydroxide to adsorbed NH3to form NH+4ions is a quasi-first-order reaction.,"

[68] D. R. Lide, "CRC Handbook of Chemistry and Physics," 2004.

[69] D. D. Wagman, W. H. Evans, V. B. Parker, R. H. Schumm, I. Halow, S. M. Bailey, K. L. Churney, and R. L. Nuttall, "Erratum: The NBS tables of chemical thermodynamic properties. selected values for inorganic and C1 and C2 organic substances in SI units," *Journal of Physical and Chemical Reference Data*, vol. 18, no. 4, pp. 1807–1812, 1989.

[70] A. Zakutayev, "Design of nitride semiconductors for solar energy conversion," *Journal of Materials Chemistry A*, vol. 4, pp. 6742–6754, 2016.

[71] P. Wu, *Epitaxial Growth and Optical Properties of* Mg_3N_2*,* Zn_3N_2*, and Alloys.* PhD thesis, 04 2019.

[72] Y. Kumagai, K. Harada, H. Akamatsu, K. Matsuzaki, and F. Oba, "Carrier-induced band-gap variation and point defects in Zn_3N_2 from first principles," *Physical Review Applied*, vol. 8, p. 014015, 2017.

[73] T. Premkumar and R. Vidya, "Crystal and electronic structure studies on transparent conducting nitrides a_3n_2 (A = Mg, Zn and Sn) and Sn_3N_4," *Materials Research Express*, vol. 6, no. 5, p. 055912, 2019.

[74] R. Long, Y. Dai, L. Yu, B. Huang, and S. Han, "Atomic geometry and electronic structure of defects in Zn_3N_2," *Thin Solid Films*, vol. 516, no. 6, pp. 1297–1301, 2008.

[75] N. Jiang, J. Roehl, S. Khare, D. Georgiev, and A. Jayatissa, "An ab initio computational study of pure Zn_3N_2 and its native point defects and dopants Cu, Ag and Au," *Thin Solid Films*, vol. 564, p. 331–338, 2014.

[76] S.-H. Yoo, A. Walsh, D. O. Scanlon, and A. Soon, "Electronic structure and band alignment of zinc nitride, Zn_3N_2," *RSC Advances*, vol. 4, pp. 3306–3311, 2014.

[77] Y. Hinuma, T. Hatakeyama, Y. Kumagai, L. Burton, H. Sato, Y. Muraba, S. Iimura, H. Hiramatsu, I. Tanaka, H. Hosono, and F. Oba, “Discovery of earth-abundant nitride semiconductors by computational screening and high-pressure synthesis,” *Nature Communications*, vol. 7, p. 11962, 2016.

[78] X. Yang, R. Zhao, Y.-H. Ji, H. Shi, and M.-H. Du, “Density functional studies of defects and defect-related luminescence in Mg_3n_2,” *Physical Review Materials*, vol. 4, p. 064604, 2020.

[79] C. Fang, R. Groot, R. Bruls, H. Hintzen, and G. With, “Ab initio band structure calculations of Mg_3N_2 and $MgSiN_2$,” *Journal of Physics: Condensed Matter*, vol. 11, p. 4833, 1999.

[80] A. Mokhtari and H. Akbarzadeh, “Ab initio calculations of the electronic and structural properties of beryllium-, magnesium- and calcium-nitrides,” *Physica B: Condensed Matter*, vol. 337, no. 1, pp. 122–129, 2003.

[81] M. Armenta and A. Reyes-Serrato, “Ab initio determination of the electronic structure of beryllium-, aluminum-, and magnesium-nitrides: A comparative study,” *Physical Review B*, vol. 62, pp. 122–129, 2000.

[82] P. Wu and T. Tiedje, “Molecular beam epitaxy growth and optical properties of Mg_3N_2 films,” *Applied Physics Letters*, vol. 113, 2018.

[83] S. Wang, X. Chen, X. Liu, Z. Chen, X. Liu, J. Zhao, L. Qiu, L. Hou, and Y. Gao, “Synthesis of magnesium nitride films with BN as protective layers by reactive radio-frequency magnetron sputtering,” *Thin Solid Films*, vol. 711, p. 138271, 2020.

[84] K. Toyoura, T. Goto, K. Hachiya, and R. Hagiwara, “Structural and optical properties of magnesium nitride formed by a novel electrochemical process,” *Electrochimica Acta*, vol. 51, pp. 56–60, 2005.

[85] Y. Uenaka and T. Uchino, “Excitonic and defect-related photoluminescence in Mg_3N_2,” *The Journal of Physical Chemistry C*, vol. 118, no. 22, pp. 11895–11901, 2014.

[86] V. Rein, O. Wenzel, R. Popescu, D. Gerthsen, and C. Feldmann, “Liquid-ammonia synthesis of microporous Mg_3N_2 showing intense red-light emission,” *Journal of Materials Chemistry C*, vol. 6, pp. 4450–4456, 2018.

[87] C. García Núñez, J. Pau, M. J. Muñoz, M. Cervera, E. Ruiz, and J. Piqueras, “Influence of air exposure on the compositional nature of Zn_3N_2 thin films,” *Thin Solid Films*, vol. 522, p. 208–211, 2012.

[88] K. Kuriyama, Y. Takahashi, and F. Sunohara, “Optical band gap of Zn_3N_2 films,” *Phys. Rev. B*, vol. 48, pp. 2781–2782, 1993.

[89] N. Yamada, K. Watarai, T. Yamaguchi, A. Sato, and Y. Ninomiya, “Transparent conducting zinc nitride films,” *Japanese Journal of Applied Physics*, vol. 53, no. 5S1, p. 05FX01, 2014.

[90] G. Paniconi, Z. Stoeva, R. Smith, P. Dippo, B. Gallagher, and D. Gregory, “Synthesis, stoichiometry and thermal stability of Zn_3N_2 powders prepared by ammonolysis reactions,” *Journal of Solid State Chemistry*, vol. 181, no. 1, pp. 158–165, 2008.

[91] M. Gómez-Castaño, J. L. Pau, and A. Redondo-Cubero, “Identification of the cubic-to-hexagonal phase transition for the production of stable zinc oxynitride layers,” *CrystEng-Comm*, vol. 20, pp. 3666–3672, 2018.

[92] Y. Wang, T. Ohsawa, Y. Kumagai, K. Harada, F. Oba, and N. Ohashi, “Achieving non-degenerate Zn_3N_2 thin films by near room temperature sputtering deposition,” *Applied Physics Letters*, vol. 115, no. 9, p. 092104, 2019.

[93] P.-C. Wei, S.-C. Tong, C.-M. Tseng, C.-C. Chang, C.-H. Hsu, and J.-L. Shen, “Structural, compositional, and photoluminescence characterization of thermal chemical vapor deposition-grown Zn_3N_2 microtips,” *Journal of Applied Physics*, vol. 116, no. 14, p. 143507, 2014.

[94] C. G. Núñez, J. Pau, M. Hernández, M. Cervera, E. Ruiz, and J. Piqueras, “On the zinc nitride properties and the unintentional incorporation of oxygen,” *Thin Solid Films*, vol. 520, no. 6, pp. 1924–1929, 2012.

[95] C. García Núñez, J. L. Pau, M. J. Hernández, M. Cervera, and J. Piqueras, “On the true optical properties of zinc nitride,” *Applied Physics Letters*, vol. 99, no. 23, p. 232112, 2011.

[96] G. Z. Xing, D. D. Wang, B. Yao, L. F. N. A. Qune, T. Yang, Q. He, J. H. Yang, and L. L. Yang, “Structural and electrical characteristics of high quality (100) orientated-Zn_3N_2 thin films grown by radio-frequency magnetron sputtering,” *Journal of Applied Physics*, vol. 108, no. 8, p. 083710, 2010.

[97] A. Trapalis, I. Farrer, K. Kennedy, A. Kean, J. Sharman, and J. Heffernan, “Temperature dependence of the band gap of zinc nitride observed in photoluminescence measurements,” *Applied Physics Letters*, vol. 111, no. 12, p. 122105, 2017.

[98] A. Trapalis, J. Heffernan, I. Farrer, J. Sharman, and A. Kean, “Structural, electrical, and optical characterization of as grown and oxidized zinc nitride thin films,” *Journal of Applied Physics*, vol. 120, no. 20, p. 205102, 2016.

[99] P. Wu, T. Tiedje, H. Alimohammadi, V. Bahrami-Yekta, M. Masnadi-Shirazi, and C. Wang, “Molecular beam epitaxy growth and optical properties of single crystal Zn_3N_2 films,” *Semiconductor Science and Technology*, vol. 31, no. 10, p. 10LT01, 2016.

[100] T. Suda and K. Kakishita, “Band-gap energy and electron effective mass of polycrystalline Zn_3N_2,” *Journal of Applied Physics*, vol. 99, no. 7, p. 076101, 2006.

[101] M. Futsuhara, K. Yoshioka, and O. Takai, “Structural, electrical and optical properties of zinc nitride thin films prepared by reactive rf magnetron sputtering,” *Thin Solid Films*, vol. 322, no. 1, pp. 274–281, 1998.

[102] A. G. Bhuiyan, A. Hashimoto, and A. Yamamoto, “Indium nitride (InN): A review on growth, characterization, and properties,” *Journal of Applied Physics*, vol. 94, no. 5, pp. 2779–2808, 2003.

[103] X. Cao, Y. Yamaguchi, Y. Ninomiya, and N. Yamada, “Comparative study of electron transport mechanisms in epitaxial and polycrystalline zinc nitride films,” *Journal of Applied Physics*, vol. 119, no. 2, p. 025104, 2016.

[104] M. Gómez-Castaño, A. Redondo-Cubero, L. Vázquez, and J. L. Pau, “Analysis of zinc nitride resistive indicators under different relative humidity conditions,” *ACS Applied Materials & Interfaces*, vol. 8, no. 42, pp. 29163–29168, 2016.

[105] K. Kumar, S. T.S, P. Vengatesh, K. Parasuraman, V. Vishwakarma, and R. D, “Highly transparent zinc nitride thin films by RF magnetron sputtering with enhanced optoelectronic behavior,” *Materials Science and Engineering: B*, vol. 232-235, 11 2018.

[106] E. Lopez-Apreza, J. Arriaga, and D. Olguin, “Ab initio calculation of structural and electronic properties of $Al_xGa_{1-x}N$ and $In_xGa_{1-x}N$ alloys,” *Revista Mexicana de Fisica*, vol. 56, pp. 183–194, 2010.

[107] I. Vurgaftman and J. R. Meyer, “Band parameters for nitrogen-containing semiconductors,” *Journal of Applied Physics*, vol. 94, no. 6, pp. 3675–3696, 2003.

[108] P. Rinke, M. Winkelnkemper, A. Qteish, D. Bimberg, J. Neugebauer, and M. Scheffler, “Consistent set of band parameters for the group-III nitrides AlN, GaN, and InN,” *Physical Review B*, vol. 77, p. 075202, 2008.

[109] P. Carrier and S.-H. Wei, “Theoretical study of the band-gap anomaly of InN,” *Journal of Applied Physics*, vol. 97, no. 3, p. 033707, 2005.

[110] M. Drechsler, D. M. Hofmann, B. K. Meyer, T. Detchprohm, H. Amano, and I. Akasaki, “Determination of the conduction band electron effective mass in hexagonal GaN,” *Japanese Journal of Applied Physics*, vol. 34, no. Part 2, No. 9B, pp. L1178–L1179, 1995.

[111] M. A. Reshchikov and H. Morkoç, “Luminescence properties of defects in GaN,” *Journal of Applied Physics*, vol. 97, no. 6, p. 061301, 2005.

[112] D. Fritsch, H. Schmidt, and M. Grundmann, “Band-structure pseudopotential calculation of zinc-blende and wurtzite AlN, GaN, and InN,” *Physical Review B*, vol. 67, p. 235205, 2003.

[113] M. Goiran, M. Millot, J.-M. Poumirol, I. Gherasoiu, W. Walukiewicz, and J. Leotin, “Electron cyclotron effective mass in indium nitride,” *Applied Physics Letters*, vol. 96, no. 5, p. 052117, 2010.

[114] M. Millot, N. Ubrig, J.-M. Poumirol, I. Gherasoiu, W. Walukiewicz, S. George, O. Portugall, J. Léotin, M. Goiran, and J.-M. Broto, “Determination of effective mass in InN by high-field oscillatory magnetoabsorption spectroscopy,” *Physical Review B*, vol. 83, p. 125204, 2011.

[115] V. Davydov, A. Klochikhin, V. Emtsev, S. Ivanov, V. Vekshin, F. Bechstedt, J. Furthmüller, H. Harima, A. Mudryi, A. Hashimoto, A. Yamamoto, J. Aderhold, J. Graul, and E. Haller, “Band gap of InN and In-rich $In_xGa_{1-x}N$ alloys ($0.36 < x < 1$),” *physica status solidi (b)*, vol. 230, no. 2, pp. R4–R6, 2002.

[116] D. Fritsch, H. Schmidt, and M. Grundmann, “Band dispersion relations of zinc-blende and wurtzite InN,” *Physical Review B*, vol. 69, p. 165204, 2004.

[117] D. F. Swearer, N. R. Knowles, H. O. Everitt, and N. J. Halas, “Light-driven chemical looping for ammonia synthesis,” *ACS Energy Letters*, vol. 4, no. 7, pp. 1505–1512, 2019.

[118] S. 2021, “Production capacity of ammonia worldwide in 2018 and 2030.”

[119] S. Chen, S. Perathoner, C. Ampelli, and G. Centi, “Chapter 2 - electrochemical dinitrogen activation: To find a sustainable way to produce ammonia,” in *Horizons in Sustainable Industrial Chemistry and Catalysis* (S. Albonetti, S. Perathoner, and E. A. Quadrelli, eds.), vol. 178 of *Studies in Surface Science and Catalysis*, pp. 31–46, Elsevier, 2019.

[120] I. Parkin and A. Nartowski, “Solid state metathesis routes to group IIIa nitrides : comparison of Li_3N, NaN_3, Ca_3N_2 and Mg_3N_2 as nitriding agents,” *Polyhedron*, vol. 17, no. 16, pp. 2617–2622, 1998.

[121] H. Ye, X. Liu, and B. Luan, “In situ synthesis of AlN particles in Mg–Al alloy by Mg_3N_2 addition,” *Materials Letters*, vol. 58, no. 19, pp. 2361–2364, 2004.

[122] R. H. Wentorf, “Synthesis of the cubic form of boron nitride,” *The Journal of Chemical Physics*, vol. 34, no. 3, pp. 809–812, 1961.

[123] J. Lu, Z. Z. Fang, Y. J. Choi, and H. Y. Sohn, “Potential of binary lithium magnesium nitride for hydrogen storage applications,” *The Journal of Physical Chemistry C*, vol. 111, no. 32, pp. 12129–12134, 2007.

[124] Y. Kojima, Y. Kawai, and N. Ohba, "Hydrogen storage of metal nitrides by a mechanochemical reaction," *Journal of Power Sources*, vol. 159, no. 1, pp. 81–87, 2006. Special issue including selected papers from the 3rd International Conference on Materials for Advanced Technologies (ICMAT 2005, Singapore, Malaysia) and the Summer School on Synthesis of Nanostructured Materials for Polymer Batteries (Augustów, Poland) together with regular papers.

[125] Y. Nakamori, G. Kitahara, K. Miwa, S. Towata, and O. Shin-ichi, "Reversible hydrogen-storage functions for mixtures of Li_3N and Mg_3N_2," *Applied Physics A*, vol. 80, pp. 1–3, 2005.

[126] U. Ash-Kurlander, G. E. Shter, S. Kababya, A. Schmidt, and G. S. Grader, "Playing hardball with hydrogen: Metastable mechanochemical hydrogenation of magnesium nitride," *The Journal of Physical Chemistry C*, vol. 117, no. 3, pp. 1237–1246, 2013.

[127] C. García Núñez, J. L. Pau, E. Ruíz, and J. Piqueras, "Thin film transistors based on zinc nitride as a channel layer for optoelectronic devices," *Applied Physics Letters*, vol. 101, no. 25, p. 253501, 2012.

[128] E. Maile and R. Fischer, "MOCVD of the cubic zinc nitride phase, Zn_3N_2, using $Zn[N(SiMe_3)_2]_2$ and ammonia as precursors," *Chemical Vapor Deposition*, vol. 11, no. 10, pp. 409–414, 2005.

[129] S. Choopun, R. D. Vispute, W. Yang, R. P. Sharma, T. Venkatesan, and H. Shen, "Realization of band gap above 5.0 eV in metastable cubic-phase $Mg_xZn_{1-x}O$ alloy films," *Applied Physics Letters*, vol. 80, no. 9, pp. 1529–1531, 2002.

[130] P. Wu, X. Cao, T. Tiedje, and N. Yamada, "Bandgap tunable $Zn_{3-3x}Mg_{3x}N_2$ alloy for earth-abundant solar absorber," *Materials Letters*, vol. 236, pp. 649–652, 2019.

[131] A. Welk, A. Reinhardt, O. Herrfurth, T. Schultz, H. von Wenckstern, N. Koch, and M. Grundmann, "Tuning material properties of amorphous zinc oxynitride thin films by magnesium addition," *APL Materials*, vol. 9, no. 2, p. 021120, 2021.

[132] B. A. Joyce and R. R. Bradley, "A study of nucleation in chemically grown epitaxial silicon films using molecular beam techniques I. Experimental methods," *The Philosophical Magazine: A Journal of Theoretical Experimental and Applied Physics*, vol. 14, no. 128, pp. 289–299, 1966.

[133] G. R. Booker and B. A. Joyce, "A study of nucleation in chemically grown epitaxial silicon films using molecular beam techniques," *The Philosophical Magazine: A Journal of Theoretical Experimental and Applied Physics*, vol. 14, no. 128, pp. 301–315, 1966.

[134] B. A. Joyce, R. R. Bradley, and G. R. Booker, “A study of nucleation in chemically grown epitaxial silicon films using molecular beam techniques III. Nucleation rate measurements and the effect of oxygen on initial growth behaviour,” *The Philosophical Magazine: A Journal of Theoretical Experimental and Applied Physics*, vol. 15, no. 138, pp. 1167–1187, 1967.

[135] P. Frigeri, L. Seravalli, G. Trevisi, and S. Franchi, “3.12 – Molecular Beam Epitaxy: An Overview,” in *Comprehensive Semiconductor Science and Technology* (P. Bhattacharya, R. Fornari, and H. Kamimura, eds.), pp. 480 – 522, Amsterdam: Elsevier, 2011.

[136] J. W. Reiner, A. M. Kolpak, Y. Segal, K. F. Garrity, S. Ismail-Beigi, C. H. Ahn, and F. J. Walker, “Crystalline oxides on silicon,” *Advanced Materials*, vol. 22, no. 26-27, pp. 2919–2938, 2010.

[137] J. D. Greenlee, W. L. Calley, W. Henderson, and W. A. Doolittle, “Halide based MBE of crystalline metals and oxides,” *physica status solidi c*, vol. 9, no. 2, pp. 155–160, 2012.

[138] D. Jena, R. Page, J. Casamento, P. Dang, J. Singhal, Z. Zhang, J. Wright, G. Khalsa, Y. Cho, and H. G. Xing, “The new nitrides: layered, ferroelectric, magnetic, metallic and superconducting nitrides to boost the GaN photonics and electronics eco-system,” *Japanese Journal of Applied Physics*, vol. 58, no. SC, p. SC0801, 2019.

[139] L. A. Walsh and C. L. Hinkle, “Van der Waals epitaxy: 2D materials and topological insulators,” *Applied Materials Today*, vol. 9, pp. 504 – 515, 2017.

[140] T. Foxon, *History of MBE*, ch. 1, pp. 1–21. John Wiley and Sons, Ltd, 2019.

[141] T. Rogers, “Molecular beam epitaxy in a high-volume GaAs fab,” *Journal of Crystal Growth*, vol. 311, pp. 1671–1675, 2009.

[142] E. Clapeyron, “Mémoire sur la puissance motrice de la chaleur,” *Journal de l’École polytechnique*, vol. 23, pp. 153–191, 1834.

[143] R. Clausius, “Ueber die bewegende kraft der wärme und die gesetze, welche sich daraus für die wärmelehre selbst ableiten lassen,” *Annalen der Physik*, vol. 155, no. 4, pp. 500–524, 1850.

[144] Y. Zhang, J. R. G. Evans, and S. Yang, “Corrected values for boiling points and enthalpies of vaporization of elements in handbooks,” *Journal of Chemical & Engineering Data*, vol. 56, no. 2, pp. 328–337, 2011.

[145] D. Bowen and B. Tanner, *High Resolution X-Ray Diffractometry And Topography*. CRC Press, 1998.

[146] M. A. Moram and M. E. Vickers, “X-ray diffraction of III-nitrides,” *Reports on Progress in Physics*, vol. 72, no. 3, p. 036502, 2009.

[147] W. L. Bragg, "The structure of some crystals as indicated by their diffraction of x-rays," *Proceedings of the Royal Society of London. Series A, Containing Papers of a Mathematical and Physical Character*, vol. 89, no. 610, pp. 248–277, 1913.

[148] W. Friedrich, P. Knipping, and M. v. Laue, "Interferenz-Erscheinungen bei Röntgenstrahlen," vol. 14, 1912.

[149] P. P. Ewald, "Zur Begründung der Kristalloptik," *Annalen der Physik*, vol. 359, no. 23, pp. 519–556, 1917.

[150] M. v. Laue, "Röntgenstrahlinterferenz und Mischkristalle," *Annalen der Physik*, vol. 361, no. 15, pp. 497–506, 1918.

[151] S. Nishikawa and S. Kikuchi, "Diffraction of cathode rays by calcite," *Nature*, vol. 122, no. 3080, pp. 726–726, 1928.

[152] J. R. Arthur and J. J. LePore, "GaAs, GaP, and $GaAs_xP_{1-x}$ epitaxial films grown by molecular beam deposition," *Journal of Vacuum Science and Technology*, vol. 6, no. 4, pp. 545–548, 1969.

[153] W. Braun, *Applied RHEED: Reflection High-Energy Electron Diffraction During Crystal Growth.* Berlin, Heidelberg: Springer Berlin Heidelberg, 1999.

[154] E. Ruska and M. Knoll, "Die magnetische Sammelspule für schnelle Elektronenstrahlen," *Zeitschrift für technische Physik*, vol. 12, pp. 389–400, 1931.

[155] E. Ruska, "Über Fortschritte im Bau und in der Leistung des magnetischen Elektronenmikroskops," *Zeitschrift für Physik*, vol. 87, no. 9, pp. 580–602, 1934.

[156] J. P. for Nobelprize.org, "The nobel prize in physics 1986, perspectives – life through a lens."

[157] M. M. Freundlich, "Origin of the electron microscope," *Science*, vol. 142, no. 3589, pp. 185–188, 1963.

[158] D. Muller, "Structure and bonding at the atomic scale by scanning transmission electron microscopy," *Nature materials*, vol. 8, pp. 263–70, 05 2009.

[159] G. Binnig, C. F. Quate, and C. Gerber, "Atomic force microscope," *Physical Review Letters*, vol. 56, pp. 930–933, 1986.

[160] M. Yasaka, "X-ray thin-film measurement techniques," *The Rigaku Journal*, vol. 26, no. 2, pp. 1–9, 2010.

[161] S. A. Veldhuis, P. Brinks, T. M. Stawski, O. F. Göbel, and E. Johan, "A facile method for the density determination of ceramic thin films using x-ray reflectivity," *Journal of sol-gel science and technology*, vol. 71, no. 1, pp. 118–128, 2014.

[162] M. Björck and G. Andersson, "*GenX*: an extensible X-ray reflectivity refinement program utilizing differential evolution," *Journal of Applied Crystallography*, vol. 40, no. 6, pp. 1174–1178, 2007.

[163] I. F. Almog, M. S. Bradley, and V. Bulović, "The Lorentz oscillator and its applications," 2011.

[164] S. Perkowitz, *Optical Characterization of Semiconductors.* Techniques of Physics, Boston: Academic Press, 1993.

[165] M. Grundmann, *The Physics of Semiconductors.* 2010.

[166] M. Bouguer, *Essai d'optique sur la gradation de la lumière.* Paris: Claude Jambert, 1729.

[167] J. H. Lambert, *Photometria, sive de mensura et gradibus luminis, colorum et umbrae.* Augsburg: Sumptibus Vidae Eberhardi Klett, 1760.

[168] A. Beer, "Bestimmung der Absorption des rothen Lichts in farbigen Flüssigkeiten," *Annalen der Physik und Chemie*, vol. 162, no. 5, pp. 78–88, 1852.

[169] J. Tauc, R. Grigorovici, and A. Vancu, "Optical properties and electronic structure of amorphous germanium," *physica status solidi (b)*, vol. 15, no. 2, pp. 627–637, 1966.

[170] L. J. van der Pauw, "A method of measuring specific resistivity and Hall effect of discs of arbitrary shape," *Philips Research Reports*, vol. 13, pp. 1–9, 1958.

[171] E. H. Hall, "On a new action of the magnet on electric currents," *American Journal of Mathematics*, vol. 2, no. 3, pp. 287–292, 1879.

[172] S. Novikov, A. Kent, and C. Foxon, "Molecular beam epitaxy as a growth technique for achieving free-standing zinc-blende GaN and wurtzite $Al_xGa_{1-x}N$," *Progress in Crystal Growth and Characterization of Materials*, vol. 63, no. 2, pp. 25–39, 2017.

[173] C. Noguera, *Physics and Chemistry at Oxide Surfaces.* Cambridge University Press, 1996.

[174] C. Lichtensteiger, "*InteractiveXRDFit*: a new tool to simulate and fit X-ray diffractograms of oxide thin films and heterostructures," *Journal of Applied Crystallography*, vol. 51, no. 6, pp. 1745–1751, 2018.

[175] H. Miyake, C.-H. Lin, K. Tokoro, and K. Hiramatsu, "Preparation of high-quality AlN on sapphire by high-temperature face-to-face annealing," *Journal of Crystal Growth*, vol. 456, pp. 155–159, 2016. Proceeding of the 9th International Workshop on Bulk Nitride Semiconductors.

[176] S. Xiao, R. Suzuki, H. Miyake, S. Harada, and T. Ujihara, "Improvement mechanism of sputtered AlN films by high-temperature annealing," *Journal of Crystal Growth*, vol. 502, pp. 41–44, 2018.

[177] S. R. Lee, A. M. West, A. A. Allerman, K. E. Waldrip, D. M. Follstaedt, P. P. Provencio, D. D. Koleske, and C. R. Abernathy, “Effect of threading dislocations on the Bragg peakwidths of GaN, AlGaN, and AlN heterolayers,” *Applied Physics Letters*, vol. 86, no. 24, p. 241904, 2005.

[178] M. Leszczynski, T. Suski, H. Teisseyre, P. Perlin, I. Grzegory, J. Jun, S. Porowski, and T. D. Moustakas, “Thermal expansion of gallium nitride,” *Journal of Applied Physics*, vol. 76, no. 8, pp. 4909–4911, 1994.

[179] H. Kroencke, s. Figge, D. Hommel, and B. Epelbaum, “Determination of the temperature dependent thermal expansion coefficients of bulk AlN by HRXRD,” *Acta Physica Polonica A*, vol. 114, pp. 1193–, 2008.

[180] L. Fengchao and Z. Bin, “The linear coefficient of thermal expansion of silicon at room temperature,” *Powder Diffraction*, vol. 6, no. 3, p. 147–152, 1991.

[181] L. Fengchao, “Confirmation of the new technique for measuring the linear thermal expansion of silicon,” *Powder Diffraction*, vol. 8, no. 1, p. 36–38, 1993.

[182] G. K. White and O. L. Anderson, “Grüneisen parameter of magnesium oxide,” *Journal of Applied Physics*, vol. 37, no. 1, pp. 430–432, 1966.

[183] H. Hayashi, T. Saitou, N. Maruyama, H. Inaba, K. Kawamura, and M. Mori, “Thermal expansion coefficient of yttria stabilized zirconia for various yttria contents,” *Solid State Ionics*, vol. 176, no. 5-6, pp. 613–619, 2005. Copyright: Copyright 2011 Elsevier B.V., All rights reserved.

[184] H. Ibach, “Thermal expansion of silicon and zinc oxide (I),” *physica status solidi (b)*, vol. 31, no. 2, pp. 625–634, 1969.

[185] H. Ibach, “Thermal expansion of silicon and zinc oxide (II),” *physica status solidi (b)*, vol. 33, no. 1, pp. 257–265, 1969.

[186] F. Mousty, P. Ostoja, and L. Passari, “Relationship between resistivity and phosphorus concentration in silicon,” *Journal of Applied Physics*, vol. 45, no. 10, pp. 4576–4580, 1974.

[187] K. Nomura, H. Ohta, A. Takagi, T. Kamiya, M. Hirano, and H. Hosono, “Room-temperature fabrication of transparent flexible thin-film transistors using amorphous oxide semiconductors,” *Nature*, vol. 432, no. 7016, pp. 488–492, 2004.

[188] D. Zhang and H. Ma, “Scattering mechanisms of charge carriers in transparent conducting oxide films,” *Applied physics A*, vol. 62, no. 5, pp. 487–492, 1996.

[189] K. K. Chinnakutti, V. Panneerselvam, and S. Thankaraj Salammal, “Impact of Cu addition on the optoelectronic properties of Zn_3N_2 thin films: n to p-type transitions,” *Materials Science and Engineering: B*, vol. 265, p. 115039, 2021.

[190] K. J. Chang and M. L. Cohen, “High-pressure behavior of MgO: Structural and electronic properties,” *Physical Review B*, vol. 30, pp. 4774–4781, 1984.

[191] S. Yadavalli, M. H. Yang, and C. P. Flynn, “Low-temperature growth of MgO by molecular-beam epitaxy,” *Physical Review B*, vol. 41, pp. 7961–7963, 1990.

[192] S. Chambers, T. Tran, and T. Hileman, “Molecular beam homoepitaxial growth of mgo(001),” *Journal of Materials Research*, vol. 9, no. 11, p. 2944–2952, 1994.

[193] A. Bolokang, D. Motaung, C. Arendse, and T. Muller, “Structural transformation and surface properties of a new magnesium oxynitride upon annealing,” *Journal of Alloys and Compounds*, vol. 646, pp. 1143–1150, 2015.

[194] H. Nagai, “Structure of vapor-deposited $Ga_xIn_{1-x}As$ crystals,” *Journal of Applied Physics*, vol. 45, no. 9, pp. 3789–3794, 1974.

[195] E. C. Young, C. S. Gallinat, A. E. Romanov, A. Tyagi, F. Wu, and J. S. Speck, “Critical thickness for onset of plastic relaxation in (112-2) and (2021) semipolar AlGaN heterostructures,” *Applied physics express*, vol. 3, no. 11, p. 111002, 2010.

[196] E. C. Young, F. Wu, A. E. Romanov, A. Tyagi, C. S. Gallinat, S. P. DenBaars, S. Nakamura, and J. S. Speck, “Lattice tilt and misfit dislocations in (112-2) semipolar GaN heteroepitaxy,” *Applied physics express*, vol. 3, no. 1, p. 011004, 2010.

[197] A. Tyagi, F. Wu, E. C. Young, A. Chakraborty, H. Ohta, R. Bhat, K. Fujito, S. P. DenBaars, S. Nakamura, and J. S. Speck, “Partial strain relaxation via misfit dislocation generation at heterointerfaces in (Al,In)GaN epitaxial layers grown on semipolar (112-2) GaN free standing substrates,” *Applied Physics Letters*, vol. 95, no. 25, p. 251905, 2009.

[198] P. S. Hsu, E. C. Young, A. E. Romanov, K. Fujito, S. P. DenBaars, S. Nakamura, and J. S. Speck, “Misfit dislocation formation via pre-existing threading dislocation glide in (112-2) semipolar heteroepitaxy,” *Applied Physics Letters*, vol. 99, no. 8, p. 081912, 2011.

[199] V. Alberts, J. Neethling, and J. Vermaak, “Nucleation and growth of germanium on silicon (111),” *Journal of Materials Science: Materials in Electronics*, vol. 3, no. 4, pp. 240–243, 1992.

[200] M. Schreck and B. Stritzker, “Nucleation and growth of heteroepitaxial diamond films on silicon,” *physica status solidi (a)*, vol. 154, no. 1, pp. 197–217, 1996.

[201] S. Shinkai and K. Sasaki, “Epitaxial growth of HfN film and sequential single-oriented growth of Al/HfN bilayered film on (001) and (111) Si,” *Japanese journal of applied physics*, vol. 38, no. 6R, p. 3646, 1999.

[202] M. Moram, T. Joyce, P. Chalker, Z. Barber, and C. Humphreys, “Microstructure of epitaxial scandium nitride films grown on silicon,” *Applied Surface Science*, vol. 252, no. 24, pp. 8385–8387, 2006.

[203] C. Rouleau, S. Kang, and D. Lowndes, “Pulsed KrF laser deposited GaN/TiN/Si (111) heterostructures by sequential TiN and liquid Ga laser ablation,” *Applied Physics A*, vol. 69, no. 1, pp. S441–S445, 1999.

[204] V. M. Kaganer, R. Köhler, M. Schmidbauer, R. Opitz, and B. Jenichen, “X-ray diffraction peaks due to misfit dislocations in heteroepitaxial structures,” *Physical Review B*, vol. 55, pp. 1793–1810, 1997.

[205] V. M. Kaganer, O. Brandt, A. Trampert, and K. H. Ploog, “X-ray diffraction peak profiles from threading dislocations in GaN epitaxial films,” *Physical Review B*, vol. 72, p. 045423, 2005.

[206] V. M. Kaganer, O. Brandt, H. Riechert, and K. K. Sabelfeld, “X-ray diffraction of epitaxial films with arbitrarily correlated dislocations: Monte carlo calculation and experiment,” *Physical Review B*, vol. 80, p. 033306, 2009.

[207] V. M. Kaganer and K. K. Sabelfeld, “X-ray diffraction peaks from partially ordered misfit dislocations,” *Physical Review B*, vol. 80, p. 184105, 2009.

[208] V. Kaganer, T. Ulyanenkova, A. Benediktovitch, M. Myronov, and A. Ulyanenkov, “Bunches of misfit dislocations on the onset of relaxation of $Si_{0.4}Ge_{0.6}$/Si(001) epitaxial films revealed by high-resolution x-ray diffraction,” *Journal of Applied Physics*, vol. 122, no. 10, p. 105302, 2017.

[209] T. Metzger, R. Höpler, E. Born, S. Christiansen, M. Albrecht, H. P. Strunk, O. Ambacher, M. Stutzmann, R. Stömmer, M. Schuster, and H. Göbel, “Coherent x-ray scattering phenomenon in highly disordered epitaxial AlN films,” *physica status solidi (a)*, vol. 162, no. 2, pp. 529–535, 1997.

[210] M. Cho, A. Setiawan, H. Ko, S. Hong, and T. Yao, “ZnO epitaxial layers grown on c-sapphire substrate with MgO buffer by plasma-assisted molecular beam epitaxy (P-MBE),” *Semiconductor science and technology*, vol. 20, no. 4, p. S13, 2005.

[211] M. Becht, F. Wang, J. Wen, and T. Morishita, “Evolution of the microstructure of oxide thin films,” *Journal of Crystal Growth*, vol. 170, no. 1, pp. 799–802, 1997. Metalorganic Vapour Phase Epitaxy 1996.

[212] A. Boulle, R. Guinebretière, and A. Dauger, “Highly localized strain fields due to planar defects in epitaxial $SrBi_2Nb_2O_9$ thin films,” *Journal of Applied Physics*, vol. 97, no. 7, p. 073503, 2005.

[213] O. Durand, A. Letoublon, D. Rogers, and F. Hosseini Teherani, “Interpretation of the two-components observed in high resolution x-ray diffraction omega scan peaks for mosaic ZnO thin films grown on c-sapphire substrates using pulsed laser deposition,” *Thin Solid Films*, vol. 519, no. 19, pp. 6369–6373, 2011.

[214] R. I. Barabash, W. Donner, and H. Dosch, “X-ray scattering from misfit dislocations in heteroepitaxial films: The case of Nb(110) on Al_2O_3,” *Applied Physics Letters*, vol. 78, no. 4, pp. 443–445, 2001.

[215] P. F. Miceli and C. J. Palmstrøm, “X-ray scattering from rotational disorder in epitaxial films: An unconventional mosaic crystal,” *Physical Review B*, vol. 51, pp. 5506–5509, 1995.

[216] P. Miceli, J. Weatherwax, T. Krentsel, and C. Palmstrøm, “Specular and diffuse reflectivity from thin films containing misfit dislocations,” *Physica B: Condensed Matter*, vol. 221, no. 1, pp. 230–234, 1996. Proceedings of the Fourth International Conference on Surface X-ray and Neutron Scatterin.

[217] H. Heinke, V. Kirchner, H. Selke, R. Chierchia, R. Ebel, S. Einfeldt, and D. Hommel, “X-ray scattering from GaN epitaxial layers-an example of highly anisotropic coherence,” *Journal of Physics D: Applied Physics*, vol. 34, no. 10A, p. A25, 2001.

[218] T. Böttcher, S. Einfeldt, S. Figge, R. Chierchia, H. Heinke, D. Hommel, and J. S. Speck, “The role of high-temperature island coalescence in the development of stresses in GaN films,” *Applied Physics Letters*, vol. 78, no. 14, pp. 1976–1978, 2001.

[219] B. W. Sheldon, K. H. A. Lau, and A. Rajamani, “Intrinsic stress, island coalescence, and surface roughness during the growth of polycrystalline films,” *Journal of Applied Physics*, vol. 90, no. 10, pp. 5097–5103, 2001.

[220] J. A. Floro, E. Chason, R. C. Cammarata, and D. J. Srolovitz, “Physical origins of intrinsic stresses in Volmer-Weber thin films,” *MRS bulletin*, vol. 27, no. 1, pp. 19–25, 2002.

[221] G. Williamson and W. Hall, “X-ray line broadening from filed aluminium and wolfram,” *Acta Metallurgica*, vol. 1, no. 1, pp. 22–31, 1953.

[222] N. Mante, S. Rennesson, E. Frayssinet, L. Largeau, F. Semond, J. L. Rouvière, G. Feuillet, and P. Vennéguès, “Proposition of a model elucidating the AlN-on-Si (111) microstructure,” *Journal of Applied Physics*, vol. 123, no. 21, p. 215701, 2018.

[223] W. Paszkowicz, M. Knapp, J. Domagala, G. Kamler, and S. Podsiadlo, “Low-temperature thermal expansion of Mg_3N_2,” *Journal of Alloys and Compounds*, vol. 328, no. 1, pp. 272–275, 2001. Proceedings of the 5th International School and Symposium on Synchrotron Radiation in Natural Science.

[224] P. Kubelka and F. Munk, “An article on optics of paint layers,” *Zeitschrift für technische Physik*, vol. 12, no. 593-601, pp. 259–274, 1931.

[225] Y. Varshni, “Temperature dependence of the energy gap in semiconductors,” *Physica*, vol. 34, no. 1, pp. 149–154, 1967.

[226] R. J. Mendelsberg, M. W. Allen, S. M. Durbin, and R. J. Reeves, “Photoluminescence and the exciton-phonon coupling in hydrothermally grown ZnO,” *Physical Review B*, vol. 83, p. 205202, May 2011.